Optical fiber tools for single cell trapping and manipulation

Ana Rita da Silva Rodrigues Ribeiro
Doctoral program in Physics
2017

Supervisor
Pedro Alberto da Silva Jorge,
Invited auxiliary professor, Faculty of Sciences of the University of Porto
Senior researcher at INESC TEC

Co-supervisor
Ariel Ricardo Negrão da Silva Guerreiro,
Auxiliary professor, Faculty of Sciences of the University of Porto
Senior researcher at INESC TEC

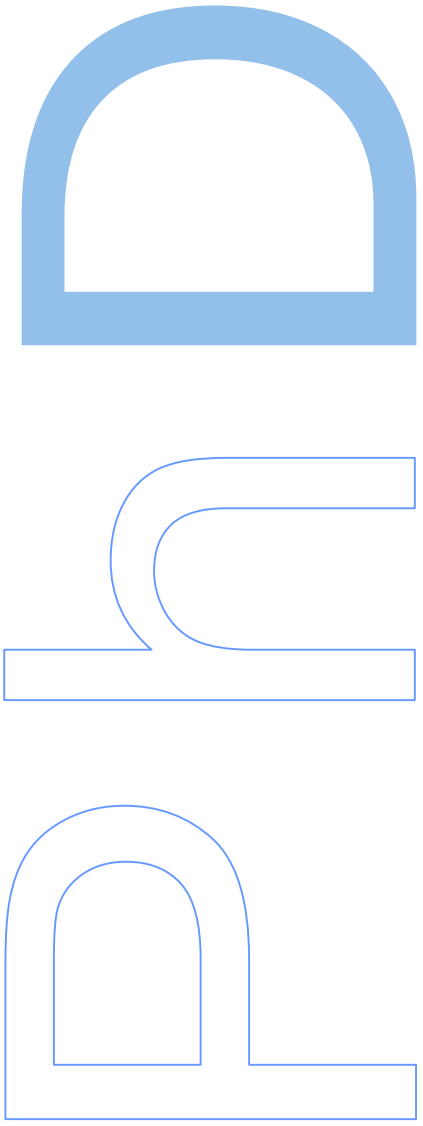

Optical fiber tools for single cell trapping and manipulation

Ana Rita Silva Rodrigues Ribeiro

Department of Physics and Astronomy

University of Porto

This dissertation is submitted for the degree of

Doctor of Philosophy

2017

Orientador
Pedro Alberto da Silva Jorge,
Professor Auxiliar Convidado do Departamento de Física e Astronomia,
Faculdade de Ciências da Universidade do Porto e Investigador Sénior no INESC TEC
Coorientador
Ariel Ricardo Negrão da Silva Guerreiro,
Professor Auxiliar do Departamento de Física e Astronomia,
Faculdade de Ciências da Universidade do Porto e Investigador Sénior no INESC TEC

Bolsa de investigação da Fundação para a Ciência e a Tecnologia com a referência SFRH/BD/87542/2012, financiada pelo POPH – QREN – Tipologia 4.1 – Formação Avançada, comparticipada pelo Fundo Social Europeu e por fundos nacionais do MCTES.

"Look closely at the present you are constructing:
it should look like the future you are dreaming."
Alice Walker

To my mother and my father
To my grandmother and my grandfather
To my sister
To Daniel

À minha mãe e ao meu pai
À minha avó e ao meu avô
À minha irmã
Ao Daniel

Acknowledgements

The process of pursuing a PhD degree in Physics was a long and joyful journey that I will always cherish for it has shaped the course of my life. This tremendous adventure could not have been possible without all the people, to whom I am sincerely grateful:

First of all, I would like to express my deepest gratitude to my supervisor, Prof. Pedro Jorge, for all the support, advices, friendship and opportunities given over these years. Specially for helping me shape this path allowing me to explore my ideas and never putting boundaries to my perseverance.

To Prof. Ariel Guerreiro, my co-supervisor, for always believing in me, for his support, friendship and knowledge passed down over the last years, which continuously helped me to successfully proceed.

To Prof. Jaime Viegas who provided me an incredible opportunity to join their team in Masdar Institute of Science and Technology, giving me access to the laboratory and research facilities, where I developed a challenging and crucial part of my PhD. I am also very grateful for all the support and friendship.

To Prof. José Luis Santos, for his wise words and for all the positivism transmitted since day one at INESC TEC! Not to forget, his essential guidance as advisor of the UP SPIE Chapter, during the year I was president.

To Prof. Paulo Marques for all the support and for the opportunities to present my research work within the COST action on Optofluidics, allowing me expand my horizons and to get to know more researchers in this area.

From INESC TEC and FCUP, to Dr. Irineu Dias, Prof. Carla Rosa, Prof. Manuel Joaquim Marques, Prof. Orlando Frazão, Prof. Orfeu Bertolami, Prof. António Pereira Leite. A special word of gratitude to Luísa Mendonça, who is always available to help!

From IS2M I thank Dr. Olivier Soppera for the fruitful collaboration within the development of the polymeric tips.

From Masdar Electron Microscopy, I appreciate all the time and help given by Dr. Cyril Aubry and Dr. Mustapha Jouiad during the long hours in the SEM/FIB.

I am grateful to Prof. Abel Oliva, from ITQB, for being the head of the project Hybrid that led me to this research area, and for plant cell samples provided to test the

polymeric optical fiber tips.

From CIMAR I thank Prof. Teresa Borges, for the microalgae samples, which I made spin with the vortex beams!

I would also like to acknowledge INESC TEC for the laboratory facilities where this work was developed. To FCT - Fundação para a Ciência e Tecnologia for my PhD fellowship (SFRH/BD/87542/2012), to Biophotonics Summer School, in Sweden, for the full scholarship allowing me to attend the event in 2013, to SPIE - the international society for optics and photonics for the officer scholarship, in the aim of UP SPIE Chapter, to attend Optics+Photonics 2014 and finally to FLAD - Fundação Luso-Americana for the scholarship to attend Photonics West 2015.

I thank my fellow lab mates and friends from INESC TEC, namely Raquel Queirós, Luís Coelho, Ivo Nascimento, Nuno Silva, Vitor Amorim, João Ferreira, Marta Ferreira, Carlos de Jesus and Ricardo André. I am specially grateful to Carlos who helped so much during my first years in INESC TEC, prior to my PhD. To Ricardo, we stepped into this journey together and together we will finish it! To us and to the great times we spent together, fighting towards the same direction, thank you for your friendship and patience!

During the months I was in Abu Dhabi my life would not have been the same without this amazing group of people! Thank you Judy, there are no words to express how welcome you made me feel! Thank you for everything! Raquel and Ricardo my portuguese friends from Abu Dhabi, thank you for all the support, friendship and good times in the lab (and beyond)! Thank you Marcus Dahlem, Peng Xing, Bruna Paredes, Ammar AlQahtani, Kenaish Al Qubaisi, Pabitra Dahal, Jason, Inas Taha, Soha Ekrima, Elangovan Elamurugu, Sueda Saylan, Hayk Gevorgyan and Ayat Taha. To the girls of Villa 14, Rocio Gonzalez, Hye Yeon Kim and Farah for making my time in Abu Dhabi so much more funny and enjoyable.

To all the people from 'Copa', Paula Quitério, Ana Pires, Ana Silva, Gonçalo Oliveira, Mónica Cerquido, Cátia Rodrigues e Pedro Rodrigues, with whom I usually have lunch, for making my days so much more funny! I am sorry if I let someone out! A special hug to Arlete Apolinário, with whom I shared so much more than lunch time since the old 'Copa' times, who listened to me so many times and with whom I had such an amazing time!

Não posso deixar de agradecer à minha prima Maria dos Anjos, por tudo o que fez por mim ao longo destes quase dez anos de FCUP. Estou especialmente grata por ter sempre um tempinho livre para me ouvir. Muito obrigada por tudo!

Em especial agradeço ao meu Pai e à minha Mãe, pela educação, valores, por todos

os concelhos dados ao longo dos anos, por estarem sempre presentes, por todo o amor que sempre me transmitiram, por acreditarem sempre em mim e por me incentivarem a ir mais longe. Tudo o que sou hoje, é devido a eles. Ao meu Avô, que sempre me ensinou a ter a cabeça erguida e a olhar em frente. À minha Avó por todo o seu carinho e bondade. À minha Irmã, a minha melhor amiga, pelo apoio, por me confrontar sempre com a verdade, e por estar sempre presente na minha vida, mesmo que longe.

Ao Daniel, o meu marido, um muito obrigada pelo amor, carinho e paciência que tem tido comigo ultimamente!

Por fim gostava de agradecer a toda a minha família por todo o apoio dado ao longos destes anos, nada teria sido da forma que foi sem todos eles.

Abstract

Through over 47 years of existence, the field of optical trapping has found no restrictions in extending across natural sciences, while fomenting cutting edge research. Currently, optical trapping setups rely on spacious and expensive microscopes, adapted to accommodate extra optical components to produce the desired optical trapping fields. Nevertheless, optical fibers are an attractive replacement offering compact and low cost solutions. Scaling down optical manipulation implicates transforming the optical fiber tips into special micro structures enabling the desired trapping by suitable intensity patterns (TIP). Therefore, this thesis draws on the development of optical fibers as platforms to produce adequate TIPs for manipulation of cells and micro particles.

In the first place, an overview of the state of the art of optical fiber TIPs is described, revealing the trending fabrication methods, most relevant findings and existing gaps in the literature. This leads to the following chapter, which presents some tools and techniques used throughout this thesis, that includes the experimental fabrication methods, a computational tool, based on finite difference time domain, to investigate the resulting optical beams and optical forces, and finally the methodology used to compute the optical forces.

Photo-polymerization of micro structures is presented at this point. This technique allows the fast production of low cost optical fiber TIPs. First, some preliminary experimental and computational results are shown regarding the micro structures designs and the materials used. Then, the polymeric optical fiber TIPs are characterized and validated by trapping yeast cells and organelles of plant cells.

In addition to the previous method, this thesis reports the fabrication of optical fiber TIPs by focused ion beam milling. Through this technique it is possible to carve micro structures with sub-wavelength resolution on optical fiber tips. First off, the potential of Fresnel zone and phase plates is explored. This covers computational studies, experimental beam profile measurements and implementation of phase plates for trapping and size-based detection of PMMA particles and yeast cells. With this technique also spiral phase plates were etched on single mode optical fibers, shaping the fundamental Gaussian mode into a Laguerre-Gaussian beam. Since these beams carry orbital angular

momentum, not only trapping but also rotation of polystyrene particles and microalgae were observed using an optical fiber with a spiral phase plate.

In general, the reported optical fiber configurations convey novel practical developments to the optical trapping area. In particular, at INESC TEC, these optical fiber TIPs will be the groundwork for further improvements towards biomedical studies.

Resumo

Durante os últimos 47 anos, a manipulação ótica tem sido aplicada em vários campos das ciências naturais, fomentando investigação de ponta. Atualmente, as configurações experimentais que são utilizadas para manipulação ótica são baseadas em microscópios adaptados com mais componentes óticos, tornando-se não só dispendiosos, mas também volumosos. No entanto, as fibras óticas são alternativas atrativas, uma vez que são compactas e de baixo custo. A miniaturização dos sistemas implica a transformação da extremidade das fibras óticas originando perfis de campo adequados para manipulação ótica. Desta forma, com esta tese pretende-se desenvolver novos dispositivos baseados em fibras óticas para manipulação de células e micropartículas.

Em primeiro lugar, é dada uma visão geral do estado da arte relativo às fibras óticas existentes para manipulação de micropartículas, sublinhando os principais métodos de fabricação, os resultados mais importantes e algumas lacunas existentes na literatura. Isto leva-nos ao capitulo seguinte, onde as ferramentas utilizadas ao longo desta tese são exploradas. Isto inclui os métodos de fabricação, o modelo computacional, baseado em diferenças finitas no domínio temporal, que tem como objetivo prever os perfis de campo e as distribuições de força ótica. Para além disto, é também apresentada a metodologia utilizada para calcular as forças óticas que atuam experimentalmente nas micropartículas e nas células.

Utilizando o método de foto-polimerização é possível obter fibras óticas com microestruturas para manipulação ótica de forma rápida e a baixo custo. Neste sentido, fizeram-se alguns estudos preliminares, quer experimental quer computacionalmente, de forma a explorar designs e as características dos materiais usados. Tendo estes aspetos em conta, as estruturas poliméricas que mais se mostraram adequadas, foram testadas para manipulação de leveduras e organelos dentro de células vegetais.

Para além do método anterior, foram também fabricadas microestruturas em fibras óticas através do feixe de iões focados. Esta técnica permite fabricar microestruturas com resolução inferior ao comprimento de onda. Desta forma, foram obtidas lentes de Fresnel com modulação em fase e em intensidade, as quais foram projetas computacionalmente e cujos perfis de campo foram estudados experimentalmente. Posteriormente, foram

testadas para manipulação e deteção de partículas de PMMA e leveduras, permitindo imobiliza-las e diferencia-las de acordo com o seu tamanho. De forma a explorar outros tipos de manipulação, fabricaram-se lentes em espiral, de forma a transformar o modo Gaussiano que se propaga em fibras monomodo, em feixes de Laguerre-Gauss, os quais têm momento angular orbital. Estas fibras óticas foram testadas com partículas de poliestireno e microalgas. Para além do aprisionamento ótico conseguiu-se também que as partículas e as microalgas rodassem. Isto deve-se à transferência de momento angular orbital do feixe para as partículas/microalgas.

No geral, as estruturas em fibra ótica apresentadas nesta tese contribuem de forma muito positiva para o progresso da área em si. No entanto são também muito relevantes para o estabelecimento desta técnica no INESC TEC, constituindo a base para trabalhos futuros na área da biomedicina.

Contents

Contents xvii

Nomenclature xxii

1 Introduction 1
- 1.1 Context of study . . . 1
- 1.2 Motivation . . . 4
- 1.3 Objectives . . . 5
- 1.4 Scientific achievements . . . 6
- 1.5 Structure of the thesis . . . 7
- 1.6 List of contributions . . . 8

2 Optical trapping using optical fibers 13
- 2.1 Introduction . . . 13
  - 2.1.1 Conventional optical tweezers setups . . . 16
  - 2.1.2 Applications . . . 19
  - 2.1.3 Discussion . . . 19
- 2.2 Towards optical fiber TIPs . . . 21
  - 2.2.1 Polishing . . . 22
  - 2.2.2 Thermal pulling . . . 24
  - 2.2.3 Chemical etching . . . 27
  - 2.2.4 High resolution micromachining . . . 29
  - 2.2.5 Other fabrication methods and OF configurations . . . 32
  - 2.2.6 Discussion . . . 35
- 2.3 Conclusion . . . 37

3 Methods and tools 39
- 3.1 Photo - polymerization method . . . 39
- 3.2 High resolution micro machining - FIB/SEM system . . . 41

3.2.1 Scanning electron microscope . . . 42
3.2.2 Focused ion beam . . . 43
3.2.3 Sample preparation and assembling . . . 46
3.2.4 System setup . . . 47
3.3 Numerical model . . . 49
3.4 Measurement of the trapping forces . . . 51
3.5 Conclusion . . . 53

4 Polymeric optical fiber TIPs 55
4.1 Background . . . 55
4.2 Fabrication methodology . . . 56
4.2.1 Considerations on the polymeric tip design . . . 56
4.2.2 Imprinting of optical modes on polymeric tips . . . 57
4.2.3 Polymeric tips with spherical profiles . . . 62
4.2.4 Discussion . . . 64
4.3 Computational simulations . . . 64
4.3.1 Towards 3D trapping . . . 70
4.4 Optical Trapping . . . 73
4.4.1 Fabrication of polymeric optical fiber tips for optical trapping . . . 73
4.4.2 Modeling the polymeric OF TIPs . . . 75
4.4.3 Optical manipulation setup . . . 77
4.4.4 Preliminary results on optical trapping of Yeast cells . . . 78
4.4.5 Optical trapping of organelles of plant cells . . . 79
4.4.6 Experimental measurement of optical forces . . . 80
4.4.7 Insights on particle sensing . . . 86
4.5 Conclusions . . . 87

5 Optical fiber TIPs using Fresnel zone and phase plates 89
5.1 Background . . . 89
5.1.1 Theory of Fresnel zone and phase plates . . . 90
5.2 Fabrication methodology . . . 92
5.2.1 Preparation of mode - expanded optical fibers . . . 92
5.2.2 Focused ion beam milling of Fresnel structures . . . 94
5.2.3 Fresnel zone plates . . . 97
5.2.4 Fresnel phase plates . . . 98
5.3 Optical characterization . . . 99
5.3.1 Fresnel zone plates . . . 100

5.3.2 Fresnel phase plates . . . 102
5.3.3 Discussion . . . 103
5.4 Optical Trapping . . . 106
5.4.1 Optical trapping setup . . . 106
5.4.2 Particles and cell samples . . . 107
5.4.3 Optical trapping of PMMA particles with a Fresnel phase plate . 107
5.4.4 Optical trapping of yeast cells . . . 115
5.4.5 Optical trapping of polystyrene beads . . . 116
5.4.6 Detection of trapped particles . . . 116
5.4.7 Discussion . . . 118
5.4.8 Optical trapping with Fresnel zone plates . . . 119
5.5 Conclusion . . . 121

6 Optical fiber TIPs with spiral phase plates 123
6.1 Background . . . 123
6.2 Modeling of the spiral phase plate . . . 126
6.3 Fabrication methodology . . . 128
6.4 Optical characterization of spiral phase plates . . . 131
6.4.1 Discussion . . . 135
6.5 Optical trapping and rotation . . . 135
6.5.1 Optical trapping setup . . . 135
6.5.2 Samples - particles and *microalgae* . . . 135
6.5.3 Rotation of $4\,\mu m$ polystyrene particles . . . 136
6.5.4 Rotation of $1\,\mu m$ polystyrene particles . . . 139
6.5.5 Rotation of microalgae *Tetraselmis suecica* . . . 142
6.5.6 Rotation of microalgae *Phaeodactylum tricornutum* . . . 143
6.6 Conclusion . . . 145

7 Conclusion and future work 147

References 151

A The Barnett model of microscopic forces 167
A.1 Lorentz force on dipoles . . . 167

B Diode laser and optical fibers specifications 171
B.1 Diode laser . . . 172
B.2 Optical fibers . . . 172

C Optical trapping video files **175**

Nomenclature

2D	2-dimensions
3D	3-dimensions
ABS	absorbing boundary conditions
COT	conventional optical tweezers
cw	continuous wave
DOE	diffractive optic element
FDTD	finite diferences time domain
FIB	focused ion beam
FPP	Fresnel phase plate
FWHM	full width at half maximum
FZP	Fresnel zone plate
Ga	gallium
GIF	graded index fiber
HF	hydrofluoric acid
HOT	holographic optical tweezers
LMIS	liquid metal ion source
LSFM	light sheet fluorescent microscopy

MEEP MIT electromagnetic equation propagation

MMF multi mode fiber

NA numerical aperture

NIR near infra-red

OAM orbital angular momentum

OF optical fiber

OVs optical vortices

PBS phosphate buffered saline

PML perfectly matched layers

PMMA poly(methyl methacrylate)

PS polystyrene

Pt platinum

RBC red blood cell

SAM spin angular momentum

SEM scanning electron microscope

SLM spacial light modulator

SMF single mode fiber

SNOM scanning near-field optical microscopy

SPP spiral phase plates

STED stimulated emission depletion

TEM transmission electron microscope

TIP trapping intensity patterns

TPL two photon lithography

W tungsten

WDM wavelength division multiplex

Chapter 1

Introduction

1.1 Context of study

Johannes Kepler was the first who perceived the effect of radiation pressure. He observed that comet tails are pushed away from the sun, as published in *De Cometis Libelli Tres* in 1619 [1]. This, together with the advent of the microscope, were fundamental discoveries that paved the way to optical trapping of micro and nanosized objects, such as particles, cells and molecules. The chronology of the main breakthroughs that led to this work can be followed in figures 1.1 and 1.2.
Nevertheless, it was only in 1970, after the invention of the laser, that optical trapping was demonstrated for the first time, by A. Ashkin. Optical trapping occurs due to the transference of momentum from photons to matter, resulting in a set of forces, that, in certain conditions, can be balanced [2].

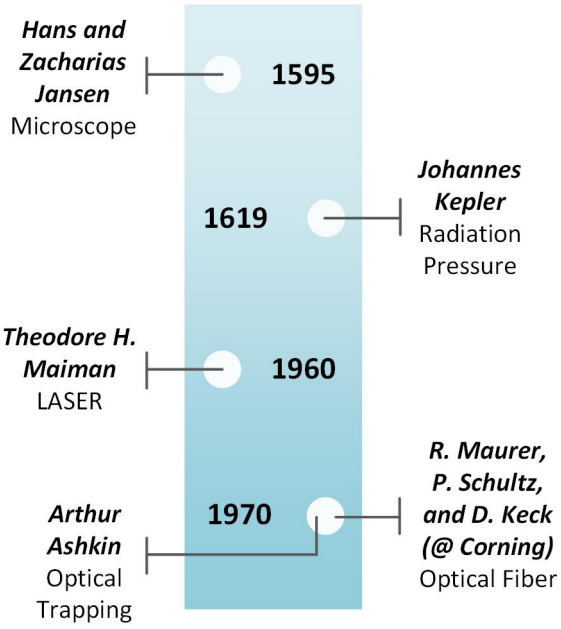

Figure 1.1: Event's chronology (part 1).

In this seminal work, micron-sized particles were immobilized between two counter propagating laser beams, due to the balance of radiation pressure effects. In 1986 the trapping of dielectric particles was accomplished by using a single tightly focused laser beam. This effect is commonly named as optical tweezers. The development of optical trapping setups based on common microscopes continued to increased at a high rate. At the same time, optical fiber (OF) based manipulation setups that excluded bulk optical elements had their advent in the early 1990s [3]. With these setups, simple optical trapping alternatives at a low cost and with a reduced footprint, became available. The first configuration was based on two counter propagating beams using two OF pigtailed sources [3]. Later, in 1995, the use of lensed fibers became obvious to two pioneering research groups [4, 5]. Ever since, optical fiber based configurations have been receiving critical attention leading to the proliferation of this research area.
In the meantime, the concept of microfluidics, which is the science and technology of systems that study and manipulate fluids at the sub millimeter scale, emerged [6].

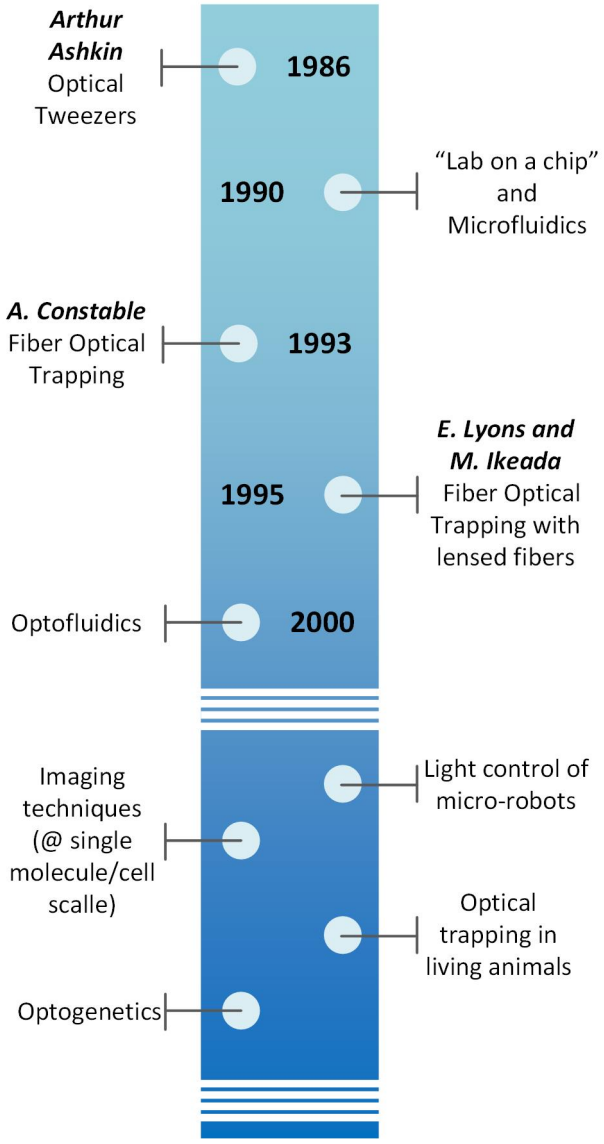

Figure 1.2: Event's chronology (part 2).

This broad area of research was primarily motivated by molecular analysis, biology, biodefense and microelectronics, in order to develop portable devices for environmental monitoring, medical diagnosis and chemical weapon detection [7, 8]. Simultaneously, the progress in miniaturized photonics, driven by the tremendous growth on the number of available micro fabrication techniques, led to the integration of optics within the previous fluidic platforms. This is known as optofluidics, and refers to the manipulation of fluids and light at the micro scale [9]. The synergy between fluids and optics improves the answer to demanding areas, such as biomedicine and chemistry. To do so, the platforms

include micro and/or nanofluidic channels and photonic elements like waveguides, optical fibers, lasers, resonators, lenses, etc [10, 11]. With this in mind, optofluidic sensors based on refractive index detection, fluorescence, surface-enhanced Raman spectroscopy, particle trapping and manipulation, are nowadays available [12].

Nano fabrication techniques, such as direct laser writing or two photon lithography, enabled the fabrication of micro objects with non arbitrary forms. The micro objects that are sculpted with particular features may be manipulated by means of normal or modified laser beams, depending on their structure and functionality [13, 14]. These tools can be implemented in the context of optofluidics, for instance, as microrotors inside micro pumps [15], or micro robots [16], working as micro syringes to deliver drugs at specific locations. The complexity and variety of micro object shapes, as well as optical field patterns opens a large number of possible configurations with potential applications within areas such as cell sorting and separation, rheology, drug delivery, among others.

Over the years, optical trapping techniques have also been implemented with imaging apparatus, such as stimulated emission depletion (STED) and light sheet fluorescent microscopy (LSFM). STED is a nano resolution imaging acquisition process, which is able to distinguish labeled proteins and protein filaments present in high density DNA, while conventional optical tweezers are use to control the conformation and tension on the DNA, by means of a double trapping point system [17]. In this case, thermal fluctuations are overcome by the use of optical tweezers, allowing sub diffraction imaging, and at the same time STED microscopy allows to have nano scale visualization of the force-dependent behavior of DNA-protein interactions. Concerning LSFM, this imaging technique uses a thin sheet of light to illuminate the sample, while fluorescent images are acquired at 90^{o}, originating images of the specimens in three dimensions [18]. While the acquisition speed of this process is increased by the simplicity of the setup, it also causes reduced photo-bleaching and photo-damage to the samples. Recent advances in this powerful imaging technique combined it with a optical trapping setup based on counter-propagating laser beams [19]. This provides more freedom regarding the sample preparation and manipulation during the acquisition process, whereas previously the samples had to be stabilized in agents such as agarose that restricted further development of living samples.

Other potential use of optical tweezers is to manipulate cells inside living animals. Normally the experiments are performed in environments mimicking the medium where the cells may be immersed, however, this does not accurately reproduce the structural body features. In this regard, manipulation of red blood cells in a ear capillary of a

mouse and manipulation of nano particles and cells inside a zebrafish, were already reported [20, 21].

Nonetheless, photonics does not cease to thrill and keeps on spreading throughout other fields. For instance, physicists and geneticists are now working together towards the development of optogenetics, the field that combines optics and genetics to accurately control proteins and cellular function using light [22].

Since the discovery of optical trapping the expectations in relation to its applicability and versatility have been very high. The increase in the number of publications, and the reported developments have proved the value of optical trapping tools leading to their widespread use.

1.2 Motivation

Optical manipulation tools have already exceeded the boundaries of research laboratories, being commercialized by some companies, such as, Thorlabs [23], Nikon [24], Zeiss [25] and Elliot Scientific [26]. Some setups rely on microscopes that are adapted to accommodate necessary optical components, while others are composed by modular parts. The first setups are indicated for professionals who want ready to use equipment, whereas modular ones are suggested for academic environments allowing easy customization. However, a closer look into these type of setups reveals some drawbacks. The acquisition costs are high, the systems are far beyond portability and have a large footprint. Therefore, one question that needs to be asked is whether there is an alternative to surpass these constrains. One solution might well be optical fiber based manipulation setups. Apart from their miniaturized size, low cost, and versatility, OF setups are likely to be implemented in micro chips. Otherwise, can also be used as transitory platforms where micro structures/lenses are developed and tested, and then are implemented in waveguides, or micro channels, within optofluidic chips.

Despite these fundamental aspects, our attention was drawn towards the use of OFs for optical trapping due to a former project, which aimed to develop a microfluidic chip for electric and optical analysis of red blood cells (RBCs) [27]. The goal of this project was to have an hybrid platform where measurement of electric impedance, refractive index, absorption and fluorescence was attainable. The optical measurements were carried out using OFs in a Fabry-Perot configuration, also useful to collect the absorption and fluorescent signals. Although validated to analyze fluids, some limitations were found regarding the measurement of particles and cells features. Most of the times, either the particles/cells were flowing too fast to be detected by the acquisition unit, or were not

located in front of the OF core. From the moment that these obstacles were identified, some improvements were implemented in the chip, notwithstanding, it seemed obvious that parallel to the optimization of the chip configuration, the development of a tool capable of immobilizing the target cells/particles was of utmost value. Since OFs were already being used inside the optofluidic chip, the idea was to maintain the use of the fibers, although outside the optofluidic chip (figure 1.3). This established the starting point of the development of OF based systems for cell manipulation at Center for Applied Photonics in INESC TEC, where that technology was not yet available.

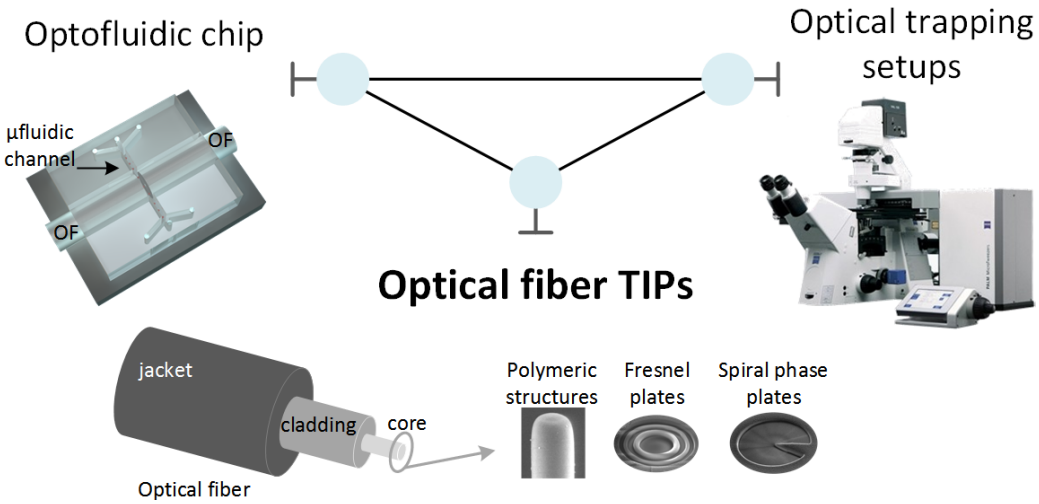

Figure 1.3: Research on OF TIPs was driven by the need to develop a tool for optical trapping, that could easily be integrated in an optofluidic chip. In this regard, the idea was to overcome the large size of bulk optical trapping setups, and try to scale down these setups towards the development of special structures on OF tips. Image of optical tweezers setup adapted from reference [25].

1.3 Objectives

The vision behind this thesis is supported by the development of the filed of optical fiber trapping over the years and the recent trends identified in today's research.

> *In a nutshell, the aim of this thesis is to develop trapping systems based on optical fibers to trap and manipulate micro particles and biological cells.*

The methodology to accomplish this challenge was organized into the following main tasks:

- Development of a computational tool to study the optical fiber configurations prior to their fabrication and understand the main physical parameters and phenomena behind the effect of optical trapping;
- Assembling of a setup to test the fabricated optical fiber structures;
- Design and fabrication of several structures using photo-polymerization and focused ion beam milling methods;
- Analysis of the output optical beam profiles;
- Test of the structures for optical trapping of dielectric particles and cells;
- Characterization of the optical trapping forces exerted by the OF TIPs.

OF TIP

At this point, it is necessary to clarify what is meant by the acronym TIP, since it will be constantly used thorough this manuscript. It stands for *trapping intensity patterns* and is normally used in the form of *OF TIP*. This refers to an optical trapping device based on an optical fiber, whose extremity is modified to produce intensity patterns suitable for optical manipulation. Athough the words are the same, *TIP* should not be confused with *tip* (extremity). Indeed, the game of words is intentional, the focus of the work was to modify optical fiber tips to produce suitable TIPs.

1.4 Scientific achievements

The research conducted over the last years in the framework of this thesis led to a number of novel scientific contributions, summarized as follows.

- **OFs with polymeric micro structures for optical trapping of yeast cells and organelles within plant cells** - Single polymeric optical fiber micro structures had been widely explored for light coupling and sensing, however, trapping applications had not yet been encompassed by the time this research work started. Studying the fabrication features involved in the process, the output geometrical characteristics and the resulting optical features led to the optimization of the micro structures. This allowed the successfully implementation of polymeric micro structures for optical trapping of yeast cells and organelles within plant cells. In this regard, the field of optical fiber based trapping counts with a novel economic and fast process, with high reproducibility and good optical quality throughputs.

- **Optical trapping and detection of micro particles and cells using OFs with Fresnel phase plates** - The fabrication of more elaborated structures on optical fiber tips rely on high resolution methods, such as focused ion beam milling. Although expensive and time consuming this method allows tailoring the optical fibers into designs otherwise impossible. With this in mind, Fresnel zone and phase plates were fabricated on optical fiber tips. Optical trapping and detection of micro particles and cells were attained using Fresnel phase plates.

- **Trapping and rotation of particles and microalgae using OFs with spiral phase plates** - The previous trapping methods allowed optical trapping through linear momentum transference, leading to the immobilization of the targets and consequent 2D movement. However, the focused ion beam milling of spiral phase elements on optical fibers enables the generation of optical vortices allowing the rotation of the trapped micro objects. This thesis not only reports the fabrication of such structures as well as the rotation movement imparted on the trapped targets (dielectric particles and microalgae). Unlike other optical fiber configurations, the developed devices do not need external modulation, relying only in the geometry of the structure milled on the top of the fiber.

1.5 Structure of the thesis

This thesis is organized in seven chapters, with the following contents:

Chapter 1 gives a brief overview of the context of this thesis, also including the motivation and objectives. Besides this, the resulting scientific publications are presented.

Chapter 2 describes the basic theory of optical trapping, some considerations on how to assemble an optical manipulation setup, and the main uses of such tool. After this, the state of the art on trapping using OFs are described and compared, concerning their fabrication method and main achievements.

Chapter 3 is dedicated to the methods and tools used in this research process. Therefore, it includes a brief description of the computational tool, the fabrication methods, photo polymerization and focused ion beam milling, the method used to calculate the experimental optical forces and some other aspects that may be needed for the understanding of this thesis.

In **chapter 4** the process of design, modelization and fabrication of polymeric OFs is described. Then, the OFs are tested for trapping of yeast cells and organelles of plant cells.

Chapter 5 details the process of design, modelization, fabrication and test of Fresnel zone and phase plates for optical trapping and detection of particles and yeast cells using optical fibers.

In **chapter 6** the design, fabrication and test of spiral phase plates are reported in the framework of optical manipulation and rotation of particles and microalgae.

Finally, in **chapter 7** the conclusions are drawn, and future work is described.

1.6 List of contributions

Over the duration of this research work were published six research articles in peer reviewed international scientific journals, one book chapter, one article in a portuguese science divugation journal, five articles in international conferences with oral presentation, seven articles in international conferences and other eight oral presentations. Also the work presented at Photonics West 2016 - Complex Light and Optical Forces was awarded the Best Oral Presentation.

Articles in International Scientific Journals:

1. R. S. Rodrigues Ribeiro, A. Guerreiro, J. Viegas and P. A. S. Jorge, Rotation of microparticles and microalgaes using a vortex beam generated by a spiral phase plate micromachined in an optical fiber, Opt. Lett. (in submission).

2. R. S. Rodrigues Ribeiro, P. Dahal, A. Guerreiro, P. A. S. Jorge, and J. Viegas, Fabrication of Fresnel plates on optical fibers by FIB milling for optical trapping, manipulation and detection of single cells, Nat. Sci. Rep. 7, 4485 (2017).

3. R. S. Rodrigues Ribeiro, P. Dahal, A. Guerreiro, P. Jorge, and J. Viegas, "Optical fibers as beam shapers: from Gaussian beams to optical vortices," Opt. Lett. 41, 2137 (2016).

4. F. Pereira, I. Bernacka-Wojcik, R. Ribeiro, M. Lobato, E. Fortunato, R. Martins, R. Igreja, P. Jorge, H. Águas, and A. Oliva, "Hybrid Microfluidic Platform for Multifactorial Analysis Based on Electrical Impedance, Refractometry, Optical Absorption and Fluorescence," Micromachines 2016, 7, 181 7, 181 (2016).

5. R. S. R. Ribeiro, O. Soppera, A. G. Oliva, A. Guerreiro, and P. A. S. Jorge, "New Trends on Optical Fiber Tweezers," J. Light. Technol. 33, 3394–3405 (2015). *Invited contribution to the special issue on Biomedical Applications of Lightwave Technologies.*

6. R. Ribeiro, R. Queirós, O. Soppera, A. Guerreiro, and P. Jorge, "Optical Fiber Tweezers Fabricated by Guided Wave Photo-Polymerization," Photonics 2015 2, 634–645 (2015).

Book chapters:

1. R. S. Rodrigues Ribeiro, J. Viegas, O. Soppera, A. Guerreiro, and P. A. S. Jorge, "Advanced fabrication of fiber optic microstructures for single cell trapping and manipulation", "Optical Fiber", InTechOpen ISBN 978-953-51-5672-7 (in submission).

Science divulgation:

1. O. Bertolami, R. S. Rodrigues Ribeiro, L. Coelho, R. André, "Luz: História, Natureza e Aplicações", Edição especial Ano Internacional da Luz, Gazeta de Física, 39 (2016).

Articles in International Conferences with oral presentations:

1. R. S. Rodrigues Ribeiro, P. Dahal, A. Guerreiro, P. A. S. Jorge, and J. Viegas, "Compact solutions for optical fiber tweezers using Fresnel zone and phase lenses fabricated using FIB milling," in SPIE OPTO, J. Glückstad, D. L. Andrews, and E. J. Galvez, eds. (International Society for Optics and Photonics, 2016), p. 97640C. - **Best Oral Presentation**

2. R. S. Rodrigues Ribeiro, P. Dahal, A. Guerreiro, P. A. S. Jorge, and J. Viegas, "Generation of Laguerre Gaussian beams using spiral phase diffractive elements fabricated on optical fiber tips using focused ion beam milling," in SPIE OPTO, J. Glückstad, D. L. Andrews, and E. J. Galvez, eds. (International Society for Optics and Photonics, 2016), p. 97640Q.

3. R. S. Rodrigues Ribeiro, O. Soppera, J. Viegas, A. Guerreiro, and P. A. S. Jorge, "The efficiency of fiber optical tweezers for cell manipulation using distinct fabrication methods," in Spie Opto, E. J. Galvez, J. Glückstad, and D. L. Andrews, eds. (International Society for Optics and Photonics, 2015), p. 93790N.

4. R. Janeiro, R. Flores, R. S. Rodrigues Ribeiro, P. Jorge, and J. Viegas, "Focused ion beam 3D nano-patterned optical fiber tips for advanced beam profile engineering," in SPIE OPTO, G. von Freymann, W. V. Schoenfeld, R. C. Rumpf, and H. Helvajian, eds. (International Society for Optics and Photonics, 2015), p. 93740E.

5. R. S. Rodrigues Ribeiro, R. B. Queirós, A. Guerreiro, C. Ecoffet, O. Soppera, and P. A. S. Jorge, "Fiber optical beam shaping using polymeric structures," in OFS2014 23rd International Conference on Optical Fiber Sensors (International Society for Optics and Photonics, 2014), p. 91573K–91573K–4.

Articles in International Conferences with poster presentations:

1. R. S. Rodrigues Ribeiro, A. Guerreiro, J. Viegas, and P. A. S. Jorge, "Special diffractive elements for optical trapping fabricated on optical fiber tips using the focused ion beam," in Sixth European Workshop on Optical Fibre Sensors, E. Lewis, ed. (2016), p. 99161N.

2. R. S. Rodrigues Ribeiro, O. Soppera, A. Guerreiro, and P. A. S. Jorge, "Polymeric optical fiber tweezers as a tool for single cell micro manipulation and sensing," in OFS2015 24rd International Conference on Optical Fiber Sensors, H. J. Kalinowski, J. L. Fabris, and W. J. Bock, eds. (2015), p. 96342K.

3. R. S. Rodrigues Ribeiro, R. B. Queirós, C. Ecoffet, O. Soppera, A. Oliva, A. Guerreiro, and P. A. S. Jorge, "Rapid fabrication of polymeric micro lenses for optical fiber trapping and beam shaping," in SPIE NanoScience + Engineering, K. Dholakia and G. C. Spalding, eds. (International Society for Optics and Photonics, 2014), p. 91642M.

4. R. S. Rodrigues Ribeiro, P. A. S. Jorge, and A. Guerreiro, "New developments on the design and modeling of fiber optical tweezers," in 8th Ibero American Optics Meeting/11th Latin American Meeting on Optics, Lasers, and Applications, M. F. P. C. Martins Costa, ed. (International Society for Optics and Photonics, 2013), p. 8785F9.

5. R. S. Rodrigues Ribeiro, A. Guerreiro, C. Ecoffet, O. Soppera, and P. A. S. Jorge, "New theoretical and experimental methods for the design of fiber optic tweezers," in Fifth European Workshop on Optical Fibre Sensors, L. R. Jaroszewicz, ed. (International Society for Optics and Photonics, 2013), p. 87941P–87941P–4.

6. R. S. Rodrigues Ribeiro, 'Towards optofluidic systems for single cell manipulation and analysis', Biophotonics'13 Summer School (June, 2013).

7. R. S. Rodrigues Ribeiro, P. A. S. Jorge, A. Guerreiro, 'Optimization of optical trapping of nanoparticles in medical chips', Nano Portugal 2013 - Nanoscience and Nanotechnology International Conference, Porto, Portugal (February, 2013).

Other oral presentations in the framework of this thesis:

1. R. S. Rodrigues Ribeiro, Optical Fibers for beam shaping and trapping, MAP-Fis conference at University of Aveiro, Aveiro, Portugal (July, 2016).

2. R. S. Rodrigues Ribeiro, Generation of optical vortices using optical fibers with spiral phase plates, Recent Trends in Modern Optics (Invited Talk), Porto, Portugal (June, 2016).

3. R. S. Rodrigues Ribeiro, New Trends on Optical Fiber Tweezers, Cost Meeting, MPNS COST Action MP1205 Advances in Optofluidics, Milan, Italy (October, 2015).

4. R. S. Rodrigues Ribeiro, New Trends on Optical Fiber Tweezers, papers@dfa, Department of Physics and Astronomy, Faculty of Sciences University of Porto, Portugal (November, 2015).

5. R. S. Rodrigues Ribeiro, Optical Fibers Tweezers, MAP-Fis conference at University of Minho, Braga, Portugal (June, 2015).

6. R. S. Rodrigues Ribeiro, Fiber based optical tweezers, from fabrication to manipulation. Cost Meeting, MPNS COST Action MP1205 Advances in Optofluidics, Porto, Portugal (May, 2015).

7. R. S. Rodrigues Ribeiro, Micromanipulação celular usando fibras óticas, Física 2014, Instituto Superior Técnico, Lisboa, Portugal (Setembro, 2014).

8. R. S. Rodrigues Ribeiro, Optofluidic devices for single cell manipulation, New Challenges in the European Area: Young Scientist's 1st International Baku Forum, Baku, Azerbaijan (May, 2013).

Chapter 2

Optical trapping using optical fibers

The goal of this thesis is to develop optical fiber based tools for particle/cell trapping and manipulation. With this in mind, this chapter aims to introduce the fundamentals on this subject, necessary to the unfolding of this work. Therefore, it describes the basic theory of optical trapping, some considerations on how to assemble an optical manipulation setup, and the main uses of such tool. After this, the need to scale down these type of setups is stressed, and optical fiber trapping based systems are presented. In this regard, a review of the state of the art of optical manipulation using optical fibers is given. This section highlights the main fabrication methods (polishing, chemical etching, thermal pulling and high resolution methods, such as focused ion beam milling and two photon lithography) used to tailor optical fibers into suitable trapping tools, focusing on the advantages and drawbacks of each method. Finally, some brief conclusions are outlined.

2.1 Introduction

Optical trapping was first reported by Arthur Ashkin in 1970, when micron-sized particles were stably trapped between two counter propagating beams due to the radiation pressure effects [2]. Later, in 1986, A. Ashkin demonstrated the same effect using a single tightly focused optical beam, also named as Optical Tweezers, to successfully trap particles in the nano to micrometer size range [28]. The optical force (picoNewton) acting on a dielectric particle is caused by the momentum transference from the reflection and refraction of the beam on the particle surface leading to a stable immobilization. From a different point of view, the radiation pressure causes the particle to propel along the optical axis, while the gradient of the light field draws the target to the beam axis.

The description of the optical forces depend on the ratio of the particle radius and

the laser wavelength. For the case where the particle is smaller than the wavelength, the Rayleigh formulation is used, and the particles are considered as point dipoles. On the contrary, for particles larger than the wavelength, the problem is within the ray optics limit, and the forces arise from the sum of the reflected and refracted ray components. Regarding the first formulation, conventionally, the total force can be decomposed in two components: the scattering force and the gradient force [29]. The **scattering force** is proportional to the intensity of the electric field, therefore, it is responsible for pushing the particles away from the beam. Considering a sphere of radius r, the scattering force is expressed as follows

$$F_{scatt} = \frac{I_0 \sigma n_m}{c}, \tag{2.1}$$

where I_0 is the intensity of the incident beam, σ is the scattering cross section of the sphere, n_m is the refractive index of the medium and c is the speed of light in vacuum. The scattering cross section of the sphere is given by

$$\sigma = \frac{128\pi^5 r^6}{3\lambda^4} \left(\frac{m^2 - 1}{m^2 + 2} \right)^2, \tag{2.2}$$

where λ is the beam wavelength and m is the ratio between the refractive index of the particle and the medium, $m = \frac{n_p}{n_m}$. The **gradient force** is proportional to the gradient of the intensity of the electric field, resulting in the redirection of the particles towards the highest intensity region. It is described by

$$F_{grad} = \frac{2\pi\alpha}{c n_m^2} \nabla I(x), \tag{2.3}$$

where α is the polarizability of the particle, represented by

$$\alpha = n_m^2 r^3 \left(\frac{m^2 - 1}{m^2 + 2} \right). \tag{2.4}$$

In the case of the two counter propagating beams, the balance of the axial scattering forces from the two beams is crucial to attain a stable trap. However, in the case of the single beam trapping, the gradient force plays the major role. Whenever the gradient of the light intensity is steep enough, the axial component of the gradient force can exceed the scattering force, establishing the conditions for attractive forces and zones of zero net force to arise, enabling 3D trapping effects. An illustration of the scattering and gradient forces exerted by a strongly focused laser beam are depicted in figure 2.1.

From the geometrical optics point of view, the optical forces acting on a micro particle

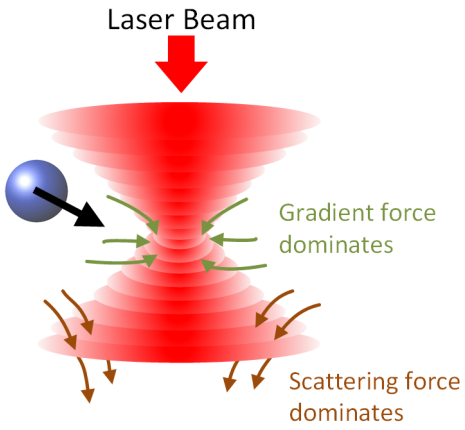

Figure 2.1: Optical immobilization of a particle is achieved by highly focused laser beams. Gradient forces are responsible to redirect the particle into the focal volume, while light pressure pushes it out along the optical axis. When gradient force prevails, the particle can be trapped in 3D in the focal region.

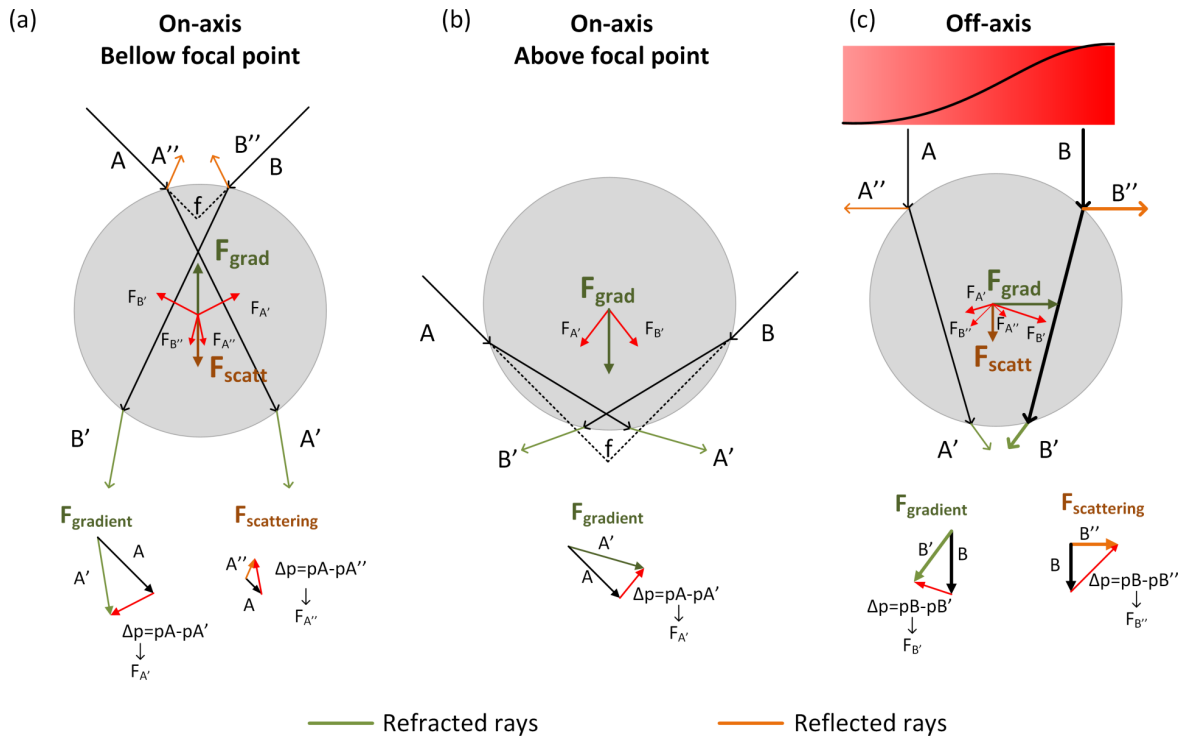

Figure 2.2: Geometrical representational of optical trapping. (a) Axial forces acting on a particle that is located bellow the focal point. (b) Axial restoring forces acting on a particle positioned above the focal point. (c) Lateral restoring forces acting on the particle towards the beam focus. (not to scale)

can be represented as depicted in figure 2.2. In figure 2.2 (a) the particle is located on-axis bellow the focal point, represented by f. Two rays, A and B hit the surface of the sphere being reflected and refracted. The reflected rays $A^{''}$ and $B^{''}$ are responsible for the scattering force F_{scatt}, through the momentum change represented by forces $F_A^{''}$ and $F_B^{''}$. At the same time, the refracted rays, $A^{'}$ and $B^{'}$, exiting the particle, originate forces $F_A^{'}$ and $F_B^{'}$ causing a restoring movement towards the focal position, F_{grad}. The nature of these forces is described by Newton's 3^{rd} law: the beam momentum change ($\triangle p$) caused either by reflection or refraction, corresponds to an equal in opposite direction momentum change imparted on the sphere. In figure 2.2 (b) the particle is located on-axis above the focal point. In this case, through the momentum transference from rays, $A^{'}$ and $B^{'}$ the particle is redirect downwards. In this case both F_{grad} and F_{scatt} contribute to drive the particle towards the focus. Finally, in figure 2.2 (c) the particle is off-axis and two beams with distinct intensities, A and B act upon the particle, where $B > A$. The force on the dielectric particle is proportional to the beam light intensity. In this scenario, the particle is driven towards the center of the Gaussian light distribution.

Trapping efficiency

The trapping is usually qualified by the efficiency factor described by the dimensionless coefficient, Q, which is given by [29]

$$Q = \frac{cF}{n_m P}, \tag{2.5}$$

where P is the power of the trapping beam and F is the force exerted on the particle. In this expression, the quantity $\frac{n_m P}{c}$ represents the fractional momentum transference per photon.

2.1.1 Conventional optical tweezers setups

The implementation of an optical trapping apparatus, as the one depicted in figure 2.3, usually relies on the following elements:

laser source - single mode, continuous wave (cw), with low power fluctuations and high point stability [30]. To avoid optocution[1], a suitable wavelength should be picked. According to the graph of figure 2.4, water absorption is minimized in the near infra-red (NIR) range. Because of this, there are many biological samples which are less absorptive in this region of the spectrum. Both solid state and diode lasers

[1] Damage in the sample caused by laser absorption.

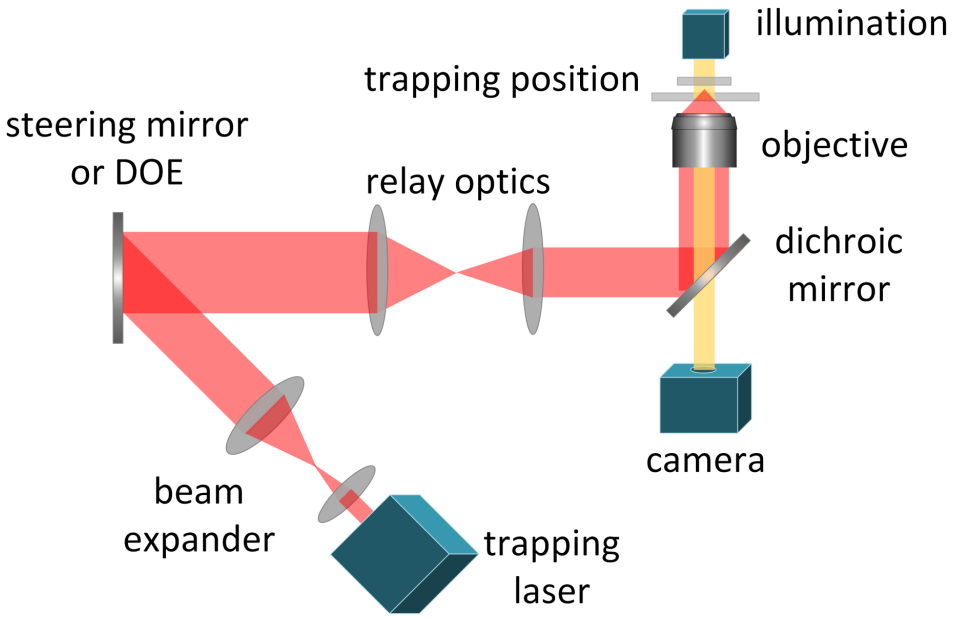

Figure 2.3: Conventional optical tweezers setup. This is composed by the trapping laser, which is first expanded and then imaged onto the back aperture of the objective. The steering mirror can be replaced for a diffractive optical element, enabling higher complexity in the degree of manipulation of the specimen. The relay optics is used to move the trapping position without further affecting the beam. The objective has a high NA, producing tightly focused laser beams. There is also a complementary visualization system to assist the trapping experiments.

have been used in trapping experiments. Examples of solid state lasers are Nd:YAG and Nd:YLF, operating at $1064\,nm$ and $1053\,nm$, respectively, while diode lasers based on GaAs semiconductors may be tuned at a wavelength between $630\,nm$ and $1100\,nm$. Normally, in trapping experiments the laser sources have powers in the $1-100\,mW$ range, although the smaller the power the less damage it will cause in the samples. However, for every trapping experiment using biological samples, it is advised to do a study of the damage on the specimen caused by the selected wavelength.

optical components to expand and steer the beam - the laser beam is expanded, to ensure that the back aperture of the microscope objective is filled. Beam steering and relay optics controls the displacement of the beam at the specimen plane with the guarantee that the filling of the objective pupil plane does not change.

Figure 2.4: Water absorption spectrum. Graph adapted from reference [31].

objective - high numerical aperture (NA) objective (typically ≥ 1.0), this maximizes the beam gradient nearby the focal region, contributing to a stable trap in 3-dimensions (3D).

observation system and **sample holder.**

These systems are usually adapted to conventional inverted optical microscopes, by externally coupling the laser beam to the objective [30]. In alternative to conventional optical tweezers (COT), complex structured light fields have demonstrated to be of great importance in achieving higher degrees of manipulation and control. This can be attained using the so-called holographic optical tweezers (HOT) by means of computer generated holograms, which are typically achieved via spatial light modulators (SLM). Figure 2.3 shows that the adaptation of the setup relies on replacing the steering mirror by the SLM. The SLM can be replaced by other diffractive optic element (DOE). These kind of configurations enable the generation of special tailored optical beams such as Hermite-Gaussian, Laguerre-Gaussian, non-diffracting beams (e.g Bessel Beams), to name a few. As a consequence, building up HOT systems promotes the versatility of more advanced optical trapping devices including, for instance, multi point optical traps or the use of beams carrying optical angular momentum [32].

2.1.2 Applications

Historically, the applicability of optical tweezers extends from fundamental disciplines such as atomic physics to broadband areas, such as biomedicine. The current literature on cooling and manipulation of atoms, supported by optical trapping tools, reports huge advances in this area [33–35]. For instance, a device based on nano structured optical gratings for magneto-optical trapping of atoms was recently demonstrated [36], opening new opportunities to introduce this technology into more complex environments, such as atomic clocks. In the case of biomedicine there is an overwhelming number of evidences corroborating how advantageous optical trapping can be as an advanced manipulation tool. The use of optical tweezers can be applied for precision measurements ranging from the molecular to the cellular level. In the first case, for example, optical trapping can be used to measure the mobility of enzymes or molecular motors in the dynamics of DNA [37]. In the second, optical trapping at the cellular level (red blood cells, yeast cells, plant cells) has provided ample support in a variety of applications on single cell manipulation, stretching, sorting, among others [38–40]. Further improvements include the integration of imaging and spectroscopic setups into trapping platforms [41, 42]. The progress and new applications of optical tweezers have been extensively reviewed by several authors [30, 43, 44]. In 2013, cutting edge improvements were reported by Zhong *et al.* where evidences of trapping and manipulation of in vivo red blood cells in a living mice ear capillary [20] were shown. Likewise, Johansen and co-workers used a zebrafish to explore trapping of nanoparticles and cells inside a living animal [21]. Zebrafishes are advantageous over other animals, since they are optically transparent and can be modified to have fluorescent cells. In their research, the authors found out that it was possible to trap nanoparticles and red blood cells and move them against the direction of the blood flow. Together, these two studies outline the critical role that optical tweezers play in understanding cell interaction inside living animals.

Since the advent of optical trapping in 1970, the number of patents and publications in the optical trapping field have been gradually increasing, as shown in the plots of figures 2.5 and 2.6. On the basis of the evidences currently available, it seems fair to suggest that optical tweezers are one of the most promising tools for micro and nano manipulation.

2.1.3 Discussion

Although significant results have been achieved using COT setups, their utilization is still limited in quite a few environments. For instance, the use of COT systems, which

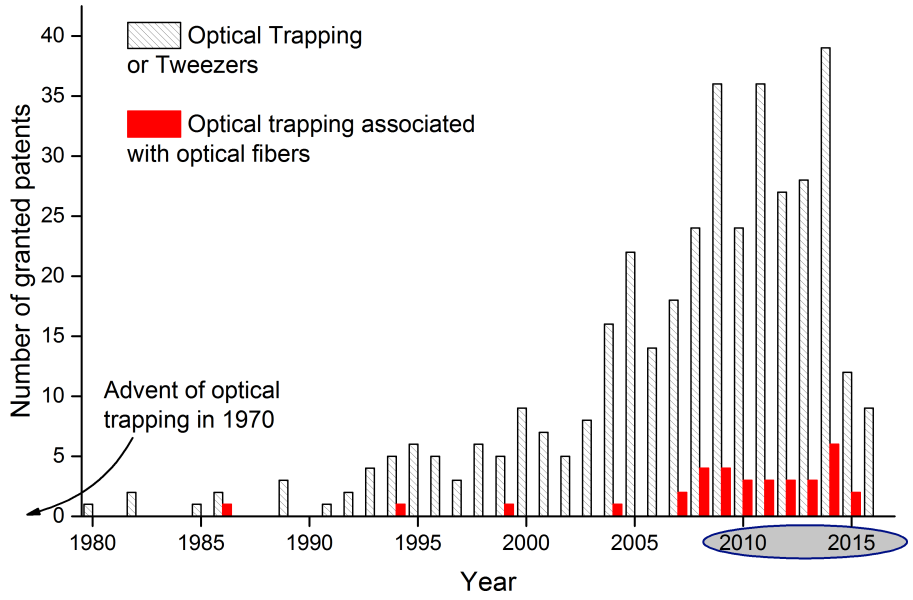

Figure 2.5: Granted patents since 1980 in optical trapping. In patterned black, search using "optical trapping", or "optical tweezers", or "optical forces" or "laser tweezers". In red, the search was done using the previous key words and "optical fibers". These data were acquired in the https://app.patentinspiration.com/ database. (Information acquired on January 28^{th} 2017)

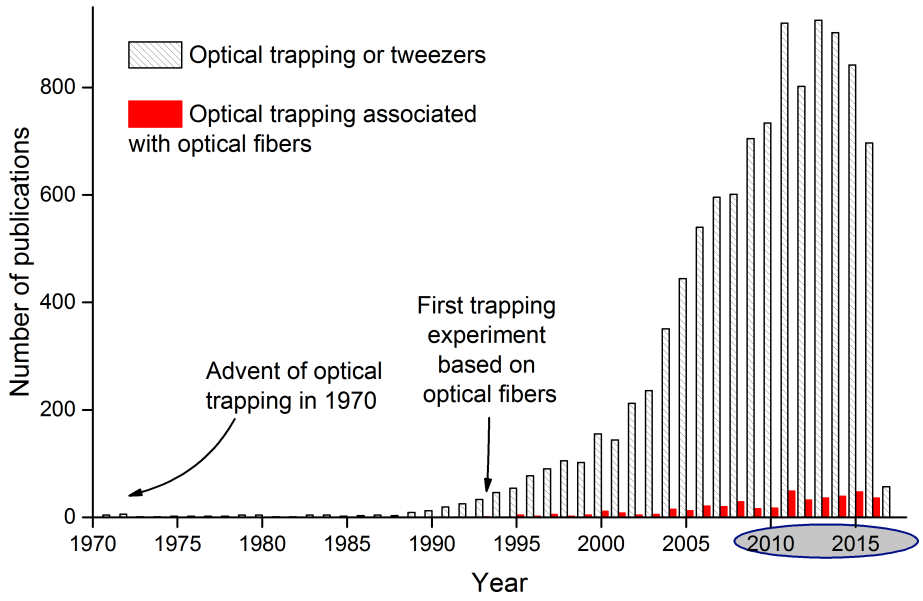

Figure 2.6: Publications on optical trapping (papers and proceedings). In patterned black, search using "optical trapping", or "optical tweezers", or "optical forces" or "laser tweezers". In red, the search was done using the previous key words and "optical fibers". These data were acquired in scopus database. (Information acquired on January 28^{th} 2017)

normally have small working distances difficult the focusing of the optical beams in thick samples or turbid media. In addition, cost and portability issues are also obstructions for their widespread use. Conversely, the implementation of optical trapping setups using optical fibers enables miniaturization and low cost systems. OF tweezers can be integrated in small devices such as optofluidic platforms or catheters introducing the extra versatility needed for more challenging applications in medical and biological environments [45]. OF trapping was presented for the first time in 1993 by Constable *et al.* [3]. The manipulation of two counter propagating beams using two pigtailed optical sources was the base for the development of optical trapping without external bulk optical elements. In 1995 two pioneering systems were described by Lyons and Sonek [4] and by M. Ikeda *et al.* [5]. Both configurations were based on lensed OFs. The first consisted in two counter propagating beams originated from two fibers with spherical tips, which reinforced the tweezing effect, and the second involved just a single lensed OF. Since then, increasingly sophisticated optical fiber based configurations have been reported exploring a range of fabrication techniques.

Presently, in spite of great progress, challenges remain in fulfilling the combination of fiber optics versatility with more advanced trapping and manipulation functions in the context of biological applications. The graphs presented in figures 2.5 and 2.6, present the number of patents and publications dedicated to optical trapping using OFs. Although the numbers are not as high as the ones regarding COT and HOT, it is notorious a continuous interest in this type of implementation over the last decade or so.

The remaining of this chapter will be dedicated to present an overview of the state of the art of optical trapping using optical fibers, focusing on the main fabrication methods, their features and main achievements in optical trapping. Most recent progresses, main challenges and current trends will be briefly discussed.

2.2 Towards optical fiber TIPs

The trapping and manipulation capabilities that can be attained with a given OF probe are tightly linked with the optical and geometrical features of the fiber tip. In this regard, it is the reliability and versatility of the fabrication technique that determines what can be achieved. While reproducibility and processing simplicity are highly desirable features, the ability to obtain complex shapes is mandatory for some applications. Ideally, both would be available with low cost and rapid processing times, however, most often compromises must be made. Presently, a diversity of well-established fabrication

techniques are being explored in the fabrication of different configurations for optical trapping using OFs. Polishing, chemical etching, thermal pulling, focused ion beam (FIB) milling and femtosecond laser machining are surely the most important ones. Whereas polishing, chemical etching and thermal processes are essentially low cost techniques, they are often limited to conical and/or spherical tip designs. In contrast, micro fabrication techniques that use FIB milling or two photon polymerization processes allow fabrication of more complex structures, but have the drawback of being expensive and time consuming. Ultimately the goal is to have strong focusing effects at the fiber tip, thus enabling stronger optical forces. This allows to operate tweezers with lower optical power, a critical aspect in many biological applications. In this section a description of these key fabrication techniques will be presented, highlighting their main features and drawbacks together with some relevant progresses reported in the literature.

2.2.1 Polishing

Grinding and polishing is an economical and simple method to micro machine OFs. It has been extensively used in the fabrication of optical fiber connectors and is also an important manufacture process of OF sensors [46, 47]. In the context of OFs for trapping applications, it is a suitable process for micro machining OFs to obtain lensed profiles. Indeed, the first OF for trapping reported in the literature by M. Ikeda *et al.* in 1995 was fabricated using this method [5]. The hemispherical profile used by the authors is the most commonly reported with this fabrication method [48]. One of its main advantages is keeping the guiding characteristics of the waveguides. The focusing of the output light is obtained by reshaping of the fiber tip profile. First studies in this area reported on polishing tips of standard single mode optical fibers into spherical-like profiles enabling the 2D and 3D trapping of dielectric particles and yeast cells.

With this method curvature radius of some micrometers can be attained. The data gathered by some authors indicates that, with a curvature radius of $2\,\mu m$, a minimum of $1.3\,mW$ is necessary to trap a $10\,\mu m$ polystyrene particle [48]. However, if the curvature radius increases to $6\,\mu m$, reducing the focusing power, a minimum of $2.5\,mW$ is required to trap the same particle. Nevertheless, in spite of the small curvature radius, the typical fiber modal profile and refractive index characteristics often result in weakly focused beams, producing relatively small optical forces. For this reason, the spatial arrangement of the polished OFs, namely the angle and trapping distance, are critical and determine the ability to stably trap the particles. Furthermore, it has been reported that a single OF is able to trap particles only in the transversal plane, and dual or multiple fiber configurations are required to levitate the particles against the force of gravity, enabling

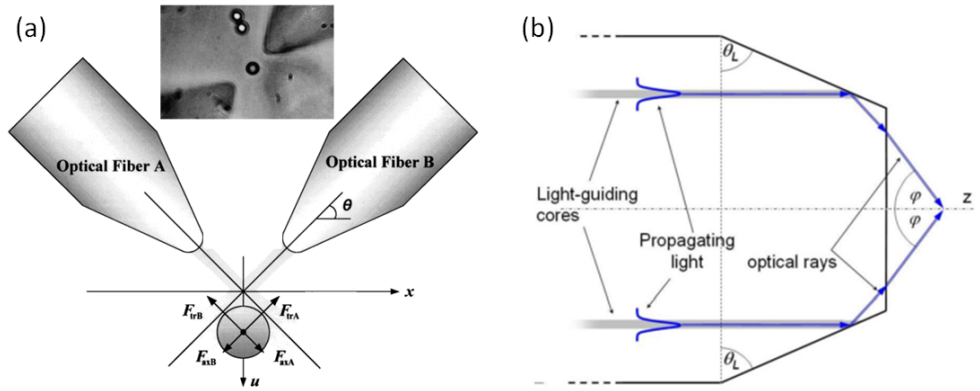

Figure 2.7: Schemes illustrating two different types of OF tweezers fabricated by polishing methods. (a) In this work, K. Taguchi and co-workers adapted two OFs to produce a 3D point trap. The low NA of a single OF is overcome by placing the two fibers in a tilted configuration. Figure adapted from reference [49]. (inset) Trapping of a microsphere with $6\,\mu m$ of diameter by the dual-OF configuration. Figure adapted from reference [50]. (b) Using an optical fiber with a dual-core, by polishing the top edges of the OF tip, both beams emerging from each separated core are directioned to a single position, where OT is possible to occur. Figure adapted from reference [51].

3D trapping [50, 52]. These studies demonstrated that dual OFs inserted at 35^o are able to trap particles located on the bottom of a sample container, and to levitate and move them around. This demonstrates that an equilibrium point can be reached, where the force of gravity and buoyancy, the gradient and scattering forces, all balance. Figure 2.7 (a) demonstrated the arrangement used for the OFs in the dual configuration. In the inset of this figure, an image of the trapping of a microsphere of $6\,\mu m$ of diameter, using a diode laser at $1480\,nm$, is shown. To circumvent the limitations arising from low focusing power, studies on plural arrangements (two or more fibers) of hemispherical lensed fibers have been performed. Multiple fibers allow not only a more effective trapping, with lower optical powers, but also introduce extra manipulation capabilities like the possibility to rotate non-spherical micro-objects [53]. This rotation effect is caused by the momentum of the force (torque) and is mainly controlled by switching on and off the different OFs. More recent trends include the use of special optical fibers introducing the possibility to obtain more advanced configurations by polishing. A multiple core fiber in an annular-distribution (e.g. two, three, or four cores), or even annular-core optical fibers, when polished at certain angles can be restructured to obtain stable trapping devices. The requirement for trapping using multiple beams of light from multiple cores is that the propagation direction of the multiple beams must intersect with an exact angle. To do so, the optical fibers are polished at specific grinding angles, yielding outputs with fixed

convergence angles. The optical beams that are guided through the individual cores are reflected by the edge of the fiber [54]. This causes their intersection at a certain distance from the extremity of the fiber, where the trapping is bound to occur. The scheme of figure 2.7 (b) depicts the working principle of this type of configuration. This work was also reported in a patent [55]. It was shown that there is a dependence of the working distances of these OFs with the grinding angle that can be explored in the optimization of the tweezer operational characteristics [56]. With such designs was demonstrated the 2D trap of single yeast cells, in the transversal plane. Further experiments using an annular core fiber with a grinding angle of 18^o have enabled the trapping of a large sphere with $45\,\mu m$ diameter. More recently, Zhao *et al.* computationally demonstrated the potential to use an OF with four cores, as a tool to oscillate particles [57]. In this case, the fiber was modeled to have each pair of opposing cores polished with the same grinding angle, causing two trapping positions. Each pair of cores was connected to the same laser. Alternating the lasers on and off with a certain period, caused the oscillatory movement of the particle ($5\,\mu m$ radius). Using this micro oscillator the authors claim that this OF configuration has potential to be used in microfluidic platforms, in fiber sensing, for instance, for biomedicine or other related areas. The same research group also developed an OF with an annular core, based on the polishing method, for trapping and excitation of oil drops [58]. In this case, the trapping was performed at $980\,nm$ and then the oil droplets was excited using a pulsed $502\,nm$ laser. Lasing at approximately $600\,nm$, depending on the drop size, was achieved. This work proves the versatility of OFs for trapping applications, and further implementation prospects.

To summarize, polishing is a reproducible process but somewhat delicate due to the small size of the tips. It allows to obtain micro lenses with good optical quality and small curvature radius and is compatible with batch processing. However, due to intrinsic characteristics of standard fibers the resulting OFs have low focusing power requiring the use of higher optical power to enable effective trapping effects. Nevertheless, it has been shown that using multiple tweezers can improve trapping abilities. In addition, more recent trends are establishing polishing of special multi core OFs as a method to obtain more versatile optical trapping devices.

2.2.2 Thermal pulling

The heating and drawing process is frequently employed in the fabrication of tapered OFs. These structures are normally used as evanescent optical sensing probes, since the core of the fibers is also tapered exposing the optical field to the surrounding medium [59]. In the context of OF trapping, the heating process can be used to fabricate micro

lenses on the extremity of optical fibers. Like the polishing and etching processes, this is also a relatively simple and inexpensive fabrication method, widely explored in the context of OFs for trapping applications. The heating process, which can be carried out by a flame, a CO_2 laser or an electric arc is applied to soften the fiber near the melting point. Simultaneous pulling, in a controlled fashion, allows to obtain distinct adiabatic or abrupt taper profiles. Adiabatic tapers usually result in very small focusing distances. To obtain devices with higher working distances, usually multistep drawing stages are required. The control of the final tip shape is very delicate as it depends on the fiber breaking. The technique is not amenable to batch processing. Nevertheless, several authors have reported distinct applications using different types of thermal tapers.

In 2006, Z. Liu *et al.* explored the use of an abruptly single mode tapered optical fiber, for 3D trapping of yeast cells in water, manufactured by heating and drawing technology [60]. The fiber was primarily heated and right away drawn. By changing the drawing speed from $0.03\,mm/s$ to $0.32\,mm/s$ the diameter of the fiber was reduced from $125\,\mu m$ to about $10\,\mu m$ with a length of $600\,\mu m$. This tapered section of the fiber was subsequently drawn at $1.6\,mm/s$ until the fiber broke in the waist position. Consequently, a parabola-like profile, with a curvature radius of approximately $5\,\mu m$ (estimated from the picture in reference [60]) was formed at the fiber tip due to the surface tension of the fused silica. With this probe the 3D trapping of yeast cells was achieved. After this work several others reported similar fabrication procedures of OFs for trapping [61, 62]. The main difference among the fiber probes reported rely on the final optical fiber taper profiles and their focusing capabilities. Wright *et al.* demonstrated that laser beams with a beam waist superior to $0.7\,\mu m$ cannot 3D trap dielectric particles [63]. Therefore, this is a crucial parameter that will define if the 3D trapping can or not be achieved by a given OF. In 2007, Abedin *et al.* developed an OF trapping tip, based on a bismuth OF [64]. In this case, the high refractive index of the bismuth OF, 2.22, decreases the spot size of the resulting focused beam, when compared with a silica fiber. Simultaneously, the refractive index difference, between the medium and the OF, allows to have higher focal distances, with lower spot sizes, allowing the manipulation of larger particles. This probe was tested for trapping and rotation of nematic liquid crystal drops in water. By controlling the polarization of the incident light beam, the liquid crystal drops were rotated, and due to the backscatered light acquired, the rotation motion was analyzed.

Later on, H. Xin *et al.* demonstrated the manipulation capabilities of a tapered OF [65] with a hemispherical tip of $1.6\,\mu m$ diameter. Exploring the effects of push, pulling and trapping at different distance of the focal point, the OFs were used to perform trapping and arrangement (linear chains) of multiple particles [66]. Also, a

sharper probe ($380\,nm$ diameter) was used in a microfluidic platform to study E-coli bacteria dynamics [61]. Rather than a standard taper a more abrupt profile yielding larger focusing distances and enabling truly contactless trapping of E-coli bacteria [62] was tested. In this particular case, the fiber tip, submitted to a multi-step drawing process, had a protruding tip, which caused a tighter focusing and the extension of the trapping region. Thus, E-coli bacteria ($1.7\,\mu m$ length and $500\,nm$ diameter) were trapped without physical contact and a detailed study on the bacteria dynamics was performed: the motility of the bacteria and the conditions for a stable trap were evaluated. Please see figures 2.8 (a) and (b). More recently, the group of Dr. Li employed two tapered fibers to study the rotation and deformation of red blood cells (RBCs) [67], as depicted in figures 2.8 (c) and (d). In this experiment they reported that one fiber was used as a contact point. The RBC was first trapped. During the trapping there was contact with the cell, therefore, after turning the laser off, the RBC adhered to the fiber tip due to Van der Wall forces. The second fiber was used to rotate the RBC. Translating the OF caused the trapping of distinct sections of the RBC, hence rotating it in relation to the fiber. The authors also demonstrated the stretching of multiple RBCs, by using two counter propagating tapered fibers system.

To reduce the necessary optical power to trap a single particle, OFs fabricated by the heating and drawing method based on the use of multiple core fibers, can be used. In this method the multiple core fibers are tapered, resulting in multiple beam interference at the hemispherical tip. In such cases, besides reducing the optical power required for trapping, the interference features may be used to attain a higher degree of control. For instance, Yuan *et al.* reported the use of a dual core OF for single particle manipulation, where the lensed fiber is linked to a Mach-Zehnder interferometer [68]. By bending the interferometer, the phase of the beams is modified and the orientation of the particle is changed, due to changes on the output field distribution. In this case the optical power threshold was $1\,mW$ and the experiments were carried out using a maximum of $5\,mW$ that produced a $5\,pN$ force. More recently, Barron *et al.* reported a lensed four core OF for manipulation of multiple particles simultaneously [69]. In this case the interference of the four beams formed a square lattice profile, located at approximately $250\,\mu m$ from the fiber tip, where the maximum of intensities is separated from each other by $2.75\,\mu m$. In this case the particles were trapped in the high intensity points of the lattice, enabling simultaneous multiple traps.

To sum up, thermal pulling methods enable a diversity of tapered profiles. However, to attain versatile OFs for trapping purposes, somewhat delicate multi-step fabrication processes are often required precluding batch processing. Nevertheless, the use of mul-

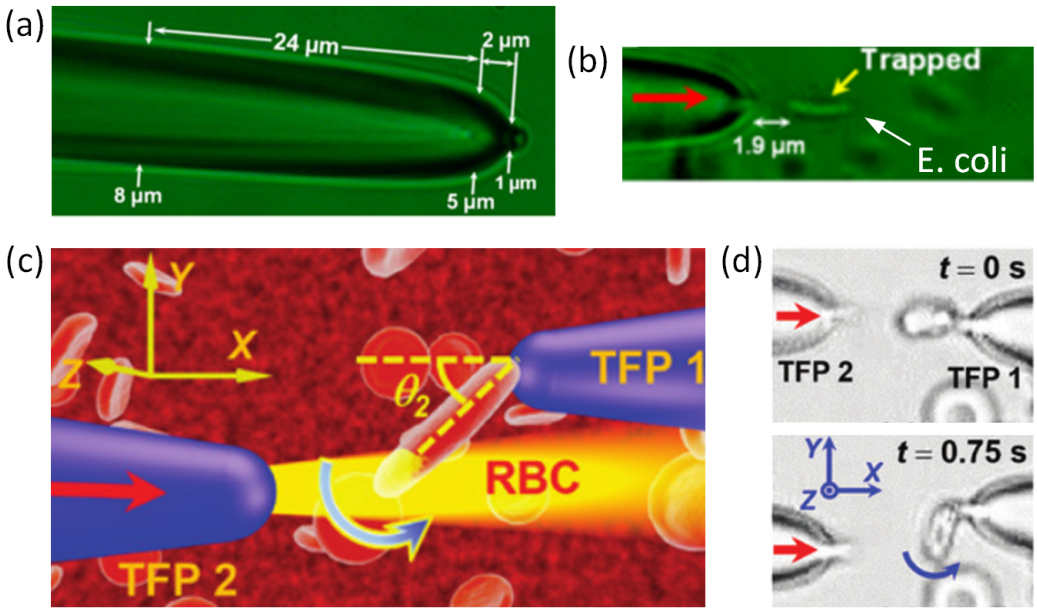

Figure 2.8: Examples of trapping of an E-coli bacteria and a RBC. (a) Tapered fiber tip fabricated using the heating method in a two step process. The tip of the fiber is shaped into a narrow spherical tip. This causes a short focal distance, of approximately $1.5\,\mu m$. (b) Trapping of an E-coli bacteria, using a $980\,nm$ laser source. Figures (a) and (b) were adapted from reference [62]. (c) Using a similar probe, fabricated by the same heating and drawing two-step method, the rotation of a RBC is performed. In this case, the authors use two probes. One is used as a contact point, holding the RBC by Van der Waals force. The other, moves the RBC by trapping it in distinct points. (d) Images of the RBC atatched to one of the probes, and then being rotated by means of an optical force. Figures (c) and (d) were adapted from reference [67].

ticore OFs is now allowing trapping probes with higher degrees of control.

2.2.3 Chemical etching

Chemical etching methods have been extensively employed in the fabrication of tapered fiber probes for Scanning Near-Field Optical Microscopy (SNOM). Etched fiber tips also play an important role in a diversity of sensor applications [70–72]. It is a well-established method, compatible with batch processing and relatively simple to implement at a low cost. Nevertheless, it can be time consuming and requires the use of very dangerous chemicals, such as hydrofluoric acid (HF). Reproducibility and low surface roughness can be obtained only at the expense of a tight control of processing and environmental parameters such as temperature, concentration and vibration. Also, the accumulation or diffusion of reaction products can play a critical role in the outcome

and should be carefully considered. Often improved control requires the use of extra chemicals or alternative techniques such as gas phase etching [73]. In spite of these challenges, etching methods are very attractive in the context of OF trapping as they allow obtaining conical surfaces at the fiber tip. Conical tips with adequate parameters are the precursors of axicon lenses, which enable the generation of Bessel beams. These are highly attractive for trapping applications as they can maintain their tight focus characteristics for extended ranges, even after interacting with the target particle. Such features enable, for instance, to simultaneously trap several particles. In the aim of OF trapping two main techniques are used for fabrication of conical axicon tips: the liquid protection layer, or 'Turner method' [74, 75], and a variation called the tube etching method [76]. In the first method the optical fiber is immersed in a HF solution having a protection overlay of a lower density organic liquid, typically silicon oil. In this case, the fiber tip is formed at the interface between the etchant solution and the protection layer. The taper is formed due to the gradually reducing height of the meniscus as the fiber diameter is reduced by the etchant solution. This is a self-terminating process where the relative surface tensions determine the meniscus features and the resulting tip angle. Modifications of this process, such as use of different overlay materials, or multi step etching, allow to set different tip profiles. In the second process, the fiber is immersed in the etchant solution without removing the polymer coating. Therefore, the etching occurs inside the fiber buffer layer, where micro convection and transient capillary effects concur for a more stable etching process. Indeed, tube etching was shown to be more insensitive to environmental parameters resulting in tips with lower surface roughness. The cone angles obtained were mostly dependent on the type of fiber used.

In 2008, Mohanty *et al.* described the use of an axicon optical fiber, produced using the tube etched method, for the trapping of low refractive index particles [77]. The apex angle of the fiber tip was approximately 17^o, producing an output beam with a doughnut profile (minimum at the center surrounded by a symmetric maximum). This allowed the 3D trapping of the water droplets in an acetophenone solution ($5\,\mu m$ to $9\,\mu m$ in diameter), at large distances from the fiber (tens of micrometers), and using optical powers in the range of $17\,mW$ to $30\,mW$. The authors concluded that placing the fiber horizontally would cause only an axial trapping of the droplets, but if the probe was fixed at angle (45^o) or vertically, both axial and transverse trapping could be achieved. This demonstrated that at an angle, the scattering force can be balanced with the buoyancy force, contributing for stable trapping in the transverse direction.

Studies of the influence of the apex angle on the working distance (near filed or far field) of the OF have also been reported [78]. An axicon with an apex angle of

60^o produced an output Bessel beam profile demonstrating stable trapping of multiple particles arranged in a linear chain, at $5\,\mu m$ from the fiber tip, at $146\,mW$ (far field trapping). For smaller apex angles, $\leq 30^o$, there is a total internal reflection effect on the conical tip. This way, the amount of light transmitted through the fiber is decreased and the trapping of particles can only be attained very close to the fiber surface (near field trapping).

While it is relatively easy to obtain axicon lenses with a broad range of apex angles using the methods just described, the diversity of shapes fabricated with standard fibers is relatively limited. Nevertheless, more recently, new studies using chemical etching of different fibers promise more sophisticated configurations to get axicon like profiles. A segment of graded index fiber (GIF) spliced to the end of a standard single mode fiber and subsequently etched [79] allows to obtain different tip profiles. The authors pointed out that the use of a GIF, which produces a periodically self-focusing effect may increase the trapping efficiency when compared with conventional OFs. Also, since the etching rate depends of the fiber doping profile, using special fibers with pre-optimized refractive index profiles can be a route to easily obtain exotic tip shapes using etching methods. Such approach has been explored in the design of some sensing devices and is bound to be a new trend to explore in the context of trapping with OFs [80].

In a nutshell, chemical etching is a well-established low cost technique, requiring a tight control of processing parameters. It is a straightforward method to obtain axicon tips using standard fibers, and it holds great promise for more sophisticated shapes if fibers with special doping profiles are made available.

2.2.4 High resolution micromachining

High resolution micromachining techniques available nowadays allow to directly write complex patterned structures in a diversity of substrates. While such methods are usually associated with very expensive instrumentation, and are often time consuming, they are unique choices for advanced prototyping and test of new devices. Regarding OF trapping, micromachining techniques are still little explored. Nevertheless, representative examples are reported using FIB milling and two photon lithography (TPL).

The FIB is a method that enables simultaneous micro/nano imaging, deposition and controlled milling. It is usually inserted in a double system composed by an ion Ga^+ ion source and an electron source, the so-called scanning electron microscope (SEM) [81, 82]. The SEM enables image acquisition through the scanning of the sample using a focused electron beam. Whereas, in the FIB system the Ga^+ ions are accelerated to and focused in the sample surface. The ions are accelerated by means of a differential

voltage and are focused using special electrostatic lenses. The accelerated ions allow milling away the substrate material with resolutions of the order of a few nanometers.

FIB micromachining tools have been used to accurately fabricate special structures on the top of optical fibers, allowing to improve some of the features achieved so far using lenses fabricated by more conventional methods. In a pioneer work, FIB milling technique was used in the fabrication of very precise axicon lenses to produce high quality Bessel beams. The tweezers fabricated in this way were used for successfully trapping $2\,\mu m$ polystyrene beads, and water bubbles of different sizes, at different distances from the fiber tip [83]. The authors were able to solve some issues regarding the linearity of the milling process by carefully adjusting the ion dose along the designed pattern. While focusing on a model structure such as an axicon, the quality of the results clearly demonstrated the potential of FIB tools for prototyping more complex tweezers. In 2007, an innovative OF tweezer configuration was reported by Liberale *et al.* [84, 85]. In this work a high numerical aperture OF bundle was presented and validated for 3D trapping of polystyrene spheres. The authors studied the effect of total internal reflection on the interface of the fiber to the surrounding medium, and its influence on the focusing of the beam. To do so, they considered an annular core fiber with a reshaped surface as a model. The calculations indicated that the trapping position should be located at approximately $35\,\mu m$ from the fiber and that the NA for this structure would be around 1.06 (akin to standard optical tweezers setups). Experimentally, the design was achieved using a four fiber bundle structure. The fibers were placed in a capillary, with $200\,\mu m$ of inner diameter, $360\,\mu m$ of outer diameter and fixed with an epoxy resin. Optical fibers with $80\,\mu m$ cladding diameter and SM at $1060\,nm$ were used. Then the fiber-end surfaces were polished and covered by a metallic film (to decrease charging effects during the FIB milling). Finally, the structures were drilled to obtain micro indentations at specific locations and with very precise angle on the top of the fibers, using a beam current of $20\,nA$. In this regard, both the location of the interference spot and the crossing angle of the multiple beams could be controlled with high precision. Please see figure 2.9 (a) and (b). To validate this new approach, the probes were tested for trapping of $10\,\mu m$ fluorescent polystyrene particles where 3D trapping was demonstrated. The OFs were also tested for trapping and simultaneous collection of the fluorescent signal resulting from the excitation of the beads. Both trapping and sensing capabilities of the fiber bundle were assessed, and validated. The authors choose to use a multiple fiber bundle instead of an annular fiber to enable specialization of each fiber.

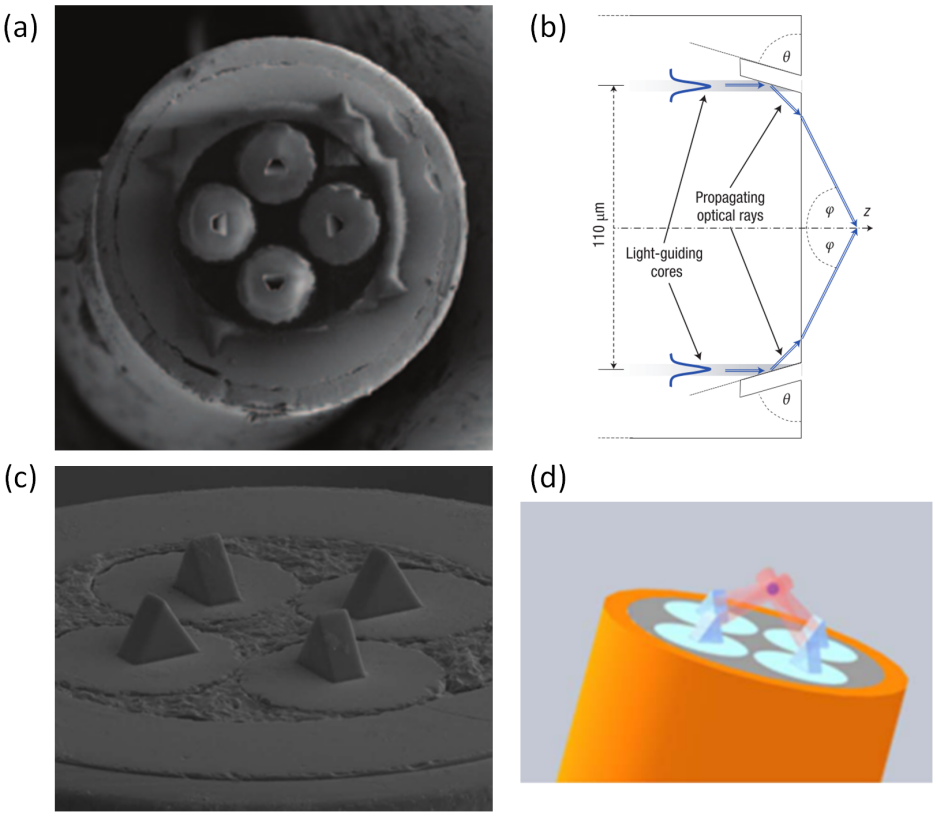

Figure 2.9: Optical fiber probes fabricated by FIB milling and TPL for manipulation of particles. (a) Image of bundle of four OFs, micromachined using FIB milling, so that a trapezium-like slanted hole is obtained on the top of each fiber. The optical fibers have a diameter of $80\,\mu m$, and the full bundle is $360\,\mu m$ wide. (b) Scheme of the OF probes working principle: the top of each fiber is modified, to redirection the light propagating in the core, due to its reflection in the core/outer-medium interface. Figures (a) and (b) were adapted from reference [84]. (c) Image of a bundle of four OFs with micro prisms on each fiber top, fabricated by TPL. (d) Scheme of the effect of the prisms on the top of the OFs. Figures (c) and (d) were adapted from reference [86].

In 2011, Liu *et al.* fabricated a surface plasmonic lens for far-field focusing, based on a series of annular slits, resembling a binary phase plate [87]. The structure was micromachined via FIB milling on the top of an OF. This probe was used to 3D trap sub-wavelength particles and cells [88].

More recently, the fabrication of special geometric structures on OF tips has been accomplished by TPL [89, 90]. TPL is a 3D high resolution fabrication method, based on two-photon absorption effect, which is accomplished when a high intensity very short laser pulse is focused into a very small spot of light inside the polymer. Because this is a non-linear process polymerization occurs only above a certain intensity threshold level. This way, the laser can be scanned through the sample and a 3D isolated structured

can be formed within the polymer. Afterwards, the remaining non polymerized material is washed out and the 3D structure is revealed. The main advantages presented by this technique are: 3D resolution, sub diffraction spatial resolution ($\sim 100nm$), high penetration depth, and ability to be applied in a diversity of materials [91], being useful for rapid prototyping. Nevertheless, while the fabrication process can be very fast, the associated instrumentation is relatively expensive.

In 2010 Liberale *et al.* presented the fabrication of several optical lenses on the top of optical fibers by TPL [92], including spherical and conical profiles, and also a ring phase mask. After this, the same group reported the fabrication of micro prism on OFs. This configuration is in line with the previous results [86], where total internal reflection of light was used to create a high NA lens using four OFs. In this case instead of carving the core of the OFs, micro prisms were used to deflect the beams and originate a high NA geometry (see figures 2.9 (c) and (d)). The outcomes achieved with this fiber bundle are quite similar to the ones presented before with the FIB milled structure, such as 3D trapping and spectroscopy. For further information please see chapter 8 of reference [93].

Apart from these high resolution methods, the fabrication of diffractive elements on optical fiber tips with prospects for optical trapping, was lately reported by Koshelev and co-workers [94], and are commercialized by aBeam technology [95]. In this case, the structures are fabricated by nano imprinting lithography, a low cost sub-wavelength resolution method for nano patterning.

While more recently other structures fabricated by TPL were reported, including micro axicon lenses [96], this technique is still little explored in the context of OF tweezers. Indeed, high resolution micromachining technologies such a FIB and TPL are very convenient for the prototyping of new complex structures. However, the associated instrumentation is expensive and is not readily available for the average user. Nevertheless, the potential for innovation is very high and will certainly be explored as the technology becomes more widespread. Such could be the case with the TPL, nano imprinting lithography and other 3D printing systems which are being the subject of rapid evolution.

2.2.5 Other fabrication methods and OF configurations

A diversity of other works has been reported using techniques that do not fall into the previous categories or use combination of different approaches that are worth mentioning.

In 2009, Valkai *et al.* reported the use of two special counter propagating OFs with built in polymeric tips for trapping of micro beads [97]. The tips were fabricated through photo-polymerization, a simple and fast fabrication method to produce auto-

aligned structures (inset of figure 2.10 (a)). The microstructures work as a continuation of the OF cores and due to the reduced dimensions are likely to be implemented in micro chips. This configuration was validated for optical trapping of multiple particles, as visible in figure 2.10 (a).

After this, Kim *et al.* reported an OF configuration for the generation of Bessel beams to be integrated in microfluidic environments [98]. In this work the authors presented a hybrid optical probe composed by three segments of optical fiber (single mode fiber (SMF), hollow optical fiber (HCF) and coreless silica fiber (CSF)) and a polymeric lens at the tip (figure 2.10 (b)). With such arrangement the Gaussian mode guided by the SMF is transformed in an annular mode in the HCF, then it is expanded in the CSF and focused by the converging polymeric lens. The output beam at $1064\,nm$ is non-diffractive over a distance of $\sim 1\,mm$. The validation of this working principle demonstrates that bulk optical elements can be replaced by common optical fibers, enabling the miniaturization of the devices. In this particular case, three optical probes were integrated in a microfluidic chip allowing to guide dielectric particles through a specific path, as visible in figure 2.10 (c).

Later, Chen *et al.* presented an OF configuration both for trapping, rotation and translation of yeast cells [99]. In their work, a $650\,nm$ laser was coupled into a graded index OF with a conical tip. Then, the LP_{21} mode was pre-selected by adjusting the coupling angle, and was converted into a Bessel-like beam by the axicon lens. Using this probe the authors accomplished trapping of a single cell and of a two-cell dimer. Using a fiber rotator, the OF could be twisted and bended, causing the rotation of the primary LP_{21} mode, and consequently a rotational torque, enabling to control the rotary motion of the dimer.

A while later, Li *et al.* explored the use of a microparticles atatched to tapered OFs for the generation of nanojets. First the authors used one polystyrene (PS) particle to explore the configuration [100], and then, to allow multiple trapping positions, they used an array of beads attached the tip of a tapered fiber [101]. Please see figure 2.10 (d) for a schematic interpretation of this configuration. The use of a nanojet array allowed to have simultaneous 3D nanotraps, able to capture nano particles and E-coli bacteria, as shown in figures 2.10 (e) and (f), respectively. With the backscatered signal, the beads could be discriminated from the bacteria. The analysis was based on their size. Only the trapping of objects with sub-wavelength diameters was observed. Targets with higher diameters were pushed away by the scattering component of the force. The application of this probe was explored using a sample of mixed E-coli and RBCs. The E-coli were trapped, while the RBCs were pushed away. After this, shining ultra-violet

(UV) radiation through the same fiber led to the killing of the E-coli, while the RBCs remained alive since the UV light was confined to the vicinity of the nanojets.

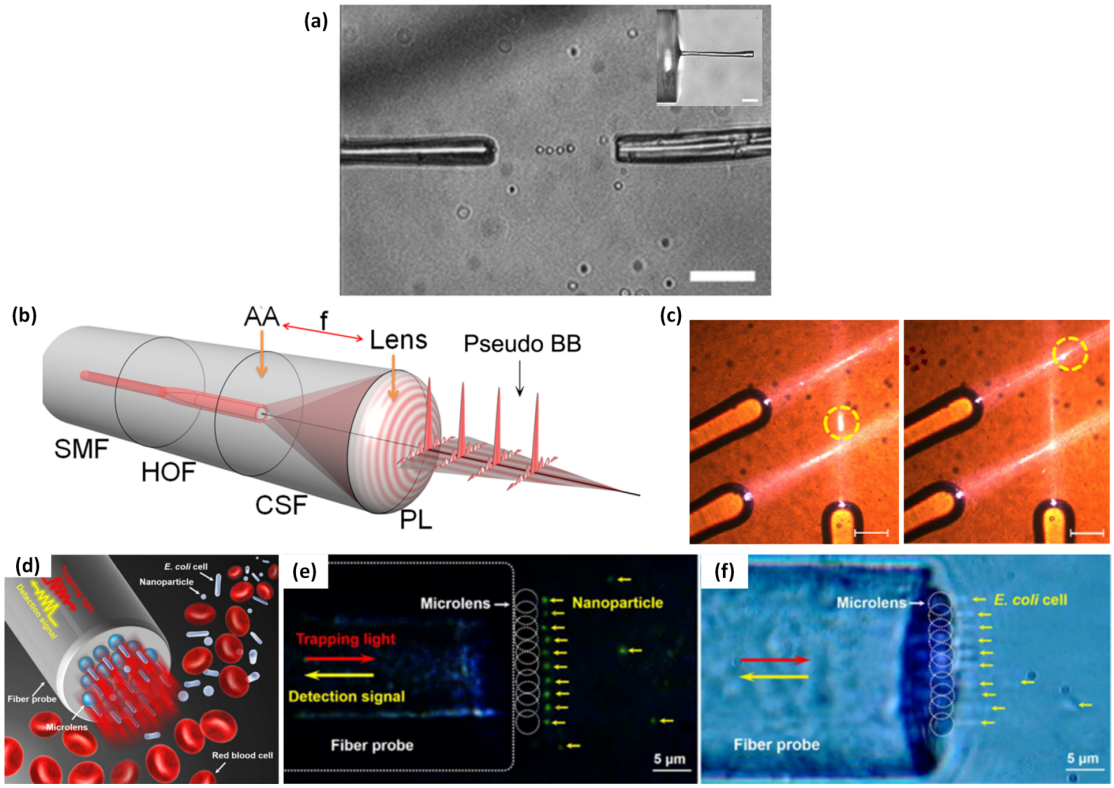

Figure 2.10: Examples of other types OF probes for optical trapping. (a) Counter propagating trapping, using two polymeric waveguides fabricated by photopolymerization on the top of common OFs. Image adapted from reference [97]. (b) and (c) OF probe for optical guiding of particles. The probe produces Bessel beams through the integration of distinct types of OFs and a convergent polymeric lens. Images adapted from reference [98]. (d) -(f) Array of beads attached the tip of a tapered fiber used to generate nanojets and trap E-coli. Images adapted from reference [101].

These examples do not follow any specific fabrication methodology previously reported. On the contrary, these works focus on the intrinsic guiding characteristics of the fibers, the ability to change them using either combinations of distinct OFs or coupling light methods and in the integration of distinct fabrication methods. This kind of approach establishes what will probably be the paradigm in the next years where the different fabrication techniques described will be used with special OFs and combined with modulation of its modal features to obtain more advanced OF devices, with a higher degree of control of its trapping ability, suitable to perform more complex operations with biological samples.

2.2.6 Discussion

The ability to trap and manipulate micro particles and single cells with light is already established as a very useful tool for many applications. More recently, efforts are being made to bring the trapping abilities to the tip of OFs, thus increasing the versatility and usefulness of optical tweezers while decreasing overall system complexity. In this context, a diversity of different techniques is being explored for the fabrication of microstructures at the OF tip, capable of creating strong intensity gradients needed for optical trapping. Most successful methods include, polishing, thermal pulling, chemical etching and high resolution micromachining. The most important features of each technique were discussed in this chapter, and are summarized in the scheme of figure 2.11, this scheme also includes the most common uses of each type of OF trapping tool.

Polishing is a low cost and reproducible technique allowing batch fabrication of OF trapping tools. However, the geometries of the fiber tips are restricted to spherical or elliptical profiles, with low focusing ability, being most of the times limited to 2D manipulation of the specimens. More complex 3D trapping is only attainable using multiple fibers, or OFs with annular or multiple cores.

Thermal based processes share similar limitations in terms of achievable tips shapes (spherical and elliptical). While it is also a low cost technique it lacks reproducibility and is not amenable to batch processing. Nevertheless, it is an attractive technique for straightforward OF trapping applications, and more advanced features can still be explored using multistep pulling or fibers with several cores.

As long as the processing parameters are carefully controlled, chemical etching provides well established methods for obtaining good quality OF tweezers. In particular, it is the most direct way to obtain conical shaped axicon lens, very attractive for trapping applications. Relaying on the use of dangerous chemicals, etching is nevertheless compatible with large scale batch processing. And while its versatility is limited when applied to standard fibers, a strong potential for the design of more advanced shapes is still to be explored using special fibers with tailored refractive index profiles.

High resolution techniques such as FIB milling or TPL are another class of fabrication methods. Being usually associated with expensive equipment and time consuming procedures, they provide, nevertheless, the ability to accurately micro machine the OF tips. This way, they stand out as preferred methods for rapid prototyping and test of new ideas. In addition to the established techniques, new approaches exploring the combination of special intrinsic characteristics of fibers, such as polarization and modal profiles, with distinct fabrication methods promises to open new possibilities for more advanced micro manipulation tools.

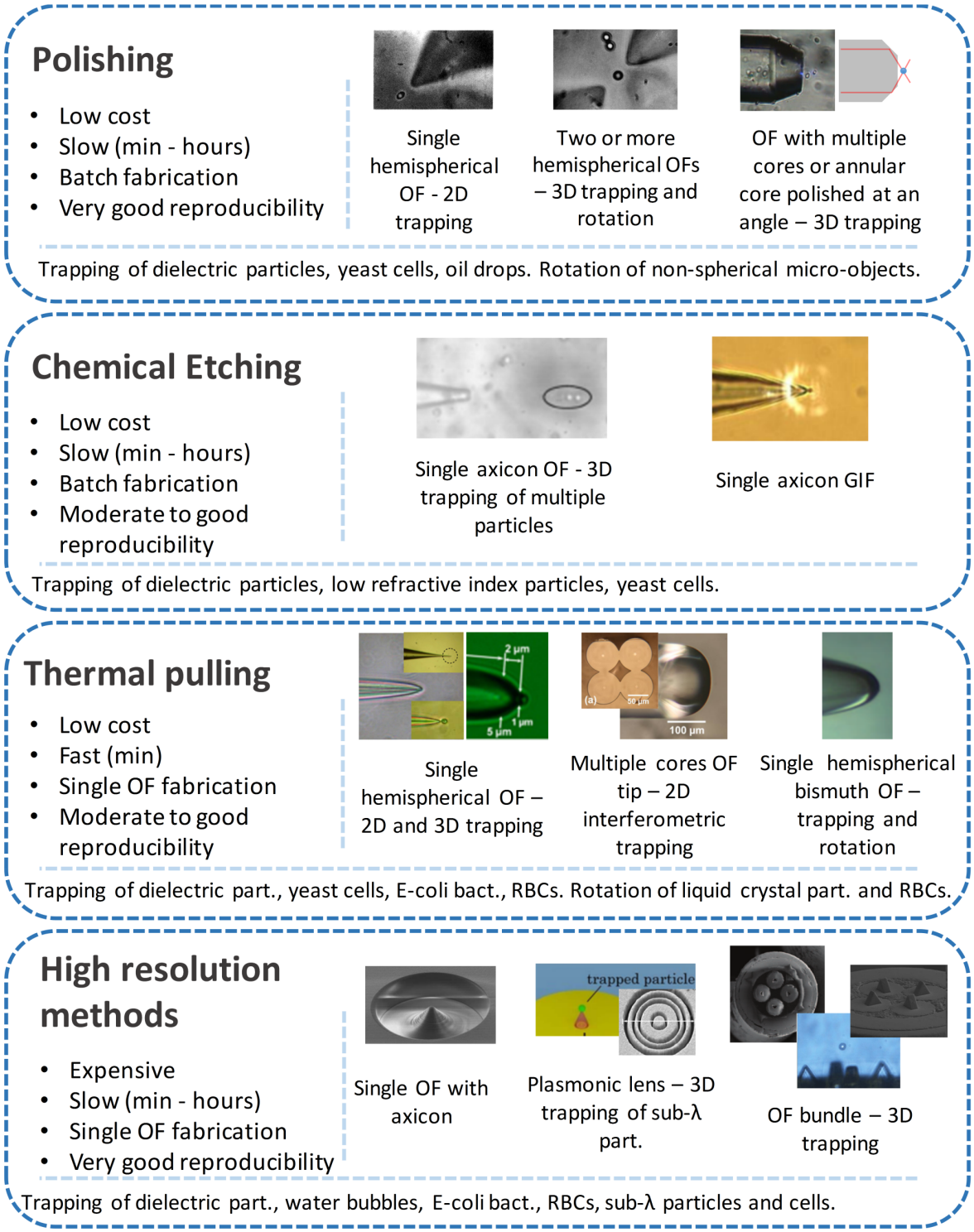

Figure 2.11: Summary of the fabrication techniques and their main features in the micro processing of OFs for trapping uses. The images were adapted from the following references: [48, 50, 56, 60, 62, 64, 77, 79, 84, 88, 102, 103]. References and images presented in the same order.

Overall, the tendency is to explore the combination of different methods with special fibers and modulation of the modal profiles as a way to obtain more advanced trapping and manipulation features. With the consolidation of these techniques and the introduction of sensing capabilities into the fiber probe, a new generation of OF tweezers with analytical capabilities is bound to appear fulfilling a critical need of single cell analysis.

2.3 Conclusion

This chapter has reviewed the fundamental aspects of optical trapping, discussing the main applications and current drawbacks of COT and HOT, such as high cost, low portability and large footprint. From this point of view, OF trapping based tools were presented as an interesting alternative. To explore this idea, the remaining part of the chapter was focused on the fabrication methods used to tailor OFs into suitable trapping tools. Polishing, chemical etching, thermal pulling, FIB milling and TPL are well established methods, commonly used to this end. While polishing, chemical etching and thermal pulling are low cost methods, with relatively limited fabrication capabilities, high-resolution techniques hold great potential in the fabrication of more complex configurations, however at a higher cost. Notwithstanding, it is the combination of OFs with special features and different micromachining fabrication methods that is expected to be on the basis of the development of prospective fiber trapping based technology.

To sum up, the present chapter aimed to explore the existing OF trapping configurations and the fabrication methods used to attained such fiber geometries. In the following chapter, the basic tools necessary for the development of this thesis are given. This includes the fabrication techniques, photo-polymerization and FIB milling, the computational method and the procedure used to calculate the experimental optical forces.

Chapter 3

Methods and tools

The fabrication of optical fibers for trapping and manipulation of micro particles and cells relies on several techniques, as previously described. The optical fiber TIPs fabricated in the framework of this thesis were based on photo-polymerization and focused ion beam milling. In this regard, the fundamentals of these techniques are described in Section 3.1 and 3.2, together with the particular methodology used in each case. Furthermore, to assess the potential of each optical fiber structure and to have a better perception of the experimental results, a computational tool, based on finite-difference time-domain method, using the freely available software package MEEP, was developed and is presented in Section 3.3. Finally, the method used to experimentally calculate the optical forces (Stokes drag force) caused by the optical fiber TIPs, providing the means to characterize their efficiency, is outlined in Section 3.4.

3.1 Photo - polymerization method

The photo-polymerization method employed to fabricate polymeric micro-lenses at the tip of optical fibers was established in CAP at INESC TEC within a collaboration with Dr. Olivier Soppera from Institute de Science des Materiaux de Mulhouse (IS2M).

The fabrication of polymeric micro structures on OF tips is based on a guided wave photo-polymerization process, first reported by Bachelot *et al.* in references [104–106]. The reaction consists of linking monomers into cross-linked polymers using light as a trigger. The polymerization is initiated by a photo-chemical process induced by the energy of a radiation source of a proper wavelength. This photo-initiator is normally a free-radical generator which can be excited either thermally or photo-chemically. In the second case, the free-radical is created from excited states by the photo-initiator.

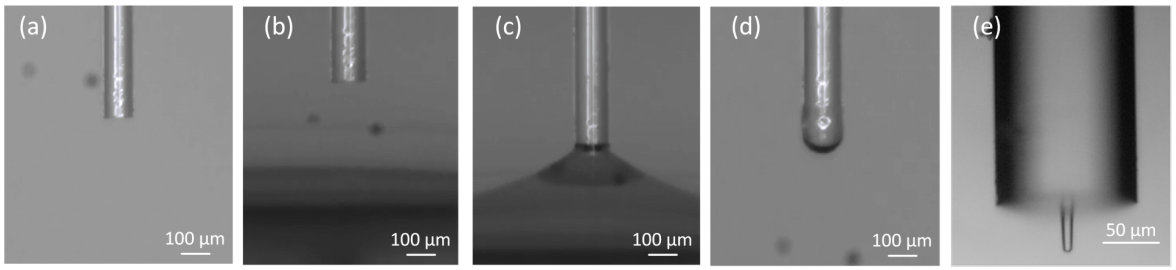

Figure 3.1: Fabrication process of polymeric structures at the extremity of OFs: (a) the OF is cleaved and placed vertically; (b) a drop of polymer placed in a glass slab approaches the end of the fiber; (c) the fiber is dipped in the drop of polymer; (d) the slab with the drop of polymer is removed and the laser is turned on to illuminate the polymer remaining on the top of the fiber; (e) the fiber is rinsed in ethanol and the non-polymerized solution is removed from the top of the fiber revealing the micro lens.

The reactive initiator free-radicals react with a monomer molecule, finally forming the polymer. The photo-initiator can be classified as type I or II [107]. Type I photo-initiators undergo an uni-molecular bond cleavage forming the free radicals. Type II photo-initiators go through a bi-molecular reaction, where the excited state of the photo-initiator reacts with the co-initiator to generate the free-radicals. The polymerization process happens in a fast chain reaction and will occur until an inhibitor stops it. In this particular case, the monomer used was pentaerythritol triacrylate (PETIA) which is a tri-functional acrylate monomer and the photo-initiator (type I) was Bis(2,4,6-trimethylbenzoyl)-phenylphosphineoxide commercially known as Irgacure 819. This initiator is sensitive to a wavelength range between 375 and $450\,nm$. Therefore, a $405\,nm$ diode laser (LuxX cw, $60\,mW$, Omicron) was used in the photo-polymerization process. Other photo-initiators, can be used to fit with visible or NIR wavelengths. For instance references [108, 109] report the use of Eosin Y, a sensitizer dye and the co-initiator methyldiethanolamine. Eosin Y is an example of a type II photo-initiator. This system is sensitive between 450 and $550\,nm$.

The procedure to fabricate the micro structures is illustrated in figure 3.1, and a scheme of the experimental setup is shown in figure 3.2. During the entire process a camera is used to verify both the fiber conditions and the fabrication development. First, an optical fiber is cleaved and placed vertically in a moving stage (figure 3.1 (a)). At that point, it is slowly dipped (figure 3.1 (b)) into the solution (figure 3.1 (c)). Then, the fiber is removed from the polymer allowing a drop of the solution to form in its extremity (figure 3.1 (d)). Next, the polymer is illuminated and consequently cured, by coupling the $405\,nm$ laser to the OF, using the experimental setup shown in figure 3.2. To finish, the remaining liquid solution is washed out with ethanol, revealing the polymerized micro

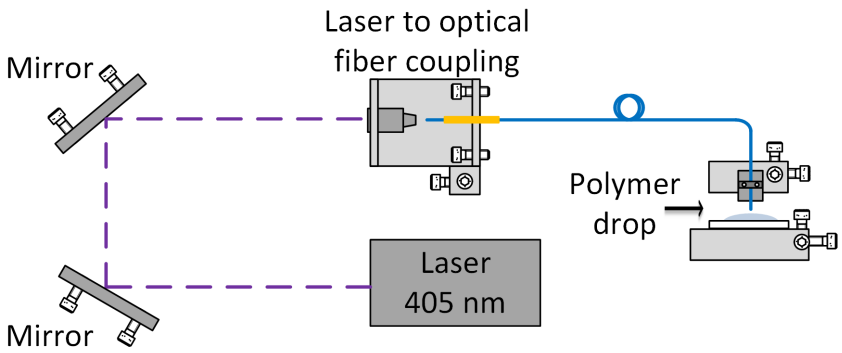

Figure 3.2: Scheme of the optical setup used to couple the 405nm laser used to photo-polymerize the micro structures on the OF tips.

structure at the fiber tip. The visual aspect of the resulting polymeric tip is shown in figure 3.1 (e). The polymeric structure is formed by means of a self assemble photo-polymerization effect [106, 110]. This means that during the solidification of the polymer, its refractive index increases, creating a guiding effect that prevents the radiation from scattering in the remaining of the drop. The monomer typically has a refractive index of 1.48 while the value of the refractive index of the polymer is 1.52. Therefore, the resulting structure generally has a diameter close to the fiber modal diameter and the length determined by the initial polymer drop thickness. Particularly, the geometry of the structure can be finely adjusted by selecting the appropriate fabrication conditions, such as, laser intensity, irradiation time, pre-excited mode profile of the optical fiber and the length of the drop. These specific features will be explored in Chapter 4. The results reported in this thesis were obtained with a polymer mixture containing 0.1 % in weight of Irgacure 819.

3.2 High resolution micro machining - FIB/SEM system

The advent of FIB dates back to the early 1970's, when the first field emission ion sources became available [111]. Nowadays, this technique is commonly used to serve a multitude of purposes, either in scientific laboratories or in the semiconductor industry.

To micro machine diffractive optical elements on optical fiber tips a dual beam high resolution FIB/SEM system, Quanta™ 3D FEG, from FEI™ company was used. This was possible due to a collaboration with Professor Jaime Viegas from the Masdar Institute of Science and Technology. Figure 3.3 depicts a photograph of the machine, where

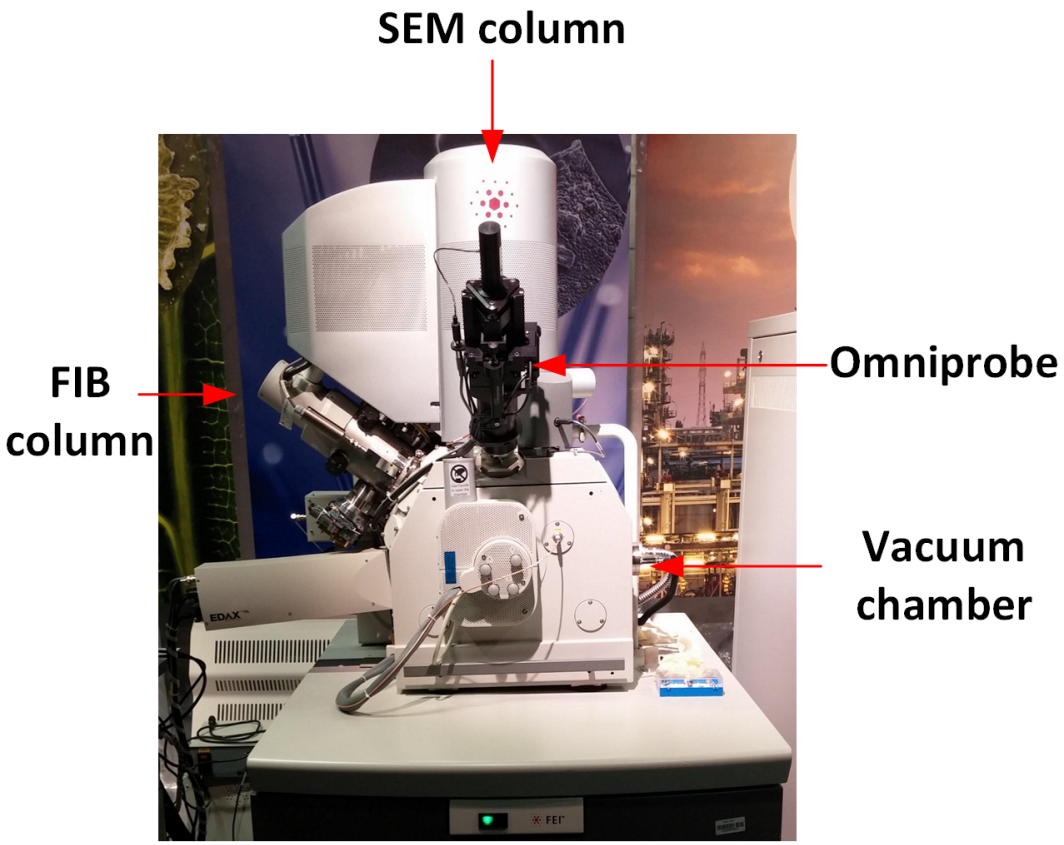

Figure 3.3: Quanta™ 3D FEG, from FEI™ company.

the FIB and SEM columns are visible. This system is also equipped with an omniprobe, which is used to prepare samples for transmission electron microscope (TEM) analysis.

3.2.1 Scanning electron microscope

The SEM is a microscope that uses a beam of electrons rather than photons to retrieve images, as in optical microscopes. An electron gun is the source of electrons, which are targeted towards the sample by means of electromagnetic lenses and fields in a vacuum chamber. Scanning the electron beam across the sample surface form an image, pixel by pixel. The electrons originated by the source, by field emission form a tungsten tip, are called primary electrons. The interactions between this focused beam of primary electrons and the sample material, originates different sources of information (figure 3.4), such as [112]:

- secondary electrons - sample topography;
- backscatered electrons - sample topography and atomic number;

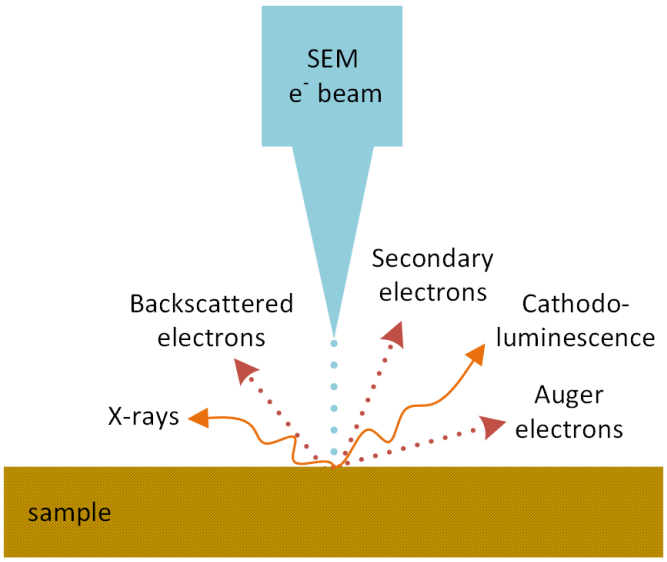

Figure 3.4: Scheme illustrating the signals emitted from the interaction between the primary electrons and the sample from SEM analysis.

- Auger electrons - sample surface composition;
- X-rays - sample composition;
- Cathodeluminescence - sample electronic structure.

From the various parameters that can be measured by the different detectors using an electron beam, a myriad of information about the sample can be gathered. In the case of this work, a secondary electrons detector was used to image the optical fibers and the fabricated structures, allowing to acquire high resolution images.

3.2.2 Focused ion beam

The FIB is an equipment similar to a SEM, however it scans an accelerated beam of focused ions on the sample surface, instead of electrons [113].

A typical ion column is composed by the following main parts (see figure 3.5) [114, 115]:

- ion source - the gallium ions (Ga^+) are generated from a liquid metal ion source (LMIS). This is composed by a tungsten (W) needle, which has a flow of Ga to the tip, forming the so called Taylor cone. Then, by field emission, the Ga^+ ions are extracted from the cone and directed towards the sample;
- electrostatic lenses - to condense the beam and then to focus it on the sample;

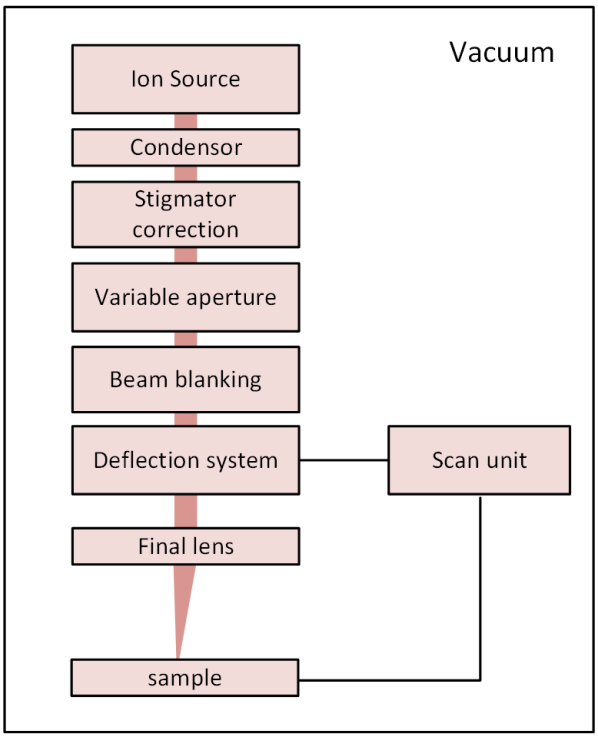

Figure 3.5: Schematic configuration of a FIB column.

- stigmator correction;
- variable aperture - to select the desired beam current;
- beam blanking system - the beam is deviated from the sample and directed to a Faraday cup;
- deflection system and scan unit - allows to raster the FIB over the sample in a costumer defined pattern.

The ion-solid interactions allow the acquisition of images, high resolution milling and to perform depositions. Figure 3.6 gives a visual interpretation of the first two processes. In **FIB image** acquisition mode, the beam is scanned over the sample surface generating secondary ions and electrons. These electrons can be used to create an image, this process is similar to secondary electrons - SEM imaging, while the secondary ions can be useful for secondary mass ion spectroscopy. However, during the sample scanning some atoms are removed and some Ga^{+}ions are implanted. In this regard, to avoid sample damage a low current should be used. On the contrary, in **FIB milling**, the sputtering of material is intentional. In this case, the beam is scanned over the sample, milling a user defined pattern onto the sample surface. The beam spot size determines the resolution

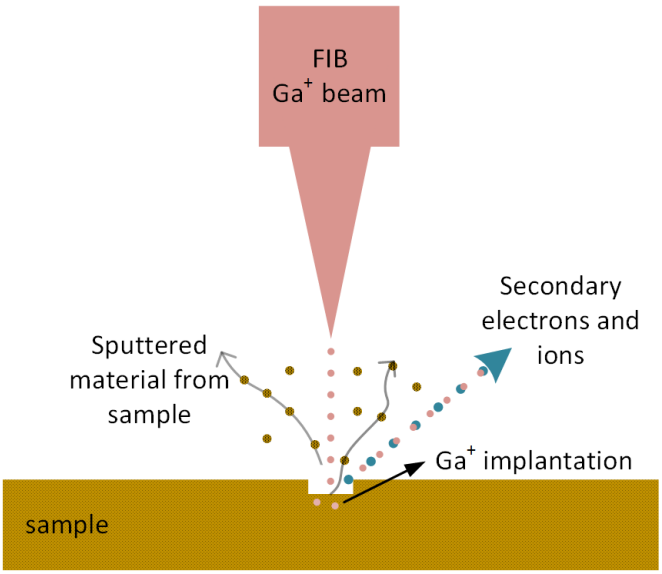

Figure 3.6: Scheme illustrating the interactions between the Ga^+ ions and the sample. Ga^+ ions are implanted during the scan of the beam over the sample. Material is sputtered from the sample, and secondary ions and electrons are generated. These secondary electrons are collected by a detector retrieving images of the sample.

of the process, both for imaging and milling. The Quanta™ 3D FEG FIB has fifteen possible ion currents, from $1.5\,pA$ to $65000\,pA$. Table 3.1 shows the correlation between beam current, beam diameter and suitable applications. Please note that currents above $300\,pA$ are not presented at this table, due to the lack of resolution at these beam sizes.

Lastly, the FIB is also suitable for the **deposition** of specific materials, such as Pt and W. The deposition method is similar to chemical vapor deposition [91]. In this process, a precursor gas is nebulized onto the sample surface by a nozzle (thin needle). The precursor molecules are first adsorbed by the sample and then decomposed by the ion beam. The volatile products of the desorption are removed by the vacuum system,

Beam current (pA)	**Beam diameter** (nm)	**Use**
1.5	7	Very high resolution imaging
10	13	Fast imaging
30	17	Milling sub micron structures
50	19	
100	24	Milling micron sized structures
300	31	

Table 3.1: Ion beam currents at $30\,keV$, corresponding beam diameters and suitable applications. Data obtained from Quanta™ 3D FEG FIB user operation manual [116].

while the reaction products remain in the substrate. This is a maskless high resolution deposition method. However, it is time consuming, and contamination by Ga^{+}ions may occur [115].

3.2.3 Sample preparation and assembling

The preparation of the OFs for FIB milling of their tips is usually a rather simple process. Nevertheless, every step plays a crucial role for good quality outcomes. Hereof, the next steps should be carefully performed:

- First the OF jacket is striped out, and then is cleaned with ethanol. After this, the OF is cleaved. Please note that in some cases more complex OFs will be used, this way additional preparation steps might be necessary.

- At this time, the OFs are placed in the stub that will be used during FIB milling.

  Stub A A stub with a 45º face is used to assemble the OFs. First a carbon tape is fixed in the stub surface. Since it is a double sided tape, it allows to be fixed on the stub on one side, while on the other the OFs are attached. The OFs are preferentially placed perpendicularly in the carbon tape, to facilitate the alignment with the FIB column. After this, a layer of copper tape is used to hold the OFs. Please see figure 3.7 (a). If only held by carbon tape after some minutes the OFs end up detached. This occurs because the OFs are cylindrical and only a small surface is in contact with the glue. Furthermore, the OFs segments are also glued to the surrounding of the stub, to avoid having the fibers loose inside the vacuum chamber. This causes tension on the fibers, causing their quick detachment. In image 3.7 (a) four OFs are assembled, however, it is visible that they are not exactly perpendicular to each other, as also noticeable in the SEM figure 3.7 (b). Therefore, this is not a reliable method to assemble the OFs, difficulting their positioning for FIB milling.

  Stub B The stub was micromachined to have v-grooves 225 μm wide on the 45º face. The optical fibers are held with a metal bar that is fastened on the extremities with two screws. This is a fast and clean way to assemble the optical fibers, and demonstrated to be much more easy to align.

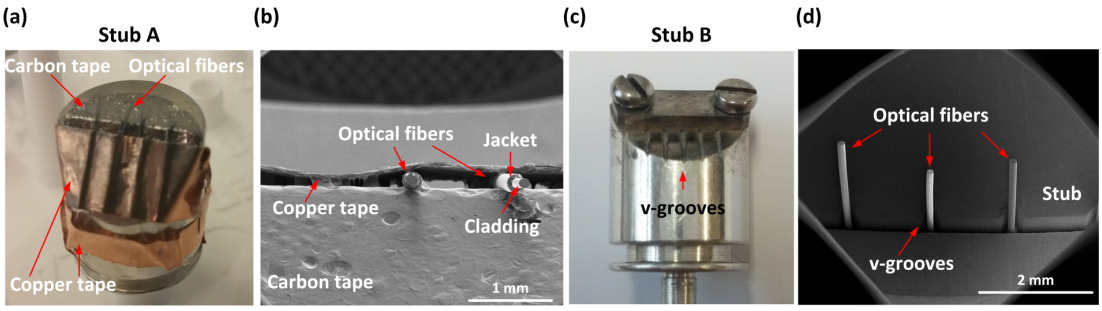

Figure 3.7: (a) Stub used to fix the OFs for FIB milling; (b) SEM image of the OFs assembled in the stub using carbon tape and copper tape; (b) Adapted stub, with micromachined v-grooves; (d) SEM image of the OFs assembled on the adapted stub.

- The final step is to cover the optical fiber with a conductive layer, to avoid charging effects during the milling. This is achieved with the OFs already assembled at the stub. To do so the Precision Etching and Coating System, Gatan 682 was used.

At this point, the OFs are ready to be micromachined by the FIB.

3.2.4 System setup

Before moving on to the standard operation procedure to assemble the OFs stub inside the SEM/FIB chamber and get the system ready to micro machine the fibers, some considerations on the dual beam system configuration should be drawn. As pointed out before, the SEM and the FIB are both placed inside the vacuum chamber. Both guns are in a separated vacuum. Therefore, each time the chamber is opened the pumping process is relatively fast, taking only some minutes. Furthermore, the SEM is positioned vertically and the FIB gun is tilted 52°. Figure 3.8 shows this arrangement. The optimal SEM working distance is at $10\,mm$ and the FIB is $19\,mm$. The coincidence of this positions is the so-called eucentric point, where maximum performance of the system is achieved. Besides having the detectors to provide images of the samples, the inside of the chamber can be monitored by means of a regular CCD camera.

Prior to micromachining the OFs some parameters and features of the SEM/FIB must be adjusted as follows:

- The SEM/FIB system is constantly in vacuum. In this regard, the user has to verify that the system is operational, and then vent the chamber. At this point, the chamber can be open and the stub containing the OFs is assembled in a 5-axis micro stage. Please see figure 3.9 (a) for a scheme of the micro stage and the OFs

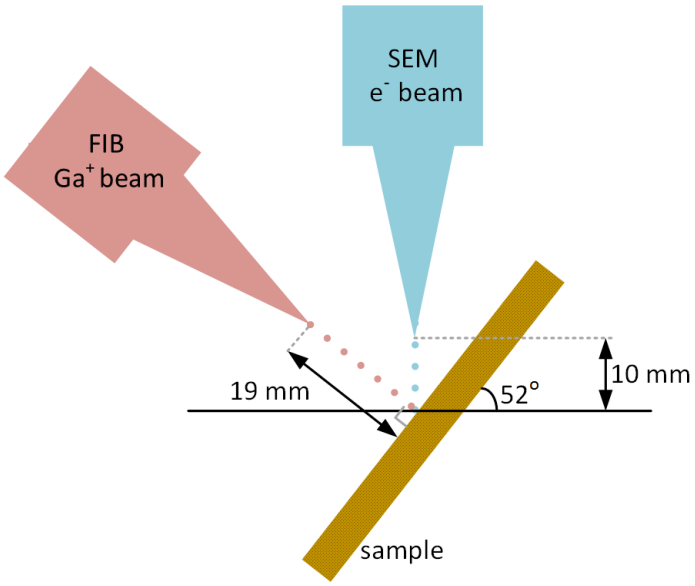

Figure 3.8: Scheme of the SEM and FIB guns. The sample is tilted so that it is at the eucentric point.

stub. In figure 3.9 (b) the inside of the vacuum chamber is visible. After this, the chamber is pumped to achieve a high vacuum ($1 \times 10^{-4}\,Pa$);

- Finding the eucentric height, which is the precise interception of the FIB and SEM. This corresponding to a distance from the SEM column and the sample of $10\,mm$ and between the FIB column and the sample of $19\,mm$ (figure 3.8).

- A perfect structure is fabricated when the OF is completely aligned with the FIB. Figures 3.9 (c-f) show the OF misaligned with the FIB column. This is distinguished by the white brightness on the fiber side. A hint to adjust this, is to minimize this brightness, as visible in figure 3.9 (g).

After this, it is either possible to mill structures according to the pre-definitions of the FIB or to mill more complex structures by uploading a bitmap file with the pattern characteristics. In this case, the exposure dose is controlled by the dwell time, which is proportional to the bitmap pixel value: for a black pixel (level 0), the beam is blanked, while for a white pixel (level 255), the dwell time is set to a certain value typically close to $1\,\mu s$. The dwell time for the pixel values in-between is linearly interpolated.

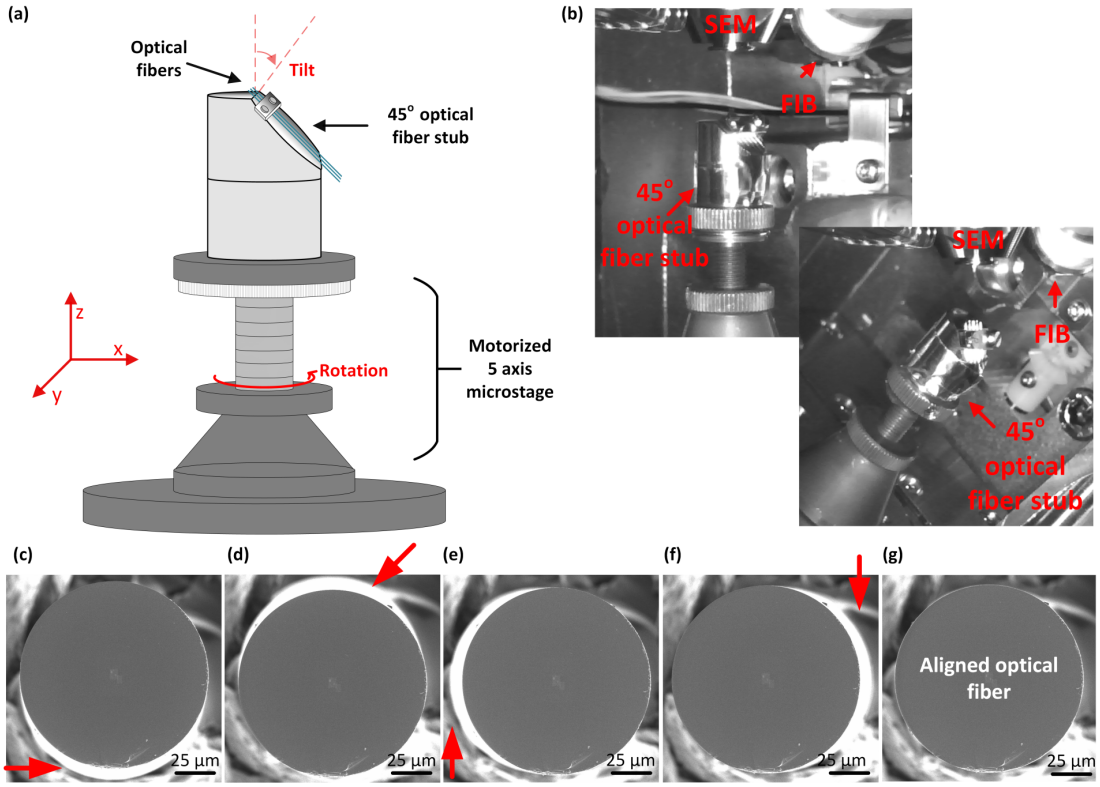

Figure 3.9: (a) Scheme of the optical fiber stub support; (b) Images of the vacuum chamber; (c-f) OF misalignment; (g) OF aligned with FIB.

3.3 Numerical model

The code developed in this thesis, to compute the field distributions characteristic of each OF structure and resulting optical force fields, incorporates an existing Finite Differences Time Domain (FDTD) [117] solver called MEEP (an acronym for MIT Electromagnetic Equation Propagation) [118]. MEEP is distributed under the GNU General Public License. It can be installed in any computer running Unix based operating systems, but it is also available as precompiled binary packages, developed for the Debian and Ubuntu distributions. The original MEEP packages are in $C++$ language, however other two script interfaces do exist, namely Libelt and Python. In this particular case the Python MEEP script was used.

The FDTD method implemented in MEEP uses the Yee grid to stage the electric and magnetic fields in space and time [117, 119]. When different components of the electromagnetic field need to be compared, for instance to compute energy density, flux or just to save an output field, they are interpolated to some common set of points.

MEEP has this tool incorporated, because it stores the field components at the center of each element of the grid. Central differences are used to do the finite differences for space derivatives, which are second order accurate [117]. The FDTD method results from direct discretization of the Maxwell's equations, thus offering no limitations on the size of the simulation, by contrast with frequency domain finite differences and finite elements methods. Finally, it is accurate, robust, and well characterized in terms of stability [117, 120]. However, the computational time and the amount of memory that is needed to perform many 3D and even 2D simulations is a major disadvantage.

The algorithm used to compute the optical forces acting on micron size dielectric particles is based on the following:

- First, the stationary distribution of the electromagnetic field for a system composed by an optical waveguide and a micrometric dielectric sphere is achieved. The beam is introduced in the waveguide using a spacial continuous wave source, and the system is modeled through the MEEP script [118] for Python.

- Second, the net optical forces acting on the dielectric particle are obtained from the previous calculated fields. This is done by computing the Lorentz force density per unit volume and integrating over the complete volume of the dielectric particle, according to equation A.12 as described in Appendix A.

The first part of the algorithm resulted from the existence of the MEEP script, and was necessary only to define the structure and parameters of the simulation. However, the remaining of the algorithm had to be entirely developed. By varying the position of the particle in front of the waveguide tip, it is possible to determine a distribution (map) of the radiation forces generated by the waveguide output beam. It should be noticed that in every position of the target it is necessary to recalculate the electromagnetic field distribution taking into account the interaction of the field with the particle (multiple reflections and refractions). The stationary state of the field is obtained by propagating the light source over several time steps and allowing the field to reach a stable configuration. The time step necessary for stabilization of the field was found to be around 1000. For time steps higher than 1000 the variation of the two components of the force, calculated using equation A.12, is negligible. Examples of this can be seen in figures 3.10 (a) and (b). Furthermore, the simulations use absorbing boundary conditions (ABC), or more specifically perfectly matched layer (PML), which prevent electromagnetic waves to be reflected back at the boundary of the simulation box. Examples of a point source in the absence and in the presence of PML are visible in figure 3.11 (a) and (b), respectively.

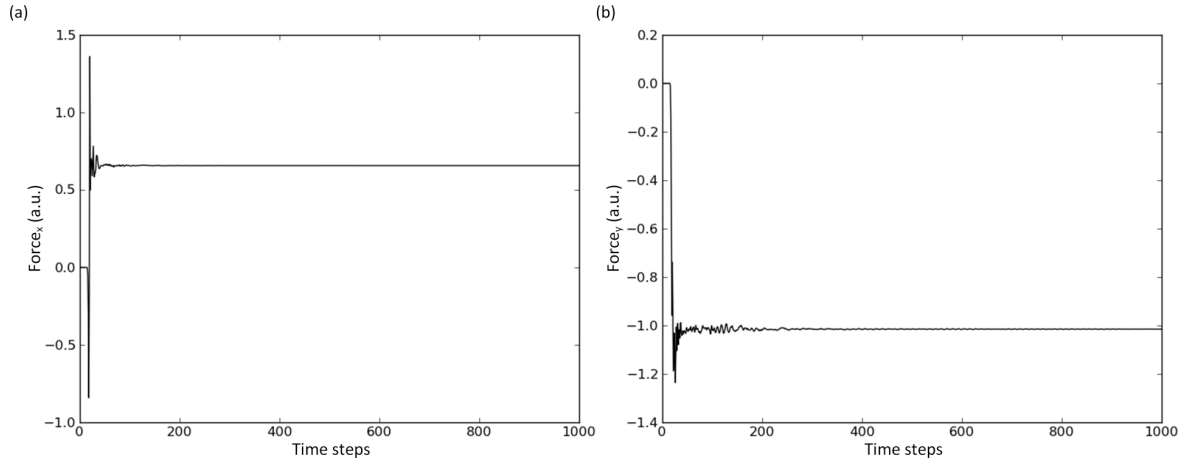

Figure 3.10: Lorentz force acting on a particle during the first 1000 time steps; x component (a), y component (b). The force is in arbitrary units.

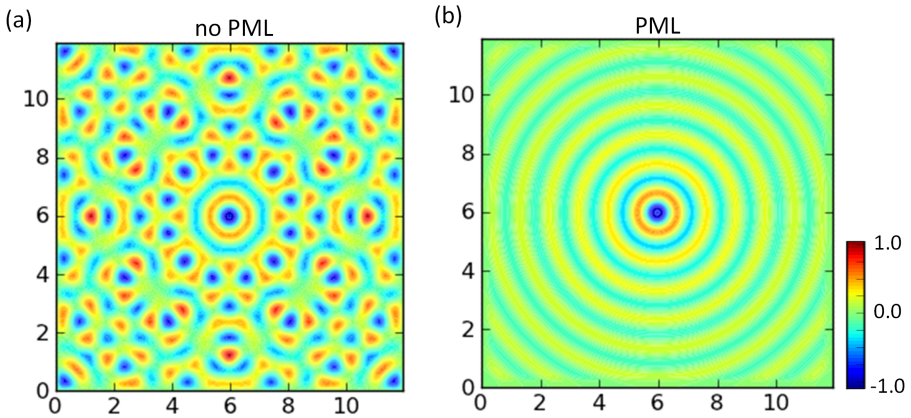

Figure 3.11: Representation of the effects of the absence and the presence of ABC when a continuous point source propagates in the simulation box, $\lambda = 1\,\mu m$. The reflections on the boundary of the simulation box in (a) lead to a complex pattern, whereas the use of ABC conditions, shown in (b) eliminate the reflections.

3.4 Measurement of the trapping forces

The method used to measure the optical forces acting on particles or cells caused by the OF probes of this thesis, is based on the revised Stokes equation, that is, Faxen's law [30, 121]. This form of the drag force equation considers the particle close to a boundary, in this case, the glass slab. The total optical force acting on the particle is given by the

sum of the inertial force (1^{st} term) and the drag force (2^{nd} term):

$$F_{opt} = F + F_{drag} = m\frac{\partial^2 s}{\partial t^2} + \beta\frac{\partial s}{\partial t}, \tag{3.1}$$

where m is the mass of the trapped object, $s(t)$ denotes the trajectory of the particle and β is the viscous drag coefficient, taking into account the Faxen's law. This includes a correction factor due to the proximity to the trapping chamber (glass slab). This coefficient is expressed as

$$\beta = 6\pi\xi\eta r, \tag{3.2}$$

where η is the viscosity of the medium (water, $8.90 \times 10^{-4}\, Pa$), r is the radius of the particle and ξ is the correction factor due to the proximity of the bead to a boundary. This is given by

$$\xi = \frac{1}{1 - \frac{9}{16}(\frac{r}{h}) + \frac{1}{8}(\frac{r}{h})^3 - \frac{45}{256}(\frac{r}{h})^4 - \frac{1}{16}(\frac{r}{h})^5}, \tag{3.3}$$

where h is the distance from the particle center to the surface of the trapping chamber. Considering that the particle is in contact with the bottom of the chamber, $\frac{r}{h} \sim 1$, this results in a correction factor to the drag coefficient, ξ, with a value of 3.08.

Besides this, the inertial force is negligible. This is justified by the low Reynolds number, which is given by

$$Re = \frac{2rv\rho}{\eta}, \tag{3.4}$$

where v is the particle velocity and ρ is the fluid density. In the case of this thesis, velocities are approximately $10\,\mu m/s$, and $r \sim 2 - 8\,\mu m$. In this regard, $Re \approx 10^{-5}$. Therefore, the optical force acting on a particle is simply obtained from the calculation of the drag force, and is given by

$$F_{opt} = F_{drag} = 6\pi\xi\eta r v. \tag{3.5}$$

Data acquisition and processing

For the purpose of force measurement the data is collected and analyzed as follows:

1. Video files of particle/cell trapping are recorded using a CMOS camera;

2. The trajectories of the particles are recovered from the analysis of the video files, using the ImageJ software MosaicSuite for particle tracking [122].

3. The segments of data relative to the movement of the particle towards the trapping are fitted to a mathematical equation, allowing to calculate the velocity of the particle/cell during the restoring movement.

4. Using the information of the velocity of the particle, the optical force is calculated according to equation 3.5.

This only conveys a simple explanation of the method, further details are presented for each case of force determination, as presented in following Chapters.

3.5 Conclusion

This chapter included the description of the fabrication methods, the computational tool to model the OF probes and the experimental approach used to calculate the optical net forces acting on the particles.

Please note that the guided wave photo-polymerization technique will be addressed in Chapter 4, while Chapters 5 and 6 will focus on the use of FIB milling for the fabrication of Fresnel plates and spiral phase plates, respectively.

Chapter 4

Polymeric optical fiber TIPs

The goal of this chapter is to evaluate the capabilities of polymeric microstructures fabricated in common optical fibers and used as optical trapping devices. There are four main reasons why this fabrication method was used: it is a fast and low cost method yielding structures with high reproducibility and good optical quality.
First, considerations on the fabrication of the tips are addressed. This takes into account the importance of the selection of the excited optical mode, prior to the photo-polymerization, on the design of the final structure. Together with this, the influence of parameters, such as, the exposure time, laser power and polymer mixture composition is discussed, on the resulting tips. This is followed by a computational study, based on the model reported in Section 3.3, where the optical and structural features of the system are analyzed.
Based on the knowledge acquired in the first part of this chapter, selected micro structures are experimentally tested for optical trapping of yeast cells and organelles of plant cells, demonstrating the viability of the tips for 2D trapping. Subsequently, further tests are performed to calculate the optical forces acting on the yeast cells during the stable 2D trapping.

4.1 Background

Historically, the development of micro structures on the top of optical fibers extends far beyond optical trapping applications. In fact, over the years, efforts have been made to optimize the coupling of lasers to OFs, using these type of structures. In 1974, Cohen and Schneider presented a method for the fabrication of micro lenses on the top of optical fibers through photo-lithography [123]. However, despite the merit of this fabrication process, no more advances on this technique were reported. After a couple of decades,

in 2001, Bachelot *et al.* presented a new low cost and fast method for the fabrication of polymeric micro structures on the top of OFs by free radical photo-polymerization [104]. Essentially, the fabrication of the structures is achieved by depositing a photo sensitive liquid on the top of a cleaved fiber, and by coupling polymerizing light to the fiber. As the polymerization occurs, a guiding effect takes place that results in the formation of a self-assembled structure at the fiber tip, that is auto aligned with the fiber core. Research on this area has provided ample support for the use of the polymeric structures in several applications: as diode lasers to waveguide couplers [106], as refractometric sensors [124], and as luminescent optrodes for chemical sensing [125]. Nevertheless, in spite of great potential, so far the method was not explored for trapping applications. From our knowledge there is only one case where two polymeric flat tips are used as counter propagating waveguides aligned to configure an optical trap [97]. In this regard, the content of this chapter is devoted to explore the potential of the polymeric micro structures as single OF TIPs.

This chapter is organized as follows: first the fabrication methodology is explored, then computational simulations are performed to evaluate the possible outcomes and finally the OFs are tested for trapping trough experimental tests.

4.2 Fabrication methodology

4.2.1 Considerations on the polymeric tip design

The photo-polymerization process, described in Section 3.1, allows obtaining a considerable number of micro tips with distinct shapes and capable of producing a wide variety of output illumination patterns. In particular, the need to use a polymerizing wavelength bellow the fiber cut off results in the fiber supporting multiple modes, during the polymerization process. This way, depending on the modal excitation conditions distinct output intensity profiles will result during the polymerization stage producing different tip shapes. Such feature can either be a tool for designing new shapes, or a mechanism that will reduce the reproducibility of the fabrication technique [104]. In the context of optical trapping, however, it is desirable that the fiber should support only a single mode at the tweezer working wavelength to guarantee stability and reproducibility of the output intensity pattern. In the present study, where trapping was performed using a $980\,nm$ DFB laser, the OFs used were SMF 980 (Thorlabs, SM $980-5.8-125$), which is a step index fiber, for more information please see Appendix B. This wavelength was selected since it is frequently used in optical trapping experiments due to its low damage

on biological samples [126]. On the other hand, during the fabrication process, working at $405\,nm$, the same fiber works in the multimode regime. Indeed, the number of modes that a multimode step index fiber supports is defined by the normalized cutoff frequency (v), which depends on the wavelength (λ), the core radius (a), and the refractive index of the core (n_{core}) and the cladding ($n_{cladding}$). The normalized cutoff frequency is given by

$$v = \frac{2\pi a}{\lambda}\sqrt{n_{core}^2 - n_{cladding}^2}. \tag{4.1}$$

For SMF 980 at $405\,nm$ the normalized frequency is ~ 4.9. The SM propagation is ensured when the v parameter is smaller than 2.405, therefore this means that the SMF 980 will be a multimode waveguide at $405\,nm$, supporting approximately 12 distinct modes. At $980\,nm$ the mode field diameter is $5.8\,\mu m$ [127]. Aiming to optimize the reproducibility of the fabrication of optical fiber tweezers, using this technique, a study was made on the impact of the modal selection on the resulting shape and corresponding output field distribution. During the fabrication, the selection of the excited mode of the SMF 980 was controlled by adjusting the input angle of the laser into the fiber. This was attained using an objective and two mirrors, arranged as shown in figure 4.1. More specifically, the beam input angles could be controlled either by adjusting the mirrors or by setting the controls of the alignment platform where the objective and the fiber were supported. The process of mode selection was then monitored using a second objective which projected the mode intensity distribution onto a flat surface.

The following sections are focused on the fabrication of polymeric micro structures on the top of OFs. Preceding experiments and studies carried out by Dr. Olivier Soppera team, worked as a starting point, allowing us to initiate this study with fabrication parameters that were already producing good optical quality tips, with good adhesion to the OFs.

4.2.2 Imprinting of optical modes on polymeric tips

Taking the previous considerations into account, three types of micro tips having different shapes were fabricated by exciting distinct polarized modes of the SMF 980, namely the LP_{02}, LP_{21} and LP_{31}. The photo-polymer mixture was composed by 0.1 % in weight of Irgacure 819. The first tip was produced using the LP_{02} mode illuminated with $4\,\mu W$ @ $405\,nm$ (measured at the end of the fiber using an optical power meter) during $10\,s$. The choice of the fabrication parameters was based on previous studies [108]. For longer exposure times (of the order of some minutes) and/or higher power the

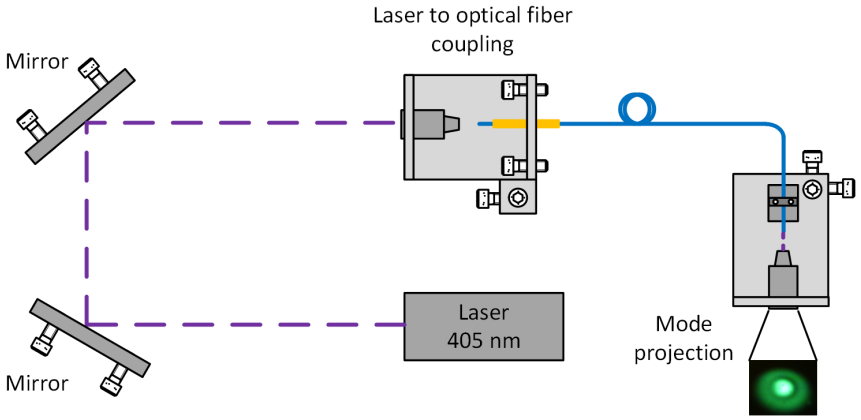

Figure 4.1: Experimental setup used in the fabrication process of the polymeric micro structures. The optical modes are selected according to the light input angle. The light is coupled to the OF using a 10× objective. Using a second objective, the output modes are projected onto a flat surface. The segment of OF does not move during the fabrication of the tips, to avoid changing the excited mode.

pre-selected structure will not be imprinted on the top of the polymeric tip. In this case a flat surface will be fabricated instead. This is caused by the saturation of the polymer response due to the elevated dose. The LP_{02} mode is composed by a concentric maximum and a surrounding ring, the intensity profile decreases from the center to the boundaries, presenting a minimum between the inner maximum and the surrounding ring. The excitation of this mode was verified by projecting the output field of the fiber on a flat target, and confirming the illumination pattern, as shown in figure 4.2 (a). Also, the image processing software ImageJ was used to obtain a 3D pixel representation of the intensity profile, as depicted in figure 4.2 (b). In figure 4.2 (c) the intensity profile of the excited mode along the x and y axis are presented, confirming the characteristics of the primary beam. Please note that 2D intensity profiles are experimentally captured and the 3D representation result from image processing using ImageJ.

The resulting structure was analyzed using SEM images, shown in figure 4.2 (g), where the structure at the end of the polymeric tip is presented in the inset. Notice that the profile of the end of the tip closely follows the intensity profile of the mode LP_{02}, which has two concentric maxima with radial symmetry. These two maxima result in a compound structure at the end of the tip: an inner structure close to the axis of symmetry with a curvature of $\sim 1.5\,\mu m$ and an outer annular structure (curvature radius $\sim 2.5\,\mu m$) near the edge, both contributing for reshaping the field distribution. The tip has a diameter of the order of the diameter of the fiber modal diameter ($\sim 5.8\,\mu m$), and a length of $\sim 40\,\mu m$. These structural parameters can be altered by adjusting the

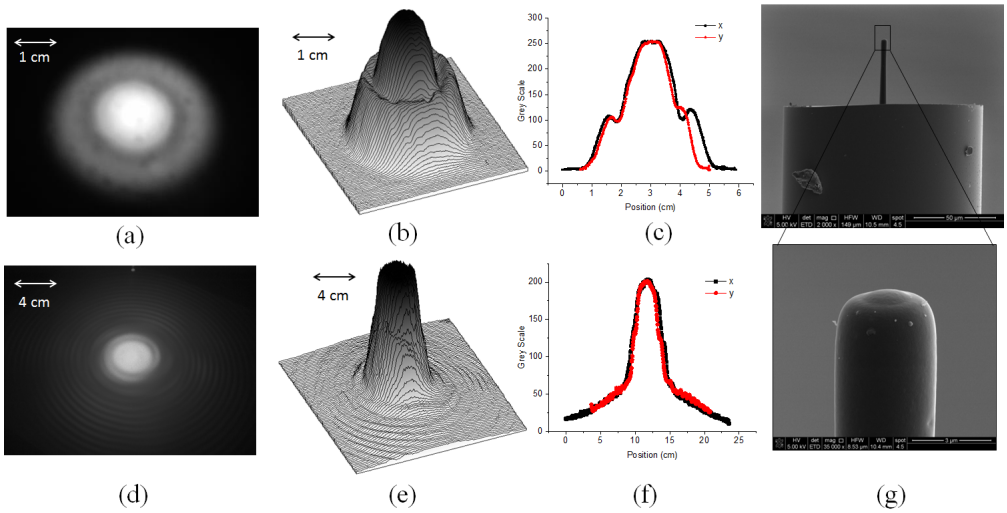

Figure 4.2: Fabrication of a polymeric tip based on the LP_{02} mode: (a) excited mode LP_{02} projected by the cleaved OF before the growth of the tip at $5\,cm$; (b) 3D representation of the pixel intensity profile of the excited mode LP_{02}; (c) cross section along x and y direction of the excited mode; (d) field intensity profile projected by the fabricated polymeric tip at $10\,cm$ (fiber tip coupled to a pigtailed SM 980 laser diode); (e) 3D pixel intensity profile of the field projected by the micro tip; (f) cross section along x and y direction of the projected mode; (g) SEM image of the polymeric tip.

exposure time and the laser power, or the amount of polymer at the tip. In order to investigate this, a study of the output curvature radius of the tip versus the exposure time was also performed, and is presented in Section 4.2.3.

After the fabrication, the tip was illuminated by a $980\,nm$ laser and the output field profile was projected onto a flat target and analyzed, as previously done for the $405\,nm$ laser beam. The resulting output pattern is shown in figure 4.2 (d) which corresponds to a Gaussian like profile with a well-defined maximum and radial symmetry. As expected, the illumination pattern at $405\,nm$ and $980\,nm$ share similarities. Even though the guided mode at $980\,nm$ has a Gaussian profile, corresponding to a LP_{01} mode, after passing through the tip it acquires a profile with some similarities to the LP_{02} mode (figure 4.2 (e)). This is most visible in figure 4.2 (e) than in 4.2 (f), where the x and y profiles are still more similar to a Gaussian. The imprinting of the radial characteristics of the original polymerizing beam into the illumination pattern of the structured tip results from the features of the fabricated polymer structure. Although the modulation is almost imperceptible it can have impact on the final features of the resulting OF trapping tool showing the importance of controlling the modal excitation during the fabrication process in order to ensure the reproducibility of the process. The second

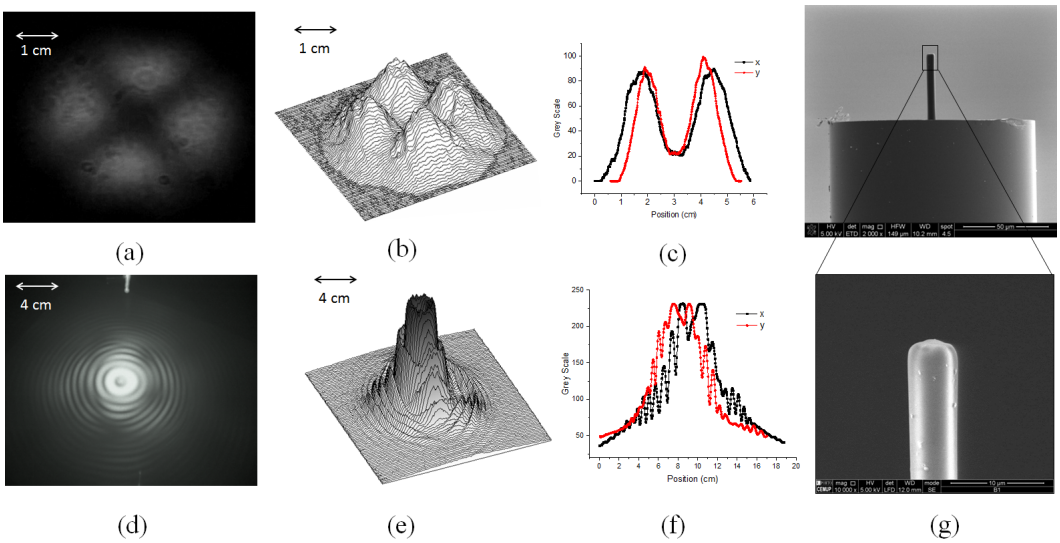

Figure 4.3: Fabrication of a polymeric tip based on the LP_{21} mode: (a) excited mode LP_{21} projected by the cleaved OF before the growth of the tip; (b) 3D pixel intensity profile of the excited mode LP_{21} at $5\,cm$; (c) cross section along x and y direction of the excited mode; (d) field intensity profile projected by the fabricated polymeric tip (fiber tip coupled to a pigtailed SM 980 laser diode) at $10\,cm$; (e) 3D pixel intensity profile of the field projected by the micro tip; (f) cross section along x and y direction of the projected mode; (g) SEM image of the polymeric tip.

and third type of tips fabricated intended to verify if more complex patterns of the initial polymerizing beam (at $405\,nm$) could be imprinted into the polymeric structure illumination pattern (at $980\,nm$).

This second type of structure was fabricated by exciting the LP_{21} mode (at $405\,nm$) with a power of $4\,\mu W$ and $10\,s$ exposure. The LP_{21} mode is composed by four intensity maxima arranged in a circular distribution with a zero at the center (see figure 4.3 (a) and (b)). During the fabrication the LP_{21} mode was efficiently excited, however, due to residual excitation of lower order modes some superposition with the output pattern of other modes was also noticed. This can be seen in the intensity profiles obtained by performing the cross section of the plot of figure 4.3 (b) along the x and y axis (figure 4.3 (c)). As a result, the intensity at the center of the fiber was not exactly zero, due to the contribution given by other modes (figure 4.3 (c)) superposed to LP_{21}. Nevertheless, the LP_{21} mode prevails and the fabricated structure mimics its intensity profile, as expected. This is confirmed by the SEM images shown in figure 4.3 (g). Notice that the non-zero light intensity at the center of the structure, produced by the superposition of the LP_{21} mode with other modes results in further polymerization in this region. This causes the smoothing of the features at the end of the tip, avoiding to attain a well defined hollow

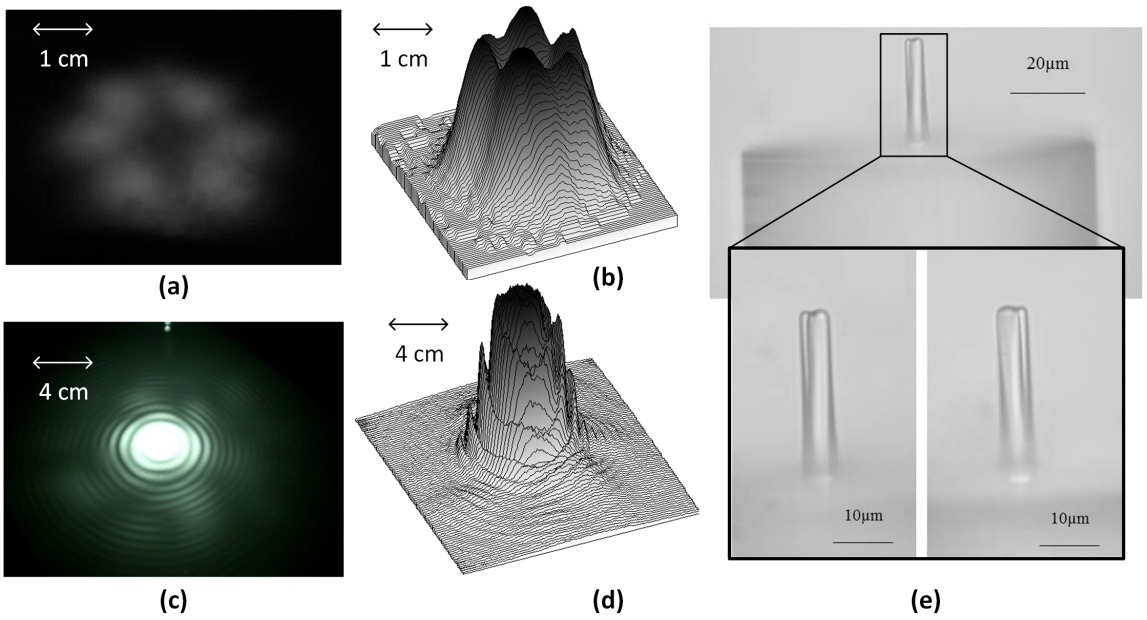

Figure 4.4: Optical fiber polymeric tip based on the excitation of the LP_{31} mode: (a) excited mode LP_{31} projected by the cleaved OF before the growth of the tip; (b) 3D pixel intensity profile of the excited mode LP_{31} at $5\,cm$; (c) field intensity profile projected by the fabricated polymeric tip (fiber tip coupled to a pigtailed SM 980 laser diode) at $10\,cm$; (d) 3D pixel intensity profile of the field projected by the micro tip; (e) SEM image of the polymeric tip; .

structure in the center of the four lobes. In this case the diameter at the base of the structure is $\sim 4-5\,\mu m$ and the length is $\sim 38\,\mu m$.

The output intensity profile obtained when illuminating with a $980\,nm$ laser is presented in figure 4.3 (d) and (e). As in the previous tip the structural features of the polymerizing beam (at $405\,nm$) are imprinted (at least partially) into the polymeric structure and in its resulting illumination pattern, at $980\,nm$. In particular, the radial symmetry of the input Gaussian beam ($980\,nm$) is broken as it goes through the polymeric structure, resulting in a beam profile which shares similarities with the mode LP_{21}. These results suggest that filtering out the input beam, at $405\,nm$, to have a more pure LP_{21} mode would result in a better defined structure and ultimately in an improved beam shaping at $980\,nm$.

In the case of the third type of tips, the LP_{31} mode was excited, as can be seen in figure 4.4 (a) and (b). This tip was fabricated using the same parameters (power of $4\,\mu W$, $10\,s$ exposure, and $405\,nm$ laser light). The produced tip is shown in figure 4.4 (e). It has a base diameter of $\sim 6-7\,\mu m$ and a length of $\sim 31\,\mu m$. At the very end, the irregular structure produced by the particular mode distribution is visible. The LP_{31}

mode is composed by six intensity maxima arranged in a circular distribution with a zero at the center (figure 4.4 (a)). From the picture of the projected transversal intensity profile of the mode it can be seen that in practice the obtained minimum is not near zero (figure 4.4 (b)). This happens, once more, due to the superposition of the multiple modes that are guided in the OF core. At $405\,nm$ the used fiber is multimodal, therefore it is not straightforward to isolate a single mode without having any contribution from the others. The projected output intensity profile presented in figure 4.4 (c) is the result of the coupling of the $980\,nm$ laser to the fiber tip. In this case there is a mixing of a diffractive pattern (the concentric rings) and the projection of the structure (maxima regions arranged in a circular distribution), as visible in the 3D reconstruction shown in figure 4.4 (d). The diffraction is likely caused by the features with size of the order of the wavelength ($980\,nm$) or even smaller. This means that there is a modulation of the input Gaussian beam, meaning that it is essential to monitor the fabrication conditions to ensure output beams with the desired characteristics.

4.2.3 Polymeric tips with spherical profiles

The previous tests enabled to study the effect of the excited modes on the features of the polymeric microstructures and the resulting output beam profiles. To avoid alterations on the Gaussian output beam profile, the best option is to excite either the LP_{01} or the LP_{02} mode. However, there are still some parameters, such as laser power and exposure time, that may affect the final structure of the OF tip. In this regard, a study of the curvature radius of the tip versus exposure time, was performed, where the laser power was fixed at $6\,\mu W$ and $8\,\mu W$. These values were selected based on previous studies, which demonstrated the connection of low radiation polymerization doses with the generation of tips with small curvature radius [108, 109]. Furthermore, through the computational simulations presented in the following Section 4.3, one can see that curvature radius of approximately $3\,\mu m$, suit the trapping purposes.

A study of the curvature radius as a function of the polymerization radiation dose was performed (at least five micro structures were fabricated for each case. After this, images of the tips were acquired with an optical microscope, enabling to estimate the its curvature radius. The images were analyzed using ImageJ, and the plot of figure 4.5 was achieved. The error bars represent the standard deviation of the measurements. From this graph, it is possible to conclude the following: increasing the polymerization radiation dose leads to larger curvature radii. For each of the power levels tested, it was verified that increasing the exposure time has a minor influence, with an average variation of $\sim 0,5\,\mu m$ being observed when the exposure was increased from 4.5 to $20\,s$.

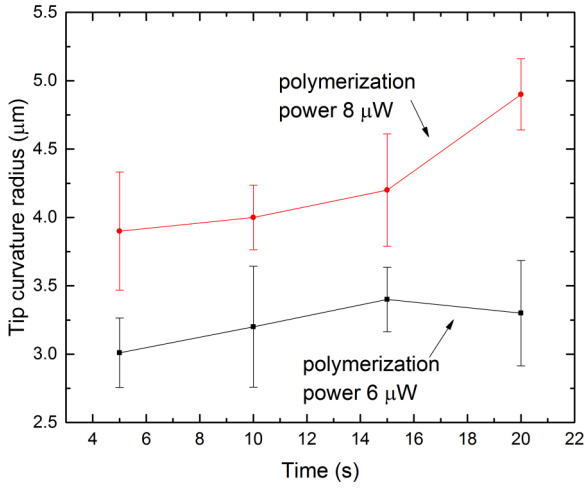

Figure 4.5: (a) Study of the tip curvature radius versus polymerization time, for laser powers of $6\,\mu W$ and $8\,\mu W$. The error bars represent the standard deviation taking into account that at least five samples were fabricated for each case.

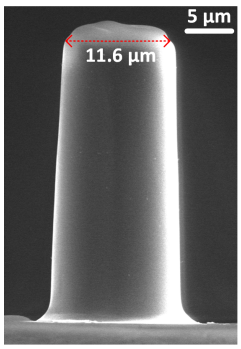

Figure 4.6: Polymeric optical fiber tip with flat profile (fabrication conditions: $405\,nm$, $20\,\mu W$, $60\,s$, polymer mixture 0.1% photo-initiator).

To illustrate what happens when the polymerization radiation dose is high, please see figure 4.6. This tip was exposed to $405\,nm$ radiation with $20\,\mu W$ during $60\,s$, leading to a flat tip. From this example, and several other experiments, one can conclude that increasing the dose of radiation results in the fabrication of microstructures with infinite curvature radius. Therefore, the use of controlled parameters plays a crucial role in the fabrication of tips suitable for optical trapping.

Besides the radiation doses, the concentration of the photo-initiator in the polymer mixture is of utmost importance. The outcomes presented in this thesis result from the use of a polymer mixture with 0.1% photo-initiator. However, if a higher concentration of photo-initiator is used, for instance 1%, rather then the low concentration mixture, even for low doses of radiation, the process leads to the fabrication of flat tips.

4.2.4 Discussion

These results provide the possibility to perform a simple preliminary analysis concerning the reproducibility of the fabrication of the polymer micro structures by the proposed technique. It was verified that, when other than the fundamental mode is excited, complex polymeric structures arise that result in altered output field patterns. From this analysis, some guidelines for the fabrication of polymer micro tips applied to optical trapping can be extracted. It is clear that control of modal excitation must be implemented for reproducible fabrication. Excitation of fundamental mode allows to obtain a structure with good quality leading to a Gaussian beam profile. Higher order modes result in more complex structures and output field profiles and its application requires a more detailed study. Indeed, it was verified that, without control of the modal distribution during the fabrication, the process reproducibility was very poor. On the other hand, after implementing controlled excitation of lower order modes the fabrication process was extremely reproducible.

Besides controlled excitation of the modal profile, the fabrication of tips with suitable features for optical trapping is attained by controlling the radiation polymerization dose, and the concentration of photo-initiator in the polymer mixture. This allows to fabricate tips with small curvature radius ($2.5\,\mu m \lesssim r \lesssim 5\,\mu m$). The tips have been reported in the literature as a suitable range for optical trapping [128].

Tailoring the micro tips to produce different outputs, such as, focal distance, which is linked with the curvature radius, can also be accomplished through the modification of the polymer refractive index. The available polymer mixture used in this thesis was characterized by a refractive index of 1.52, after photo-polymerization. In the future, this feature can be tuned to meet specific parameters, for instance, allowing to increase the efficiency of the tweezers.

4.3 Computational simulations

In order to evaluate the optical profiles and force maps resulting from polymeric OF tips fabricated through photo-polymerization, the computational model described in Section was used. Figure 4.7 describes the typical configuration of the system. The simulation were performed with a fixed resolution of $\frac{1}{15}\,\mu m$. The light source produces a guided electric field at $980\,nm$ along the OF, and it is linearly polarized along the direction perpendicular to the simulation plane. The tip width, curvature radius and refractive index were fixed during the various simulations to $6\,\mu m$, $3\,\mu m$ and 1.52, respectively. These values correspond to the width and average curvature radius of the fabricated tips,

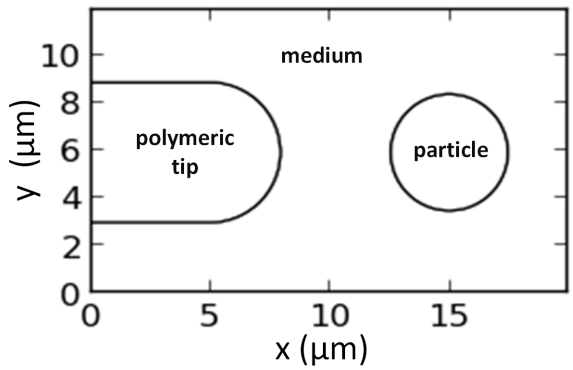

Figure 4.7: (a) Configuration of the computational system composed by the polymeric tip and circular dielectric particle.

as discussed in Section 4.2. Also the refractive index matches the one of the polymerized structure. However, the following parameters were modified during the simulations so that various scenarios could be analyzed:

- refractive index of the medium, n_{medium};
- refractive index of the dielectric particle, n_p;
- radius of the particle, r_p.

First, the effect of the refractive index of the medium on the focal characteristics of the tip was analyzed. To do this, three distinct media were considered: namely air, water and phosphate buffered saline (PBS), whose refractive indexes at $980\,nm$ are 1.000, 1.327 and 1.360, respectively. Figure 4.8, presents the field intensity profile for each of the refractive index of the embedding media, where it is noticeable that the focal length increases, while the refractive index step between the tip and the medium decreases. Simultaneously, the transversal and longitudinal beam waist spot size increases and the focal power[1] decreases.

The calculations of the radiation force can be done for different positions of the particle, resulting in the spatial distribution of optical forces, this is presented in the insets of figures 4.8 (b) and (c). From the resulting images the following can be concluded:

- the particle is guided towards the optical axis if offset in the transversal direction (y);
- along the optical axis (x) the net forces are very small when compared with other regions;

[1]The focal power is defined by $P = 1/f$, where f is the focal length.

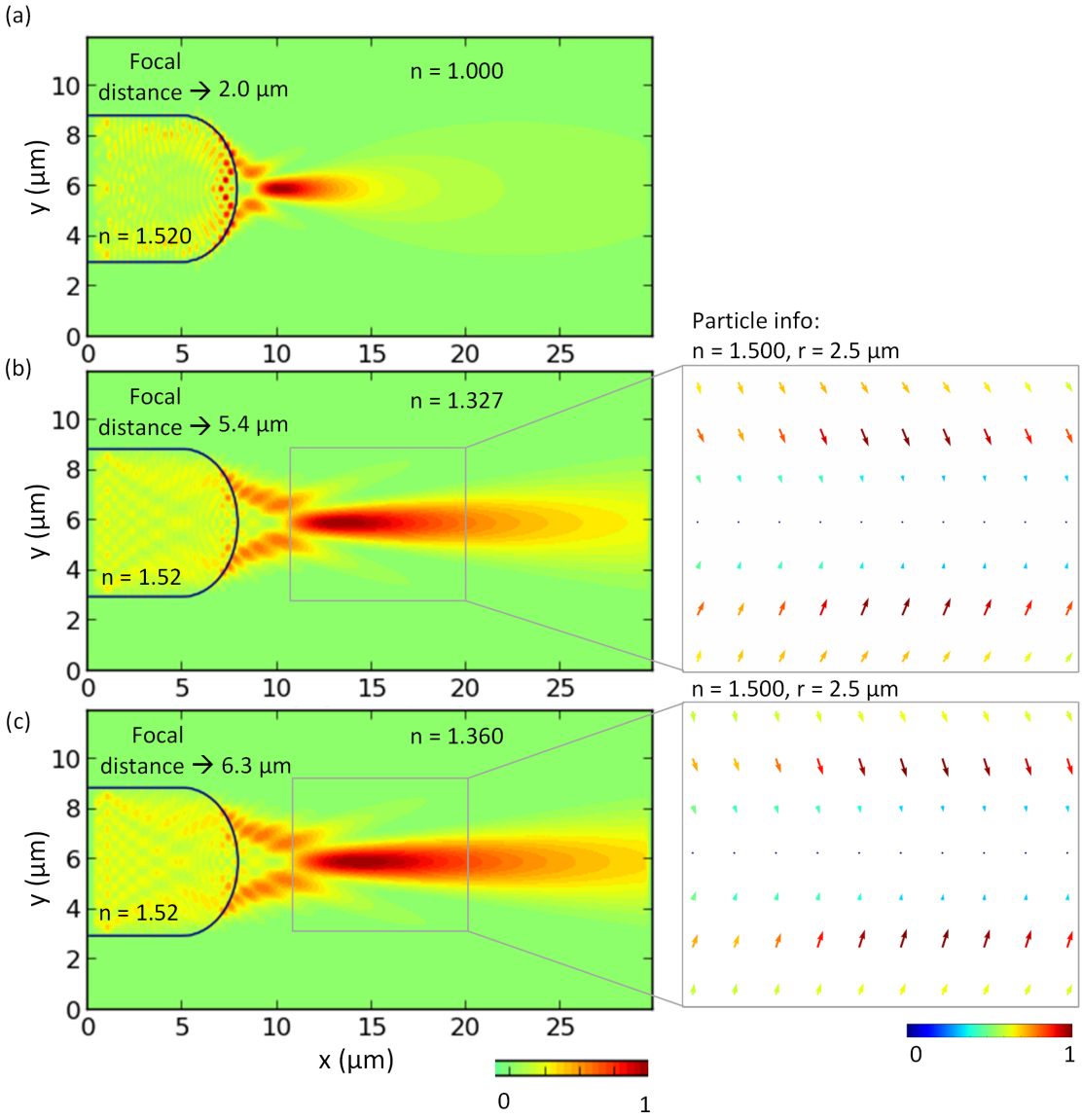

Figure 4.8: Field intensity profile for a polymeric tip with a refractive index of 1.520 immersed in several media: (a) air; (b) H2O; (c) PBS. The insets of figure (b) and (c) are the optical force maps for a circular particle with 2.5 μm curvature radius and refractive index of 1.500 on each medium.

Samples	Experimental Refractive Index	Size (μm)	Simulations Particles	Simulations Refractive Index
Polystyrene	1.5731 [129]	$8, 4, 1$	1	1.58
Yeasts	1.49–1.53 [130, 131]	$4-5$	2	1.50
PMMA	1.4843 [129]	8	3	1.48
RBCs	1.4 [132]	$6-8$ [**133**]	4	1.40

Table 4.1: Refractive index values and size of several particle and cell samples according to published data and values used in the simulations.

- although the focal position increases from $5.4\,\mu m$ to $6.3\,\mu m$, when the refractive index is altered from water to PBS, the most stable trapping seems to occur, for both cases, at $\sim 7\,\mu m$;
- there is only transversal confinement, this means that the trapping is in 2D.

The refractive index of the particles is one of the features that can easily affect the resulting optical forces (please see equations 2.1 and 2.3). In this regard, the transversal (y) component of the forces for four particles with increasing value of refractive index are represented in the graph of figure 4.9. Table 4.1 depicts the correspondence of the refractive index used in the simulations, and experimental data of real particle/cell samples. The values represented in this plot correspond to the positions along x where the transversal confinement was stronger. Generally speaking, the values of the forces increase with the refractive index, causing a stronger confinement of the particle. From this plot it is also possible to see that the value of the force is maximum when the particle is displaced $2.5\,\mu m$ from the optical axis, which corresponds to the magnitude its radius.

To understand how the position of the particle influences the optical forces, simulations for particles with different radii were performed: 1, 2.5 and $4\,\mu m$. These values are within the range that will be experimentally tested, as visible in Table 4.1. The refractive index value of the particles was set to 1.500. The values of the transversal component of the force are plotted in figure 4.10. From these results it is possible to observe that the force increases with the particle size, and its maximum value is obtained when the particle offset corresponds to the magnitude of its radius. The first effect results from equation 2.3, where it is visible that the gradient force is proportional to r^3. The second effect is due to the amount of electric field that contributes positively to the

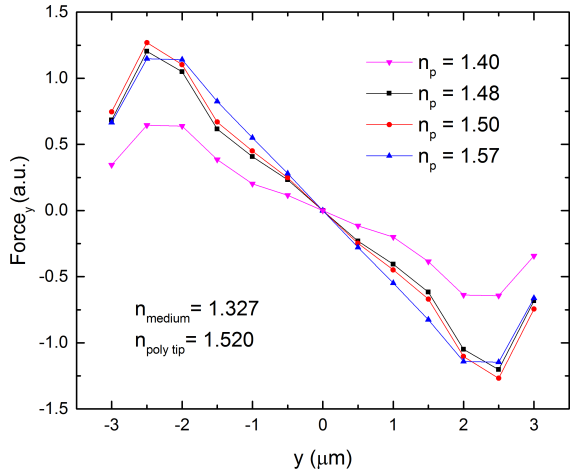

Figure 4.9: Study of the transversal component of the optical force as a function of the particle refractive index, n_p.

force. For instance when the particle is located at a distance smaller then the radius, there is a negative contribution to the net force due to the area that is located bellow the optical axis. However, this does not happen if the particle is located at a distance that is precisely equal to its radius.

From these results its seems to be possible to implement 2D trapping capabilities taking advantage of the transversal confinement presented either in the force maps depicted in figures 4.8 (b) and (c) or in the plot of figures 4.9 and 4.10. Along the optical axis, the x component of the force is the one that plays the major role, since y components are usually negligible. In this regard, the graph of figure 4.11 includes the axial components of the force, along the optical axis for several case studies. The most stable trapping position is located at $15\,\mu m$, corresponding to $\sim 7\,\mu m$ away from the fiber tip, as previously seen in the force distribution maps, in figures 4.8 (b) and (c). Beyond this, one can see that the force increases with the refractive index of the particle, since it scatters more light.

Please note that features such as the refractive index of the polymer can be modified, allowing to increase the focal power. However, it is important to take into account the size of the particles to be manipulated and the focal distance. For instance, if the focal distance is smaller than the particle radius, it is possible that the trapping does not happen, or is too close to the OF. In this case this can result in physical contact between the tip and the particle/cells. This is a disadvantage for the method, because it is likely to cause damage to the cells.

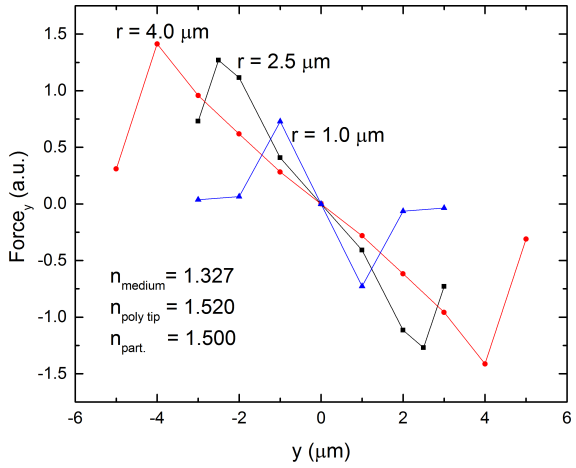

Figure 4.10: Study of the transversal component of the force as a function of particle size.

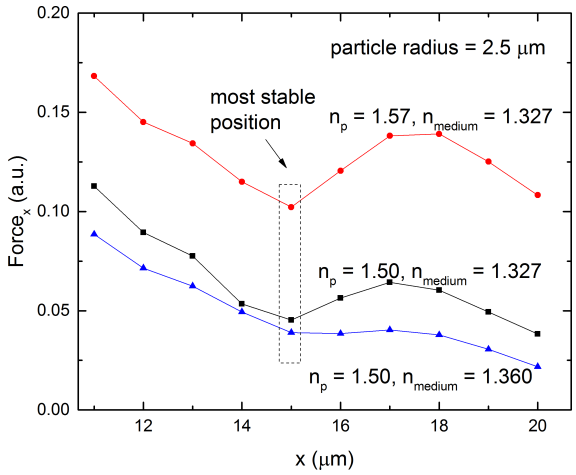

Figure 4.11: Study of the axial component of force along the optical axis direction for distinct particles and media.

4.3.1 Towards 3D trapping

3D trapping occurs when there is transversal and axial confinement, meaning that there is balance between the gradient and scattering forces. Figure 4.11 shows that particles with lower refractive indices suffer less intense scattering forces along the axial direction. This agrees with equation 2.1, where it visible that the scattering force scales much faster with the refractive index mismatch between the particle and the medium than the gradient force (equation 2.3). Figure 4.12 depicts the map of forces for a particle, with a radius of $2.5\,\mu m$, $n = 1.440$, immersed in water ($n = 1.327$). It indicates axial trapping, which is validated by the graph of figure 4.13, where F_x is plotted along the optical axis. For particles with the same geometry and refractive indices bellow 1.44, 3D trapping was confirmed. However, above this value, no axial confinement was verified in the simulations. Taking into account the value of the refractive index of the media and the particle, this indicates that $\triangle n < 0.113$[2] results in 3D trapping.

Since these results presented evidences of 3D trapping, scenarios where the refractive index of the tip is altered to higher values, were simulated. The values of the refractive index were considered to be: 1.62; 1.72 and 1.82. The simulations were performed in water, mimicking the experimental cases. The resulting electric field intensity profiles are depicted in figures 4.14 (a), (b), (c) and (d). Please note that the previous case, considering a tip with 1.52 of refractive index, was also included so that the comparisons with it can be drawn. From figures 4.14 (a), (b), (c) and (d) it is possible to see that the focal distance decreases for larger values of refractive index of the tip. This is corroborated by plotting the electric field intensity profile along the optical axis for the all the cases, which is presented in figure 4.15. From this graph it is also possible to see that the beam waist along x decreases for larger values of the tip refractive index, producing more confined focal areas. To understand the correlation between the confinement of the beam focus and the resulting trapping forces, simulations for a particle with a radius of $2.5\,\mu m$, $n = 1.440$, immersed in water ($n = 1.327$), were performed for each polymeric tip refractive index. The graph of figure 4.16 shows the net optical force along the axial direction for all the cases. From this plot it is possible to see that the confinement of the focal region leads to stronger traps, and that the trap position gets closer to the tip as the refractive index increases. The scheme on the bottom of figure 4.16 depicts the polymeric tip and the particle trapping location for every computed case. From this scheme one can see that there should be a limit for the refractive index of the polymeric tip, if one wants to avoid contact between the particle and tip. Generally, increasing the refractive index of the tip will contribute to a more stable trap. These indications can

[2] $\triangle n$ refers to the refractive index contrast between the medium and particle.

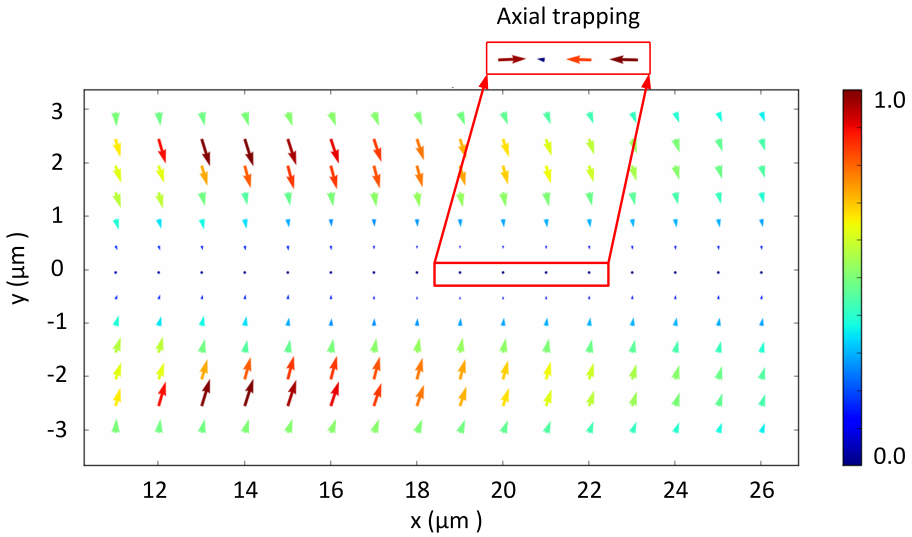

Figure 4.12: Map of forces for a particle, with a radius of $2.5\,\mu m$, $n = 1.440$, immersed in water ($n = 1.327$).

be used in the future to improve the trapping conditions.

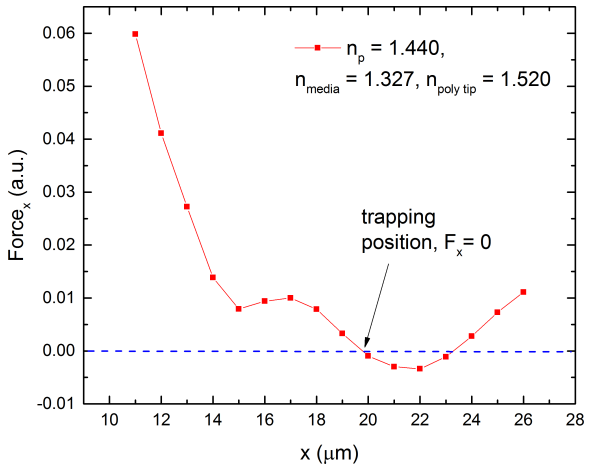

Figure 4.13: Axial force along the optical axis considering a particle, with a curvature radius of $2.5\,\mu m$, $n = 1.440$, immersed in water ($n = 1.327$).

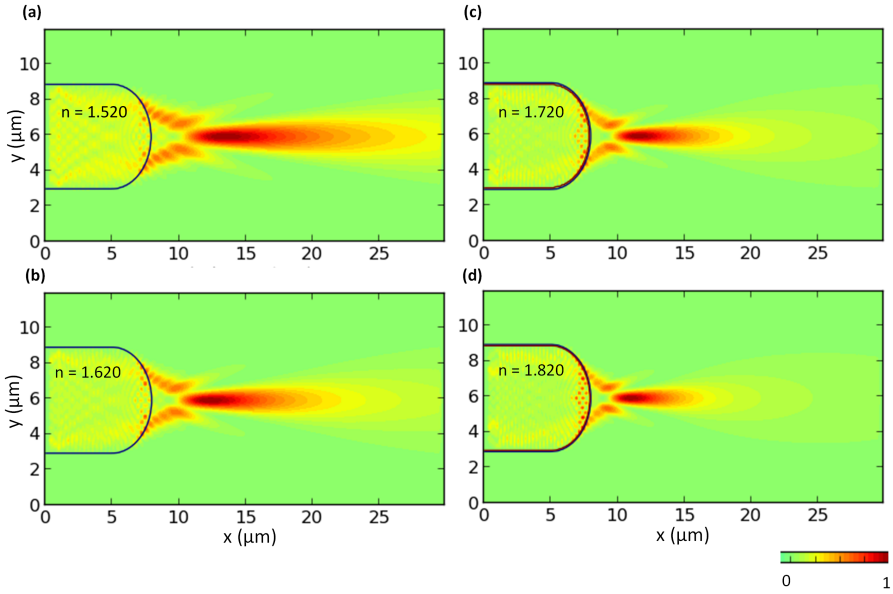

Figure 4.14: Computational study of the effect of the refractive index of the polymeric tip on the focal position, the simulations were performed in water, and the refractive index of the tips was: (a) 1.520; (b) 1.620; (c) 1.720; (d) 1.820.

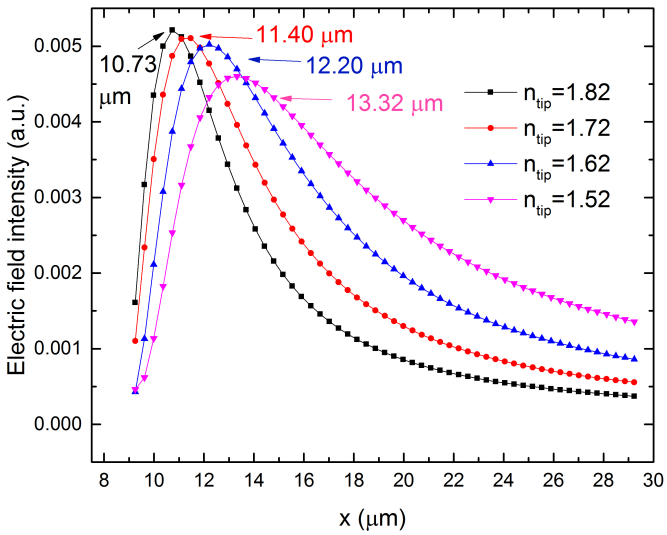

Figure 4.15: Representation of the electric field intensity profile along the optical axis, for polymeric tips with distinct refractive indices.

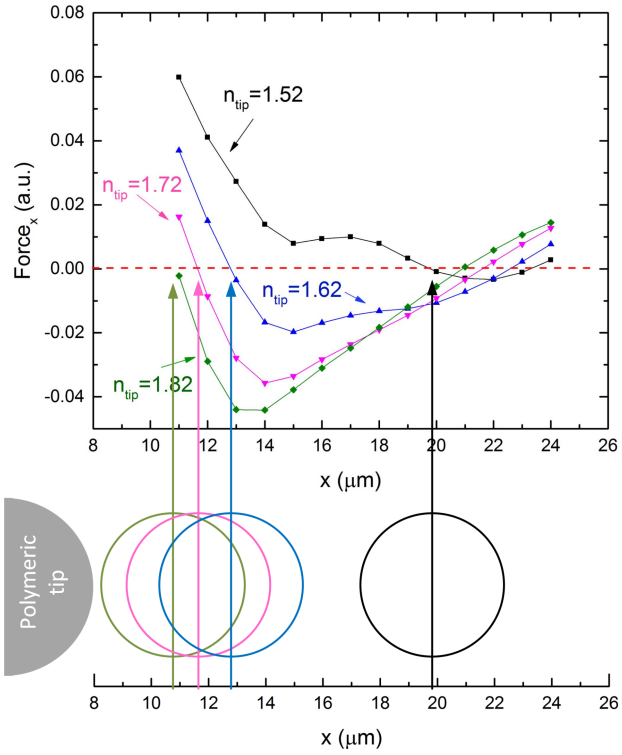

Figure 4.16: Axial force along the optical axis considering a particle, with a curvature radius of $2.5\,\mu m$, $n = 1.440$, immersed in water ($n = 1.327$) produced by polymeric tips with distinct refractive indices. The scheme on the bottom depicts the polymeric tip and the trapping location of the particle for every case.

4.4 Optical Trapping

4.4.1 Fabrication of polymeric optical fiber tips for optical trapping

In order to apply the polymeric tips as optical trapping tools, further optimization of its geometry was addressed, testing distinct geometries. A regular polymeric OF tip, as the ones previously described, has a high a aspect ratio, as shown in figure 4.17 (a) labeled as type A. This can results in some fragility, leading for instance to the detachment or breaking of the micro structures. However, if the drop of polymer located at the top of the OF is illuminated externally (sideways), the entire drop can be polymerized. Therefore, a structure covering the entire OF cleaved top can be formed. Such type of structure can be visualized in the scheme of figure 4.17 (a) labeled as type B. In this case, the final characteristics of the outer layer obtained are governed only by the polymer drop features such as viscosity and thickness. In practice, the two approaches can be

used in combination to obtain different types of structures, having tips with different curvatures and also a mechanical reinforcement effect.

In order to verify the utility of the polymeric structures for optical trapping, three distinct configurations (A, B and C) were fabricated, as represented in figure 4.17 (a). The different tips were then tested and compared for optical trapping of yeast cells. The structure of type A is a single tip. It has a length of $\sim 48\,\mu m$ and a curvature radius of $\sim 3\,\mu m$. It was fabricated by guided wave photo-polymerization exciting the LP_{02} mode in the 980 Thorlabs SM fiber (see Appendix B). Consequently, the profile of this mode (two concentric rings) was imprinted on the end of the polymeric structure, and a nearly spherical tip was obtained, as can be seen seen if figure 4.17 (b). The power and exposure time used were $6\,\mu W$ and $10\,s$, respectively. The diameter of the tip is approximately $6\,\mu m$, matching the fiber mode field diameter. In the second case, structure B is composed by an inner tip, similar to tip A, surrounded by a reinforcement structure. For this case also the LP_{02} mode was excited in the optical fiber. The inner structure was fabricated using the same process and parameters used for type A. However, after this first step, the resulting micro structure was dipped in the polymer again, and was illuminated externally. This way, the whole drop was polymerized forming a protection layer to the original micro tip, as can be seen in the SEM image in figure 4.17 (c). The tip was exposed during $30\,s$ to $10\,mW$ of $405\,nm$ radiation, directly from the laser. The final characteristics of the lenses were: a curvature radius of $3\,\mu m$, and a length of $35\,\mu m$ for the inner lens, while the protective structure has a curvature of $65\,\mu m$ and a length of $30\,\mu m$. This means that the inner lens is not totally covered by the protection layer, and it stands out at the tip extremity as can be seen in the figure 4.17 (c). Finally the structure C, was achieved making a larger protection layer totally covering the inner polymeric micro lens. The SEM figure 4.17 (d) shows a lens of $40\,\mu m$ length and $65\,\mu m$ curvature radius. In the example shown in figure 4.17 (d), lens C was obtained by submitting twice a lens of type A to additional dipping and external polymerization steps, using the same power and exposure time settings. In this particular case, the same polymer was used in both instances. With no optical contrast the whole structure will behave as a single spherical lens with a curvature radius of $65\,\mu m$. Nevertheless, the use of polymers with different refractive indexes can be explored to further control the light confinement in the first micro lens, and adjust the overall result of the lensed fiber tip. To sum up, this fabrication process is a fast (some seconds) and low cost way to produce spherical like lenses, with high reproducibility, and good optical quality (as can be seen in the images of the fiber tips).

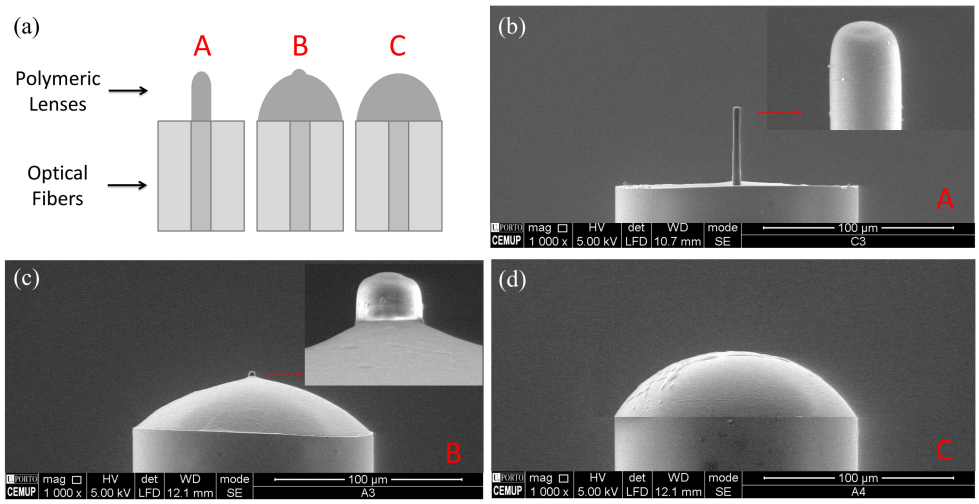

Figure 4.17: (a) Scheme of different polymeric OF tips. SEM images of the polymeric lenses: (b) Tip A, (c) Tip B, (d) Tip C.

4.4.2 Modeling the polymeric OF TIPs

Using the computational method described in Section 3.3, the three structures were modeled and the intensity beam profile and the optical forces resulting from their features were generated.

The dimensions of the structures simulated where set according with the experimental measured values, as described for structures A, B and C. In figure 4.18 one can identify the structures outline design in the graphs. The waveguides were considered to be immersed in water ($n = 1.327$ at $980\,nm$) and the refractive index of the polymer and particle was considered 1.52 and 1.48, respectively. The radius of the test particle was set to $4\,\mu m$. The value of the refractive index of the fiber core and cladding at $980\,nm$ was set to 1.458 and 1.451, respectively, as provided by the manufacturer. In figure 4.18 the electromagnetic field intensity profiles for the three structures are shown. As follows from the graphs, generally the polymeric structures A and B act as focusing diffractive structures, creating strong field gradients at their output. Structure C, on the other hand, has a mild focusing effect on the fiber output. Overall they all produce distinct output field distributions due to their different structural characteristics. In case of structure A and B both produce a tightly focused profile, and the beam waist is located $\sim 7\,\mu m$ from the polymeric tip end. This proves that the protective lens does not have an effect on the output of the optical field. Regarding the beam waist of lens C, on the other hand, it is located exactly in the lens to medium interface. The low focal power of the lens is caused by the high curvature radius, $65\,\mu m$. This way, structure C causes almost no focusing effect, but slightly reduces the divergence of the beam, since

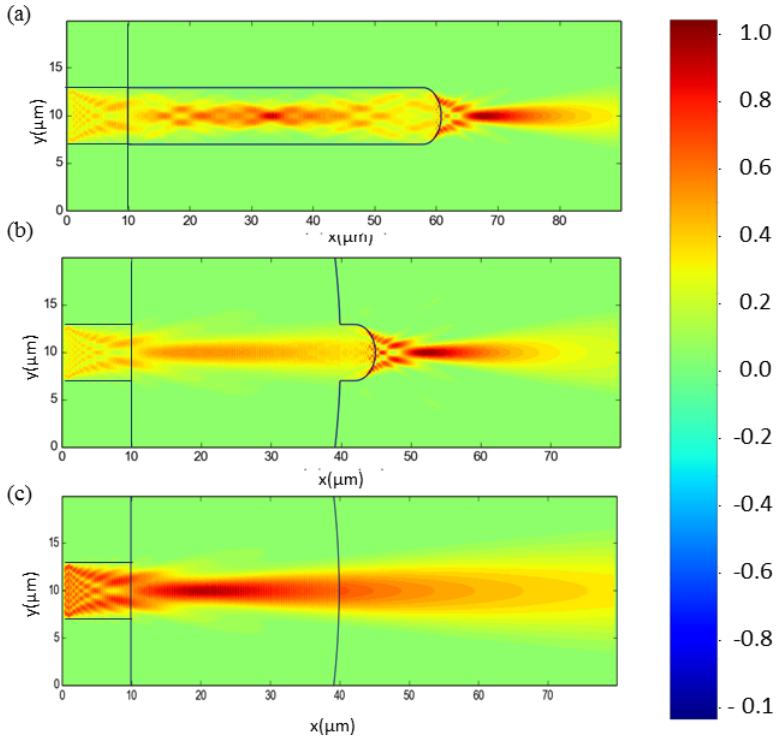

Figure 4.18: Electric field intensity profile for tips A, B and C, respectively.

the refractive index of the polymer is higher than the one of the OF. The calculations of the radiation force can be done for different positions of the particle, to obtain the spatial distribution of the optical forces.

The resulting "force field" distributions for lenses A, B and C can be observed in figures 4.19 (a)–(c), respectively. According to the results, all the three micro structures produce a net force that attracts the particle into the optical axis, therefore suitable for 2D trapping experiments. Once again, there are details that differentiate them. Due to the similar intensity profiles, lens A and B cause a similar force distribution. As can be seen in figure 4.19 when irradiated through these micro lenses the particles experience forces that redirect them to the optical beam axis and a transversal confinement is produced. For tips A and B the maximum gradient regions extend for $10\,\mu m$ and are quite similar (see figures 4.19 (a) and (b)). The difference between tip A and tip B is located in the outer regions. In the case of tip A, away from the beam axis, there are almost no optical forces acting to redirect the particle, whereas tip B produces a more intense force field as can be seen in figure 4.19 (b) pushing the particles away. The tip C, also produces an attractive gradient distribution, characterized by a transversal confinement of the particle, however, this is located much closer to the end of the tip (see figure 4.19 (c)). According to these simulations it is expected that tips A, B and C

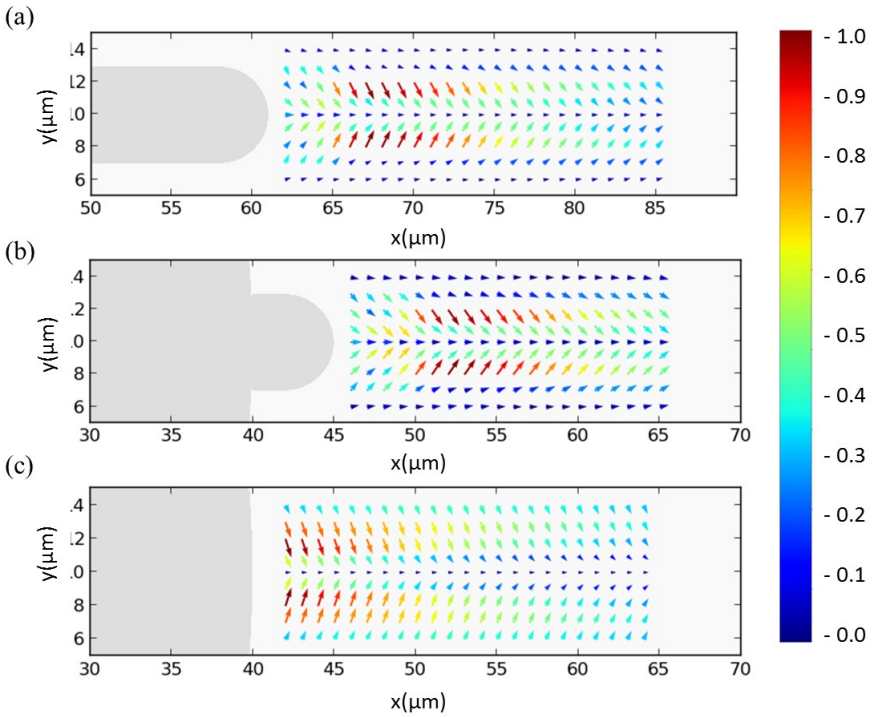

Figure 4.19: Map of the forces for a particle of $4\,\mu m$ diameter for lens A, B and C, respectively.

are able to guide and trap micro particles, although causing different force fields.

4.4.3 Optical manipulation setup

In order to test the fabricated polymeric OF tips, an experimental setup was assembled. It is composed by an inverted microscope connected to an image acquisition system, enabling the visualization of the OF micro lenses immersed in a sample. The setup can be seen in figure 4.20.

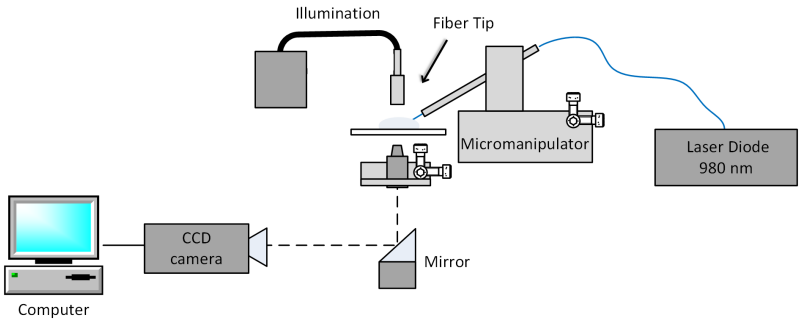

Figure 4.20: Optical trapping setup.

A pigtailed $980\,nm$ laser diode was connected to the optical fiber probes. The micro lensed fiber was placed within a capillary and then it was carefully positioned on a 4-axis motorized micromanipulator (x, y, z and angular). The probe was tilted at 35°, and the laser power was $\sim 20\,mW$. After this, a drop of the sample was placed on a glass slide over the inverted microscope setup, and the tip was immersed. The sample was composed by yeast cells with average diameters of $4-5\,\mu m$ in de-ionized water.

4.4.4 Preliminary results on optical trapping of Yeast cells

The video frames of the trapping experiments are presented in figure 4.21. The first set of images show the trapping of yeast cells by tip A (figure 4.17 4(b)). The cell marked as A was first trapped and isolated from the other cells (figure 4.21 (a)). Then, it was was pushed towards cells in position B. When irradiated the cells in B were aligned due the transversal force field (figure 4.21 (b)). In figure 4.21 (c) the three cells were aligned together. In figures 4.21 (d) and (e), it is visible the particles being pulled to $+y$ and $-y$ directions. This shows that this type of structures produce strong enough transversal gradient fields to pull the particles along the x directions. However, pulling the particles along the $-x$ direction could not be demonstrated with this tip, it was only possible to push and align them along the $+x$ direction. The second group of images shows the 2-D trapping of yeast cells by tip B (figure 4.17 (c)). The cell marked by the square is the reference cell that does not move during the whole experiment. Therefore the reader can use it as a reference to identify the movement of the trapped cell. One yeast cell was first trapped (figure 4.21 (f)), then it was pulled along the $-x$ direction (figure 4.21(g)). In figure 4.21 (h) the cell is moved along $+y$ direction. After this it was pushed along the $+x$ direction (figure 4.21 (i)), and then it was moved towards the reference cell (figure 4.21 (j)), demonstrating full 2D trapping.

The last group of images also shows the 2-D trapping of yeast cells using tip C (see figure 4.17 (d)).Once again the cell in the square is the reference cell and the trapped yeast is in marked by the circle (figure 4.21 (k)). First the yeast is driven in the $-x$ direction, and then it is moved along the $+y$ direction. After this, it is pushed along $+x$ and finally it is dislocated along $-y$.

These results clearly demonstrate 2D trapping of yeast cells using polymeric micro lenses. Although the lens of type A have shown effective trapping of the cells, overall these lenses produced a weaker trapping effect than in structures of types B, where this last one enabled full 2D trapping. For structure A it was observed that the minimum power necessary to trap the cells was higher when comparing to tip B. This can be caused by the losses at fiber to polymer interface, reducing the overall power available

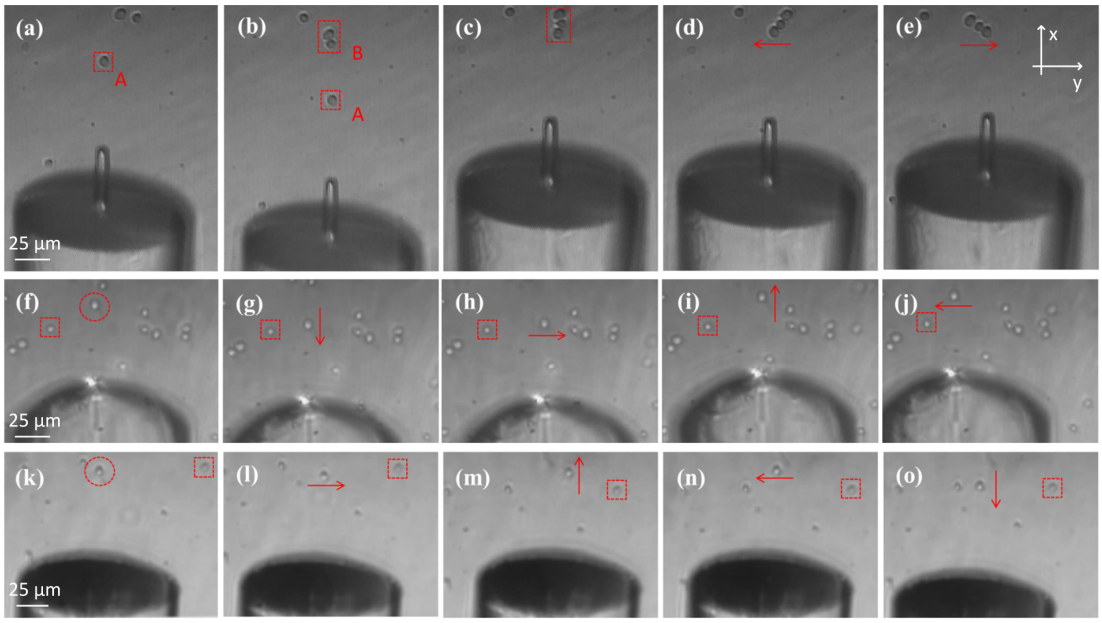

Figure 4.21: Video frames of optical trapping of yeast cells ($\sim 4\mu m$ diameter) experiments using tip A, (a) to (e), tip B (f) to (j), and tip C (k) to (o).

in the focal point. In addition, these types of lenses are more fragile, meaning that they are likely to break or detach from the fiber when in use. Tips B and C, on the other hand, did not displayed considerable losses at the fiber polymer interface, and are both very resistant due to the second protective polymer layer. Considering tip B and C, tip B demonstrated to be more effortless in positioning and moving the cells, leading to the what seems to be the most promising results. Regarding tip C, its geometry is not that different from a cleaved OF, since it has a large curvature radius ($65\,\mu m$). However, with the polymer it is possible to decrease the divergence of the output light beam, as demonstrated in the simulations. This resulted in 2D trapping, nevertheless, the performance of the trapping was considerably weak when compared with tip B. To sum up, tips A and B are the ones that will be further tested and analyzed, since the first enabled trapping of multiple particles and the second demonstrated efficient 2D trapping.

4.4.5 Optical trapping of organelles of plant cells

The large dimension of plant cells is normally out of the optical trapping manipulation range. In this regard the manipulation of the cell itself, using the relatively low powers needed to avoid damage, is hardly feasible. However, the cells present an internal structure having several organelles with sizes of a few microns.Therefore, these internal

structures of the plant cells, are suitable targets for manipulation using optical trapping effects. Indeed, using the reinforced version of the polymer tweezers it was possible to demonstrate for the first time the ability to manipulate internal organelles of *Medicago Sativa* cells. This demonstration configures a truly non-invasive way of manipulating the internal structure of a cell. An example of such features can be observed in the set of images in figure 4.22 where the movement of some organelles inside a vegetable cell by action of the OF TIP is shown.

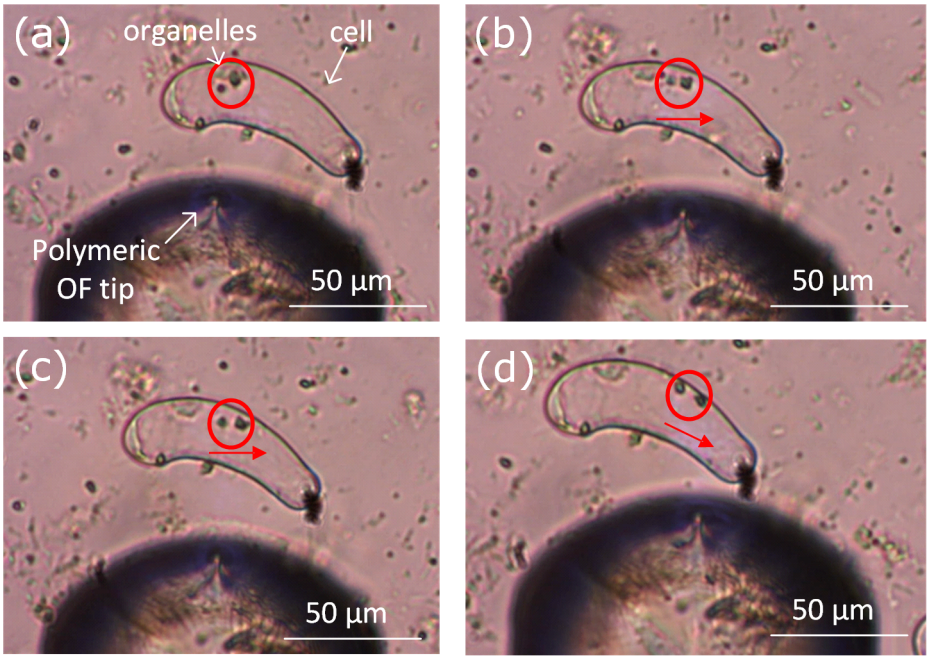

Figure 4.22: Manipulation of inner organelles of *Medicago Sativa* plant cell.

4.4.6 Experimental measurement of optical forces

So far the polymeric OF tips were qualitatively validated for optical trapping of micro targets, such as yeast cells and organelles of plant cells. However, the trapping forces were not measured due to constrains with the setup in the early stage of the experiments. At a later stage, with a more consolidated setup, the previous tests were repeated using the polymeric OF tip presented in figure 4.23. This tip has a length of $\sim 28\,\mu m$ and a curvature radius of $\sim 3\,\mu m$. It was fabricated using the previous photo-polymerization method: the LP_{01} mode was first excited and then imprinted on the top of the polymeric structure, laser power $10\,\mu W$ and exposure time of $10\,s$. In order to assess the output beam profile of the micro tip a CCD camera was used to acquire consecutive images, at different positions along the optical axis.

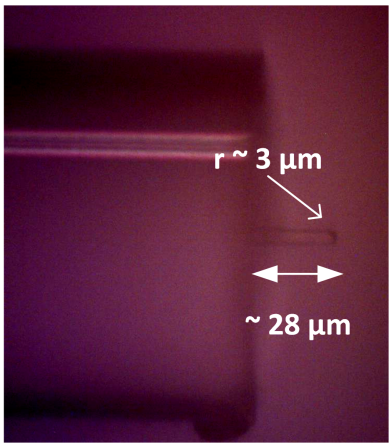

Figure 4.23: Polymeric optical fiber tip with $\sim 28\,\mu m$ length and $3\,\mu m$ curvature radius.

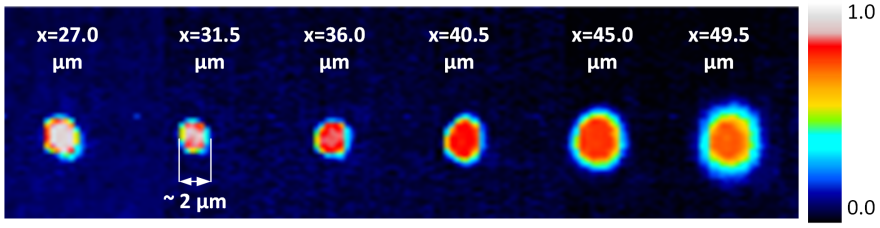

Figure 4.24: Experimental transversal optical output beam profile acquired at several positions along the optical axis.

Figure 4.24 depicts the consecutive snapshots of the output beam, acquired along the optical axis at each $4.5\,\mu m$. Please note that the micro tip is $28\,\mu m$ long, and the first image was taken at a distance of $27\,\mu m$ from the OF, meaning that the camera was focused inside the micro tip. Note that the position where the images are acquired is controlled by first focusing the camera at the fiber top, and then scanning it along the x direction, therefore $x = 0\,\mu m$ corresponds to the top of the fiber. From figure 4.24 it is possible to observe that the waist of the output beam becomes narrower at $31.5\,\mu m$, with a diameter of $\sim 2\,\mu m$, where its intensity reaches a maximum value (white in the normalized scale). After this, at $36.0\,\mu m$, the intensity decreases and the spot size enlarges. In other words, the tip acts as a convergent lens focusing the beam, at a focal distance of $\sim 3\,\mu m$.

To confirm the experimental observations, the tip was studied computationally. To do this, the experimental features of the tip were taken into account. The results are depicted in figure 4.25 (a). The focal spot is located at $30\,\mu m$ approximately $2.2\,\mu m$ away from the tip. The the beam spot size (transversal, along y) is $\sim 1\,\mu m$. Since

the spacial resolution of the experimental data is relatively low, it is not possible to precisely locate the focal spot. However, it is feasible to conclude that experimental and computationally the data are within the same range. These studies were carried out for a tip surrounded by air ($n = 1.000$), nevertheless, the trapping experiments are accomplished in water. With this in mind, a second simulation was performed for the case of the waveguide immersed in water. In this case the focal power of the lens was reduced, as visible in figure 4.25 (b), the focal distance increased $2.8\,\mu m$, being located at $5\,\mu m$ from the tip. Besides this, the beam waist became wider ($\sim 1.5\,\mu m$). The trapping ability of the tip was assessed as well, for a dielectric particle ($r = 2.5\ \mu m$, $n = 1.500$, mimicking the size and refractive index of an yeast cell). The map of forces acting on such a particle is depicted in the inset of figure 4.25 (b), where the mapped zone corresponds to the delimited area. The results indicate that 2D trapping of the yeast is bound to occur, and the most stable position is between 33 and $34\,\mu m$, i.e, 5 to $6\,\mu m$ away from the tip, near the focal position.

To test the tip it was assembled in the setup depicted in figure 4.20. Please note that the fiber was tilted 35^o. Prior to this experiment, some other angles were tested, demonstrating that bellow $\sim 30^o$ trapping could no be observed. Furthermore, this range of values was also successfully used by other authors as reported in the literature[134, 135]. The snapshots of figure 4.26 show a series of tests performed to evaluate the optical trapping of yeast cells. The cell to be trapped is identified by the white square. Three other cells will be used as references during the trapping tests: a cell bellow in a red circle and other two at the right in a red ellipsis. In figure 4.26 (a) the laser is off, then in figure 4.26 (b) the laser is turned on (@ $20\,mW$), the fiber is approximated to the cell, and then it is immediately trapped. The distance between the cell and the fiber is approximately $3\,\mu m$ matching with the computational data. In figure 4.26 (c) the particle is moved to the $-x$ direction, it is visible that it is more distant from the cells in the right side. In figure 4.26 (d) the particle is moved in the $+x$, and is again closer to the reference cells. This demonstrated the axial trapping abilities of the OF TIP. Subsequently, the particle was driven to the $+y$ direction and and then $-y$, as visible in figures 4.26 (e) and (f). Therefore it was first moved in the direction of the reference cell in the red circle and then it was moved away. This second part of the tests prove the transversal confinement of the optical trap, thus validating 2D trapping.

The dynamic of the yeast cell in the trapping position was studied according to the following procedure. First the yeast was trapped, then the laser was turned off, and the fiber was moved. After this, the laser was again turned on, and since the fiber is only a few micrometers away from the yeast, it was attracted towards the stable position. This

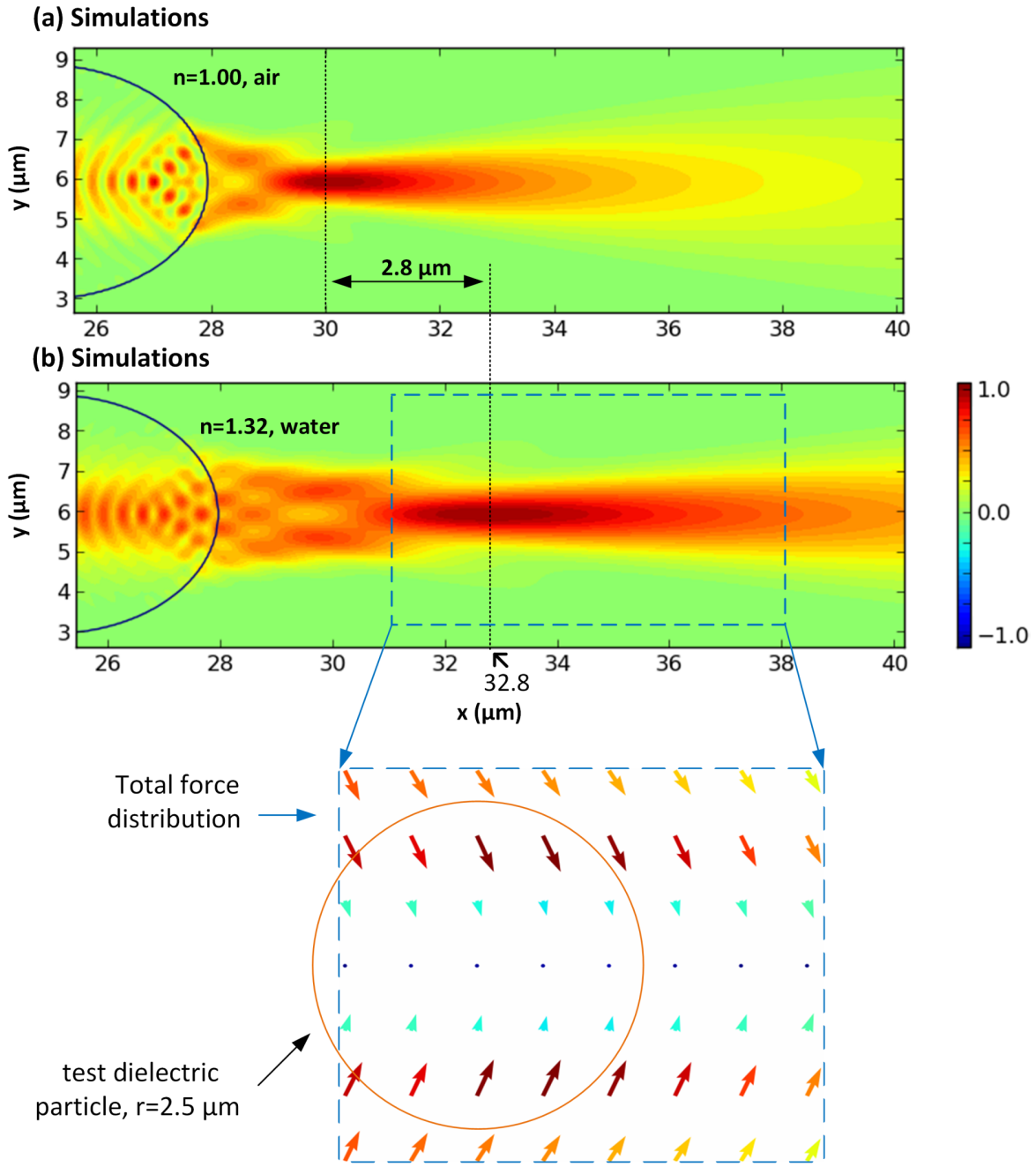

Figure 4.25: Modelization of polymeric micro structure used in the trapping experiments: (a) in air; (b) in water; (inset) map of optical forces acting on a particle mimicking the yeast cell.

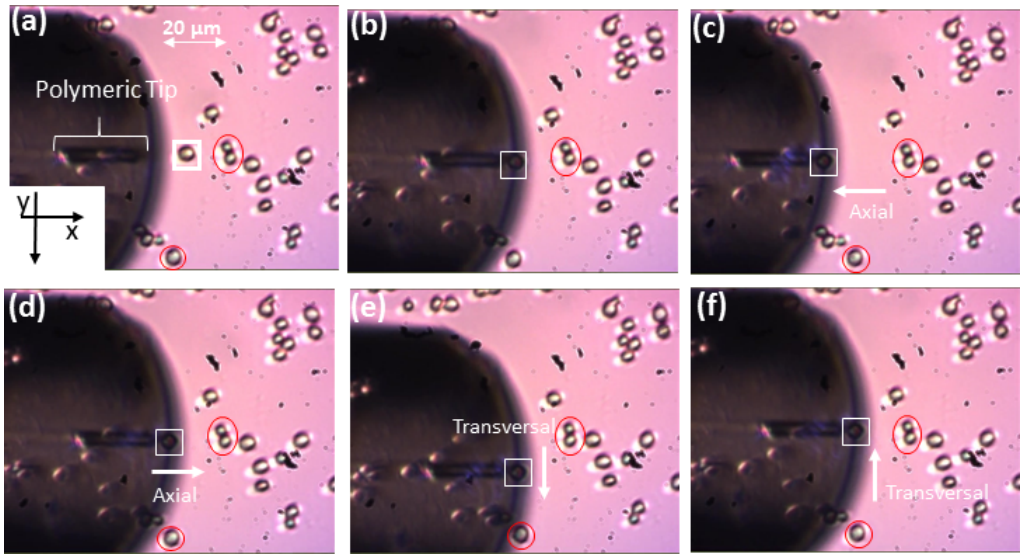

Figure 4.26: 2D trapping of an yeast cell using a polymeric lensed OF.

was performed for each direction, $-x$, $+x$, $-y$ and $+y$ using a laser power of $10\,mW$, and $20\,mW$ with the fiber tilted at 35°. It is important keep the laser power as low as possible so that damage of the trapped targets trough heating is avoided. After this, using a particle tracking software from ImageJ [122], the trajectories of the particles were obtained from the recorded videos, enabling to calculate the optical force, according to equation 3.5. The graph of figure 4.27 is a representative example for the case of the transversal components of the optical force. This picture demonstrates an attractive force, pulling the yeast towards the stable position, within a range of $\sim 5\,\mu m$.

Table 4.2 shows the measured optical force values along the axial and transversal directions for $10\,mW$ and $20\,mW$. Overall, one can see that the values of the optical force increase with the laser power, and that the trap is symmetric along the transversal direction while in the axial direction it is not. This can be explained by the scheme of figure 4.28. While the particle is before the trapping position, i.e., in the axial (x) direction, both the axial components of the scattering and gradient force add positively to drive the particle towards the stable position. However, when the yeast/particle is located beyond the trapping position, the axial component of the gradient force must overcome the axial component of the scattering force, thus resulting is smaller net values.

Optical force efficiency

The trapping efficiency, for the configuration described above can be calculated though equation 2.5. The values are presented in table 4.3. Transversely the trapping is sym-

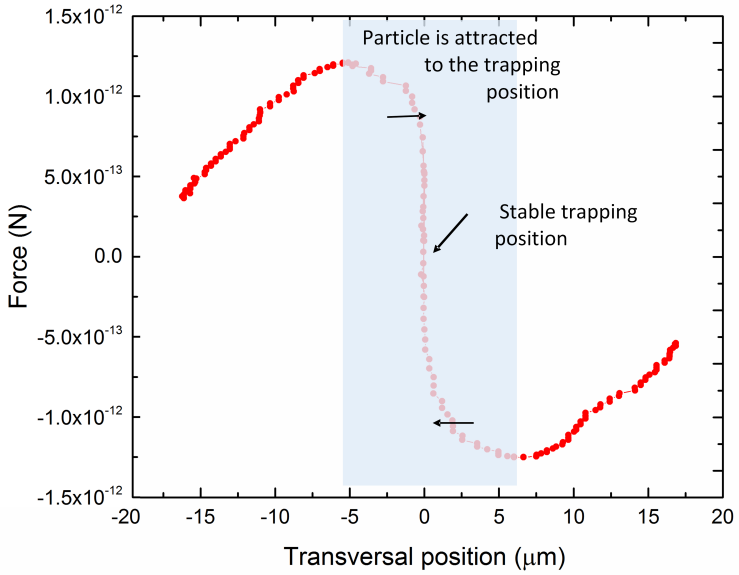

Figure 4.27: Transversal force (y) acting on an yeast cell moved using the polymeric OF tip shown in figure 4.23.

Power (mW)	$F_{+y}(N)$	F_{-y} (N)	$F_{+x}(N)$	$F_{-x}(N)$
10	1.11×10^{-12}	-1.14×10^{-12}	1.40×10^{-12}	-0.40×10^{-12}
20	1.41×10^{-12}	-1.45×10^{-12}	1.61×10^{-12}	-0.72×10^{-12}

Table 4.2: Experimental optical force values along the axial (x) and transversal (y) directions.

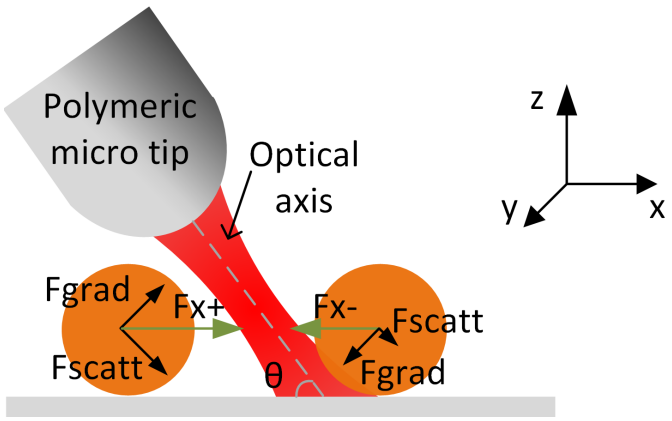

Figure 4.28: Optical forces acting on the particle, when it is at different locations.

metric and the average Q_y is 0.02. However axially, the trapping is not symmetric, meaning that it is more easy to push particles, Q_{+x} of 0.03, than pull them, Q_{+x} of 0.01.

Q_y	Q_{+x}	Q_{-x}
0.02	0.03	0.01

Table 4.3: Optical force efficiency.

Comparatively to other efficiency values reported in the literature for conventional and OF trapping setups $(0.35-0.01)$ [29, 85, 136], the efficiency of the polymeric tips is relatively low. However, in this work, the values are used to compare the efficiency of the x and y axis, which have been found to respond differently, and also to compare the devices presented in this Chapter and on the following one.

4.4.7 Insights on particle sensing

Although not predicted by the simulations, the tips were tested for the 3D trapping. To do this, the polymeric OF tip was moved upwards and downwards in the z direction. This should result in the shift of the trapping point (zero net force) along the z axis. In case of effective 3D trapping, the cell should also describe movement along z, which should show as a focusing and defocusing effect of the trapped cell in the images. However, a different result was observed instead. Indeed, the particle moves, but in the axial direction (x in figure 4.29 (a)). It moves away, when the fiber is moved up, returning to the same position when the fiber is moved down. Since the particle does not move along z, the movement of the fiber results in an oscillation of the trapping force, thus modulating the yeast position.

This modulation on the particle position was induced during $45\,s$, and the resulting trajectory is plotted in figure 4.29 (b), represented in the black curve. At the same time, the stability of the trapping in the transverse position was monitored (red curve). From these results it can be concluded that the particle is not trapped in the third dimension, but, on the other hand, it is possible to modulate its position in the axial direction. This ability can pave the way to new sensing applications. For instance, if the optical trap is extremely well characterized (including knowledge of the optical forces in both directions and the trapping stiffness) parameters such as the mass of the particle can be extracted from the modulation data, since the trajectory represented in figure 4.29 (b) is basically an harmonic oscillator.

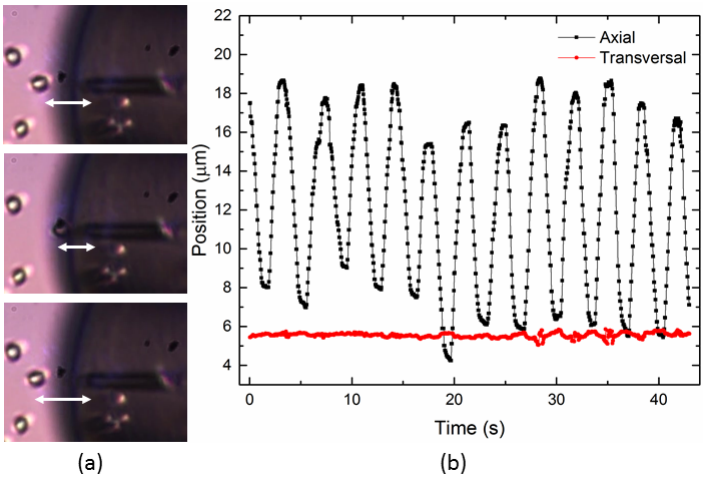

Figure 4.29: (a) Frames of the resulting movement of the yeast cell when the fiber is moved in the z direction. (b) Modulation caused in the particle trajectory.

4.5 Conclusions

The present Chapter was designed to investigate the use of polymeric OF micro structures as optical trapping tools. The study included a preliminary evaluation of the fabrication conditions more suitable to produce micro tips with the desired optical quality and geometrical features, multiple computational simulations contemplating several trapping scenarios, test of the tips for trapping of cells and finally measurement of the experimental optical forces.

Overall the results obtained demonstrated the suitability of guided wave photo polymerization as a very attractive technique for the fabrication of OF TIPs. It is a rapid low cost process eligible for batch processing. Micro tips with curvature radius of $\sim 3\,\mu m$ are obtained by exciting either the LP_{01} mode or LP_{02} mode and setting the laser power and exposure time to $6\,\mu W$ and $10\,s$, respectively. These structures were investigated computationally for optical trapping of dielectric particles with refractive indices mimicking cell samples, i. e., between 1.44 and 1.57. 2D trapping was immediately demonstrated, motivating experimental tests.

The polymeric structures were validated experimentally for 2D trapping of yeast cells and organelles of plant cells. The maximum optical force measured in the case of the yeast cells was $1.61 \times 10^{-12}\,N$.

To conclude, though successfully implemented, there is still room for improvement by combining this technique with different fibers, selective modal polymerization and indicator dyes can have a strong potential for the design of new OF TIPs with ad-

vanced capabilities of manipulation and sensing. Besides this, the preliminary results on 3D trapping indicated that using particles with small refractive indices or tuning the refractive index of the polymer of the tip will contribute to improve the trapping capabilities.

Chapter 5

Optical fiber TIPs using Fresnel zone and phase plates

The aim of this chapter is to explore the potential of mode expanded optical fiber tips with Fresnel zone and phase plates for optical trapping of microscopic cells and dielectric particles. The diffractive optical elements are fabricated through focused ion beam milling, and contrarily to the photo-polymerization method, this has sub-wavelenght resolution, enabling more flexible designs.

The fabrication methodology is presented in the first place, describing particularly the procedure used in the fabrication of a set of four Fresnel plates. These are then optically characterized, and the output beam profiles are compared with computational simulations. These results demonstrate that Fresnel phase plates are successfully designed and have an optical efficiency conversion higher than zone plates.

After this, the use of the phase and zone plates for optical trapping of cells and particles is investigated. In the case of phase plates, yeast cells and PMMA beads are trapped in 2D and together with a backscattered light detection system the trapped targets are differentiated based on their size. Unlike the phase plates, the zone plates do not enable such effects. In this case, large gas microbubbles are generated on the top of the optical fibers due to heating effects preventing the immobilization of the particles.

5.1 Background

The implementation of DOE in optical trapping, for instance, by means of SLMs, brought undeniable versatility to this area. From the generation of multiple optical traps to the transference of optical angular momentum, dynamic engineered light fields become

crucial for the progress of optical trapping tools [137]. Simultaneously, the development and accessibility of fabrication methods with sub-wavelength resolution enabled a new era in photonics, where the synergy between optical manipulation and optofluidics is for sure a consequence [138].

From this point of view, the development of OF trapping tools based on more complex designs allowing higher degrees of control, such as DOE, is inevitable and represents a valuable step towards the miniaturization of the devices and their widespread use. Please refer to Section 2.2.4, for a detailed state of the art of OF trapping tools fabricated by high resolution methods. In the present chapter, Fresnel zone and phase plates are fabricated by FIB milling on OF tips.

The preference for Fresnel plates is linked with three main reasons: Fresnel lenses are an alternative to conventional trapping objectives, since their design allows tailoring features like focusing distance and numerical aperture, matching the desired values necessary for OT; the planar design offers significant chances to be implemented in microfluidic channels, incorporated in optofluidic devices [139, 140]; and finally, the possibility to replicate these structures using nanoimprinting lithography [94], to fabricate a large number of fiber probes.

There is some literature reporting the fabrication of Fresnel plates on optical fiber tips using femtosecond laser micromachining and FIB milling. The first method was employed in the fabrication of structures mainly focused on light coupling devices [87, 141, 142]. Nevertheless, the second process was used to fabricate a structure designed for optical trapping of sub-wavelength particles [88], on the contrary, the present work reports trapping, manipulation and detection of micron-sized particles and cells, foreseeing applications to larger target sizes, such as mammalian cells.

This chapter is composed by the following topics: first the fabrication methodology used to achieve phase and zone plates on OFs is presented, then the structures are characterized optically and finally the OFs are tested for optical trapping.

5.1.1 Theory of Fresnel zone and phase plates

A Fresnel zone plate (FZP) , is a diffractive optical element, composed by a sequence of concentric alternating opaque and transparent zones, with axial symmetry [143], as visible in the scheme of figure 5.1 (a). The zones are dimensioned so that the path length from two adjacent rings differs by $\lambda/2$ causing constructive interference at the desired

focus. The radii of the successive rings are given by:

$$r_n = \sqrt{n\lambda f + \frac{n^2\lambda^2}{4}}, \tag{5.1}$$

where n is an integer, λ is the wavelength and f is the focal distance. For $\lambda \ll f$, equation 5.1 reduces to:

$$r_n = \sqrt{n\lambda f}. \tag{5.2}$$

The intensity of the focal point is proportional to the number of zones. These structures have chromatic aberration, just like ordinary convex lenses, since f is inversely proportional to λ. In contrast, Fresnel plates have multiple foci: composed by the main focal point, f, and higher order focal points at $f/3$, $f/5$, ..., with decreasing brightness [144]. From this, a Fresnel zone plate is basically an amplitude device. Nevertheless, an alternative plate may be achieved if the opaque zones are replaced by transparent π-phase steps. In this case the resulting focal spot will be brighter, increasing the optical conversion efficiency of the plate, since the light is no longer blocked [145]. This is the so-called Fresnel phase plate (FPP) (figure 5.1 (b)). The depth (d) of the zones is given by

$$d = \frac{\lambda}{2(n_{plate} - n_{medium})}, \tag{5.3}$$

where n_{plate} and n_{medium} are the refractive index of the plate and the surrounding medium, respectively.

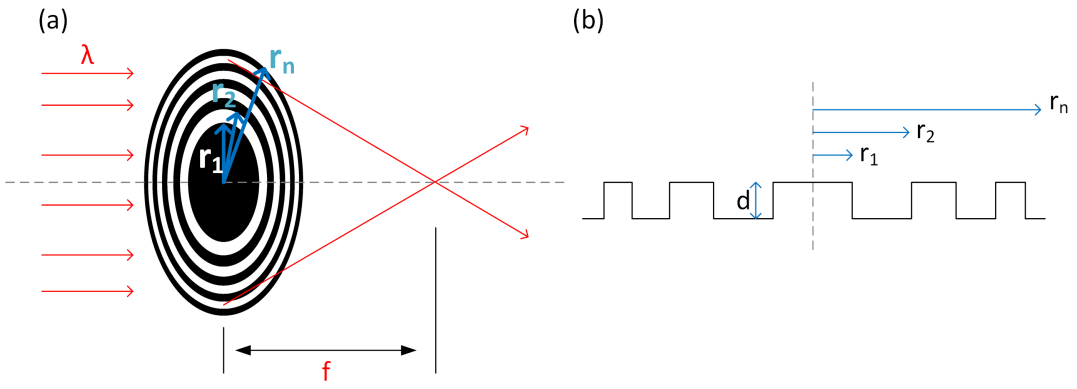

Figure 5.1: (a) Fresnel zone plate; (b) Fresnel phase plate.

5.2 Fabrication methodology

5.2.1 Preparation of mode - expanded optical fibers

A single mode optical fiber is usually characterized by a mode field diameter of a few micrometers, thus limiting the effective micromachining area. Since the number of zones directly affects the intensity and width of the central peak generated by the FZP or FPP, it is pertinent to use mode-expanded optical fibers [141], enabling a broader effective area available to be micromachined. A scheme illustrating this is presented in figure 5.2. This is attained by splicing the single mode fiber (SMF) to the multimode fiber (MMF), allowing the fundamental Gaussian mode that propagates in the SMF to expand in the MM segment. The cross section that is covered by the beam depends of the length of the MMF and it can be calculated through the numerical aperture relation, given by

$$NA = nsin\theta = \sqrt{n_{core}^2 - n_{cladding}^2}, \tag{5.4}$$

where θ will be the divergence angle of the beam propagating in the MM segment, n is the refractive index of the MMF and n_{core} and $n_{cladding}$ refer to the refractive index of the core and cladding of the SMF, respectively.

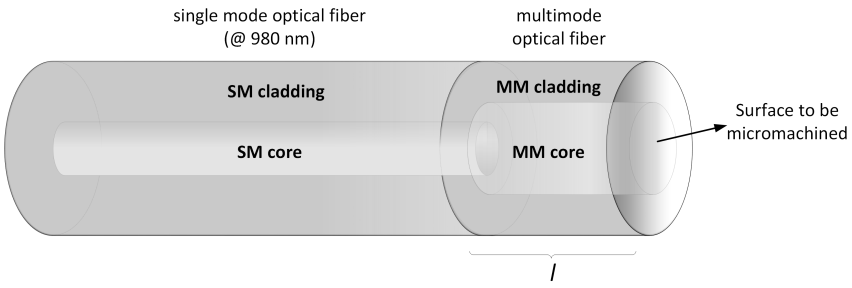

Figure 5.2: Scheme of the single mode optical fiber and the multimode segment.

The plot of figure 5.3 shows the relation between the MMF length and the beam size, calculated using equation 5.4. Figure 5.4 illustrates the same result, though computed through simulations taking into account the beam propagation along the MMF, emerging from the SMF. The single and multi-mode fibers described in this work are HI 980 (Corning) and AFS 50/125Y (Thorlabs), respectively (Appendix B). The procedure starts with the splice of a SM with a MM fiber segment.

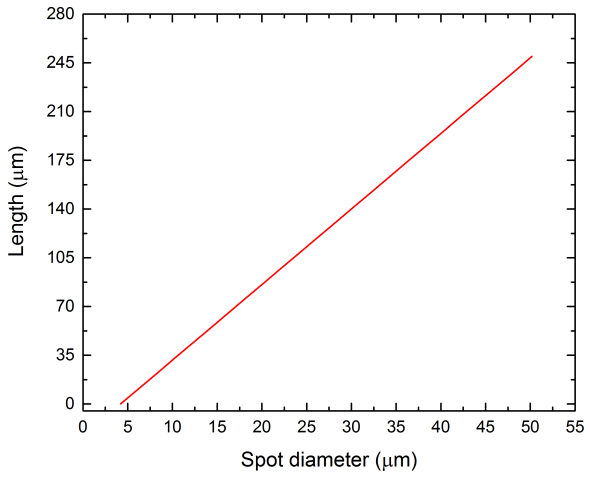

Figure 5.3: Beam spot size diameter versus length of the MMF.

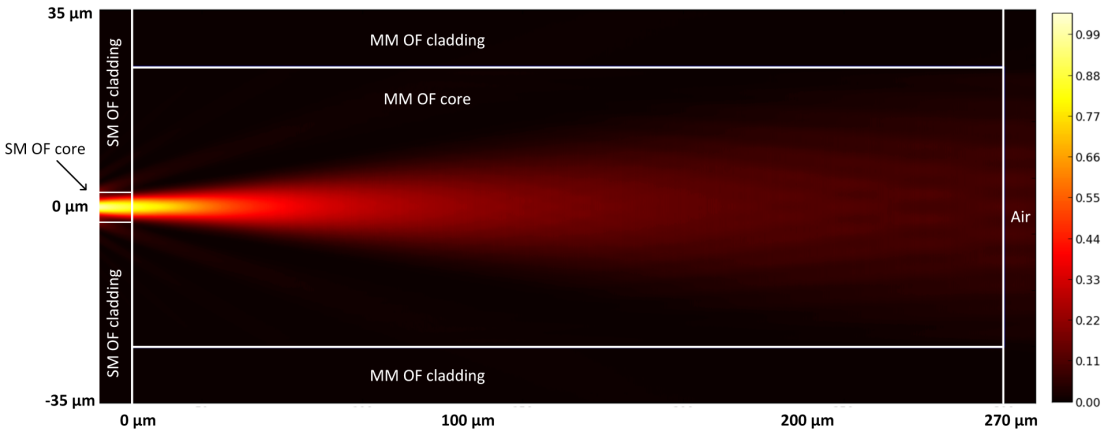

Figure 5.4: Computational simulation of the expansion of the laser beam in the MMF segment. The parameters used in the simulation are depicted in Appendix B.

Cleaving process

After this, the MMF is cleaved at an optimal length, l. A USB camera with a magnifying lens is placed above the cleaving machine allowing the observer to control the process. The fiber is moved, relatively to the blade, using a micrometric positioner placed before the machine, as visible in the scheme of figure 5.5. The imaging setup allows a continuous magnification range from 50× to 500×, and the micro stage has a resolution of $0.5\,\mu m$ thus enabling to cut the MMF with enough accuracy. The length of the MM is important because it determines the dimensions of the fiber cross section covered by the beam. In this case, the extent of the MMF is optimized so that the beam covers the diameter of

the plate that will be milled on the fiber tip. Once cleaved and cleaned, the fibers are finally mounted in a 45^o stub, that is suitable to be used in the FIB and for the coating deposition, as described in Section 3.2.

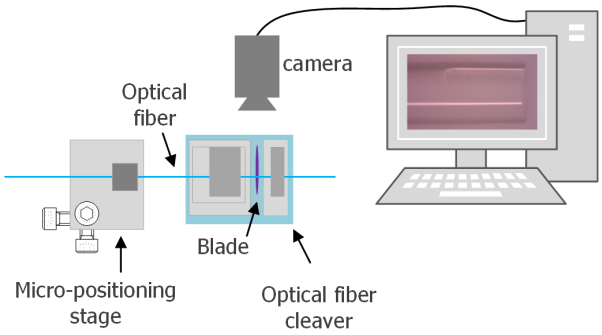

Figure 5.5: Scheme of the setup used to cleave the OF tips.

5.2.2 Focused ion beam milling of Fresnel structures

Conductive coating

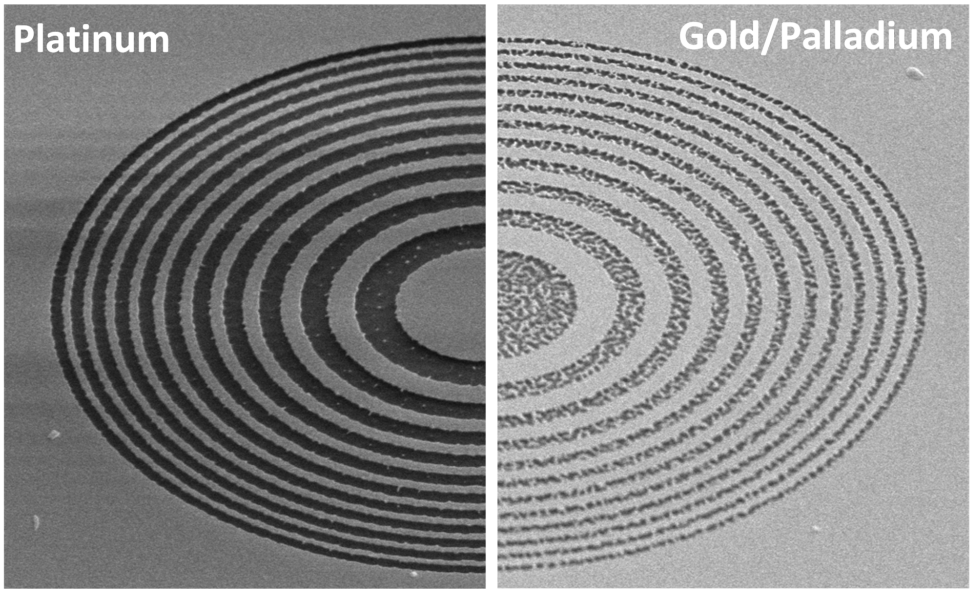

Figure 5.6: Zone plate milled in an OF cover by Pt (left) and Au/Pd (right).

Prior to the milling of the OFs, these have to be coated with a conductive material. This film is necessary for two reasons: to avoid charging effects on the dielectric fiber surface during the FIB milling and to block the light, by alternated rings, in the case of

FZP. In the case of the zone plates, a (Pt) layer of $20\,nm$ is used, while for the phase plates, a $5\,nm$ Au/Pd film is enough, since it is only use to avoid charging effects.

Some tests were carried out to check the roughness of the OFs surface (figure 5.6). For the case of OFs covered with a layer of Au/Pd, after the milling, the surface was quite rough. This is caused by the different sputtering rates of each metal type. However, using only one metal as Pt, resulted in a smooth surface.

Centering the structures at the OF tip

The process of centering the structures at the OF tip is illustrated in figure 5.7. First the OF is aligned with the FIB column, as described in Section 3.2.4. Then its diameter is measured, represented by circle 1, as shown in figure 5.7 (a). After this, a concentric ring pattern (2), with a thickness of $5\,\mu m$ and a diameter of $50\,\mu m$, is milled. This is visible in figure 5.7 (b). The center of this structure, 2, is concentric with the OF. This process is repeated afterwards, and the final structure, 3, is micromachined in the center of the OF. This last step, (5.7 (c)), is carried out at 2.5× the previous magnification, allowing to have more resolution to center the DOE with the OF.

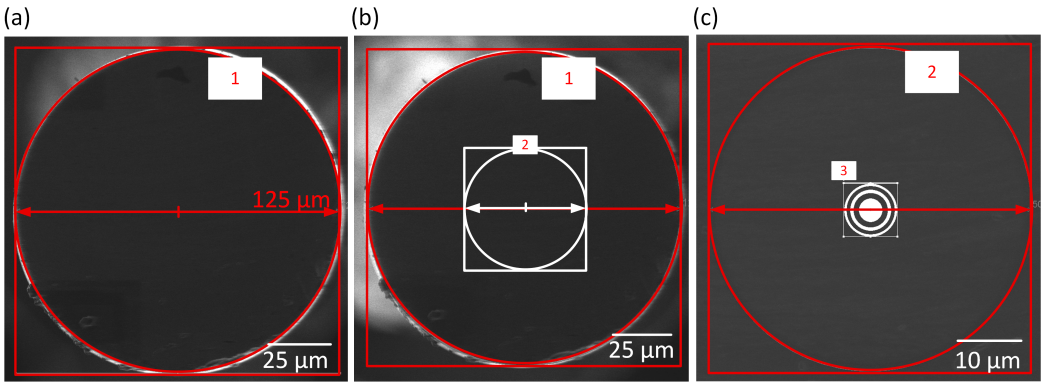

Figure 5.7: Methodology used to center the structure with the optical fiber surface.

Other particularities of the fabrication process

Sometimes, the OFs are cleaved with a sightly inclination, which is difficult to compensate for, as the FIB stage has a maximum resolution of 0.1^o. Figure 5.8 (a) and (b) shows the consequences of an angular offset on a circular milling pattern. The bottom part of the structure is blurred because the FIB is not perpendicular with the surface of the fiber. Therefore the effective cross section of the beam is an ellipsis rather than a circle, as shown in the scheme of figure 5.8 (d). Figure 5.8 (c) shows the same effect, but in a zone plate.

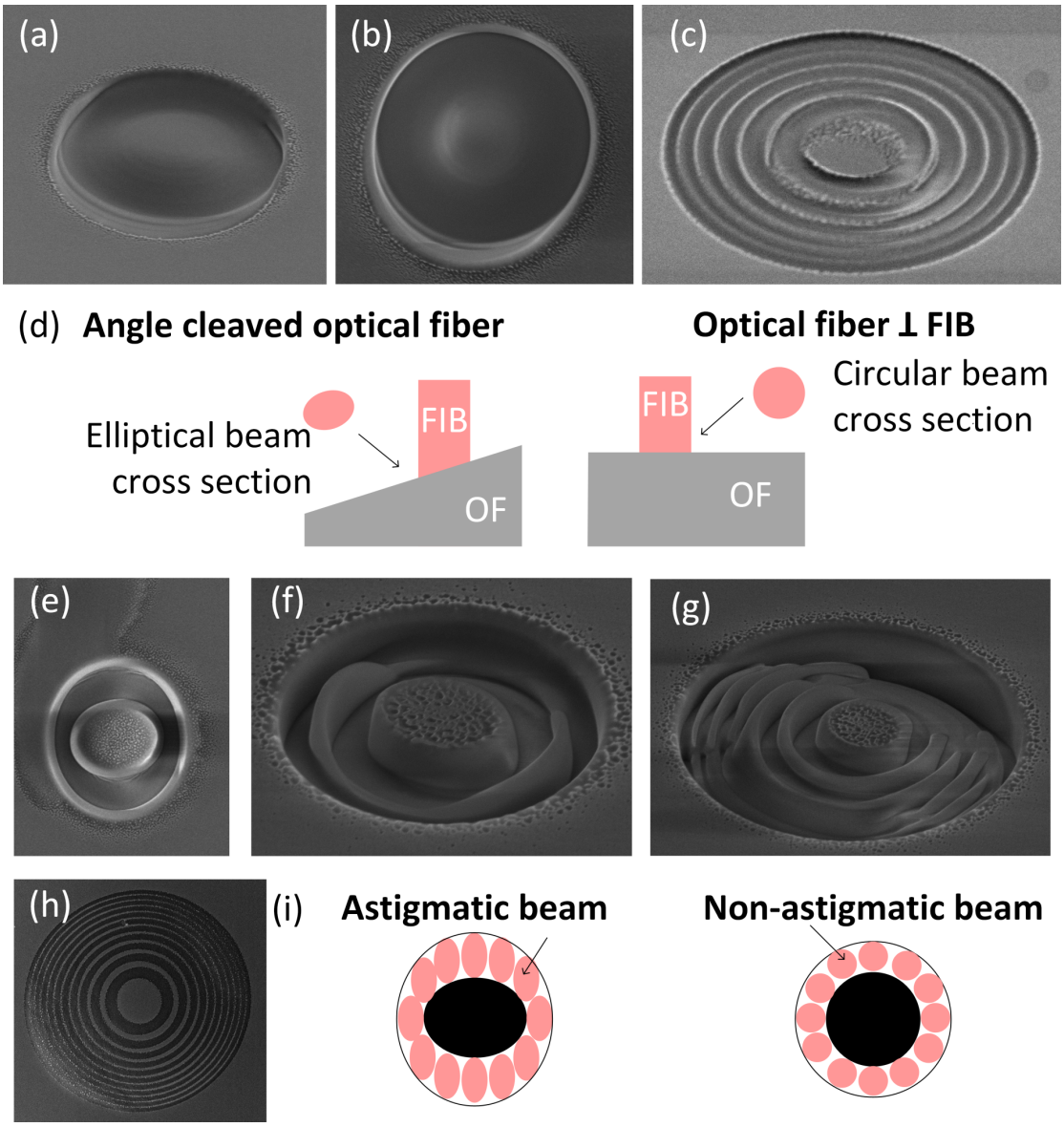

Figure 5.8: Deformations caused in the milled structures due to an angle cleaved OF (a) - (d) and astigmatic ion beam (e)-(i).

In the previous case the issue was related with the OF. Nevertheless, if the ion beam is astigmatic[1], the resulting structure is also distorted. Examples of these deformations are visible in figure 5.8 (e), (f), (g) and (h). In the first example the aim was to mill a ring shaped structure, however as the beam is astigmatic along the vertical direction, the inner structure is elongated horizontally and the external boundary vertically. This is explained in the scheme of figure 5.8 (i), where the milled area is compared for an ellipsoid beam and a circular one. Normally the astigmatism can be corrected through the FIB

[1]The transversal cross sections along x and y have different dimensions.

software, by adjusting the electrostatic lenses, however it depends on the conditions of the FIB column. Based on this, milling a circular pattern is a good hint on the beam and fiber conditions.

5.2.3 Fresnel zone plates

The first structure presented here, FZP-1, composed by 10 zones, is projected to have a focal distance of $3\,\mu m$ and a radius (r_{10}) of $5.42\,\mu m$. The amplitude mask used during the fabrication process is shown in figure 5.9 (a). During the fabrication, the exposure dose is controlled by the dwell time, corresponding to a bitmap pixel value (figure 5.9 (a)). In this fashion, for a white pixel (level 255) the dwell time[2] was set to $2\,\mu s$, while for a black pixel (level 0) the beam is blanked. The ion beam current was set to $0.3\,nA$ (beam diameter $31\,nm$), corresponding to a total milling time of approximately $41\,s$. An image of the OF with the FZP can be seen in figure 5.9 (b), and the corresponding zoom in figure 5.9 (c). Analyzing this image, a radius of $5.57\,\mu m$ is measured. This value is slightly larger than the projected one, presenting a relative error of $2.73\,\%$. Please note that the structures visible in the boarder or the fiber are just for control of the fabrication conditions, the performance of the central plate is not influenced by those.

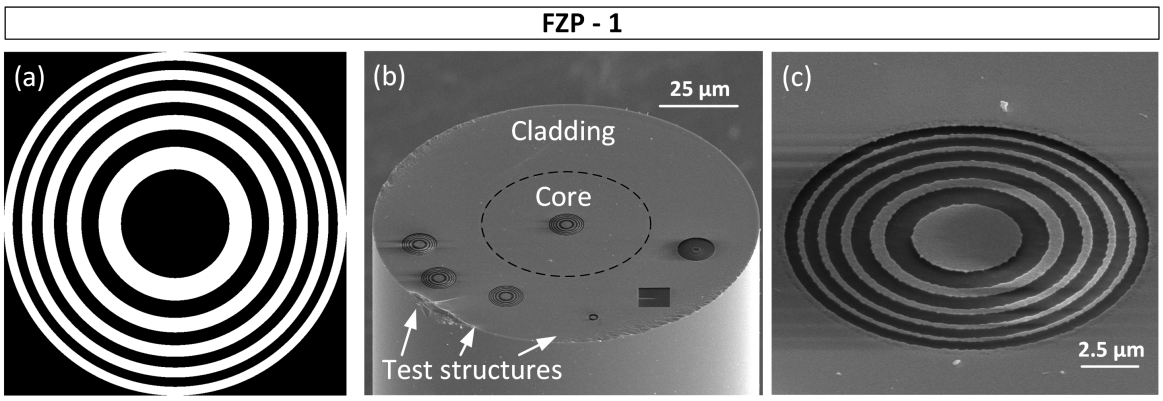

Figure 5.9: Fresnel zone plate - 1 : (a) amplitude mask used to fabricate FZP-1; (b) image of the optical fiber with FZP-1; (c) zoom of FZP-1.

The second amplitude plate, FZP-2 is composed by 22 zones, and is dimensioned to have a focal distance of $6\,\mu m$, corresponding to a radius (r_{22}) of $11.37\,\mu m$. The amplitude mask corresponding to the profile imprinted on the top of the fiber is presented in figure 5.10 (a). The beam current and dwell time were $0.3\,nA$ and $1\,\mu s$, respectively. The overall milling time was approximately $4\,min$. The resulting zone plate can be seen in

[2]Dwell time - exposure time t the ion beam at a given position.

figure 5.9 (b) and (c). From the images, a radius (r_{22}) of 12.18 μm was estimated, with a relative error of 7.05%.

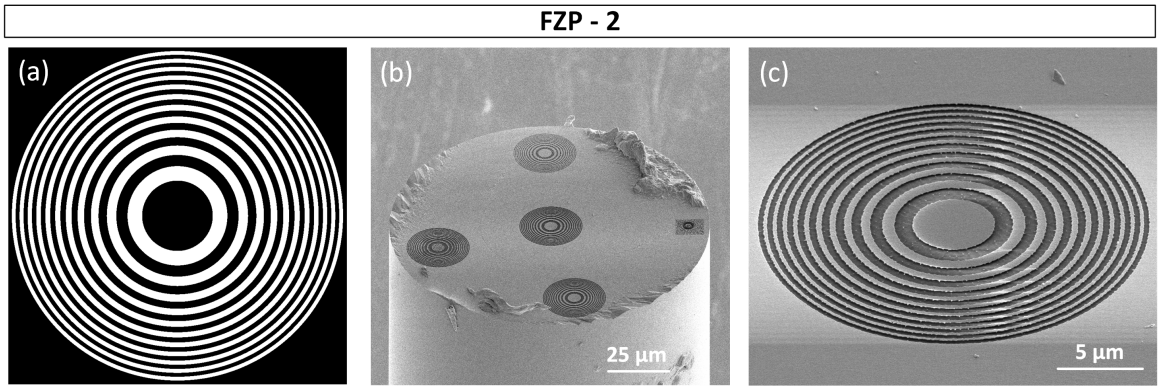

Figure 5.10: Fresnel zone plate - 2 : (a) amplitude mask used to fabricate FZP-2; (b) image of the optical fiber with FZP-1; (c) zoom of FZP-2.

5.2.4 Fresnel phase plates

FPP-1 is composed by 4 zones of alternated depths. It was designed to have a focal distance of 10 μm, corresponding to a radius (r_4) of 6.2 μm. The OF tip used in this case, has a MM segment with a length of $\sim 30\,\mu m$. Figure 5.11 (a) depicts the amplitude mask used in this particular case. The beam current and dwell time were 0.1 nA (beam size13 nm) and 1 μs, respectively. The overall milling time was approximately 15 min. The resultant plate can be seen in figure 5.11 (b) and (c). Once again, the radius of the fabricated plate ($r_4 = 6.11\,\mu m$, relative error = 2.35%) was slightly different from the projected one. From the SEM images, the height of the phase discontinuities is estimated to be around 534 nm. After the FIB milling, the optical fibers were cleaned with aqua regia, to remove the metallic film. In order to verify the influence of the number of rings a second phase plate is here presented.

FPP-2 is composed by 10 zones, and is also dimensioned to have a focal distance of 10 μm, corresponding to a calculated radius (r_{10}) of 9.90 μm. The length of the MM segment is $\sim 50\,\mu m$. Figure 5.12 (a) depicts the amplitude mask used in this particular case. The beam current and dwell time were 0.1 nA and 1 μs, respectively. The overall milling time was approximately 18 min . The phase plate can be seen in figures 5.12 (b) and (c). The radius was estimated to be 10.14 μm presenting a relative error of 2.43%. The height of the phase steps is 419 nm. The inset of figure 5.12 (c) shows some imperfections on the surface of the plate, due to some constrains of the FIB gun.

However, the dimensions are very reduced and no effects were observed on the output beam profile.

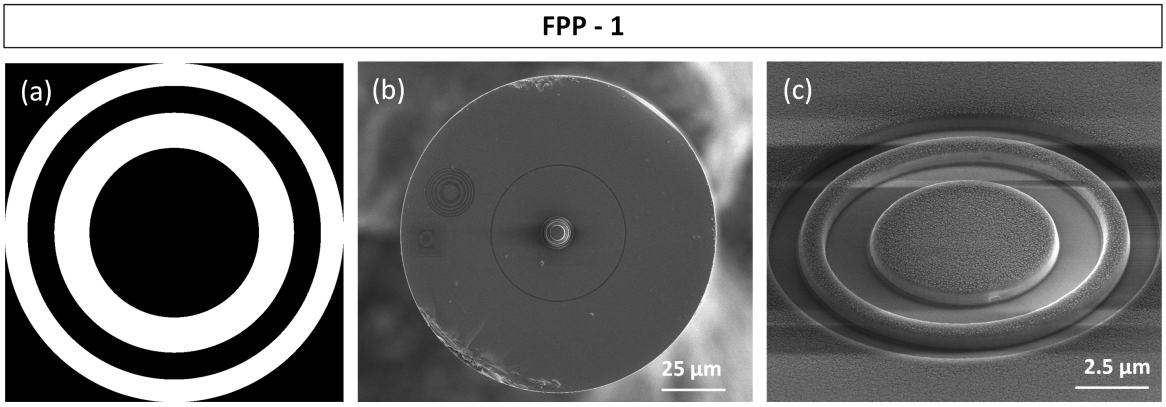

Figure 5.11: Fresnel phase plate - 1: (a) amplitude mask used to fabricate FPP-1; (b) image of the optical fiber with FPP-1; (c) zoom of FPP-1.

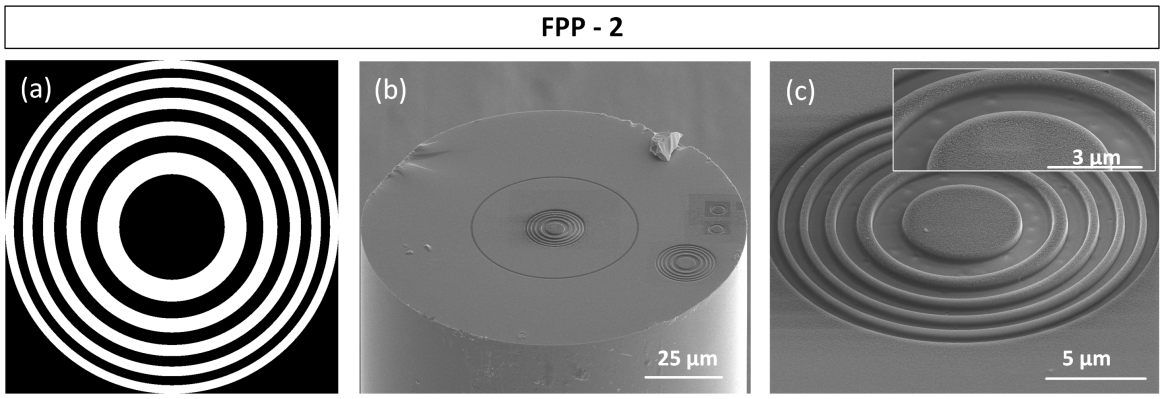

Figure 5.12: Fresnel phase plate - 2: (a) amplitude mask used to fabricate FPP-2; (b) image of the optical fiber with FPP-2; (c) zoom of FPP-2; (inset) details of the first three zones of FPP-2.

5.3 Optical characterization

The characterization of the output beams generated by the Fresnel zone and phase plates was performed using the setup presented in figure 5.13. First, the optical fiber tips were spliced to a pigtailed laser source (Lumix, $980nm$, $500mW$). Then, they were placed in a micro manipulation stage, which can be moved horizontally. This allows to acquire images of the optical beam at different distances from the optical fiber, since the beam is projected into a CMOS camera using a $60\times$ objective.

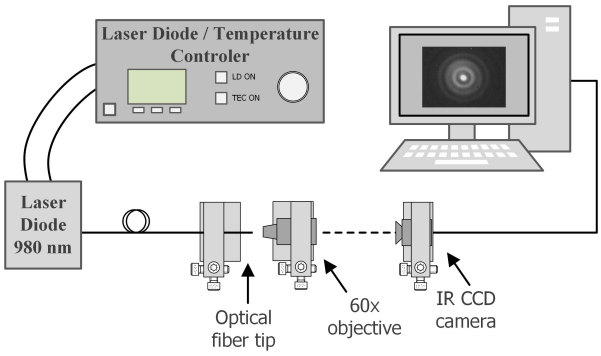

Figure 5.13: Experimental setup used to analyze the output beam from the optical fiber tips with the Fresnel zone and phase plates.

5.3.1 Fresnel zone plates

The experimental output optical beam profile of FZP-1 is shown in 5.14 (a). To achieve this, sequential cross sections (yz) were first acquired at different distances (along x), using the setup presented in 5.13. Then, using ImageJ software [146], the pictures were combined into a 3D view, allowing to have orthogonal profiles (yx and zx). In figure 5.14 (a) the yx profile is shown. The zx is similar to this one, since the structure has cylindrical symmetry. With the purpose of investigating the resulting features of the structures, computational simulations mimicking the fabricated plates were performed. The electromagnetic system was modeled based on the implementation of the FDTD method described in Section 3.3. A 2D representation of the optical fiber was selected, considering the cylindrical symmetry of the system, and to avoid time consuming simulations. The refractive index of the optical fiber and the surrounding media were set to 1.458 and 1.000, respectively, while the source wavelength was $980\,nm$. In this particular case, the profile obtained in figure 5.14 (b) was computed. Observing both, computational and experimental representations of the output electric intensity, the focal spot is located at $3\,\mu m$ and at $5\,\mu m$, respectively. This is demonstrated by the plot of the intensity curves, along the propagation direction, in figure 5.14 (a) and (b). Besides the main focal point, the plate exhibits two secondary focusing positions. The number of extra focal points is supported by the simulations, although the locations are not exactly the same.

To analyze the second zone plate, FZP-2, an analogous process was followed. Hereof, figure 5.15 (a) and (b) depicts the experimental and computational results, respectively. In this case, FZP-2 was dimensioned to have a focal distance of $6\,\mu m$, which is verified by the simulations. Regarding the experiments, the focal distance is situated at $5\,\mu m$.

Similarly to FZP-1, this structure also causes secondary focal points, which are also corroborated by the simulations.

In figure 5.16 (a) and (b), the experimental transversal profiles at the main focal points for each zone plate are depicted. In this case, the data allows to calculate the full width at half maximum (FWHM) of the central peak of the resultant patterns. For FZP-1, the inner peak has a diameter of $0.9\,\mu m$, whereas for FZP-2 is $0.6\,\mu m$. This shows the influence of the number of zones, i.e., though FZP-2 presents a higher focal distance and the focusing of the light is stronger, since the plate is composed by twice the number of diffractive rings, and has a larger radius.

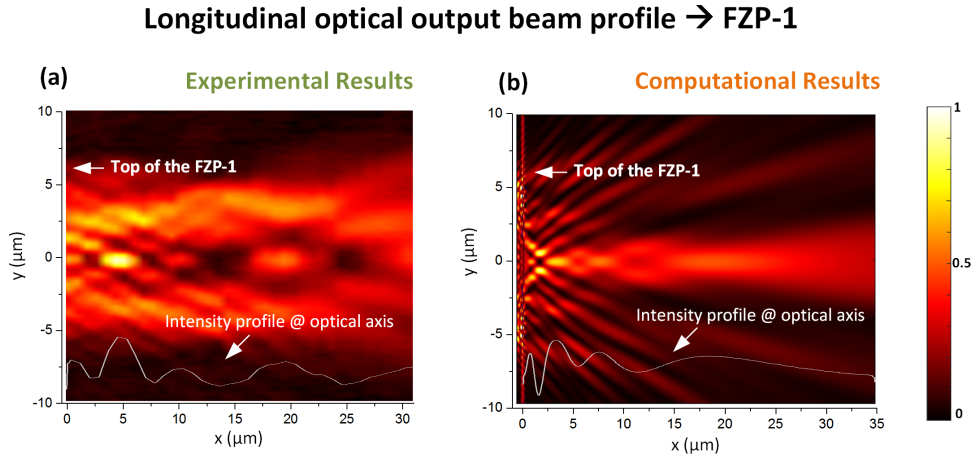

Figure 5.14: Longitudinal optical output beam profile for FZP-1: (a) experimental; (b) computational.

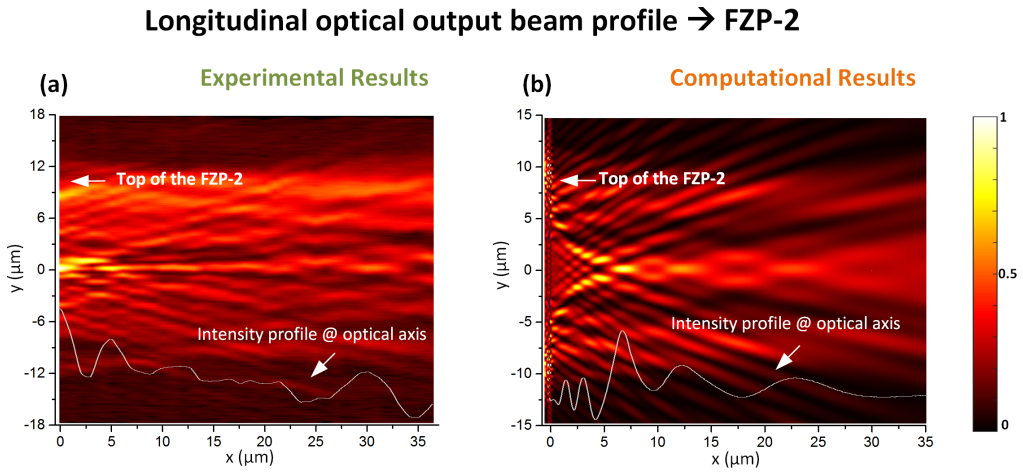

Figure 5.15: Longitudinal optical output beam profile for FZP-2: (a) experimental; (b) computational.

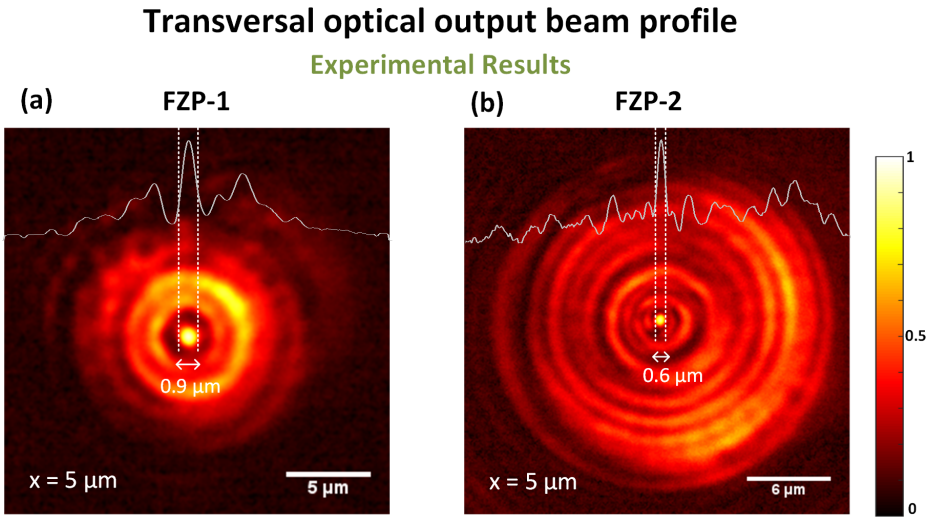

Figure 5.16: Transversal optical output beam profile at the main focal point: (a) FZP-1; (b) FZP-2.

5.3.2 Fresnel phase plates

The analysis of the output beams of the phase plates (FPP-1 and FPP-2) follows a similar approach. Hereupon, figures 5.17 (a) and (b) depict the results for FPP-1, which is projected to have a focal distance of $10\,\mu m$. Overall, the experimental and computational results match with the projected value. Looking at the measured intensity profile plotted in figure 5.17 (a), the maximum of intensity should be located at $\sim 10\,\mu m$. In this regard, this is in line with the computational results, 5.17 (b), where the intensity maximum is located at $10\,\mu m$, and slightly decreases after this point.

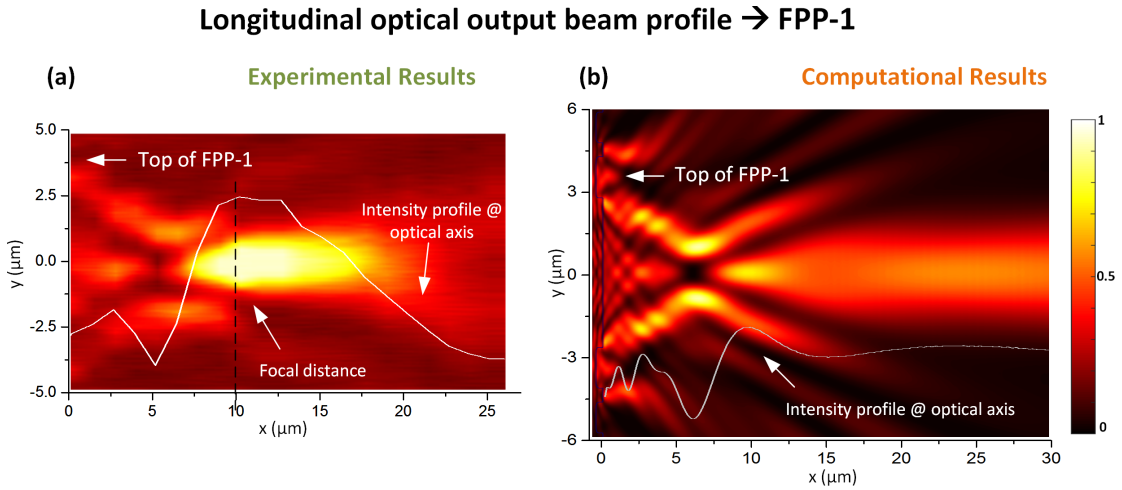

Figure 5.17: Longitudinal optical output beam profile for FPP-1: (a) experimental; (b) computational.

Figures 5.18 (a) and (b) depict the results for FPP-2, which was also projected to have a focal point at $10\,\mu m$, however, containing more rings than the previous structure. Once again, from the experimental results (figure 5.18 (a)) one may conclude that the maximum of intensity is located at $\sim 10\,\mu m$. The simulations also present a maximum at $\sim 10\,\mu m$, that slowly loses intensity along a few micrometers. This results are coherent with the previous ones, presented for FPP-1.

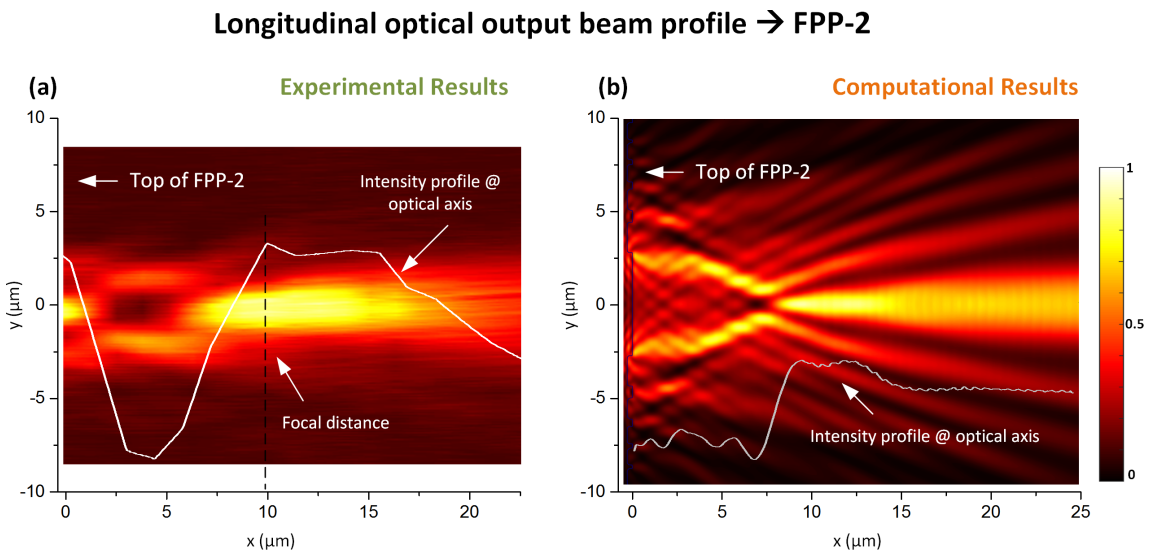

Figure 5.18: Longitudinal optical output beam profile for FPP-2: (a) experimental; (b) computational.

Figures 5.19 (a) and (b) show the transversal profiles experimentally acquired at the maximum intensity positions for each phase plate. The FWHM of the central peak for FPP-1 is $\sim 1.7\,\mu m$ and for FPP-2 is $\sim 2.3\,\mu m$. In this case, increasing the number of diffractive rings caused a slightly broader peak.

5.3.3 Discussion

The studies of the optical properties of the zone and phase plates presented in the previous sections demonstrated some important features that differentiates both Fresnel diffractive structures. Table 5.1 summarizes some of the measured parameters. The zone plates cause a narrower central peak at the focal point, however, present two extra focal spots in addition to the main one. In contrast to the zone plates, the phase plates only originate one focal point, nevertheless, the central peak is wider in both longitudinal and transversal direction.

The efficiency of the devices was calculated based on the ratio between the power

detected at the output of a cleaved optical fiber and the output detected at the output of each device. The measured values were: 33% and 38% for FZP-1 and 2 and 60% and 67% for FPP-1 and 2, respectively. This proves that the losses are higher for the case of the zone plates, since the light is blocked by alternated zones, while the phase plates are more efficient in the conversion of the optical profiles.

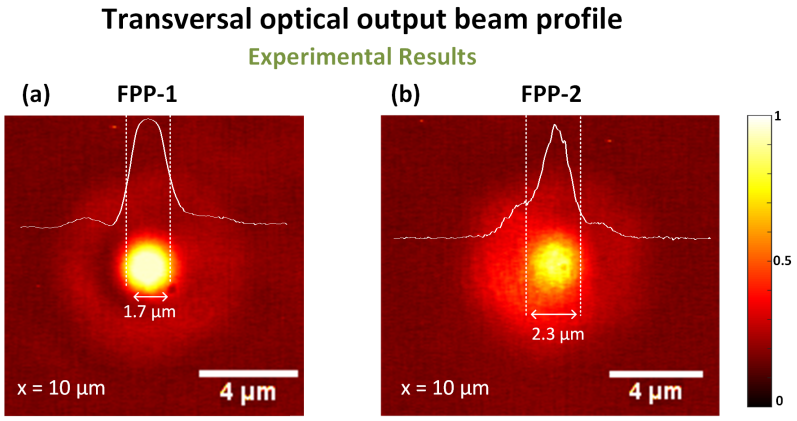

Figure 5.19: Transversal optical output beam profile at the main focal point: (a) FPP-1; (b) FPP-2.

Fresnel Plate	N	$f\,(theor.)$	$r_N\,(theor.)$	$r_N\,(exp.)$	$E(r_N)$	$f\,(simul.)$	$f\,(exp.)$
FZP-1	10	3	5.42	5.57	2.73%	3	5
FZP-2	22	6	11.37	12.18	7.05%	6	5
FPP-1	4	10	6.26	6.11	2.35%	10	10
FPP-2	10	10	9.90	10.14	2.34%	10	~ 10

Table 5.1: Features of Fresnel phase and zone plates (distances in μm).

Besides this, a general comment concerning the differences between the computational and experimental optical field profiles should be done. Looking at figures 5.14 (a), 5.15 (a), 5.17 (a) and 5.18 (a), the fabricated tips generate an output optical field that maintains some degree of collimation, while in the simulations (figures 5.14 (b), 5.15 (b), 5.17 (b) and 5.18 (b)) it is more evident that the resulting output beams diverge. Although the simulated structures have been dimensioned to reproduce the fabricated ones, there are always some parameters that may deviate from the intended ones. For instance, the fabricated structures may lack absolute circular symmetry, causing an impact on the structure of the output beam. Furthermore, during the scan of the ion

beam, the milling is more pronounced in the edges that in the center, inducing a lensing effect [147]. On the other hand, during the fabrication there is also a possibility to have Gallium ions implanted on the fiber surface, as well as carbon residues, due to the contamination of the FIB chamber. These can be responsible for blockage or absorption of the light, as addressed by Janeiro et al. [148]. In the particular case of the zone plates, the simulations have taken into account the dominant effect of the structure produced by the pattern on the fiber tip, but have left out second order corrections. These are associated with the dispersion of the metal and the possibility of producing localized surface plasmons that might result in a small contribution of the spatial distribution of light of the output beam. Although most of the electric field is parallel to the surface of the metal rings, and thus is not effective in producing surface plasmons, at the edges of the rings it is indeed possible to have plasmonic excitation, which changes the effective dimensions of the rings and introduces a minor correction in the spatial distribution of the beam structure. As a result, some spatial components of the beam dispersed by the metallic structure may gain slightly different phase delays than predicted by the simulations, thus justifying the differences in contrast and definition between simulations and experimental results. However, including more realistic parameters at such level would add to much complexity to the model, which at present was simply intended to guide the design. Nevertheless, these properties will be explored in futures works as the plasmonic features may provide interesting mechanisms for further focusing and sensing abilities. Overall, from the comparison of the two types of devices it can be said that FPP are definitely more easily fabricated to fit a simple modeling approach providing interesting features as micro manipulation devices. Instead, the FZP show a more complex behavior, that requires a more complex modeling approach to explore its full potential.

In the following section, FPP-1 will be tested for optical trapping of dielectric particles and yeast cells, and some considerations on the use of zone plates will be outlined, although not successfully implemented. On the one hand, the match between the computational and experimental results, regarding Fresnel phase plates, proves that the methodology presented in this work is adequate and trustworthy. Besides this, the phase plates have better optical conversion efficiency then zone plates. On the other hand, the zone plates experimental results differ from the projections, due to the facts above mentioned: implantation of Ga ions, defects on the ring size and possible excitation of plasmons. At the same time, zone plates are also covered with a metallic film, which might act as a source of heating, that can compromise the trapping effect, and the sample integrity. In this regard, choosing a phase plate not only fits the need for

optical trapping but also represents less constrains from the fabrication to the application. Regarding the choice of FPP-1 rather than FPP-2, this relies on the dimension of the central peak, which is narrower at the focal distance, contributing to an increase of the optical force responsible for the trapping.

5.4 Optical Trapping

5.4.1 Optical trapping setup

The setup used to test the OFs with Fresnel plates for optical trapping and detection of particles and cells is depicted in figure 5.20. It is composed by an image acquisition system, a 4-axis motorized micro manipulator to precisely handle the OF TIPs and a backscatered light detection module. The imaging system is essentially a home made inverted microscope, composed by a CMOS camera (EO-2018C, Edmund Optics) and an objective, which are connected to a computer. Using an optical fiber coupler (50/50, $980\,nm$) the photodetector (PDA 36A-EC, Thorlabs), used to acquire the backscatered signal, and the pigtailed laser diode ($980\,nm$, $500\,mW$, Lumix) are connected to the optical fiber with the Fresnel plate. Furthermore, a function generator is included in the setup so that laser diode signal may be modulated if necessary. The OF probe is spliced to the output of the optical fiber coupler, and inserted into a metallic capillary, which is attached to the stage and adjusted at a suitable angle. The capillary is also useful to keep the OF protected. Then, the fiber is inserted into the sample that is placed over the glass slide.

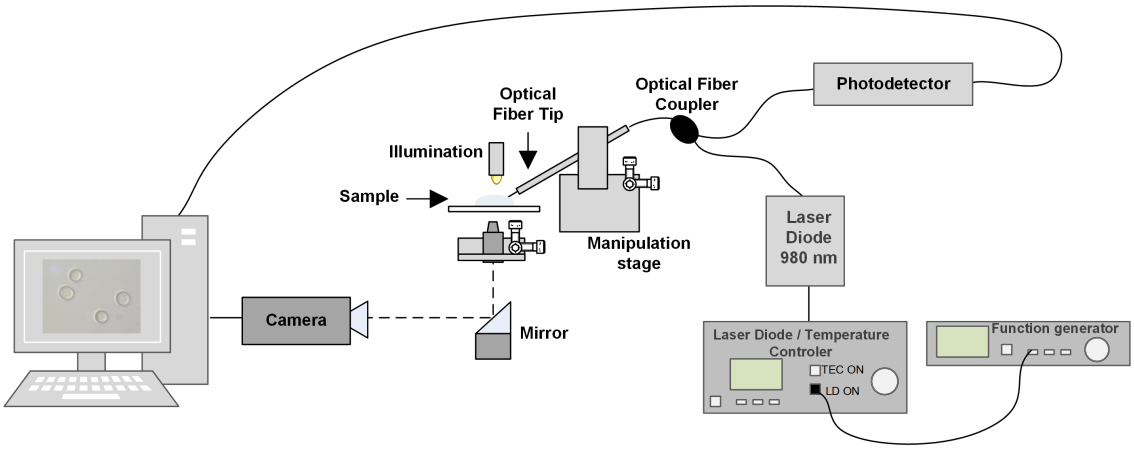

Figure 5.20: Setup used to test the optical tips with Fresnel plates for optical trapping and detection of particles and cells.

5.4.2 Particles and cell samples

The optical trapping tests are usually performed with dielectric particles. In the following testes, the viability of the optical probes is assessed using distinct aqueous solutions with beads in suspension, namely $4\,\mu m$ and $8\,\mu m$ PS particles, $8\,\mu m$ Poly(methyl methacrylate) (PMMA) particles and yeast cells with diameters within the range of 4 to $6\,\mu m$. The values of the refractive index of the particles and yeast cells are presented in table 5.2. The available samples, allow to explore the potential of the OF TIPs for optical trapping considering materials with diverse optical properties.

Samples	**Refractive Index**
Polystyrene	1.5731 [129]
Yeasts	1.49–1.53 [130, 131]
PMMA	1.4843 [129]

Table 5.2: Refractive index of particles and yeast cells.

5.4.3 Optical trapping of PMMA particles with a Fresnel phase plate

Computational simulations

To get a better perception on how the optical beam is affected by the media, and how do the optical forces act, some simulations, based on the FDTD method (Section 3.3), were performed. First of all, a system composed by the waveguide with the FPP with the projected parameters was simulated. Contrary to the simulations presented in Section 5.3, the medium here is considered to be water ($n = 1.327$), mimicking the particle samples. The electric field intensity profile in the xy plane, is presented in figure 5.21 (a), and as expected, the focal distance is located at $10\,\mu m$ away from the plate and the beam spot became wider. After this, the fiber was modeled using the experimental features of FPP-1. The resulting optical pattern is visible in figure 5.21 (b). Since the height of the rings is $534\,nm$, the focal region increased to $\sim 50\,\mu m$, extending further.

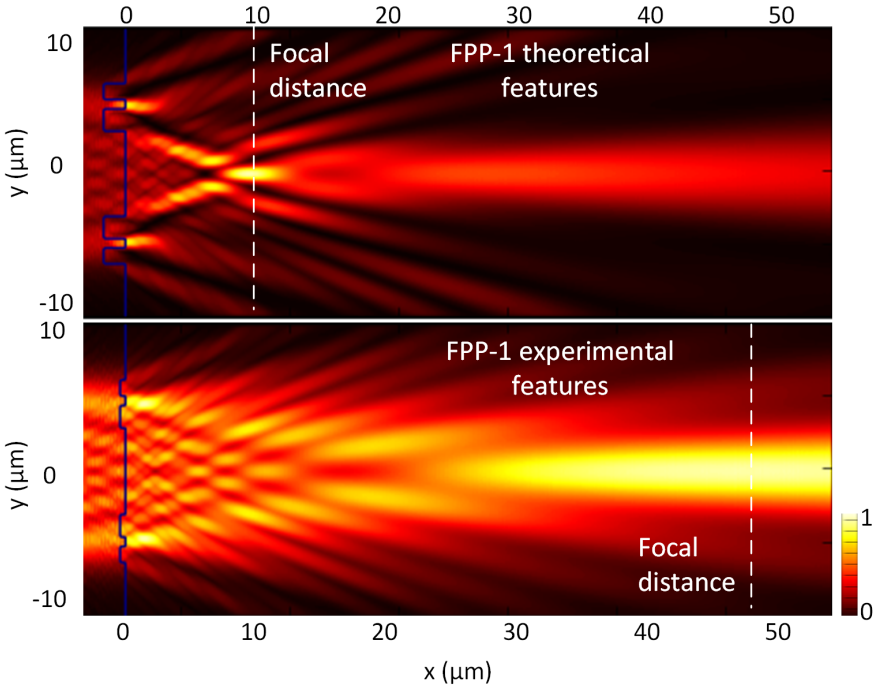

Figure 5.21: Electric field intensity profile: (a) FPP-1 theoretical features; (b) FPP-1 experimental features. The refractive index of the medium is 1.327, corresponding to water, mimicking the test of the phase plates in the particle sample medium.

Taking this into account, the simulations were repeated but considering that the fiber was tilted at 45º, and including a surface representing the glass slide where the sample is placed. These parameters were included to better reproduce the experimental conditions. Figure 5.22 (a) represents a transversal cut (xz) of the electric field intensity, simulated in the mentioned circumstances. In this configuration the focal spot is located near the glass slab surface, which is located $62.5\,\mu m$ away from the OF tip. The optical forces acting on PMMA particles ($4\,\mu m$ radius, $n = 1.4843$) are calculated based on the Lorentz model as indicated in 3.3. The calculations of the optical forces are performed for different positions of the particle, allowing to obtain a map with the distribution of the net forces, as depicted in figure 5.22 (b). The results show that when the bead is located aside the stable trapping position, it is first driven to the optical axis, and then towards the optical trap, close to the glass slab, enabling 2D trapping.

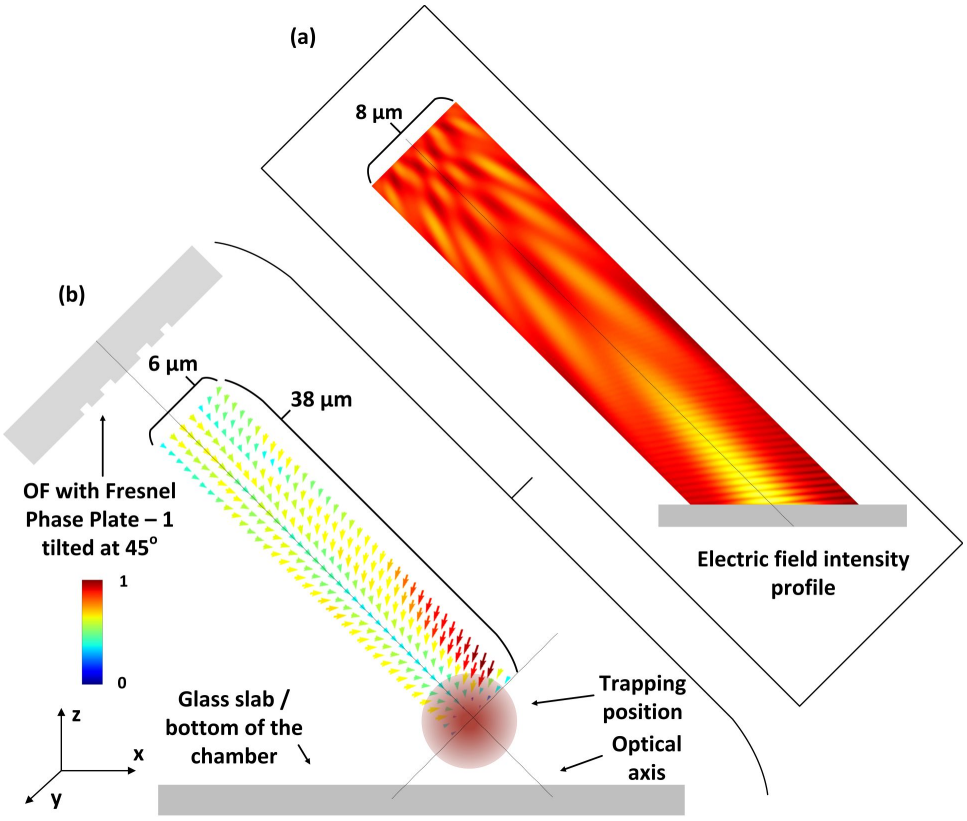

Figure 5.22: (a) Electric field intensity profile for FPP-1 tilted at 45º immersed in water; (b) corresponding force distribution map, for the particular case of $8\,\mu m$ PMMA beads.

Experimental results

The optical fiber probe, containing FPP-1, was assembled accordingly to the procedure previously described, with an inclination angle of 45°. After this, a drop of an aqueous sample containing $8\,\mu m$ diameter PMMA beads was placed on the glass slide. Using the motorized micro manipulator, the fiber was then immersed in the sample. Through the imaging system, the OF was adjusted to be close to the glass slide, and when in the vicinity of some PMMA beads, the laser was turned on. Figure 5.23 depicts the ability to trap a particle that is within the range of the output laser beam while the OF is stationary. At $t = 0.00\,s$, the laser was off, and several particles were close to the OF, namely the particles highlighted by the white circle and square. After this, the laser was turned on, and at $t = 0.46\,s$ the particle within the circle was slightly moved inwards along the $-y$ and then along $+x$. Please note some laser reflections at the particle and at the cover slide, while the particle moves towards a stable position, as can be seen in the frame acquired at $t = 1.18\,s$. It is also noticeable that the bead within the square is

moved in the $+y$ direction, when the other bead is trapped. Whereas the bead in the circle was not trapped, the particle in the square was not close enough to be attracted to the trap, remaining static. Nevertheless, as soon as the circled bead was trapped, it worked as a divergent lens, causing the movement of the non-trapped particle in the $+y$ direction, away from the trapping point. In other conditions, this particle could have been attracted towards the trapping position.

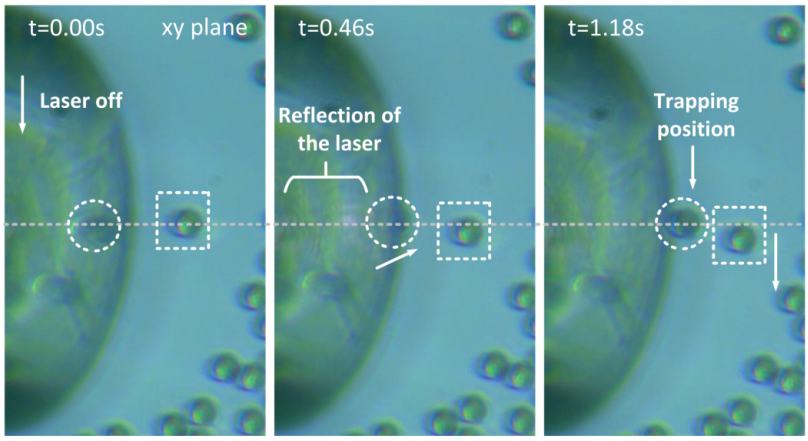

Figure 5.23: Example of guiding and trapping of an $8\,\mu m$ PMMA bead.

Taking the former experiment and the computational simulations into account, a second test was performed, to evaluate the ability to trap and move a bead within the sample. The conditions were kept unchanged. Please see figure 5.24. At $t = 0.05\,s$ the laser was off, and the fiber was positioned so that a bead was very close to the trapping point found in the prior experiment. After this, the laser was turned on $(2.50\,s)$ and the fiber was moved in the $-x$ direction $(12.35\,s)$. The frame acquired at $t = 17.30\,s$ shows that the bead (within the white circle) was moved towards the trapping position, while the particle delimited by the white square remained in the same position during the experiment. This was followed by the displacement of the fiber in the $-y$ direction $(23.30\,s)$, and simultaneous movement of the particle. The probe was lastly moved in the $+x$ $(31.09\,s)$ and $+y$ $(33.09\,s)$ directions driving the particle with it. This demonstrates that the phase plate is able to trap and move PMMA particles in 2D, i.e., the xy plane. To make the OF configuration more clear to the reader, close attention should be paid to the scheme in figure 5.24, where it becomes evident that the fiber does not touch the beads during the trapping process. In the acquired frames the bead and the upper border of the fiber are superposed in the image but are located at different planes, explaining the defocusing of the fiber, while the particle is focused.

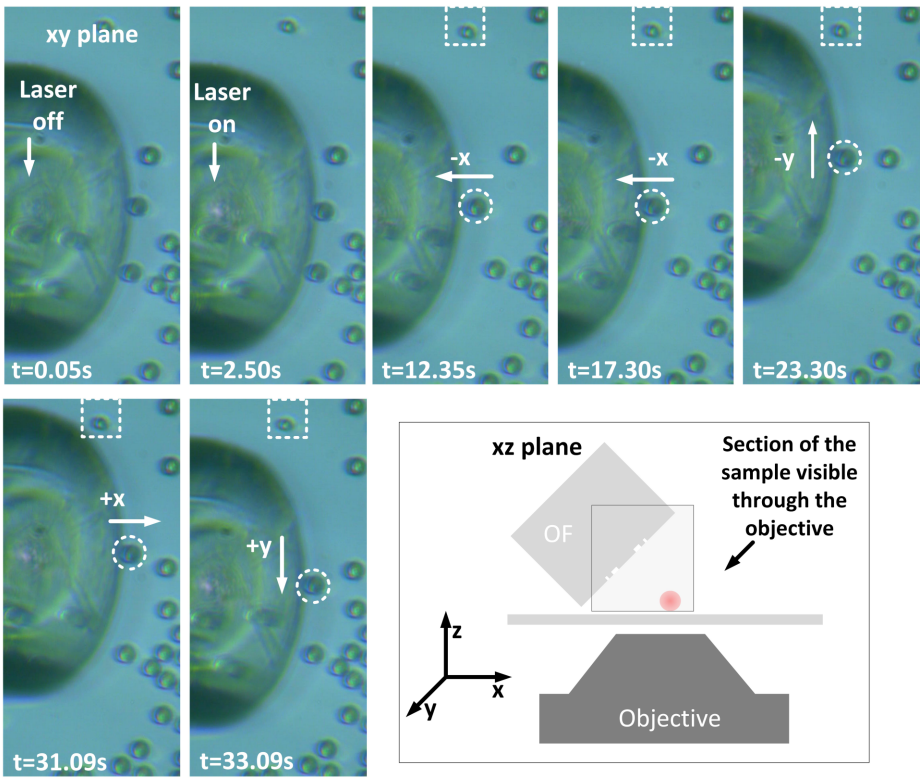

Figure 5.24: Demonstration of optical trapping of a PMMA particle in the xy plane. Scheme depicting the observer view, to demonstrate that the optical fiber does not touch the trapped particle.

The optical forces acting on the particle can be described by the scheme depicted in figure 5.25. Since the fiber is tilted, the optical axis does not match the x direction in the xyz referential. Instead, it is rotated by θ. Consider figure 5.25 (a) where the particle is located nearby the trapping point. In this case, the particle feels two forces, the axial and the transversal force. When they balance with each other, the particle is stably trapped. Otherwise, if the particle is beyond the trapping position, figure 5.25 (b), the transversal force acts as a restoring force, and the particle is driven to the trap. At last, when the bead is before the trap, the transversal and axial forces will positively contribute to guide the particle towards the steady position (see figure 5.25 (c)). These components of the force contribute to a stable trap in the xy plane, corresponding to a 2D trapping. In the meantime, in the z direction, the particle is confined in the vicinity of the glass slab.

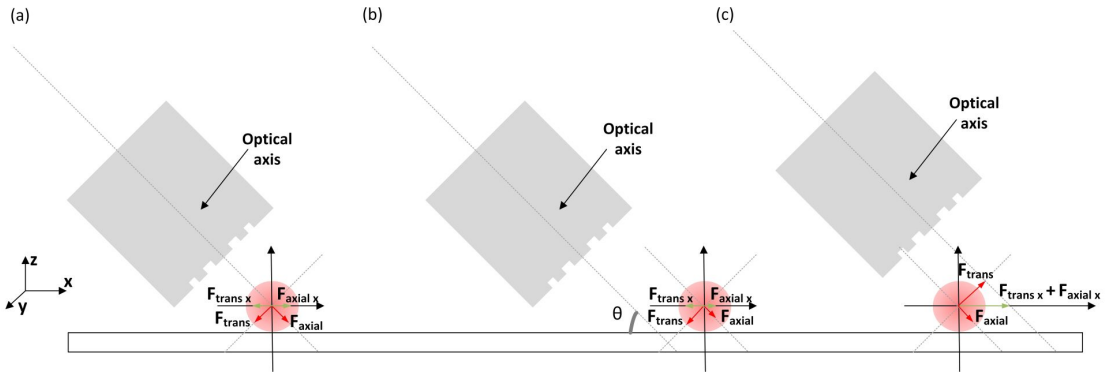

Figure 5.25: Optical forces acting on the particle, when it is at different locations: (a) at the trapping position $F_{trans\,x}$ and $F_{axial\,x}$ balance in the xy plan; (b) after the trapping point $F_{trans\,x}$ exceeds $F_{axial\,x}$ moving the particle towards the stable point; (c) before the trapping point, both $F_{trans\,x}$ and $F_{axial\,x}$ contribute positively to drive the particle to the stable position.

Optical force measurement

The dynamics of the particle in the trap was studied according to the procedure bellow. First a bead was trapped, then the laser was turned off, and the fiber was moved. After this, the laser was again turned on, and since the bead is only a few micrometers away from the fiber, it was attracted towards the stable position. This was performed several times for each direction, $-x$, $+x$, $-y$ and $+y$ and the process was repeated for a range of powers with the fiber tilted at 45° and 35°. After this, using a particle tracking software from ImageJ [122], the trajectories of the particles were obtained from the recorded videos. Please see figure 5.26. These plots show the typical trajectory described by one particle towards the trapping position in the transversal direction (y). The OF was tilted at 45°, and the power of the laser was $15\,mW$. Regarding figure 5.26 (a), at $t = 0\,s$ the laser was off, immediately after, it was turned on, and the particle, that was static at $y \approx 4.2\,\mu m$ was moved to $y \approx 0.0\,\mu m$. The bead was attracted to the trap with a maximum velocity of $\sim 5.25\,\mu m/s$. The second plot, 5.26 (b) describes a similar situation, but in the opposite direction.

Afterwards the data of figures 5.26 (a) and (b) were fit to the Langevin equation. Using this, the velocity of the particle was calculated for every position, enabling to calculate the optical force, according to equation 3.5. The results are presented in figure 5.27.

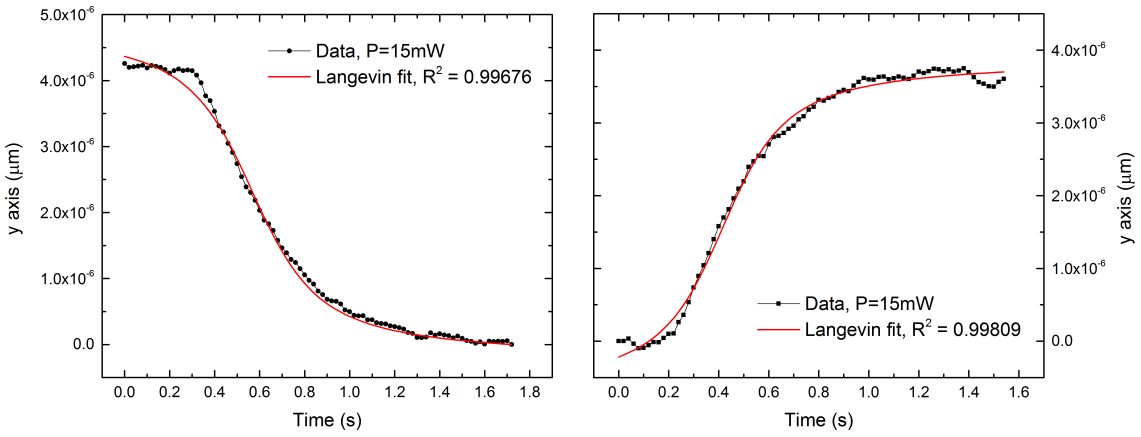

(a) (b)

Figure 5.26: Trajectories of an $8\,\mu m$ PMMA particle in the transversal direction: (a) $-y$ and (b) $+y$.

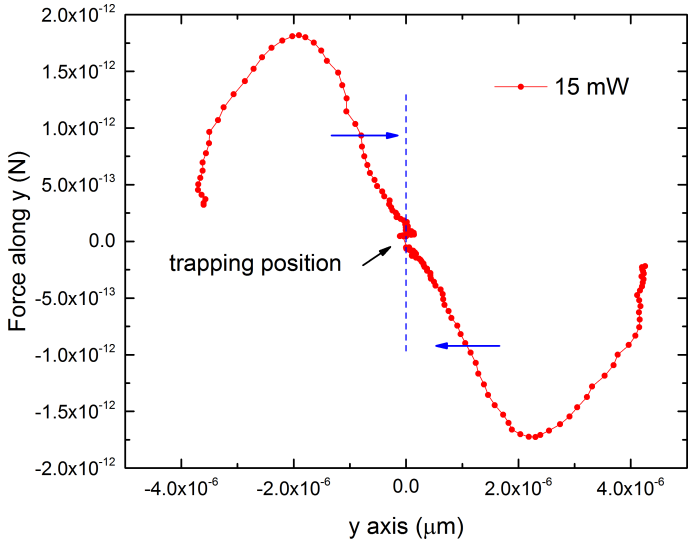

Figure 5.27: Experimentally measured optical trapping force, acting on an $8\,\mu m$ particle, along the y axis.

This procedure was repeated for the y and x direction, for a set of powers from $9\,mW$ to $21\,mW$.

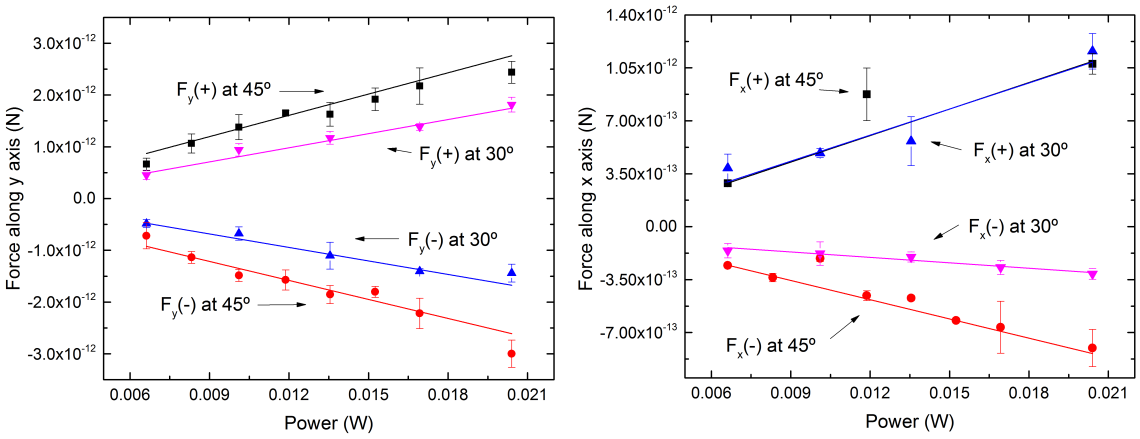

(a) (b)

Figure 5.28: (a) Experimental optical trapping force along the y axis, measured with the optical fiber positioned at 45° and 30°. (b) Experimental optical trapping force along the x axis, measured with the optical fiber positioned at 45° and 30°. The error bars correspond to the standard deviation of the measurements. The experiments were repeated at least three times for every trapping case.

The plots presented in figure 5.28 show the calculated values for the optical force along the y and x directions considering the particle tilted at 45° and 30°. As expected, the net optical force increases with the power, and as commonly measured, the values are within the pN range. Also, the insertion angle of the fiber affects the force. Concerning the force along the y axis, the maximum values measured were $2.99\,pN$ and $1.81\,pN$, at 45° and 30°, respectively. From figure 5.28 (a) one can also say, that the trap is quite symmetric. At 45° the PMMA particle reached a maximum velocity of $10.5 \pm 0.7\,\mu m/s$, while moving towards the trapping point. This means that if the stage is moved with a constant velocity along y inferior to $10.5\mu m/s$, the particle will remain trapped. Regarding the force along the x direction, plotted in figure 5.28 (b), it is stronger along the $+x$ direction than $-x$. This is due to the positive contribution of the axial force, pushing the particles towards the trap. When the particle is located beyond the trapping point, the optical force is weaker, reaching a maximum value of $0.80\,pN$. In this case the particle reached a maximum velocity of $3.76 \pm 0.54\,\mu m/s$. The graphs of 5.28 also show that both in transversal and axial directions, the optical trapping net force generally increases for higher tilting angles. The exception occurs along the direction of positive x, where the forces are very similar for both angles. This is likely related with the nature of the optical forces in this direction. In the direction of negative x the optical forces are the least intense, since the gradient force has to surpass the scattering, while in the direction of positive x, both scattering and gradient add positively to drive

the particle to the trapping position. In this case, the contribution of the scattering and gradient components are possibly accountable for masking the effect of the tilt angle.

Trapping efficiency

The trapping can be evaluated by the dimensionless parameter Q, as given in equation 2.5. The calculated values are presented in table 5.3, for the x and y directions and taking into account the fiber tilted at 30^o and 45^o. The efficiency of the trap is higher in the y direction, both for the 45^o and 30^o case, with values of 0.029 ± 0.002 and 0.020 ± 0.001, respectively. However, along the x direction, the trap is less efficient, presenting a Q of 0.011 ± 0.003 and 0.008 ± 0.005, for 45^o and 30^o. These values are in line with efficiency calculated for polymeric optical fiber TIPs.

Fiber tilted at 45^o		**Fiber tilted at** 30^o	
Q_y	Q_x	Q_y	Q_x
0.029 ± 0.002	0.011 ± 0.003	0.020 ± 0.001	0.008 ± 0.005

Table 5.3: Merit parameter Q for each direction at 45^o and 30^o.

5.4.4 Optical trapping of yeast cells

In a similar fashion, the trapping of yeast cells was also tested using FPP-1. Keeping the fiber tilted at 45°, the yeasts could be stably trapped in 2D. The range of measured forces is in line with the previous calculations, reaching the maximum trapping force of $7.96\,pN$ experienced along y direction, and $3.36\,pN$ in x direction. The ability to trap in 2D, was already verified with PMMA beads. Nevertheless, it is also important to demonstrate the capacity to move a specific target to a specific point. This is demonstrated in figure 5.29. In this particular case, yeasts A and B, are driven separately to a defined point, indicated by the arrows. These end up aligned and between two other yeast cells.

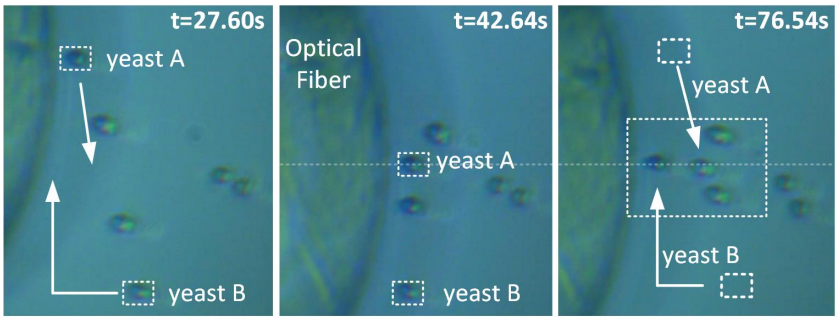

Figure 5.29: Rearrangement/ sorting of two yeast cells, A and B, to a specific location.

5.4.5 Optical trapping of polystyrene beads

Concerning the PS beads, $4\,\mu m$ and $8\,\mu m$ particles were tested separately, however none could be trapped, only pushed away. The discrepancies in the trapping capacity, compared to PMMA particles and yeast cells, are due to the differences of the refractive index of the material that constitutes the beads and cells, as visible in table 5.2. The refractive index of the PS particles is 1.5731, while for the PMMA beads is 1.4843. Although higher refractive indices cause a higher transversal force, the axial force, corresponding to the scattering, also increases. In this regard, a compromise between refractive index and the transversal force must happen to have a stable trap [149].

5.4.6 Detection of trapped particles

Taking into account the setup described in figure 5.20, with a slight modification of the setup it is straightforward to automatically detect and coarsely identify that a target particle is in the trapping area. Such particle detection system is composed by a photodetector (PDA 36A-EC, Thorlabs), connected to the OF tip, using an OF coupler. Thus, the laser can be injected in the probe and the backscatered light can be read by the PD. The $980\,nm$ laser was modulated with a sinusoidal signal (frequency $1\,MHz$, amplitude $4\,V$) and the scattered light signal was then filtered with a second order Butterworth filter. An example of the acquired signal can be seen in figure 5.30.

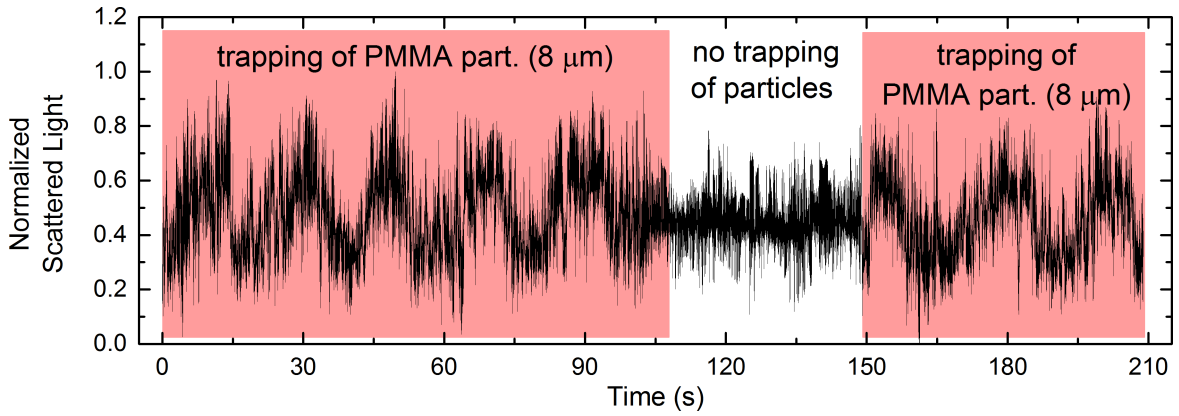

Figure 5.30: Acquired backscattered signal: during the trapping of an $8\mu m$ PMMA bead, and in the absence of trapping.

The presence or absence of an $8\mu m$ bead near the trapping zone is made clear through the different response signals, as indicated in the graph. Acquiring multiple data for different targets (yeast cells, PMMA beads, and clusters of beads with a maximum size of $15\mu m$) allowed to identify significant differences in the scattered light, which could be the base of an identification system.

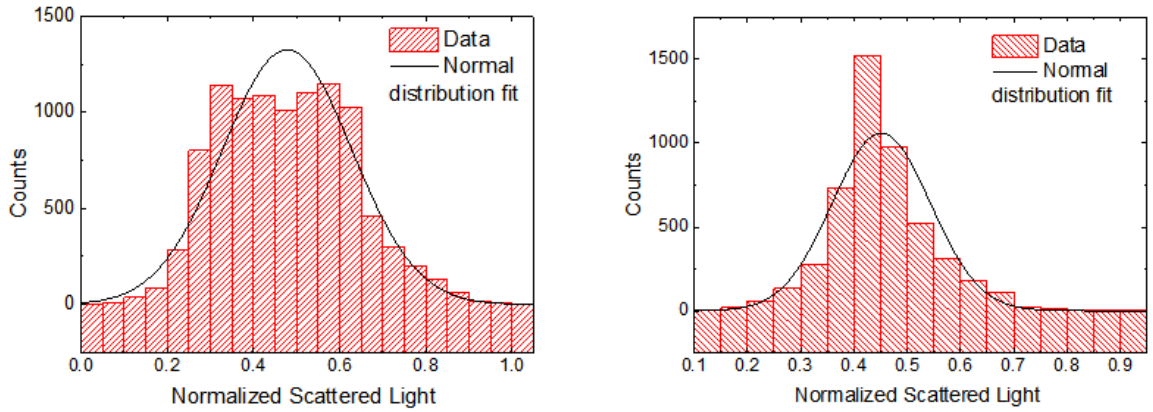

Figure 5.31: (a)Normal distribution fit correspondent to the first trapping event shown in figure 5.30. (b) Normal distribution fit of the data representative of the absence of trapped particles.

To study this possibility, the data was statistically analyzed, and each interval of information was fitted to a normal distribution. For every test, the standard deviation (σ) of the signal in the presence (σ_{trap}) or absence (σ_{notrap}) of targets, considered as the reference signal, was computed. Figure 5.31 (a) shows the fit done to the first set

of data (figure 5.30, trapping of a PMMA particle) while figure 5.31 (b) shows the fit in the absence of a particle. Looking at these plots, one can see that σ_{notrap} should be smaller than σ_{trap}. From the difference of these quantities, $\triangle\sigma = |\sigma_{notrap} - \sigma_{trap}|$, one can estimate ranges where particles of different sizes will belong to. This is depicted in figure 5.32. In this case, it is visible that yeast cells, with an average diameter of 4 to 5 µm are characterized by an average of 0.00387, while for PMMA particles the value of is 0.04686, and for clusters or aggregates of particles the value of 0.06473. These results show that larger particles do scatter more light and by this method it is possible to differentiate them.

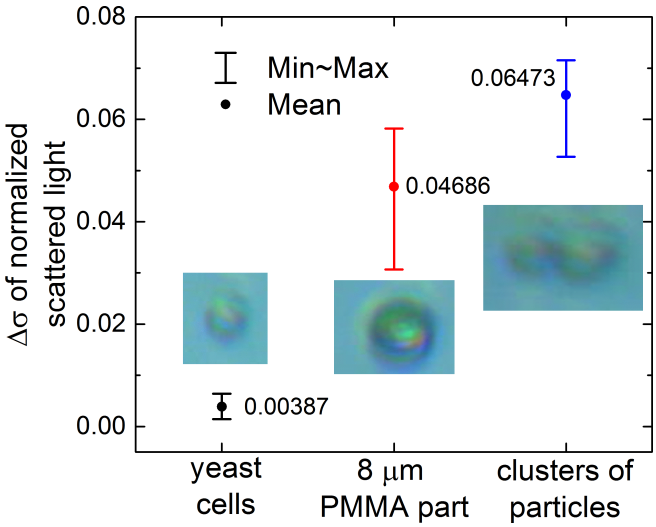

Figure 5.32: Study of $\Delta\sigma$ for yeast cells, 8μm PMMA bead and clusters of particles. The images inside the graph are examples of the detected targets (scale photos). Please note that the bars indicate the distribution of the data and the mean is represented by the dot point.

5.4.7 Discussion

The OF configuration using diffractive structures allows to have full 2D trapping, allowing to push and pull dielectric particles as well as yeast cells. This unveils possible applications in biology related fields. Beyond this, the data gathered also proves that it is possible to select and arrange targets in a precise manner, which can be particularly useful in studies dedicated to single targets, where their isolation from the remaining sample population is required. The lack of evidences of z trapping (3D), computational and experimentally verified, may be a constraint.

However, for cell sorting and arrangement, the available capabilities hold great potential. To increase the trapping capabilities, as well as efficiency, further developments

on the fabrication of the phase plates, that may lead to higher phase steps, is needed. In this case, the focal spot needs to be more confined, so that the electric field intensity gradient becomes steeper. According to Wright et al., beam spot sizes larger than $0.7\,\mu m$ are not able to form 3D stable traps [63]. Such reduced spot sizes have recently been accomplished using binary phase plates fabricated by electron-beam lithography and dry etching. This validates the possibility to improve Fresnel plates using FIB milling, since both fabrication methods have resolutions of a few nanometers [150].

The particle detection system, by analysis of the scattered light, enhances the applicability of the trapping setup, since sorting based on the specimen average size can be attainable in an automatic fashion, if adequate feedback systems are implemented. With such approach, fiber tweezers enable immobilization, manipulation and detection all in the same platform, reducing the system cost and footprint, and greatly improving its potential applicability. Similar results, such as trapping and detection, have been recently reported by Yu-Chao Li *et al.*, using nanojets to trap sub-wavelength targets [100, 101]. In this regard, this indicates the current trends on developing probes suitable for trapping but also having detection and sensing capabilities, that cover a wide range of scales from micro to nano.

5.4.8 Optical trapping with Fresnel zone plates

Using the apparatus described in Section 5.4.1. The zone plates were tested in a water based solution with yeast cells. When the laser was turned on with a power bellow $\sim 10-15\,mW$, nothing was observed. However, with the increase of the laser power, above $\sim 15\,mW$, microbubbles were generated in the surface of the OF tip. This is visible in figure 5.33. Keeping the laser on for a couple of minutes caused the bubble to expand (5.33 at $t=104.23\,s$, $t=226.33\,s$), as shown by the plot of figure 5.34. Maximum microbubbles diameters of approximately $150\,\mu m$ could be reached, either by waiting for the bubble to expand at a continuous laser power, or by increasing the power of the laser (figure 5.33 at $t=605.32\,s$). In any case, the moment the laser was turned off, the microbubble size reduced. The microbubble was atatched to the OF tip, and could be moved in 3D without being released from the fiber surface.

The origin of the microbubbles is related with the high temperature in the fiber tip due to the presence of metal. This occurs either for OFs with Pt or Au/Pd. There are two possible causes for the generation of bubbles, both triggered by the high temperature [151]. In the one hand, it can be based in the nucleation of pre-existing nuclei already in the solution. On the other hand, small air vacancies in the metallic fiber tip may end up nucleating into microbubbles.

In the vicinity of the microbubbles, the fluid is driven towards regions of higher surface tension, due to the Marangoni effect. Because of these flows the yeast cells are attracted to the microbubble [152]. Please see figure 5.33 at $t = 605.32\,s$. However, once the laser is turned off, the particles no longer feel the balance between surface tension and pressure, and are released (figure 5.33 at $t = 678.43\,s$) [153].

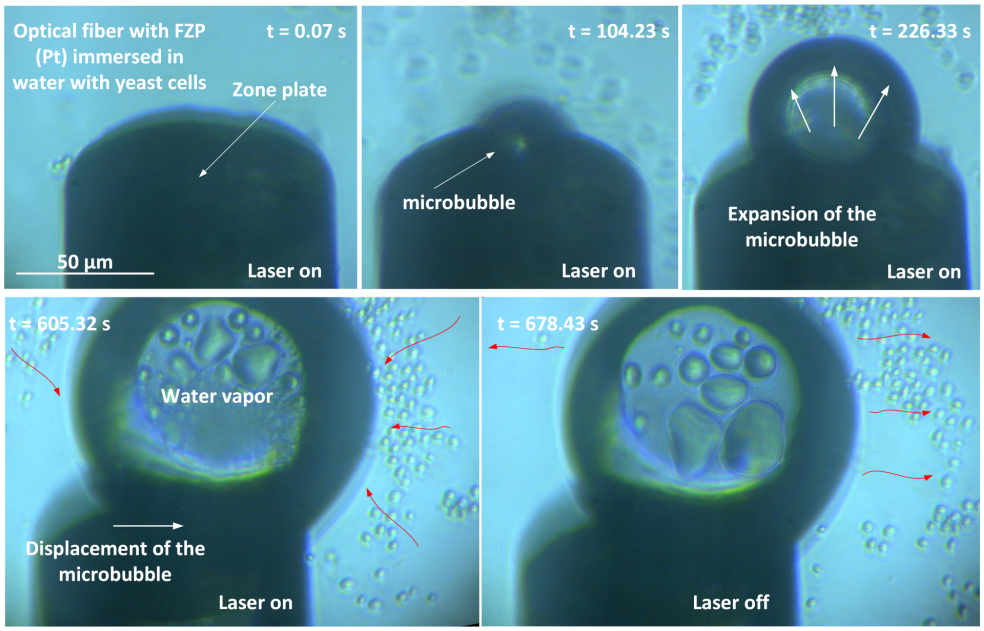

Figure 5.33: Dynamics of microbubble growth and Marangoni effect.

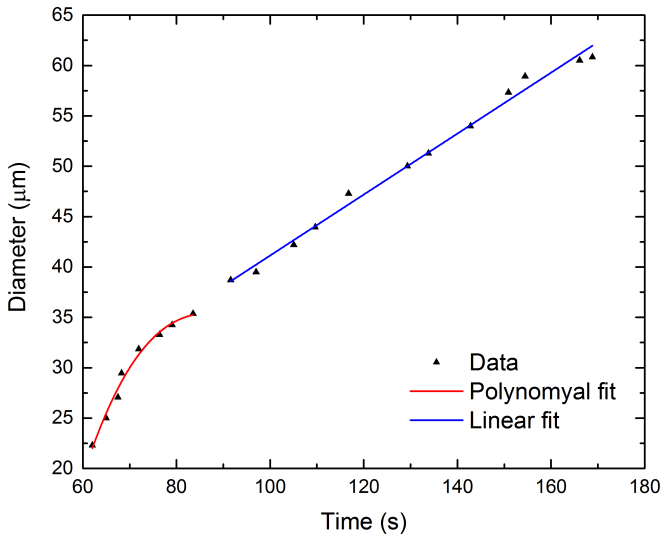

Figure 5.34: Microbubble diameter versus time, for a continuous laser power of $\sim 20\,mW$.

The possibility to generate microbubbles was not a goal of this thesis. Nonetheless,

these very preliminary results demonstrated how the microbubbles are originated and gives some insights on the dynamics of the beads around such structures. In the literature these structures are used as microvalves in microfluidic [154], in light driven micro tools with syringe function [16], among other applications.

5.5 Conclusion

This chapter reports the fabrication of Fresnel zone and phase plates by FIB milling on optical fiber tips. The design and fabrication of the structures was supported by computational simulations. In the case of the zone plates, the experimental data differs from the simulations. This reveals that the metallic rings might produce second order effects, that lead to the excitation of plasmons on the surface of the zone plane leading to modified light patterns. Contrary to this, the phase plates experimental and computational data agree, demonstrating that this fabrication method allows to produce diffractive structures, that despite presenting some minimal error, still comply with the prediction.

With this in mind, the capacity of phase plates for trapping of cells and particles was tested and characterized. This is the first time, to our knowledge, that Fresnel phase plates fabricated by FIB milling on optical fiber tips are used to trap micrometric particles and cells. The use of such diffractive structures have been tested in the past for manipulation of sub-wavelength particles, but not for targets resembling mammalian cells. Beyond this, the OF TIP was simultaneously used to size-detect the particles. Regarding the zone plates, experiments in aqueous media led to the generation of microbubbles, precluding optical trapping tests.

To summarize, new applications for Fresnel plates fabricated on optical fiber tips have been reported, beyond their common use as coupling devices. In the future, such devices may enable advanced monitoring and manipulation devices equipped with a feedback system, for automatic single particle/cell sorting according to their size.

Chapter 6

Optical fiber TIPs with spiral phase plates

So far, optical trapping through linear momentum transference was described in Chapter 4 and 5, allowing 2D manipulation of particles and cells. Nevertheless, rotational movements induced through the transference of angular momentum are becoming essential in a micro manipulation toolset. One of the techniques used to generate beams carrying orbital angular momentum is based on spiral phase plates. In this regard, these type of structures were carved on the top of single mode optical fibers using the sub-wavelenght resolution focused ion beam milling method. These structures act as beam shapers, transforming the fundamental Gaussian mode into Laguerre Gaussian beams. To achieve this, a preliminary study was done computationally, allowing to estimate the features of the spiral phase plates. After this, several attempts were made to fabricate such structures on the top of optical fibers, revealing to be successful in the generation of Laguerre Gaussian beams of order 1, as confirmed through interferometry tests. Moreover, experiments to test the ability to trap and rotate micro targets are performed with polystyrene particles and microalgae samples, validating the transference of orbital angular momentum through the observation of rotation.

6.1 Background

The nature of the angular momentum of light was initially investigated by Poynting in 1909, when he proposed that beams with circular polarization possess angular momentum [155]. Evidences supporting this phenomenon were published in 1936, where a birefringent wave plate was rotated, due to the angular momentum of light, while trans-

forming left hand into right hand circular polarization, and *vice-versa* [156]. Currently the angular momentum linked with the circular polarization is mentioned as the spin angular momentum (SAM). Later on, in the 90's, Allen *et al.* revealed that optical beams with an azimuthal phase dependency ($\exp(il\phi)$), i.e. helical beams, carry orbital angular momentum (OAM) [157]. Helical beams are represented by Laguerre-Gaussian modes (LG_l^p), which are the solutions of the paraxial wave equation in cylindrical coordinates [158]. These beams are characterized by indices p and l:

p is the radial index and defines the number of radially distributed field amplitude nodes;

l is the azimuthal index, or topological charge, and expresses the number of 2π phase shifts per helicoid pitch.

The amplitude distribution of Laguerre - Gaussian modes can be written as

$$\begin{aligned} LG_l^p &= \sqrt{\frac{2p!}{\pi(p+|l|)!}}\frac{1}{w(z)}\left[\frac{r\sqrt{2}}{w(z)}\right]^{|l|}\exp\left(\frac{-r^2}{w(z)^2}\right)L_p^l\left(\frac{2r^2}{w(z)^2}\right)\exp(il\phi)\times \\ &\quad\times\exp\left[\frac{-ik_0r^2z}{2(z^2+z_r^2)}\right]\exp\left[-i(2p+l+1)\arctan\left(\frac{z}{z_r}\right)\right]. \end{aligned} \tag{6.1}$$

In this expression, the $\frac{1}{e}$ radius of the Gaussian term is given by

$$w(z) = w(0)\sqrt{(z^2+z_R^2)/z_R^2}, \tag{6.2}$$

where z_R is the Rayleigh distance, $w(0)$ is the beam waist size, $(2p+l+1)\arctan\left(\frac{z}{z_r}\right)$ is the Gouy phase, r is the radial distance, ϕ is the azimuthal angle and L_p^l represents the Laguerre polynomials. These beams are generally mentioned in the literature as optical vortices (OVs), due to the screw dislocation along the axial direction, and also their phase singularity at the center [159]. Such features make OVs of broad and current interest. To give some examples, beams carrying OAM have been employed in a diversity of applications ranging from optical trapping and rotation of particles [160, 161], cells [162] and molecules [163] to the manipulation of atoms [164]. Simultaneously, quantum communication or rheological and viscometric methods have also take advantage of their unique features [165].

In the case of optical trapping, vortex beams are used to immobilize and rotate the targets. This results from the transference of angular momentum, from the beam to the particle, imparting a rotational movement on the second. Adding rotation capabilities to optical tweezers toolsets highly increase their potential of application.

The OAM density of a monochromatic beam of light, with frequency, ω, is given by

$$\frac{d\vec{L}}{dV} = \frac{\varepsilon_0}{2i\omega} \sum_{j=x,y,z} \left[E_j^* (\vec{r} \times \nabla) E_j \right], \tag{6.3}$$

where L is the OAM, ε_0 is the vacuum permittivity, E is the electric field and $\overrightarrow{r}$ is the vector position. This means that a beam does not carry the same amount of angular momentum along the intensity profile. Figure 6.1 shows the density of angular momentum for a LG_1^0 beam.

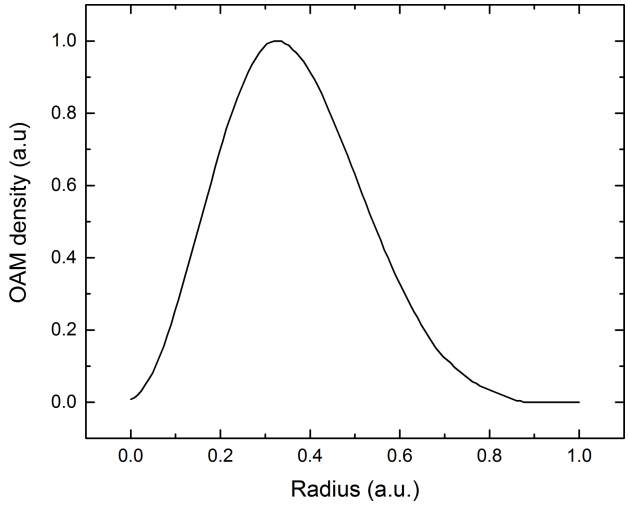

Figure 6.1: Radial OAM density for LG_1^0 beam.

This distribution affects the capacity of rotating a particle depending on its relative position on intensity profile of the beam. When such a beam acts on a large single particle, the resulting trapping forces usually tend to center the particle on the optical axis, also imparting rotational movement described by the following equation

$$\tau = 8\pi\eta r^3 \Omega, \tag{6.4}$$

where η is the viscosity (for water it takes the value of $8.90 \times 10^{-4}\, Pa$), r is the radius of the sphere and Ω is the angular frequency of rotation.

However, when there are several particles under the influence of the beam, depending on their number and their relative mutual position and position relative to the beam axis, complex behavior can be observed. Indeed, for particles of adequate size, the center of the particle may fall on the region of the beam with the highest angular momentum concentration. These particles will experience the strongest torques and are more likely to experience fast rotation. Another aspect of this process is that groups of particles

can aggregate and acquire angular momentum from the beam in several ways:

- spin around themselves,
- rotate around others,
- rotate together.

This also depends on their relative spatial distribution inside the beam, the viscous drag force exerted by the fluid, and the friction between themselves. In general, one should expect a combination of these three types of motion.

Typically, the techniques used to generate OVs are based on free space bulk setups, using diffractive gratings [166], via spatial light modulators [167, 168] or specially designed optical components, such as cylindrical [169] or spiral phase plates (SPP) [170, 171]. More recently, optical fibers have been used in the generation and propagation of OVs foreseeing a large number of distinct applications such as polarization maintaining fibers, nano-imaging, quantum entanglement, among others, as extensively reviewed in reference [172]. For instance, specially modified fibers, with helical cores have been theoretically studied and experimentally explored in the generation of optical singularities [173–175]. However, the use of OFs as alternatives to bulk setups is just in the initial stage of development. In this thesis, the optical vortices are generated uniquely by an optical fiber which has a SPP carved on the tip by FIB milling. This simple system aims to replace large and costly setups. Simultaneously, this work is motivated by the need to have special beam tailoring tools for further use in the area of optical manipulation with OFs. To our knowledge there is only one research work where OFs with SPP, fabricated by FIB milling, are used to generate OVs [176], and it was published simultaneously with the work presented in this thesis [147].

This chapter comprises the modelization of spiral phase plates, followed by the fabrication methodology and optical characterization. Finally, the test of the structures for optical trapping and rotation of particles and microalgae are presented.

6.2 Modeling of the spiral phase plate

A SPP is a structure composed by helical phase steps, resulting in a thickness increasing proportionally to the azimuthal angle ϕ (figure 6.2 (a)). The plate has a maximum step height, s, given by

$$s = \frac{l\lambda}{n_{SPP} - n_{medium}}, \tag{6.5}$$

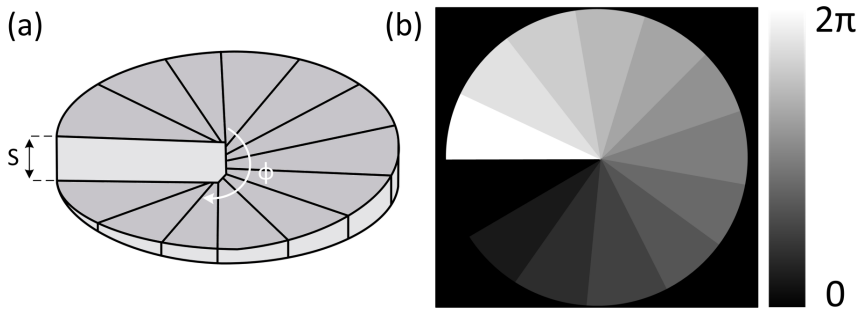

Figure 6.2: (a) Sketch of a spiral phase plate used to generate vortex beams. (b) Phase distribution of the desired SPP.

where l represents the topological charge of the produced vortex, whereas n_{SPP} and n_{medium} are the refractive index of the plate and the medium, respectively. With a SPP, Gaussian beams ($l = 0$) can be shaped into higher orders beams ($l \neq 0$), and already existing LG modes can be reshaped into other orders.

In this particular case, the SPP is projected to produce a $l = 1$ charged vortex (at $980\,nm$, $n_{SPP} = 1.457$, in air), thus having a maximum step size of $2\,\mu m$. With the purpose of investigating the performance of the SPP a solver of the Maxwell's equations, based on the FDTD method (Lumerical), was used. In this particular case, the software used to model the OFs was the Lumerical, instead of python-MEEP, since the first presents more flexibility in the implementation of 3D structures. The parameters used to model the OF match the experimental data given by the fiber supplier (Corning HI 980 nm). The SPP is $3.5\,\mu m$ wide (matching the core diameter), with depth increasing azimuthally in phase steps of $0.483\,rad$, corresponding to 13 levels, going from zero to a maximum step height of $2\,\mu m$ at 2π. Figure 6.3 shows the output electric field intensity, in the zy, yx and zx planes, where x is the propagation axis. In figures 6.3 (a), (b), (c) and (d), consecutive cross sections (zy), along the propagation distance, of the output electric field intensity are presented.

In the near field, figures 6.3 (a), (b) and (c), the intensity output is characterized by a doughnut shape ($3.7\,\mu m$ of outer diameter), preserving the intensity null ($0.5\,\mu m$ diameter) at the center. Regarding the far field region shown in figure 6.3 (d), the profile corresponds to a spiral shaped intensity distribution. The external rings visible in the yz plane are likely due to diffraction in the boundaries of the plate. These features are confirmed by the yx and zx cross sections, visible in figures 6.3 (e) and (f), respectively. The areas marked with the doted rectangles identify the zero intensity regions, characteristic of the phase singularities of optical vortices. The structure is well

preserved over the first $2\,\mu m$, after this, the field starts twisting.

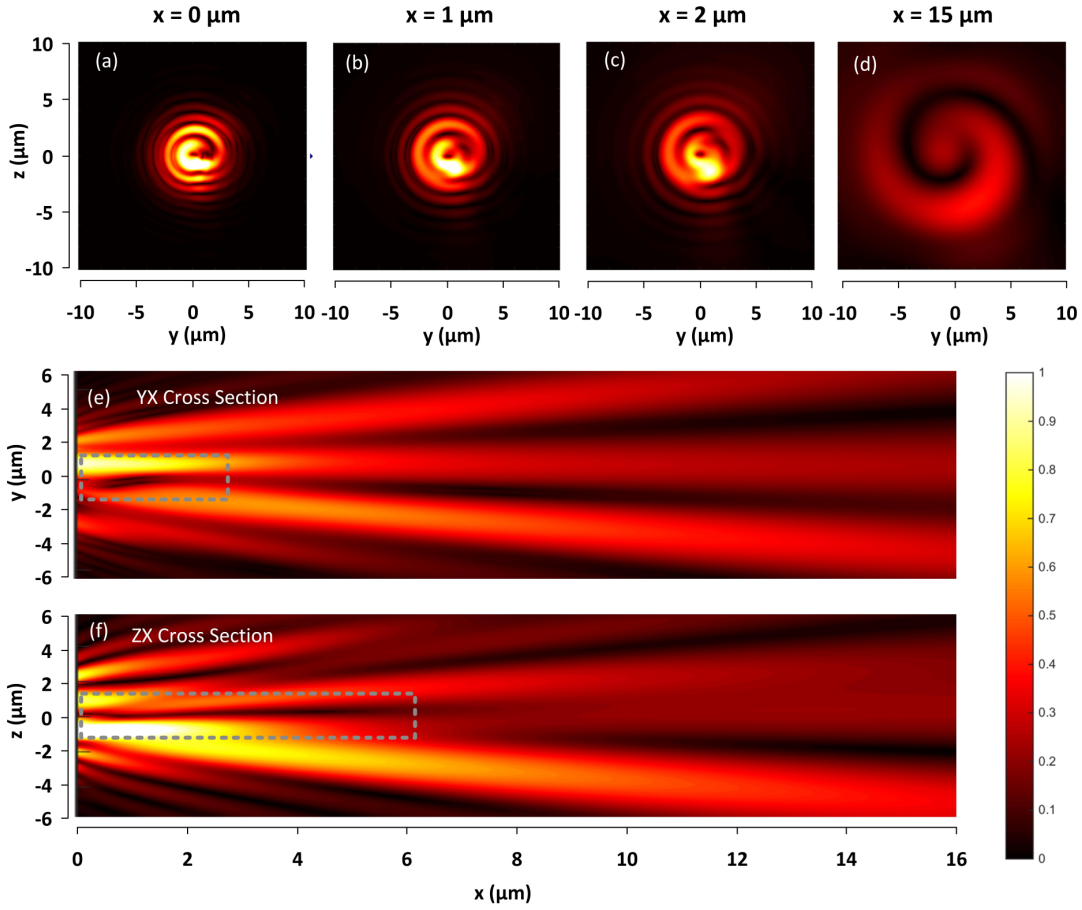

Figure 6.3: 3D simulations obtained by Lumerical FDTD solver. (a) Snapshots of the electric intensity profile of the OF tip output; tangential and sagittal views (x is the propagation direction) of the output profile: (b) yx and (c) zx.

6.3 Fabrication methodology

To fabricate the SPP, the tip of the fiber (Corning HI 980 nm) is first cleaned and cleaved. Then, a 9.6% hydrofluoric acid etchant gel is used to delimit the core of the OF [177]. This gel is generally used by dentists as a porcelain etchant. The gel is packed in dispensing syringes and has an etching rate considerably slower than the ones obtained with the usual 48 % HF solution. However this HF based etchant allows a safer handling as small amounts are used and the hazardous fumes released are residual. Since the fiber core is chemically etched more rapidly than the cladding, and this gel has a slow etching rate, after $15\,s$, a nanoscale circular depression is visible on the surface of the fiber (figure

6.4), matching the core location. This unevenness allows an easy identification of the core and the correct and centered positioning of the design to pattern on the SEM/FIB microscope.

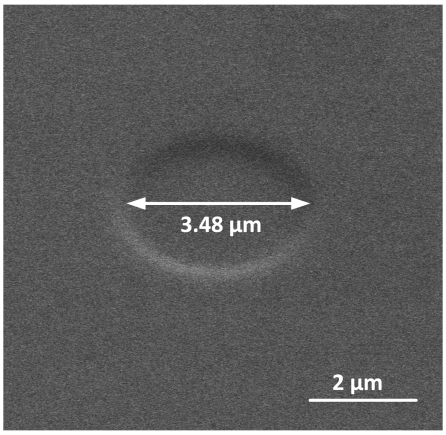

Figure 6.4: Image of the OF core depression visible after 15 s of chemical etching.

To fabricate the SPP on the optical fibers a dual beam scanning electron microscope also equipped with a focused ion beam (Quanta 3D, FEI Company), is used. The fibers are first coated with an organic conductor polymer, PEDOT: PSS (poly(3,4-ethylene dioxythio-phene):poly(stryrene sulfonate)), by dip coating to guarantee a good conductive surface and avoid charging effects during the milling and imaging processes [177]. The final goal of this process is to have a silica fiber with the structure milled on its surface, without any trace of the metallic film, avoiding back reflections. The PEDOT is water-soluble; thus, after milling the surface, it is possible to remove it by dipping the OF tip in water. However, during the milling, the conductivity properties of the PEDOT did not assure the ideal conditions for the fabrication of the phase plate, namely on the sharp discontinuity near the center of the pattern, due to the ion-beam induced charging and beam drift. Therefore, an extra film of gold-palladium, 5 nm thickness, was deposited onto the surface of the fiber, covering the PEDOT layer. Overall, this two-step process ensures good fabrication conditions and by doing a lift off process, the metallic film can be easily removed. It is possible to mill complex structures using the FIB by uploading a bitmap file with the pattern characteristics. The pattern imprinted on the top of the fiber to obtain the SPP is shown in figure 6.2 (b). The exposure dose is controlled by the dwell time, which is proportional to the bitmap pixel value. For a black pixel (level 0), the beam is blanked. For a white pixel (level 255), the dwell time is set to 1 μs. The dwell time for the pixel values in-between is linearly interpolated. The ion beam current was set to 0.1 nA, which corresponded to a beam spot size of 24 nm,

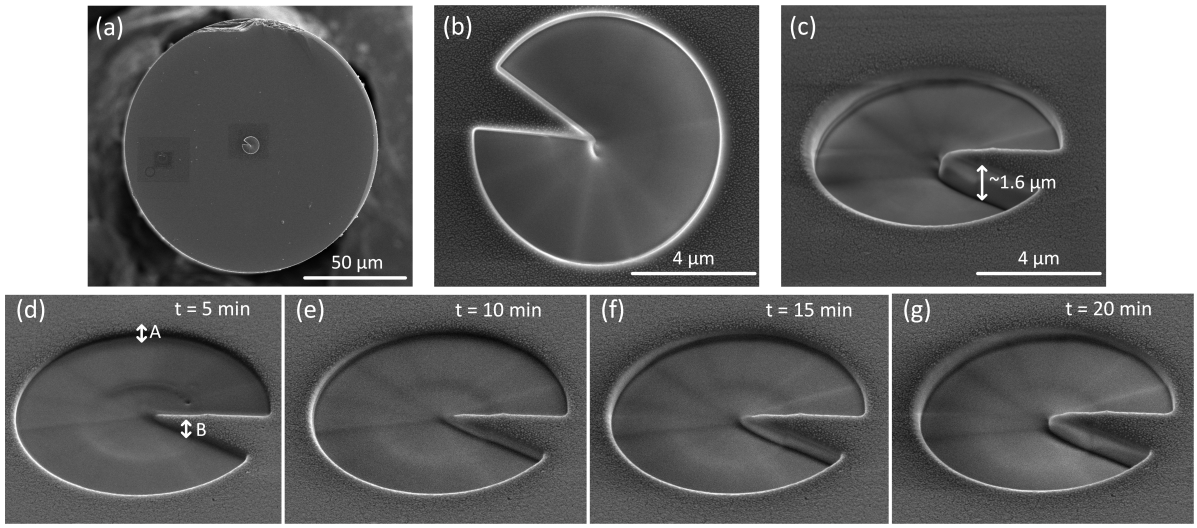

Figure 6.5: (a) SEM image of the OF with the SPP; (b) zoom of the SPP (top view); (c) zoom of the SPP (side view); (e)-(g) SEM images of the milling process acquired every $5\,min$, allowing to estimate the etching rates in different positions of the SPP.

allowing an optimal trade-off between patterning resolution and patterning duration. The milling process lasted for $29\,min$, resulting in the structure depicted in figure 6.5 (a). In figure 6.5 (b) one can see a top view of the SPP and in figure 6.5 (c) a side view is visible, showing the features of the plate. The plate, with a diameter of $8\,\mu m$, is centered on the fiber core (figure 6.5 (b)), and the maximum step height (s), achieved during the milling process, is $1.6\,\mu m$ (figure 6.5 (c)). The step height was controlled during the milling process, by acquiring SEM images every $5\,min$, this is shown in figures 6.5 (d) - (g). By measuring depths A and B for every case, as illustrated in figure 6.5 (d), the etching rate was calculated for this two positions, through the analysis of the plot of figure 6.6. Position A refers to a level of 65 in the intensity mask of figure 6.2 (b), and the etching rate in this position was approximately $0.02\,\mu m/min$, while in position B, corresponding to a white pixel zone (level 255), the estimated etching rate was $0.05\,\mu m/min$. As expected the etching rate was larger for locations of the mask with higher pixel levels $(0-255)$.

The diameter of the plate was made larger than the core of the fiber ($3.5\,\mu m$) in order to avoid diffractive contributions from the plate edges. In figure 6.5 (b) one can see that the center of the plate is slightly eroded. This results from the multiple scans of the ion beam over the entire structure, during the milling process. Sharper edges can be obtained by protecting the glass region of interest with an ion-beam induced platinum deposition, which requires a strong acid mixture (aqua regia) for its removal, after the milling is complete. For such reason, it has been avoided.

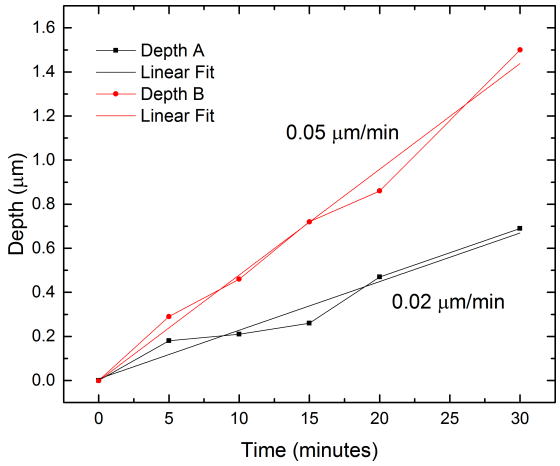

Figure 6.6: Etching rate for position A (pixel level 65) and B (pixel level 255).

6.4 Optical characterization of spiral phase plates

In order to analyze the output beam profile, the fiber tip was spliced into a pigtailed diode laser (@$980\,nm$), and the field was projected, using a $60\times$ objective, into an infrared camera. After this, the beam was scanned axially using a micrometer positioner, and snapshots of the output field were taken at each $1\,\mu m$, along $14\,\mu m$. The resulting output profile is visible in figure 6.7 (a). The mode field diameter is $4.2\,\mu m$, corresponding to the radius of the SPP, avoiding to illuminate the borders of the plate. Work developed by Brasselet *et al.* also demonstrated that keeping the illuminating beam waist diameter smaller than the SPP increased the quality of the output vortex [171]. Overall the field has a doughnut shape profile with asymmetric intensity distribution and is slightly focused. Doing a reconstruction of the intensity profile, through the interpolation of the images using ImageJ software, allows a better perception of the OV features. In figures 6.7 (b) and (c) the cross sections yx and zx are presented. Analyzing the yx and zx cuts the central zero intensity, characteristic from OVs, is evident along the $14\,\mu m$. From 0 to $4\,\mu m$ the annular intensity outline is highly asymmetric, showing almost a distorted profile. In the range of $4\,\mu m$ to $6\,\mu m$ the features of the doughnut are more regular, and the side dimensions are reduced suggesting a focusing area. The outer diameter of the annular field is approximately $6\,\mu m$, and the inner diameter corresponds to $1\,\mu m$. Finally, from $6\,\mu m$ till $14\,\mu m$ the field diverges and the annular profile vanishes. This is more significant in the zx plane, and can be identified in figure 6.7 (c).

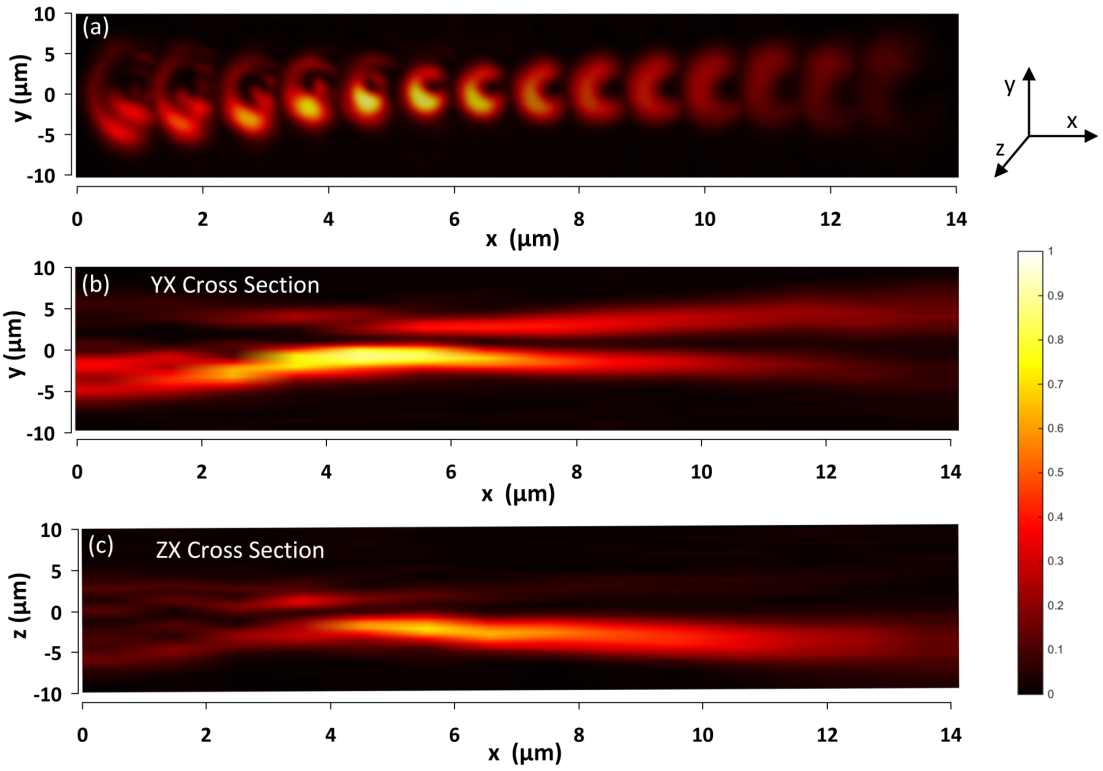

Figure 6.7: (a) Snapshots of the experimental optical intensity profile of the optical fiber tip output; Orthogonal views of the output profile obtained through an interpolation of the field: (b) yx and (c) zx. x is the optical axis direction.

On the basis of the results presented above, it is clear that the output optical intensity profile has some constraints regarding its symmetry. There are some possible causes, most probably associated with the fabrication process. First, a closer look into figure 6.5 (b) shows that the SPP is misaligned with the fiber core by a $300\,nm$ shift to the left. Therefore, when the fundamental Gaussian mode faces the spiral phase plate, the intensity peak will not be centered with the phase singularity of the plate, and an uneven distribution of the optical profile can arise. Second, the maximum step depth does not correspond exactly to a 2π phase shift due to unavoidable fabrication errors and the non-uniform discretization of the number of levels on the phase plate introduces some degree of phase error [178]. Likewise, the deformation in the center of the plate, caused by the multiple scans of the FIB over the fiber surface, can cause a flawed doughnut shape. Also the initial chemical etching to locate the OF core can induce some modifications on the output, although being almost invisible on the final structure (figures 6.5 (b) and (c)). Apart from these traits, the SPP also imprints a focusing outline on the electric field intensity. This effect is due to a curvature of the SPP caused during the

milling process. In the course of the scanning of the ion beam over the fiber tip, there is always a higher milling near the edges. Comparing the computational and experimental results, there is an agreement regarding the extent of vortex and the general profile, where the doughnut shape is observable in both cases. Nonetheless, the focus effect was achieved only experimentally for the reasons previously explained. Particularly, the simulations presented here model an ideal spiral 2π phase plate, with gradual phase step increase, centered in the fiber tip. In contrast, experimentally, the resulting SPP had some limitations, as indicated above, which were not accounted for in the model and can explain the discrepancies observed.

While the intensity profile of the output optical beam is studied using a magnification system and a CMOS camera to acquire the images, the phase profiles are assessed using an interferometer. The literature on beams carrying orbital angular momentum abounds with examples of such measurement systems [158]. In this case, the interference of the beam carrying the optical vortex and a reference beam, will result in a characteristic pattern. The setup used to test the SPP is presented in figure 6.8. The $980\,nm$ diode laser is first connected to an optical fiber coupler (50/50@980). After this, one of the fibers is cleaved, and is used as the reference beam, while the other is spliced to the SPP tip. The fibers are then placed on two micromanipulators and two $20\times$ objective are used to collimate the output beams. Finally, a beam splitter is used to recombine the beams and the interference pattern is generated. The result is projected onto a CMOS camera. Please note that the lengths of the interferometer arms are adjusted to match.

Figures 6.9 (a) and (b), show the reference (Gaussian profile) and the SPP output beam (doughnut shape), respectively. The coaxial interference of these two beams originates the pattern of figure 6.9 (c). In this case the interference fringes nucleate in a spiral profile, where the number of fringes defines the charge of the vortex. In this case there is only one fringe, indicating that the beam should carry a vortex of charge 1. This can be confirmed by the off-axis interference of the two beams, that according to the literature must create a pattern with a discontinuity caused by the vortex, visible through the presence of degenerated/extra fringes, which are commonly called as 'forklets' [179]. Figure 6.9 (d) shows the transition between the coaxial and off-axis interference. Finally, after increasing the angle between the two beams, the forklet structure is visible, in figure 6.9 (e), confirming the presence of the phase singularity that constitutes the optical vortex.

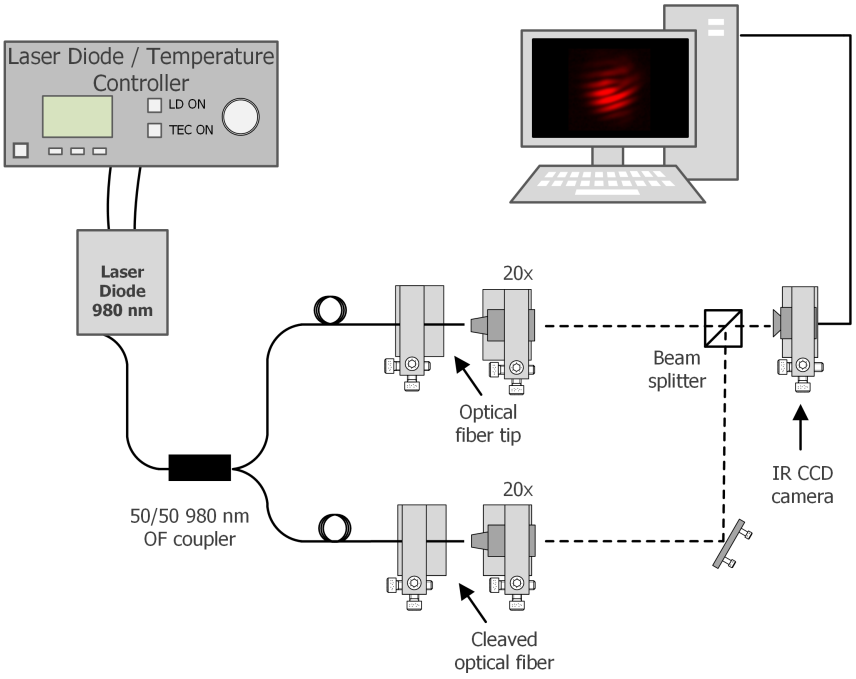

Figure 6.8: Interferometer scheme used to study the vortex charge.

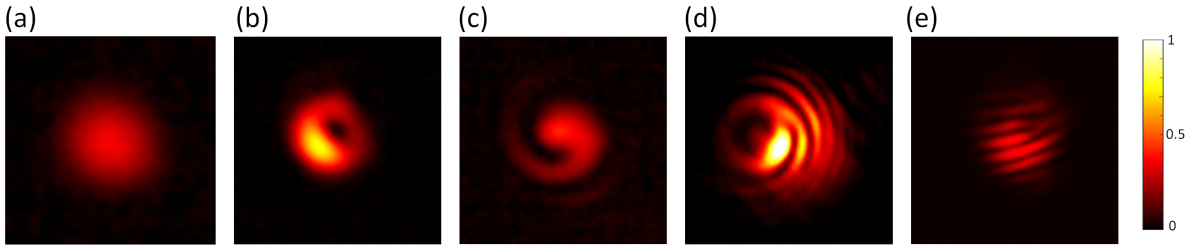

Figure 6.9: (a) Reference beam; (b) doughnut shaped beam; (c) axial interference; (d) transition from axial to off-axis interference; (e) off-axis interference.

6.4.1 Discussion

The results obtained validate the SPP fabricated on optical fiber tips as devices suitable to transform Gaussian beams into a combination of Gaussian and Laguerre-Gaussian beams. From the analysis of the electric field intensity and the interferometric measurements, it can be said that the output is a LG_1^0. The generation of higher order modes should be therefore possible by increasing the height of the phase steps of the SPP, the number of steps and also by improving the fabrication conditions to avoid the misalignment and the non-uniform phase steps height. The number of phase steps is an important parameter with high impact on the mode conversion efficiency, as demonstrated by Scipioni *et al.* [178], where they found that 16 or 32 are values that highly increase the purity of the modes, for their particular case. A more detailed study, with calculation and measurements of mode purity is essential to assess the full potential of the devices and will be the subject of future work.

6.5 Optical trapping and rotation

6.5.1 Optical trapping setup

The setup used to test the potential for trapping and rotation of micro targets using the OF probes with SPPs is depicted in figure 6.10. It is composed by an image acquisition system and a 4-axis motorized micromanipulator to precisely handle the optical probes. The imaging system is essentially a home made inverted microscope, composed by a CMOS camera (EO-2018C, Edmund Optics) and an objective, which are connected to a computer. Using a wavelength division multiplexer (WDM) ($980/1550\,nm$) a Braggmeter (FS2200SA, FiberSensing), used to measure the distance from the OF and the cover glass at $1550\,nm$, and a pigtailed laser diode ($980\,nm$, $500\,mW$, Lumics) are connected to the optical fiber with the SPP. The OF probe is spliced to the output of the WDM, and inserted into a metallic capillary. The capillary is attached to the stage and can be vertically adjusted, also acting as a protection to the OF. Then, the fiber is inserted into the sample that is placed over the glass slide.

6.5.2 Samples - particles and *microalgae*

The optical trapping and rotation tests were assessed using distinct aqueous solutions with beads or microalgae in suspension. The first were polystyrene beads with diameters of $1\,\mu m$ and $4\,\mu m$, whereas the microalgaes were *Tetraselmis suecica* and *Phaeodactylum*

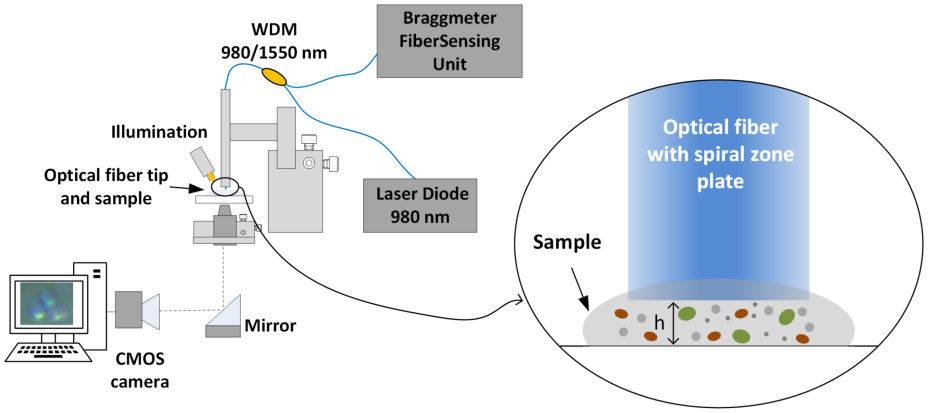

Figure 6.10: Optical trapping setup used to test the OFs with SPPs.

tricornutum.

6.5.3 Rotation of $4\,\mu m$ polystyrene particles

To understand if the OF with the SPP was useful for trapping and induce rotation in micro objects, the previous probe was tested in a water based solution with $4\mu m$ PS particles dispersed. The position of the OF could be estimated from the Fabry-Perot cavity that is formed between the OF extremity and the glass slab. The spectrum of the cavity is retrieved by the the Braggmeter $(1500-1600\,nm)$ through the WDM. Without this configuration, the only way to estimate the distance from the fiber to the glass slab is visually. To do this, the camera is focused on a particle deposited in the glass slab, and then the fiber is lowered until it is also focused. At this moment the location of the fiber is known. Then, if the micromanipulator used to move the fiber is calibrated, one may relate to this, to know where the fiber is located. However, the first method presented, is much more reliable.

From the information presented in table 6.1, the working range of the OF with the SPP is divided into three regions. When the fiber was located at $44.03 \pm 0.66\,\mu m$ weak trapping of single particles was achieved. In this case, the particle was moved from the resting position towards the highest intensity region of the beam. No rotation was visible, either for a single particle or more. Decreasing the height of the fiber to $34.72 \pm 0.36\,\mu m$ lead to trapping and rotation of the particles. For distances smaller than $15.96 \pm 0.11\,\mu m$ trapping was observed, but rotation was not imparted on the particles.

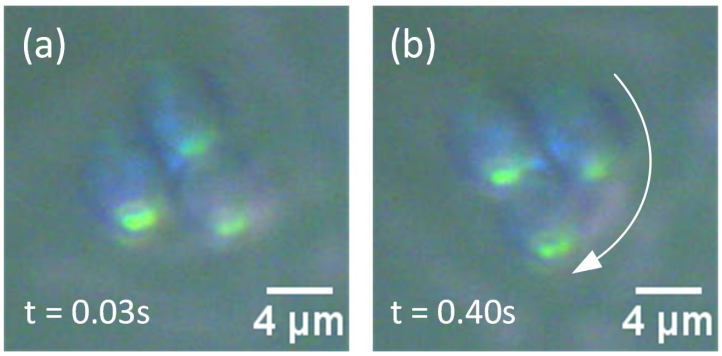

Figure 6.11: Clockwise rotation of a system of three PS particles, with individual diameters of $4\,\mu m$.

OF height, $h(\mu m)$	**Observations**
44.03 ± 0.66	Weak trapping
34.72 ± 0.36	Trapping and rotation
25.12 ± 0.27	Trapping and rotation
15.96 ± 0.11	Trapping

Table 6.1: Study of the distance between the optical fiber and the cover glass and the effects on trapping and rotation of micro PS beads.

Figure 6.11 shows the rotational movement imparted on the PS particles due to the transference of AOM from the beam to the beads, while the fiber was positioned at $\sim 20\,\mu m$. The particles rotate clockwise as demonstrated in figure 6.11 (a) and (b). The rotation frequency was calculated while gradually increasing the laser powers from 40 to 180 mW, as depicted in figure 6.12. The observation and data collected reveal that the frequency of rotation increases with the laser power, in agreement with the dependency of AOM and the field intensity.

During the analysis of the videos, it was noticeable that the trajectory described by the particles was not perfectly circular. Due to this, the trajectories of the particles for $0.03\,Hz$ and $0.21\,Hz$ were plotted in a polar graph, as visible in figure 6.13. From the analysis of this graph, one can see that at $0.21\,Hz$ the particle has a stable trajectory. However, at $0.03\,Hz$ the movement of the particle is more irregular, since the optical force is smaller. This plot also corroborates that the beam is not symmetric hence resulting in an irregular trajectory.

Besides the rotation experiments, it is also possible to measure the optical force that attracts the beads towards the beam. This test is performed in a similar fashion to the

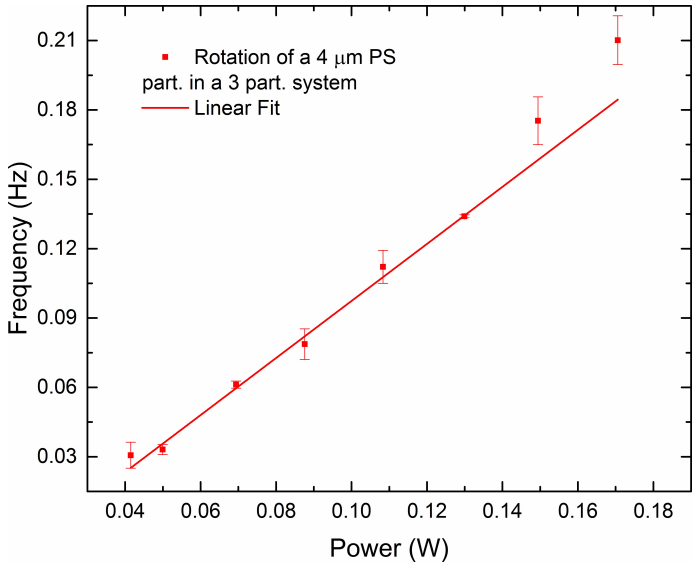

Figure 6.12: Rotation frequency of $4\mu m$ PS particles versus output optical power. The error bars represent the standard deviation of the measurements, since the trapping and rotation process was repeated at least three times for every data point.

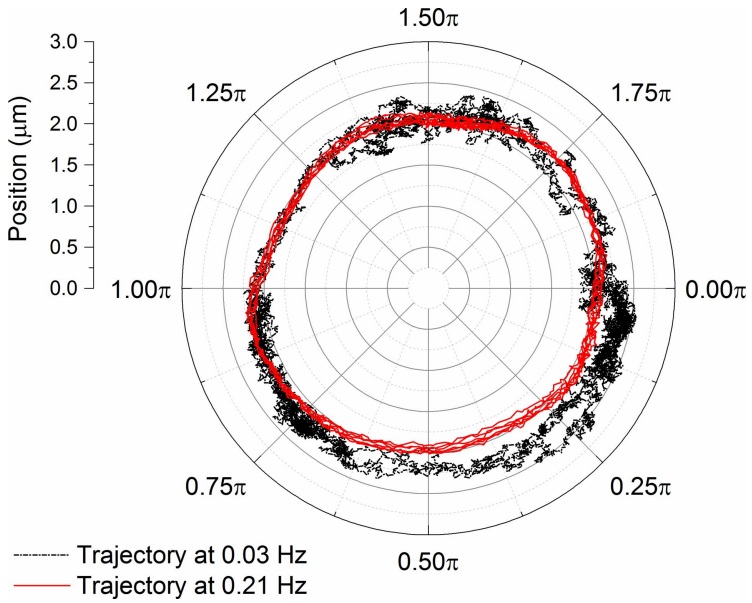

Figure 6.13: Circular trajectory of one PS particle ($4\mu m$) in a 3 particle system for two distinct rotation frequencies.

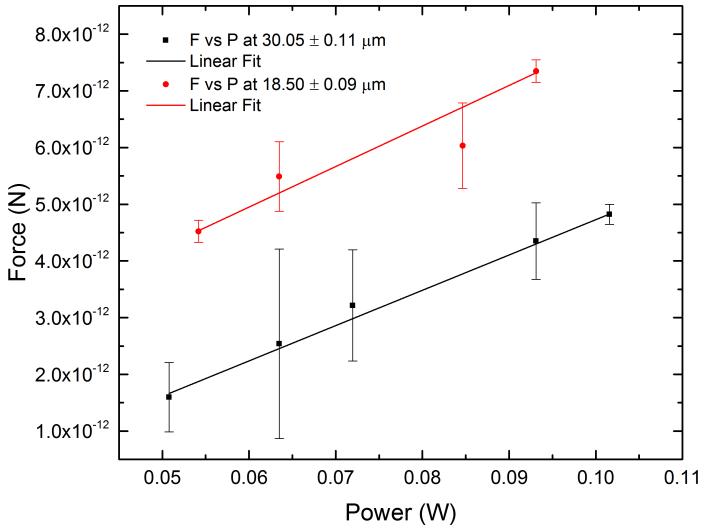

Figure 6.14: Optical force acting on a single $4\,\mu m$ PS particle, considering two distances between the OF and the cover glass. The error bars represent the standard deviation of the measurements, since the trapping process was repeated at least three times for each data point.

ones presented in the previous chapters. Basically the bead is trapped and then the laser is turned off, after this, the fiber is displaced in the x and y directions, and the the laser is turned on. From the trajectories corresponding to the $+x$, $-x$, $+y$ and $-y$ directions the optical forces are calculated using equation 3.5. This was performed for two positions of the OF with the SPP, namely at $30.05 \pm 0.11\,\mu m$ and $18.50 \pm 0.09\,\mu m$. The results are plotted in figure 6.14. In this graph is possible to see that for lower distances (h), the optical force is higher. This is caused by the proximity to the OF, which increases the intensity of the laser beam. Please note that in this case the bead is trapped in the center of the optical beam, and no rotation is imparted on it.

6.5.4 Rotation of $1\,\mu m$ polystyrene particles

Using the OF in the same configuration, the device was tested for trapping and rotation of PS particles with a diameter of $1\,\mu m$. The fiber was positioned at approximately $\sim 16\,\mu m$ from the glass slide and the laser was turned on with a power of $70\,mW$. The dynamics of the trajectories of the particles, while trapped, are not as straightforward as for the PS particles ($4\,\mu m$ diameter). In this case, particles organized in different arrangements were observed, as shown in figure 6.15, and described bellow:

(a) This frame shows six particles disposed in a circular pattern, and another one placed inside the circle. The six particles rotate clockwise, with a frequency close to $1\,Hz$

while the other particle is confined in the center.

(b) In this picture, two circular patterns are created by the PS particles: the inner one is composed by three particles, whereas the outside has eight particles. Both groups rotate independently and the rotation frequency of the inner one is higher than the external group. Please note that the external group seems to be lacking particles in order to be able to form a closed circumference, explaining the odd configuration of the beads.

(c) and (d) At this point the height of the fiber increased to $\sim 20\,\mu m$. When the laser is turned on in the vicinity of nine beads, after a couple of seconds these are displaced as shown in image (c). No rotation was observed, although the particles were struggling to be positioned as shown. After moving the OF, the beads readjusted their positions, as visible in (d) but still no rotation was noticeable. In this case the particles are further away from the center, than in the previous snapshots (a) and (b).

(e) This image shows that one particle was expelled from the inner region, allowing the bead in the center to rotate at a high frequency (the videos do not have enough spacial and temporal resolution to measure this). The external particles remained approximately in the same position.

(f) This frame depicts the rotation of five particles located in the center of the trapping region, while externally seven particles rest in a semi circular pattern. Please note that the five inner particles are not displaced in a perfect circumference.

(g) This image depicts the rotation of the three central particles, while the external ones do not rotate.

The previous observations may be explained by the following grounds. The optical beam generated by this OF does not present symmetry in the ring-shaped intensity pattern, as visible in figure 6.7. Considering that these measurements were performed in air, this means that when immersed in water, the effect will likely be more notorious, due to a small beam contrast between the medium and the OF. In this regard, it is comprehensible that the particles are more stable when they are located at the maximum of intensity due to the transversal confinement caused by the approximate Gaussian distribution of this section, thus forming a partial circumference. Being located at the zone of maximum intensity causes the particles to acquire more OAM leading to their fast rotation. At the same time, it is also noticeable that the particles are distributed in distinct concentric

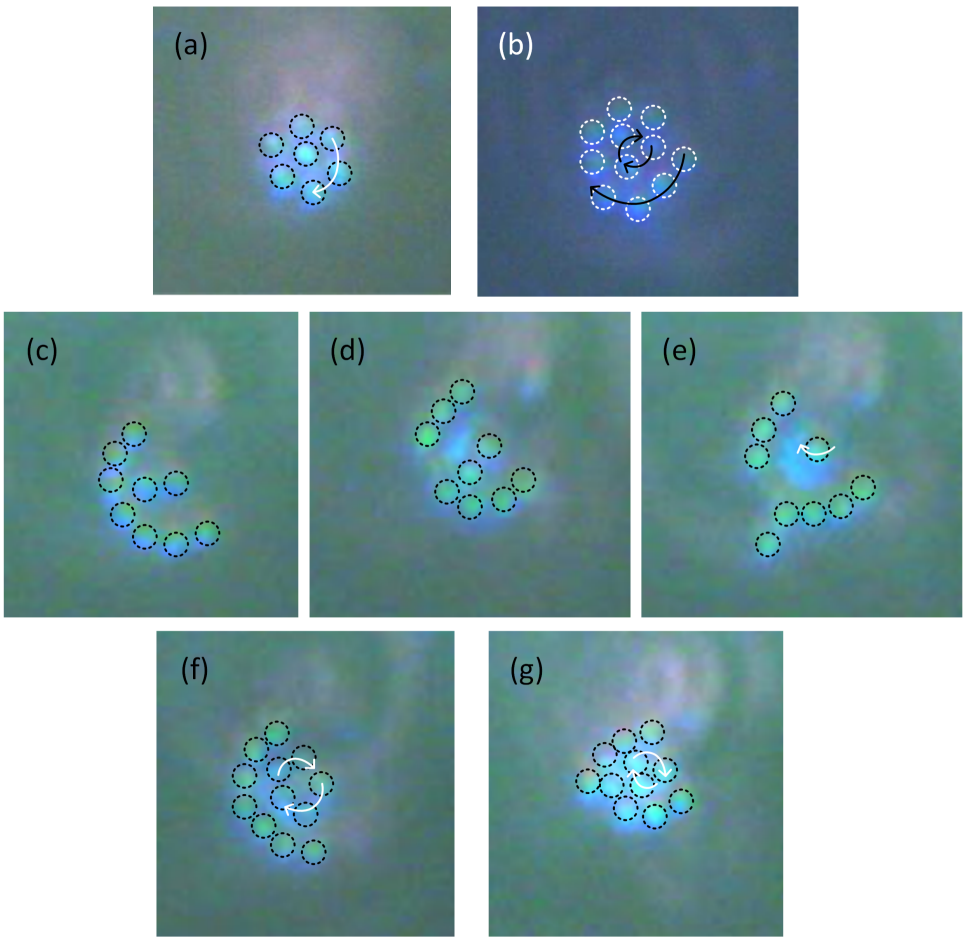

Figure 6.15: Trapping and rotation of PS particles with $1\,\mu m$ diameter. (a) and (b) the OF is positioned at $\sim 16\,\mu m$ from the glass slide, leading to a more confined arrangement of the beads. (c) - (g) The height of the OF increased to $\sim 20\,\mu m$ leading to the trapping and rotation of the particles in a larger cross section of the beam.

rings, and this depends on the height of the fiber. This is explained by the increasing in the divergence of the beam, as the OF is further away from the glass slab. As there is no axial confinement, the trapping occurs in this surface, and the beads are exposed to a different cross sections of the beam as the distance between the fiber and the glass slab changes. Generally speaking the equilibrium positions of the particles are rather unstable and complex. Beyond the previous considerations, the PS particles can also affect the local beam, as these are small lenses, causing small perturbations to the local distribution of the field.

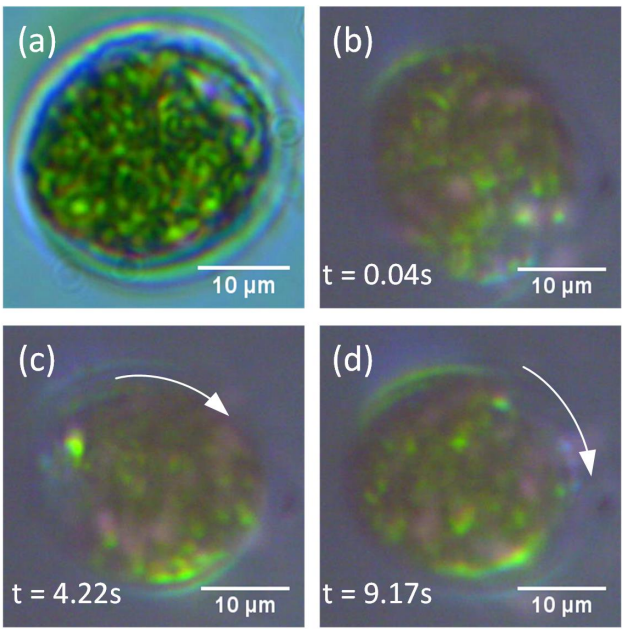

Figure 6.16: (a) *Tetraselmis suecica* microalga. (b) - (d) Rotation of the microalga through the transference of AOM.

6.5.5 Rotation of microalgae *Tetraselmis suecica*

Tetraselmis suecica is a spherical-like microalga with approximately $25\,\mu m$ of diameter, as shown in figure 6.16 (a). Using the previous OF TIP, the trapping and rotation of this microalga was tested. Figures 6.16 (b) - (d) show consecutives frames where the microalgae moves clockwise. In this case, the microalga rotates around its own axis. In contrast, the previous results demonstrated the rotation of the PS particles around the center of the beam. In this case the size of the microalga is larger than the beam cross section, leading the rotation around its own axis. As the OV intensity profile is not symmetric, the particle will likely be trapped by the highest intensity region of the beam simultaneously acquiring rotational movement.

During the experiments it was verified that the threshold power necessary to induce rotation was around $50-60\,mW$. The rotation frequency was then calculated, as visible in the graph of figure 6.17. Since the microalga is larger, the rotation frequency measured is considerably smaller than for the case of the $4\,\mu m$ beads. From these data the torque was computed through equation 6.4 and a maximum value of $41.58\,pN\mu m$ was found. Note that besides the rotation imparted on the microalgae, it is also possible to move them in 2D.

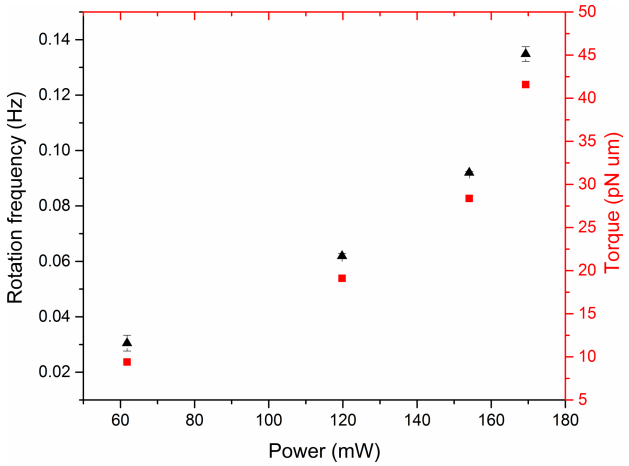

Figure 6.17: Rotation frequency vs laser power and torque vs laser power for *Tetraselmis suecica* microalgae.

6.5.6 Rotation of microalgae *Phaeodactylum tricornutum*

After testing the OF with PS particles and *Tetraselmis suecica* microalgae, experiments with microalgae *Phaeodactylum tricornutum* were performed. These microalgae are elongated structures, as visible in 6.18 (a), with a length of approximately $10\,\mu m$ and $5\,\mu m$ wide. This particular test was performed with two microalgae that were somehow atatched to each other. When the laser is turned on, the microalgae flip vertically, to aligned their major axis with the optical axis. Therefore, in the acquired frames, 6.18 (c) - (d) the structures seem smaller than in image 6.18 (a), because we are observing them from the top/bottom perspective. In this case, one of the microalgae is located in the center of the beam, while the other rotates around the beam axis anticlockwise, what differentiates from the previous experiments. In addition, the central microalga also rotates, since they it is atatched to the external one. As the optical characteristics of microalgae are unknown, and its structure is likely inhomogeneous, it is probably that the anticlockwise rotation is due to a complex interaction between the system of particles and the field.

To evaluate the type of trajectories that both microalgae perform, figure 6.19 (a) and (b) should be consulted. The first shows the trajectories plotted in a polar graph, showing that the central microalga is slightly off the beam axis, while the second rotates around it. Figure 6.19 (b) displays the same results, however, in this image a snapshot of the particle tracking software is visible. The irregular trajectory may be caused by the non-symmetry of the OV beam, causing the particle to accelerate when it is in regions of lower intensity and to maintain a more stable trajectory where the beam intensity is higher.

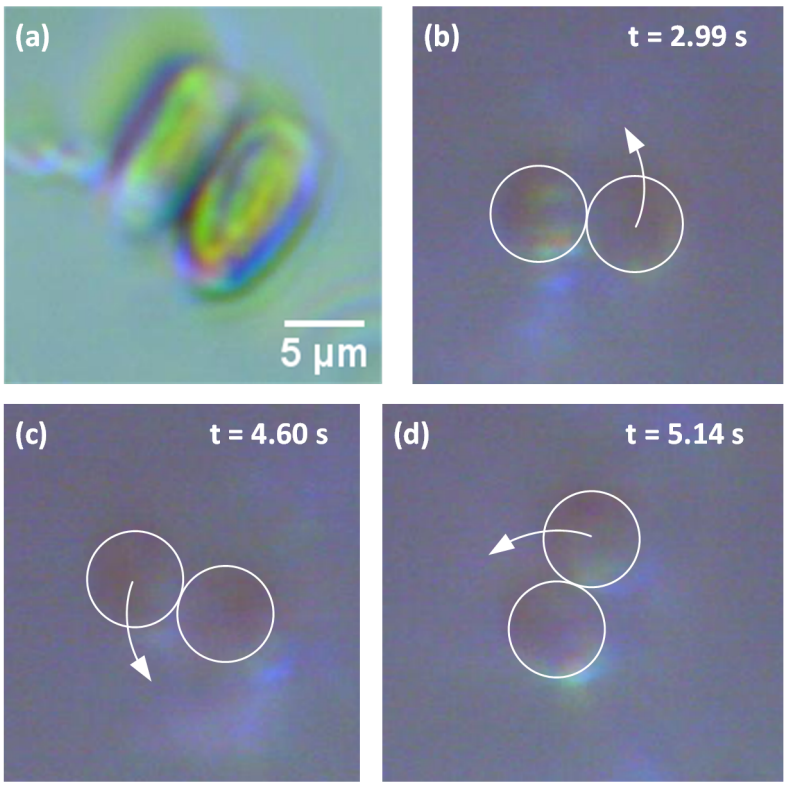

Figure 6.18: (a) Image of two *Phaeodactylum tricornutum* microalgae atatched to each other. (b) - (d) Rotation of the microalgae through the transference of AOM.

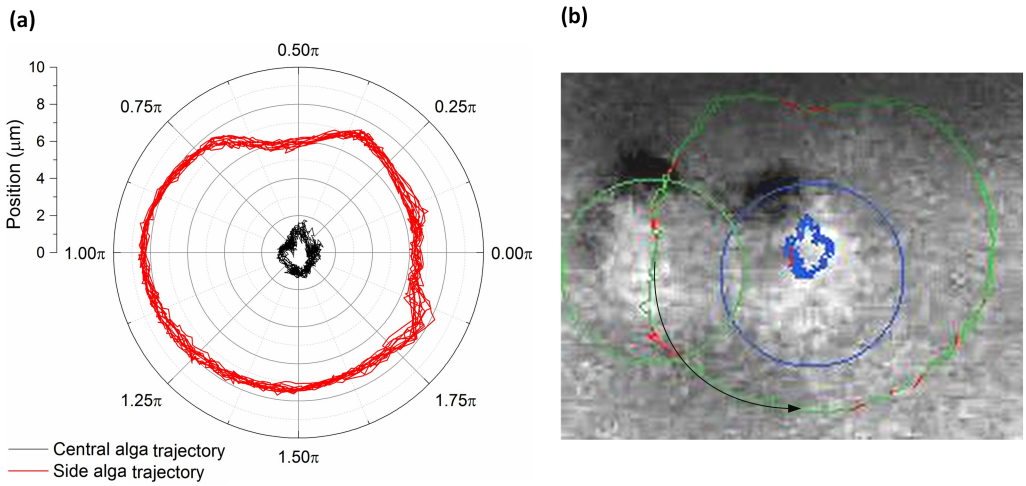

Figure 6.19: Rotational trajectories for the two microalgae. (a) polar plot of the trajectories; (b) snapshot of the particle tracking software where the trajectory of the central particle is illustrated in blue, and the lateral particle in green.

Power (mW)	**Frequency** (Hz)
67.7	0.31 ± 0.01
93.7	0.39 ± 0.01

Table 6.2: Rotation frequency for the two algae system versus laser power.

The rotation frequency was measured for two optical powers as presented in table 6.2. Although the frequencies are relatively low, one can see that they increase for higher values of optical power. Furthermore, as this system is smaller than the previous one (section 6.5.6) the particles have a higher frequency for smaller laser intensities. This last experiment allowed to study a different system with non spherical particles, where a different dynamic was observed.

6.6 Conclusion

In a nutshell, this work describes a straightforward method for the generation of LG modes, based on optical fibers with spiral phase plates. The fabrication method is based on the micro machining of optical fiber tips with the focused ion beam. In this particular case, the optical fiber tip was projected to tailor a Gaussian beam into the LG_1^0 mode, which was demonstrated experimentally. The experimental results were preceded by computational simulations, indicating the potential of the expected outcomes.

Furthermore, the structures were validated experimentally for the trapping and rotation of dielectric particles and microalgae. It was verified that the distance from SPP to the particles influentiate the trapping efficiency and rotation of PS particles. The smaller the particle the more efficient was the rotation, meaning that less power was necessary to rotate the targets at higher frequencies. The size of the particle is also important to the type of rotation that is imparted on the particle/microalgae. For instance, in the case of $1\,\mu m$ PS particles, these form circular patterns and rotate around the center of the beam. On the contrary, microalgae *Tetraselmis suecica* rotate around themselves, since they occupy the entire beam pattern. These evidences demonstrate that the rotational movement is complex and depends of several factors, such as particle size, beam dimension and OAM distribution. Moreover, anticlockwise rotation was imparted to microalgae *Phaeodactylum tricornutum*, due to their complex inhomogeneous composition, with unknown optical characteristics.

Chapter 7

Conclusion and future work

The purpose of this thesis was to develop optical fiber TIPs for manipulation of particles and cells, either using a low cost and fast fabrication method, or a high resolution technique. One of the reasons that led to this work was the need to scale down optical trapping devices, and to have reliable and cost efficient alternatives. Nevertheless, it was also instigated by a previous project on optofluidics. This project aim was to develop a microfluidic based chip [27], where optical and electrical measurements on RBCs could be performed. The optical information was acquired with optical fibers inserted inside the chip, in a suitable configuration to retrieve refractometric and absorption data. Regarding the optical sensor, the microchip presented some limitations: the particles were going too fast to be seen by the refractometric sensor, and most of the times were not located at the optical fiber core level. To circumvent this, the microfluidic channel was offset to match the OF core, but there were still constrains in acquiring the data relative to the RBCs. At this moment, it seemed obvious that optical trapping might be a possible solution to overcome this problem. This set the beginning of the research developed in this thesis, where optical fibers were developed for optical trapping of particles and cells, but also work as a preliminary way of testing structures that may be implemented within optofluidic chips.

The Center for Applied Photonics of INESC TEC has long been known for its capacities in optical fiber sensing of physical and chemical parameters. Nonetheless, the use of such tools for optical trapping had not yet been explored. In this regard, this thesis was the first approach of the laboratory to the field of optical trapping using optical fibers. Regarding the fabrication of the devices, these resulted from collaborations with the Masdar Institute of Science and Technology in the United Arab Emirates and with

the Institute de Science des Materiaux de Mulhouse (IS2M) in France. Concerning the trapping samples, such as cells and microalgae, these were provenient from collaborations with Instituto de Tecnologia Química e Biológica (ITQB) in Portugal and Centro Interdisciplinar de Investigação Marinha e Ambiental (Ciimar) also in Portugal.

An overview of the state of the art of optical fiber TIPs allowed to get a perception of the methods already used to fabricate these type of devices and their main capabilities. Optical fibers modified using fiber polishing, chemical etching and thermal processes are prone to be rather simple. The normal structure achieved with these methods are spherical and axicone tips. However, using a more complex optical fiber, then just a single mode one, leads to more complex and interesting configurations. For instance, multiple core OFs can be polished in an adequate angle causing a superposition of each beam at the same position, increasing the numerical aperture of the fiber, thus generating stronger electric field gradients. Besides this, OF tappers achieved by thermal pulling have been atatched to micro spheres to create nanojects, for near field trapping due to their sub-wavelength beams. These examples illustrate some of the improvements that can be done to upgrade the performance of OF TIPs fabricated by relatively simple and cheap methods. On the contrary, high resolution methods, such as FIB milling and TPL are naturally more flexibility in the fabrication of more complex structures. In this context, the key to maintain the growth of the OF trapping area is to conjugate different fabrication methods and OFs with special properties.

Regarding the polymeric micro structures an extensive description of the optimization process from the the design, fabrication to the analysis of polymeric OF TIPs was presented. A preliminary test allowed to conclude that the optical mode excited during the photo-polymerization of the structures on the top of the OFs played an important role in the output field pattern. In this regard, the fabrication features were adjusted so that the shape of the structures resembles a spherical lens. The best conjugation of parameters was: excitation of the fundamental Gaussian or LP_{01} mode, using an exposure time of $10\,s$, a power of $6\,\mu W$ and a monomer mixture (PETIA) with $0.1 - 0.2\,\%$ of photo initiator (Irgacure) in weight. Simultaneously, some computational simulations were performed to validate the optical forces generated by these type of structures on dielectric particles, indicating that 2D trapping was feasible. The trapping of yeast cells and organelles of plant cells was thereafter demonstrated, validating the use of these tools for optical trapping. Nevertheless, there is still room for improvement in this topic.

For instance, in the future OFs with polymeric tips may be combined with a detection system of particles/cells, as the one demonstrated in FPP TIPs, to simultaneously trap and detect them. Furthermore, modification on the polymer refractive index, leading to stronger trapping effects, leading to 3D trapping, may be implemented. The dimensions of the micro structures are somehow limited by the features of the OF core, therefore, fabrication of polymeric structures on mode expanded OFs will allow to have a higher range of curvature radius available. Finally, by functionalizing the polymer structures, sensing capabilities in the trapping devices may be implemented. Nevertheless, other uses can be envisaged for such structures in different applications.

FIB milling enabled the fabrication of diffractive structures, such as Fresnel zone and phase plates, on the top of mode expanded OF tips. Computational simulations assisted the design and study of the fib milled structures, predicting the expected effects. The phase plates were tested with $8\,\mu m$ PMMA particles and $4-5\,\mu m$ yeast cells, demonstrating 2D trapping abilities. In addition to this, the OFs were used for particle detection, being able to differentiate particles/cells with different sizes. To optimize these devices, advances on the fabrication are necessary to accomplish higher phase steps leading to the improvement of the output optical field patterns. Besides this, the particle/cells detection measurements should be repeated for a wider range of samples. Contrary to the phase plates, the zone plates were not positively evaluated for trapping due to the generation of micro bubbles. These are caused by micro-defects existent on the fiber tip, where there is still metal. In addition, around these bubbles, the Marangoni effect is visible by the flow of particles towards the surface of the bubble, precluding optical trapping effects.

Besides FZP and FPP, the fabrication of spiral phase plate on the top of SM OF were accomplished through FIB milling. This last configuration introduces the rotation movement to the trapped micro objects. This is due to the transformation of the Gaussian beam into a vortex beam, which possesses orbital angular momentum. The OFs were analyzed and the output vortex beam was verified using the interferometric technique, were the beam is made interfere with a reference Gaussian beam. This led to an interference pattern with the so called 'forklet', demonstrating the presence of the vortex of charge 1. The transference of OAM from the beam to the particles leads to the rotation of the second. This was proved using particles with distinct dimensions: 1, and $4\,\mu m$. Nevertheless, with microalgae with $25\,\mu m$ of diameter, rotation around its own axis was visible. This demonstrates that the induced movement depends of the size of the micro particle used and their position in the beam cross section. Also the rotation frequency is larger for smaller particles, and increases with the beam power.

The improvement of these devices could be achieved by increasing the phase step, or change the wavelength to generate a perfect doughnut beam. Also the conjugation of the existing setup with backscattered data, can provide more information on the particles rotation dynamics.

To summarize, the developments on optical fiber trapping reported in this thesis hold great potential for immobilization and manipulation of different targets (dielectric particles, cells, microalgae). Beyond this, the flexibility of OF platforms offer the possibility to introduce further analytical sensing techniques leading to more advanced devices suitable to biomedical environments.

References

[1] J. Kepler. *De Cometis Libelli Tres*. 1619.

[2] A. Ashkin. Acceleration and Trapping of Particles by Radiation Pressure. *Physical Review Letters*, 24(4):156–159, jan 1970.

[3] A. Constable, J. Kim, J. Mervis, F. Zarinetchi, and M. Prentiss. Demonstration of a fiber-optical light-force trap. *Optics Letters*, 18(21):1867, nov 1993.

[4] E. R. Lyons and G. J. Sonek. Confinement and bistability in a tapered hemispherically lensed optical fiber trap. *Applied Physics Letters*, 66(13):1584, mar 1995.

[5] M. Ikeda, M. Kashihara, and T. Ogawa. Optical trapping using optical fibres. *Proc. 5th Sino-Japanese Joint Meeting*, pages B22–B27, 1995.

[6] E. K. Sackmann, A. L. Fulton, and D. J. Beebe. The present and future role of microfluidics in biomedical research. *Nature*, 507(7491):181–189, mar 2014.

[7] G. M. Whitesides. The origins and the future of microfluidics. *Nature*, 442(7101):368–373, jul 2006.

[8] D. Psaltis, S. R. Quake, and C. Yang. Developing optofluidic technology through the fusion of microfluidics and optics. *Nature*, 442(7101):381–386, jul 2006.

[9] C. Monat, P. Domachuk, and B. J. Eggleton. Integrated optofluidics: A new river of light. *Nature Photonics*, 1(2):106–114, feb 2007.

[10] Y. Fainman. *Optofluidics : fundamentals, devices, and applications*. McGraw-Hill, 2010.

[11] A. R. Hawkins and H. Schmidt. *Handbook of optofluidics*. CRC Press, 2010.

[12] X. Fan and I. M. White. Optofluidic microsystems for chemical and biological analysis. *Nature Photonics*, 5(10):591–597, sep 2011.

[13] L. Kelemen, P. Ormos, and S. Valkai. Integrated optical motor. *Applied Optics, Vol. 45, Issue 12, pp. 2777-2780*, 45(12):2777–2780, 2006.

[14] J. Kohler, S. I. Ksouri, C. Esen, and A. Ostendorf. Optical screw-wrench for microassembly. *Microsystems & Nanoengineering*, 3:16083, feb 2017.

[15] S. Maruo, A. Takaura, and Y. Saito. Optically driven micropump with a twin spiral microrotor. *Optics Express*, 17(21):18525, oct 2009.

[16] M. J. Villangca, D. Palima, A. R. Bañas, and J. Glückstad. Light-driven micro-tool equipped with a syringe function. *Light: Science & Applications*, 5(9):e16148, apr 2016.

[17] I. Heller, G. Sitters, O. D. Broekmans, G. Farge, C. Menges, W. Wende, S. W. Hell, E. J. G. Peterman, and G. J. L. Wuite. STED nanoscopy combined with optical tweezers reveals protein dynamics on densely covered DNA. *Nature Methods*, 10(9):910–916, aug 2013.

[18] Z. Yang, P. Haslehurst, S. Scott, N. Emptage, and K. Dholakia. A compact light-sheet microscope for the study of the mammalian central nervous system. *Scientific Reports*, 6:26317, may 2016.

[19] Z. Yang, P. Piksarv, D. E. Ferrier, F. J. Gunn-Moore, and K. Dholakia. Macro-optical trapping for sample confinement in light sheet microscopy. *Biomedical Optics Express*, 6(8):2778, aug 2015.

[20] M.-C. Zhong, X.-B. Wei, J.-H. Zhou, Z.-Q. Wang, and Y.-M. Li. Trapping red blood cells in living animals using optical tweezers. *Nature Communications*, 4:1768, apr 2013.

[21] P. L. Johansen, F. Fenaroli, L. Evensen, G. Griffiths, and G. Koster. Optical micromanipulation of nanoparticles and cells inside living zebrafish. *Nature Communications*, 7:10974, mar 2016.

[22] E. Papagiakoumou. Optical developments for optogenetics. *Biology of the Cell*, 105(10), jul 2013.

[23] Thorlabs. https://www.thorlabs.com/navigation.cfm?guide_id=2323, 2017-02-13, Optical Tweezers Systems.

[24] Nikon. Optical Tweezers, https://www.nikoninstruments.com/en_EU/Learn-Explore/Techniques/Optical-Tweezers, 2017-02-13.

[25] Zeiss Germany. https://www.zeiss.com/microscopy/int/products/laser-microdissection/microtweezers.html, 2017-04-11, MicroTweezers Microscope.

[26] Elliot Scientific. http://www.elliotscientific.com/Optical-Tweezers, 2017-02-13, Optical Tweezers Systems.

[27] F. Pereira, I. Bernacka-Wojcik, R. Ribeiro, M. Lobato, E. Fortunato, R. Martins, R. Igreja, P. Jorge, H. Águas, and A. Oliva. Hybrid Microfluidic Platform for Multifactorial Analysis Based on Electrical Impedance, Refractometry, Optical Absorption and Fluorescence. *Micromachines 2016, Vol. 7, Page 181*, 7(10):181, 2016.

[28] A. Ashkin, J. M. Dziedzic, J. E. Bjorkholm, and S. Chu. Observation of a single-beam gradient force optical trap for dielectric particles. *Optics Letters*, 11(5):288, may 1986.

[29] A. Ashkin. Forces of a single-beam gradient laser trap on a dielectric sphere in the ray optics regime. *Biophysical journal*, 61(2):569–82, feb 1992.

[30] K. C. Neuman and S. M. Block. Optical trapping. *The Review of scientific instruments*, 75(9):2787–809, sep 2004.

[31] S. Prahl. Optical Absorption of Water Compendium, 1998.

[32] K. Dholakia, P. Reece, and M. Gu. Optical micromanipulation. *Chemical Society reviews*, 37(1):42–55, jan 2008.

[33] W. D. Phillips, J. V. Prodan, and H. J. Metcalf. Laser cooling and electromagnetic trapping of neutral atoms, 1985.

[34] A. Ashkin. Optical trapping and manipulation of neutral particles using lasers. *Proceedings of the National Academy of Sciences*, 94(10):4853–4860, may 1997.

[35] A. Ashkin. History of optical trapping and manipulation of small-neutral particle, atoms, and molecules. *IEEE Journal of Selected Topics in Quantum Electronics*, 6(6):841–856, nov 2000.

[36] J. Estève. Cold atoms: Trapped by nanostructures. *Nature Nanotechnology*, 8(5):317–318, may 2013.

[37] F. M. Fazal and S. M. Block. Optical tweezers study life under tension, 2011.

[38] I. A. Sparkes, T. Ketelaar, N. C. A. de Ruijter, and C. Hawes. Grab a Golgi: laser trapping of Golgi bodies reveals in vivo interactions with the endoplasmic reticulum. *Traffic (Copenhagen, Denmark)*, 10(5):567–71, may 2009.

[39] M. D. Wang, H. Yin, R. Landick, J. Gelles, and S. M. Block. Stretching DNA with Optical Tweezers. *Biophys Journal*, 72:1335–1346, 1997.

[40] R. Dasgupta, R. S. Verma, and P. K. Gupta. Microfluidic sorting with blinking optical traps. *Optics letters*, 37(10):1739–41, may 2012.

[41] E. O. Eriksson, D. Engström, J. Scrimgeour, and M. Goksör. Automated focusing of nuclei for timelapse experiments on single cells using holographic optical tweezers. *Opt. Express*, 17(7):5585–5594, 2009.

[42] A. Bankapur, E. Zachariah, S. Chidangil, M. Valiathan, and D. Mathur. Raman tweezers spectroscopy of live, single red and white blood cells. *PloS one*, 5(4):e10427, jan 2010.

[43] D. J. Stevenson, F. Gunn-Moore, and K. Dholakia. Light forces the pace: optical manipulation for biophotonics. *Journal of Biomedical Optics*, 15(4):041503, 2010.

[44] K. Ramser and D. Hanstorp. Optical manipulation for single-cell studies. *Journal of biophotonics*, 3(4):187–206, apr 2010.

[45] Y.-F. Chen, L. Jiang, M. Mancuso, A. Jain, V. Oncescu, and D. Erickson. Optofluidic opportunities in global health, food, water and energy. *Nanoscale*, 4(16):4839–57, aug 2012.

[46] R. Slaik, J. Homola, J. Ctyroky, and E. Brynda. Novel spectral fiber optic sensor based on surface plasmon resonance. *Sensors and Actuators B: Chemical*, 74(1):106–111, 2001.

[47] E. Klantsataya, P. Jia, H. Ebendorff-Heidepriem, T. Monro, and A. François. Plasmonic Fiber Optic Refractometric Sensors: From Conventional Architectures to Recent Design Trends. *Sensors*, 17(1):12, dec 2016.

[48] K. Taguchi, H. Ueno, T. Hiramatsu, and M. Ikeda. Optical trapping of dielectric particle and biological cell using optical fibre. *Electronics Letters*, 33(5):413, 1997.

[49] K. Taguchi, M. Tanaka, and M. Ikeda. Dual-Beam Trapping Method for an Object with Large Relative Refractive Index. *Japanese Journal of Applied Physics*, 39(Part 2, No. 12B):L1302–L1304, dec 2000.

[50] K. Taguchi, K. Atsuta, T. Nakata, and M. Ikeda. Levitation of a microscopic object using plural optical fibers. *Optics Communications*, 176(1-3):43–47, mar 2000.

[51] C. Liberale, P. Minzioni, I. Cristiani, M. Graecia, and V. Europa. All Optical 3-D Trapping through Single-Fiber Tweezer. page 88100, 2001.

[52] K. Taguchi, M. Tanaka, Y. Takahashi, K. Atsuta, and M. Ikeda. Three dimensional optical trapping using plural optical fibers. In *Conference Digest. 2000 Conference on Lasers and Electro-Optics Europe (Cat. No.00TH8505)*, page 1. IEEE, 2000.

[53] M. Ikeda, K. Tanaka, M. Kittaka, M. Tanaka, and T.-a. Shohata. Rotational manipulation of a symmetrical plastic micro-object using fiber optic trapping. *Optics Communications*, 239(1-3):103–108, sep 2004.

[54] C. Liberale, P. Minzioni, and I. Cristiani. All Optical 3-D Trapping through a Single-Fiber Tweezer. In *2007 European Conference on Lasers and Electro-Optics and the International Quantum Electronics Conference*, pages 1–1. IEEE, jun 2007.

[55] I. Cristiani, C. Liberale, and P. Minzioni. Method and optical device for trapping a particle, 2007.

[56] Y. Zhang, Z. Liu, J. Yang, and L. Yuan. A non-contact single optical fiber multi-optical tweezers probe: Design and fabrication. *Optics Communications*, 285(20):4068–4071, sep 2012.

[57] H. Zhao, G. Farrell, P. Wang, and L. Yuan. Investigation of Particle Harmonic Oscillation Using Four-Core Fiber Integrated Twin-Tweezers. *IEEE Photonics Technology Letters*, 28(4):461–464, feb 2016.

[58] Z. Liu, Y. Chen, L. Zhao, Y. Zhang, Y. Wei, H. Li, Y. Liu, Y. Zhang, E. Zhao, X. Yang, J. Zhang, and L. Yuan. Single-fiber tweezers applied for dye lasing in a fluid droplet. *Optics Letters*, 41(13):2966, jul 2016.

[59] G. Y. Chen, M. Ding, T. P. Newson, and G. Brambilla. A Review of Microfiber and Nanofiber Based Optical Sensors. *The Open Optics Journal*, 7(1), dec 2013.

[60] Z. Liu, C. Guo, J. Yang, and L. Yuan. Tapered fiber optical tweezers for microscopic particle trapping: fabrication and application. *Optics Express*, 14(25):12510, dec 2006.

[61] H. Xin, Y. Li, L. Li, R. Xu, and B. Li. Optofluidic manipulation of Escherichia coli in a microfluidic channel using an abruptly tapered optical fiber. *Applied Physics Letters*, 103(3):033703, jul 2013.

[62] H. Xin, Q. Liu, and B. Li. Non-contact fiber-optical trapping of motile bacteria: dynamics observation and energy estimation. *Scientific reports*, 4:6576, jan 2014.

[63] W. Wright, G. Sonek, Y. Tadir, and M. Berns. Laser trapping in cell biology. *IEEE Journal of Quantum Electronics*, 26(12):2148–2157, 1990.

[64] K. S. Abedin, C. Kerbage, A. Fernandez-Nieves, and D. a. Weitz. Optical manipulation and rotation of liquid crystal drops using high-index fiber-optic tweezers. *Applied Physics Letters*, 91(9):091119, aug 2007.

[65] H. Xin, R. Xu, and B. Li. Optical trapping, driving, and arrangement of particles using a tapered fibre probe. *Scientific reports*, 2:818, jan 2012.

[66] H. Xin, R. Xu, and B. Li. Optical formation and manipulation of particle and cell patterns using a tapered optical fiber. *Laser & Photonics Reviews*, 7(5):801–809, sep 2013.

[67] X. Liu, J. Huang, Y. Li, Y. Zhang, and B. Li. Rotation and deformation of human red blood cells with light from tapered fiber probes. *Nanophotonics*, 6(1):309–316, jan 2017.

[68] L. Yuan, Z. Liu, J. Yang, and C. Guan. Twin-core fiber optical tweezers. *Optics Express*, 16(7):4559, mar 2008.

[69] A. L. Barron, A. K. Kar, T. J. Aspray, A. J. Waddie, M. R. Taghizadeh, and H. T. Bookey. Two dimensional interferometric optical trapping of multiple particles and Escherichia coli bacterial cells using a lensed multicore fiber. *Optics express*, 21(11):13199–207, jun 2013.

[70] M. S. Ferreira, J. Bierlich, S. Unger, K. Schuster, J. L. Santos, and O. Frazão. Optical Phase Refractometer Based on Post-Processed Interferometric Tip Sensors. *J. Lightwave Technol.*, 32(17):3002–3007, 2014.

[71] L. Coelho, J. M. M. M. de Almeida, J. L. Santos, and D. Viegas. Fiber optic hydrogen sensor based on an etched Bragg grating coated with palladium. *Applied Optics*, 54(35):10342, dec 2015.

[72] R. M. André, S. C. Warren-Smith, M. Becker, J. Dellith, M. Rothhardt, M. I. Zibaii, H. Latifi, M. B. Marques, H. Bartelt, and O. Frazão. Simultaneous measurement of temperature and refractive index using focused ion beam milled Fabry-Perot cavities in optical fiber micro-tips. *Optics Express*, 24(13):14053, jun 2016.

[73] J. Bierlich, J. Kobelke, D. Brand, K. Kirsch, J. Dellith, and H. Bartelt. Nanoscopic tip sensors fabricated by gas phase etching of optical glass fibers. *Photonic Sensors*, 2(4):331–339, oct 2012.

[74] D. R. Turner. Immiscible liquid layer on top of etching liquid, sep 1984.

[75] P. Hoffmann, B. Dutoit, and R.-P. Salathé. Comparison of mechanically drawn and protection layer chemically etched optical fiber tips. *Ultramicroscopy*, 61(1-4):165–170, dec 1995.

[76] R. Stockle, C. Fokas, V. Deckert, R. Zenobi, B. Sick, B. Hecht, and U. P. Wild. High-quality near-field optical probes by tube etching. *Applied Physics Letters*, 75(2):160, jul 1999.

[77] K. S. Mohanty, C. Liberale, S. K. Mohanty, and V. Degiorgio. In depth fiber optic trapping of low-index microscopic objects. *Applied Physics Letters*, 92(15):151113, apr 2008.

[78] S. K. Mohanty, K. S. Mohanty, and M. W. Berns. Organization of microscale objects using a microfabricated optical fiber. *Optics Letters*, 33(18):2155, sep 2008.

[79] Y. Gong, A.-Y. Ye, Y. Wu, Y.-J. Rao, Y. Yao, and S. Xiao. Graded-index fiber tip optical tweezers: Numerical simulation and trapping experiment. *Optics Express*, 21(13):16181, jun 2013.

[80] P. A. R. Tafulo, P. A. S. Jorge, J. L. Santos, F. M. Araujo, and O. Frazao. Intrinsic Fabry Perot Cavity Sensor Based on Etched Multimode Graded Index Fiber for Strain and Temperature Measurement. *IEEE Sensors Journal*, 12(1):8–12, jan 2012.

[81] R. Watkins, P. Rockett, S. Thoms, R. Clampitt, and R. Syms. Focused ion beam milling. *Vacuum*, 36(11-12):961–967, nov 1986.

[82] J. Melngailis. Focused ion beam technology and applications. *Journal of Vacuum Science & Technology B: Microelectronics and Nanometer Structures*, 5(2):469, mar 1987.

[83] S. Cabrini, C. Liberale, D. Cojoc, A. Carpentiero, M. Prasciolu, S. Mora, V. Degiorgio, F. De Angelis, and E. Di Fabrizio. Axicon lens on optical fiber forming optical tweezers, made by focused ion beam milling. *Microelectronic Engineering*, 83(4-9):804–807, apr 2006.

[84] C. Liberale, P. Minzioni, F. Bragheri, F. De Angelis, E. Di Fabrizio, and I. Cristiani. Miniaturized all-fibre probe for three-dimensional optical trapping and manipulation. *Nature Photonics*, 1(12):723–727, nov 2007.

[85] P. Minzioni, F. Bragheri, C. Liberale, E. Di Fabrizio, and I. Cristiani. A Novel Approach to Fiber-Optic Tweezers: Numerical Analysis of the Trapping Efficiency. *IEEE Journal of Selected Topics in Quantum Electronics*, 14(1):151–157, 2008.

[86] C. Liberale, G. Cojoc, F. Bragheri, P. Minzioni, G. Perozziello, R. La Rocca, L. Ferrara, V. Rajamanickam, E. Di Fabrizio, and I. Cristiani. Integrated microfluidic device for single-cell trapping and spectroscopy. *Scientific reports*, 3:1258, jan 2013.

[87] Y. Liu, H. Xu, F. Stief, N. Zhitenev, and M. Yu. Far-field superfocusing with an optical fiber based surface plasmonic lens made of nanoscale concentric annular slits. *Optics express*, 19(21):20233–43, oct 2011.

[88] Y. Liu, F. Stief, and M. Yu. Subwavelength optical trapping with a fiber-based surface plasmonic lens. *Optics Letters*, 38(5):721, mar 2013.

[89] M. Madou. *Manufacturing Techniques for Microfabrication and Nanotechnology, volume 11*. CRC Press, 2011.

[90] M. Farsari and B. N. Chichkov. Materials processing: Two-photon fabrication. *Nature Photonics*, 3(8):450–452, aug 2009.

[91] S. Cabrini and S. Kawata, editors. *Nanofabrication Handbook*. CRC Press, 2012.

[92] C. Liberale, G. Cojoc, P. Candeloro, G. Das, F. Gentile, F. De Angelis, and E. Di Fabrizio. Micro-Optics Fabrication on Top of Optical Fibers Using Two-Photon Lithography. *IEEE Photonics Technology Letters*, 22(7):474–476, apr 2010.

[93] A. Cusano. *Lab-on-Fiber Technology*, volume 56 of *Springer Series in Surface Sciences*. Springer International Publishing, Cham, 2015.

[94] A. Koshelev, G. Calafiore, C. Piña-Hernandez, F. I. Allen, S. Dhuey, S. Sassolini, E. Wong, P. Lum, K. Munechika, and S. Cabrini. High refractive index Fresnel lens on a fiber fabricated by nanoimprint lithography for immersion applications. *Optics Letters*, 41(15):3423, aug 2016.

[95] Photonics on a fiber - aBeam technologies.

[96] H. Huang, S. Chen, H. Zou, Q. Li, J. Fu, F. Lin, and X. Wu. Fabrication of micro-axicons using direct-laser writing. *Optics express*, 22(9):11035–42, may 2014.

[97] S. Valkai, L. Oroszi, and P. Ormos. Optical tweezers with tips grown at the end of fibers by photopolymerization. *Applied Optics*, 48(15):2880, may 2009.

[98] J. Kim, S. Lee, Y. Jeong, J.-K. Kim, Y. Jung, F. Merenda, R.-P. Salathè, J.-S. Shin, and K. Oh. Crossed fiber optic Bessel beams for curvilinear optofluidic transport of dielectric particles. *Optics express*, 21(20):23021–9, oct 2013.

[99] S. Chen, H. Huang, H. Zou, Q. Li, J. Fu, F. Lin, and X. Wu. Optical manipulation of biological particles using LP 21 mode in fiber. *Journal of Optics*, 16(12):125302, dec 2014.

[100] Y.-C. Li, H.-B. Xin, H.-X. Lei, L.-L. Liu, Y.-Z. Li, Y. Zhang, and B.-J. Li. Manipulation and detection of single nanoparticles and biomolecules by a photonic nanojet. *Light: Science & Applications*, 5(12):e16176, jun 2016.

[101] Y. Li, H. Xin, X. Liu, Y. Zhang, H. Lei, and B. Li. Trapping and Detection of Nanoparticles and Cells Using a Parallel Photonic Nanojet Array. *ACS nano*, may 2016.

[102] C. Liberale, S. K. Mohanty, K. S. Mohanty, V. Degiorgio, S. Cabrini, A. Carpentiero, E. Ferrari, D. Cojoc, and E. Di Fabrizio. Optical micromanipulation of microscopic particles using axicon tipped fiber. page 60950F. International Society for Optics and Photonics, feb 2006.

[103] C. Liberale, G. Cojoc, F. Bragheri, P. Minzioni, G. Perozziello, R. La Rocca, L. Ferrara, V. Rajamanickam, E. Di Fabrizio, and I. Cristiani. Integrated microfluidic device for single-cell trapping and spectroscopy. *Scientific reports*, 3:1258, jan 2013.

[104] R. Bachelot, C. Ecoffet, D. Deloeil, P. Royer, and D.-J. Lougnot. Integration of Micrometer-Sized Polymer Elements at the End of Optical Fibers by Free-Radical Photopolymerization. *Applied Optics*, 40(32):5860, 2001.

[105] M. Hocine, R. Bachelot, C. Ecoffet, N. Fressengeas, P. Royer, and G. Kugel. End-of-fiber polymer tip: manufacturing and modeling. *Synthetic Metals*, 127(1):313–318, 2002.

[106] R. Bachelot, A. Fares, R. Fikri, D. Barchiesi, G. Lerondel, and P. Royer. Coupling semiconductor lasers into single-mode optical fibers by use of tips grown by photopolymerization. *Optics Letters*, 29(17):1971, 2004.

[107] K. Matyjaszewski and T. P. Davis. *Handbook of Radical Polymerization*, volume 125. 2002.

[108] S. Jradi, O. Soppera, D. J. Lougnot, R. Bachelot, and P. Royer. Tailoring the geometry of polymer tips on the end of optical fibers via control of physico-chemical parameters. *Optical Materials*, 31(4):640–646, feb 2009.

[109] O. Soppera, C. Turck, and D. J. Lougnot. Fabrication of micro-optical devices by self-guiding photopolymerization in the near IR. *Optics Letters*, 34(4):461, feb 2009.

[110] A. S. Kewitsch and A. Yariv. Self-focusing and self-trapping of optical beams upon photopolymerization. *Optics Letters*, 21(1):24, jan 1996.

[111] J. Orloff, M. Utlaut, and L. Swanson. *High resolution focused ion beams: FIB and its applications*. Springer Science+ Business Media New York, 2002.

[112] L. Reimer. *Scanning Electron Microscopy*, volume 45 of *Springer Series in Optical Sciences*. Springer Berlin Heidelberg, Berlin, Heidelberg, 2nd edition, 1998.

[113] P. Munroe. The application of focused ion beam microscopy in the material sciences. *Materials Characterization*, 60(1):2–13, jan 2009.

[114] C. A. Volkert and A. M. Minor. Focused Ion Beam Microscopy and Micromachining. *MRS Bulletin*, 32(05):389–399, 2007.

[115] S. Reyntjens and R. Puers. A review of focused ion beam applications in microsystem technology. *Journal of Micromechanics and Microengineering*, 11(4):287–300, jul 2001.

[116] FEI-Company. Quanta 3D FEG 200/600 User Operation Manual, 2010.

[117] A. Taflove and S. C. Hagness. *Computational electrodynamics : the finite-difference time-domain method*. Artech House, 2005.

[118] A. F. Oskooi, D. Roundy, M. Ibanescu, P. Bermel, J. Joannopoulos, and S. G. Johnson. Meep: A flexible free-software package for electromagnetic simulations by the FDTD method. *Computer Physics Communications*, 181(3):687–702, mar 2010.

[119] Kane Yee. Numerical solution of initial boundary value problems involving maxwell's equations in isotropic media. *IEEE Transactions on Antennas and Propagation*, 14(3):302–307, may 1966.

[120] U. S. Inan and R. A. Marshall. *Numerical electromagnetics : the FDTD method*. Cambridge University Press, 2011.

[121] K. Svoboda and S. M. Block. Biological Applications of Optical Forces. *Annual Review of Biophysics and Biomolecular Structure*, 23(1):247–285, jun 1994.

[122] I. F. Sbalzarini and P. Koumoutsakos. Feature point tracking and trajectory analysis for video imaging in cell biology. *Journal of structural biology*, 151(2):182–95, aug 2005.

[123] L. G. Cohen and M. V. Schneider. Microlenses for coupling junction lasers to optical fibers. *Applied optics*, 13(1):89–94, jan 1974.

[124] O. Frazão, P. Caldas, J. L. Santos, P. V. S. Marques, C. Turck, D. J. Lougnot, and O. Soppera. Fabry-Perot refractometer based on an end-of-fiber polymer tip. *Optics Letters*, 34(16):2474, aug 2009.

[125] P. A. S. Jorge, C. Maule, O. Soppera, and P. V. S. Marques. Rapid Fabrication of Dual Analyte Luminescent Optrodes by Self-Guiding Photo-Polymerization. *IEEE Photonics Technology Letters*, 23(8):492–494, apr 2011.

[126] S. P. Gross. Application of optical traps in vivo. *Methods in enzymology*, 361:162–74, jan 2003.

[127] Thorlabs. Single Mode Fiber: 980 / 1064 / 1550 nm, 2015.

[128] K. Taguchi, M. Tanaka, and M. Ikeda. Investigation on the radius of a hemispherical microlens of an optical fiber end for three-dimensional trapping. *Optical and Quantum Electronics*, 34(10):993–999, 2002.

[129] N. Sultanova, S. Kasarova, and I. Nikolov. Dispersion Properties of Optical Polymers. *Acta Physica Polonica A*, 116(4), 2009.

[130] Sigrist-Photometer AG. Refractive Index.

[131] D. R. Rines, D. Thomann, J. F. Dorn, P. Goodwin, and P. K. Sorger. Live cell imaging of yeast. *Cold Spring Harbor protocols*, 2011(9), sep 2011.

[132] Y. Park, M. Diez-Silva, G. Popescu, G. Lykotrafitis, W. Choi, M. S. Feld, and S. Suresh. Refractive index maps and membrane dynamics of human red blood cells parasitized by Plasmodium falciparum. *Proceedings of the National Academy of Sciences of the United States of America*, 105(37):13730–5, sep 2008.

[133] Red Blood Cell (RBC) Size Variation, LabCE.com, Laboratory Continuing Education.

[134] K. Taguchi, K. Atsuta, T. Nakata, and M. Ikeda. Single laser beam fiber optic trap. *Optical and Quantum Electronics*, 33(1):99–106, 2001.

[135] Z. Hu, J. Wang, and J. Liang. Manipulation and arrangement of biological and dielectric particles by a lensed fiber probe. *Optics Express*, 12(17):4123, aug 2004.

[136] J. E. Molloy and M. J. Padgett. Lights, action: Optical tweezers. *Contemporary Physics*, 43(4):241–258, 2002.

[137] M. Woerdemann, C. Alpmann, M. Esseling, and C. Denz. Advanced optical trapping by complex beam shaping. *Laser & Photonics Reviews*, 7(6):839–854, nov 2013.

[138] A. H. J. Yang, S. D. Moore, B. S. Schmidt, M. Klug, M. Lipson, and D. Erickson. Optical manipulation of nanoparticles and biomolecules in sub-wavelength slot waveguides. *Nature*, 457(7225):71–75, jan 2009.

[139] E. Schonbrun, C. Rinzler, and K. B. Crozier. Microfabricated water immersion zone plate optical tweezer. *Applied Physics Letters*, 92(7):071112, feb 2008.

[140] J.-N. Kuo and H.-Z. Hu. Optical Trapping of Beads and Jurkat Cells Using Micromachined Fresnel Zone Plate Integrated with Microfluidic Chip. *Japanese Journal of Applied Physics*, 50(10):100211, oct 2011.

[141] J. K. Kim, J. Kim, K. Oh, I.-B. Sohn, W. Shin, H. Y. Choi, and B. Lee. Fabrication of Micro Fresnel Zone Plate Lens on a Mode-Expanded Hybrid Optical Fiber Using a Femtosecond Laser Ablation System. *IEEE Photonics Technology Letters*, 21(1):21–23, jan 2009.

[142] J. Kim, W. Ha, J. Park, J. K. Kim, I.-B. Sohn, W. Shin, and K. Oh. Micro Fresnel Zone Plate Lens Inscribed on a Hard Polymer Clad Fiber Using Femtosecond Pulsed Laser. *IEEE Photonics Technology Letters*, 25(8):761–763, apr 2013.

[143] D. C. O'Shea and Society of Photo-optical Instrumentation Engineers. *Diffractive optics : design, fabrication, and test*. SPIE, 2004.

[144] E. Hecht. *Optics*. Addison Wesley, 4th edition, 2002.

[145] T. Hansch, editor. *Handbook of Lasers and Optics*. Springer International Publishing, 2013.

[146] C. A. Schneider, W. S. Rasband, and K. W. Eliceiri. NIH Image to ImageJ: 25 years of image analysis. *Nature Methods*, 9(7):671–675, jun 2012.

[147] R. S. Rodrigues Ribeiro, P. Dahal, A. Guerreiro, P. Jorge, and J. Viegas. Optical fibers as beam shapers: from Gaussian beams to optical vortices. *Optics Letters*, 41(10):2137, may 2016.

[148] R. Janeiro, R. Flores, P. Dahal, and J. Viegas. Fabrication of a phase photon sieve on an optical fiber tip by focused ion beam nanomachining for improved fiber to silicon photonics waveguide light coupling. *Optics Express*, 24(11):11611, may 2016.

[149] S. E. S. Spesyvtseva and K. Dholakia. Trapping in a Material World. *ACS Photonics*, 3:719–736, 2016.

[150] A.-p. Yu, G. Chen, Z.-h. Zhang, Z.-q. Wen, L.-r. Dai, K. Zhang, S.-l. Jiang, Z.-x. Wu, Y.-y. Li, C.-t. Wang, and X.-g. Luo. Creation of Sub-diffraction Longitudinally Polarized Spot by Focusing Radially Polarized Light with Binary Phase Lens. *Scientific Reports*, 6(1):38859, dec 2016.

[151] R. S. Taylor and C. Hnatovsky. Growth and decay dynamics of a stable microbubble produced at the end of a near-field scanning optical microscopy fiber probe. *Journal of Applied Physics*, 95(12):8444–8449, jun 2004.

[152] D. W. Berry, N. R. Heckenberg, and H. Rubinszteindunlop. Effects associated with bubble formation in optical trapping. *Journal of Modern Optics*, 47(9):1575–1585, jul 2000.

[153] C. Zhao, Y. Xie, Z. Mao, Y. Zhao, J. Rufo, S. Yang, F. Guo, J. D. Mai, T. J. Huang, P. L. Coletta, and S. D. Evans. Theory and experiment on particle trapping and manipulation via optothermally generated bubbles. *Lab Chip*, 14(2):384–391, 2014.

[154] K. Zhang, A. Jian, X. Zhang, Y. Wang, Z. Li, H.-y. Tam, F. Zhang, Q. Zhu, and B. Wang. Laser-induced thermal bubbles for microfluidic applications. *Lab on a Chip*, 11(7):1389, 2011.

[155] J. H. Poynting. The Wave Motion of a Revolving Shaft, and a Suggestion as to the Angular Momentum in a Beam of Circularly Polarised Light. *Proceedings of the Royal Society A: Mathematical, Physical and Engineering Sciences*, 82(557):560–567, jul 1909.

[156] R. A. Beth. Mechanical Detection and Measurement of the Angular Momentum of Light. *Physical Review*, 50(2):115–125, jul 1936.

[157] L. Allen, M. W. Beijersbergen, R. J. C. Spreeuw, and J. P. Woerdman. Orbital angular momentum of light and the transformation of Laguerre-Gaussian laser modes. *Physical Review A*, 45(11):8185–8189, jun 1992.

[158] A. M. Yao and M. J. Padgett. Orbital angular momentum: origins, behavior and applications. *Advances in Optics and Photonics*, 3(2):161, may 2011.

[159] M. R. Dennis, K. O'Holleran, and M. J. Padgett. Chapter 5 Singular Optics: Optical Vortices and Polarization Singularities. *Progress in Optics*, 53:293–363, 2009.

[160] N. B. Simpson, K. Dholakia, L. Allen, and M. J. Padgett. Mechanical equivalence of spin and orbital angular momentum of light: an optical spanner. *Optics Letters*, 22(1):52, jan 1997.

[161] A. V. Arzola, P. Jákl, L. Chvátal, and P. Zemánek. Rotation, oscillation and hydrodynamic synchronization of optically trapped oblate spheroidal microparticles. *Optics express*, 22(13):16207–21, jun 2014.

[162] R. Dasgupta, S. Ahlawat, R. S. Verma, and P. K. Gupta. Optical orientation and rotation of trapped red blood cells with Laguerre-Gaussian mode. *Optics Express*, 19(8):7680, apr 2011.

[163] J. Lipfert, M. M. van Oene, M. Lee, F. Pedaci, and N. H. Dekker. Torque Spectroscopy for the Study of Rotary Motion in Biological Systems. *Chemical Reviews*, 115(3):1449–1474, feb 2015.

[164] X.-j. Liu, X. Liu, L.-C. Kwek, and C. H. Oh. Manipulating atomic states via optical orbital angular-momentum. *Frontiers of Physics in China*, 3(2):113–125, may 2008.

[165] D. Andrews. *Structured Light and its applications*. Elsevier, 2008.

[166] S. Li and Z. Wang. Generation of optical vortex based on computer-generated holographic gratings by photolithography. *Applied Physics Letters*, 103(14):141110, oct 2013.

[167] N. Londoño, E. Rueda, J. A. Gómez, and A. Lencina. Generation of optical vortices by using binary vortex producing lenses. *Applied optics*, 54(4):796–801, feb 2015.

[168] R. K. Tyson, M. Scipioni, and J. Viegas. Generation of an optical vortex with a segmented deformable mirror. *Applied Optics*, 47(33):6300, nov 2008.

[169] J. Courtial and M. Padgett. Performance of a cylindrical lens mode converter for producing Laguerre Gaussian laser modes. *Optics Communications*, 159(1-3):13–18, jan 1999.

[170] K. Sueda, G. Miyaji, N. Miyanaga, and M. Nakatsuka. Laguerre-Gaussian beam generated with a multilevel spiral phase plate for high intensity laser pulses. *Optics Express*, 12(15):3548, jul 2004.

[171] E. Brasselet, M. Malinauskas, A. Zukauskas, and S. Juodkazis. Photopolymerized microscopic vortex beam generators: Precise delivery of optical orbital angular momentum. *Applied Physics Letters*, 97(21):211108, nov 2010.

[172] S. Ramachandran and P. Kristensen. Optical vortices in fiber. *Nanophotonics*, 2(5-6):455–474, jan 2013.

[173] C. N. Alexeyev, A. N. Alexeyev, B. P. Lapin, G. Milione, and M. A. Yavorsky. Spin-orbit-interaction-induced generation of optical vortices in multihelicoidal fibers. *Physical Review A*, 88(6):063814, dec 2013.

[174] C. N. Alexeyev, B. P. Lapin, and M. A. Yavorsky. Helical core optical fibers maintaining propagation of a solitary optical vortex. *Physical Review A*, 78(1):013813, jul 2008.

[175] Y. V. Kartashov, V. A. Vysloukh, and L. Torner. Dynamics of topological light states in spiraling structures. *Optics letters*, 38(17):3414–7, sep 2013.

[176] P. Vayalamkuzhi, S. Bhattacharya, U. Eigenthaler, K. Keskinbora, C. T. Samlan, M. Hirscher, J. P. Spatz, and N. K. Viswanathan. Direct patterning of vortex generators on a fiber tip using a focused ion beam. *Optics Letters*, 41(10):2133, may 2016.

[177] R. Janeiro, R. Flores, A. R. Ribeiro, P. Jorge, and J. Viegas. Focused ion beam 3D nano-patterned optical fiber tips for advanced beam profile engineering. In G. von Freymann, W. V. Schoenfeld, R. C. Rumpf, and H. Helvajian, editors, *SPIE OPTO*, page 93740E. International Society for Optics and Photonics, mar 2015.

[178] M. Scipioni, R. K. Tyson, and J. Viegas. Mode purity comparison of optical vortices generated by a segmented deformable mirror and a static multilevel phase plate. *Applied Optics*, 47(28):5098, sep 2008.

[179] G. V. Bogatiryova and M. S. Soskin. Detection and metrology of optical vortex helical wave fronts. *Semicondoctur Physics, Quantum Electronics and Optoelectronics*, 6(2):254–258, 2003.

[180] S. M. Barnett and R. Loudon. On the electromagnetic force on a dielectric medium. *Journal of Physics B: Atomic, Molecular and Optical Physics*, 39:671–684, 2006.

Appendix A

The Barnett model of microscopic forces

A.1 Lorentz force on dipoles

The demonstration presented here follows the formulation of Barnett and Loudon reported in reference [180].

To compute the force acting on a medium composed of electric dipoles one considers the limit of two charges of equal magnitude but opposite sign, spaced by d. The dipole moment $\vec{p}$ is given by

$$\vec{p} = q\vec{r}'_+ - q\vec{r}'_- = q\vec{d}, \tag{A.1}$$

where $\vec{r}'_+$ and $\vec{r}'_-$ are the position of the positive and the negative charges, and $\vec{d} = \vec{r}'_+ - \vec{r}'_-$.

The total force acting on the electric dipole is the sum of the forces acting on each individual charges. Then making $\vec{r}'_- = \vec{r}$, one has

$$\vec{f} = q[\vec{e}(\vec{r} + \vec{d}) - \vec{e}(\vec{r})], \tag{A.2}$$

where $\overrightarrow{e}$ is the microscopic electric field

Expanding the field in Taylor series around $\vec{r}$ up to the first order yields for the x component of the force

$$\begin{aligned} f_x &= q[e_x(x+dx, y+dy, z+dz) - e_x(x,y,z)] \\ &= q[e_x(x,y,z) + dx\frac{\partial e_x}{\partial x} + dy\frac{\partial e_x}{\partial y} + dz\frac{\partial e_x}{\partial z} + \ldots - e_x(x,y,z)]. \end{aligned} \tag{A.3}$$

Then, up to the second order in $\vec{d}$, it holds that

$$\overrightarrow{f_x} = \vec{p}\cdot\nabla\overrightarrow{e_x}, \tag{A.4}$$

where $\vec{p}$ is the point dipole moment.

Considering all the Cartesian components (x, y, z) through the same process, one has the force written as

$$\vec{f} = \vec{p}\cdot\nabla\vec{e}. \tag{A.5}$$

The polarization is also described from the electric dipole moment,

$$\vec{P}(\vec{r}) = \sum_i \vec{p_i}\delta(\vec{r} - \vec{R_i}), \tag{A.6}$$

where $\vec{R_i}$ is the position of the dipole. The current density can be obtained from the derivative of the polarization in relation to time, by $\vec{j} = \frac{\partial\vec{P}}{\partial t}$. This fact together with equations (A.5) and (A.6) allows us to write the Lorentz force for a dipole in therms of the polarization

$$\vec{F} = (\vec{p}\cdot\nabla)\vec{e} + \frac{\partial\vec{p}}{\partial t}\times\vec{b}. \tag{A.7}$$

Then, the force density is given by

$$\vec{f'}_L^d = \left[(\vec{p}\cdot\nabla)\vec{e}(\vec{r}) + \frac{\partial\vec{p}}{\partial t}\times\vec{b}(\vec{r})\right]\delta(\vec{r} - \vec{R_i}), \tag{A.8}$$

or, more explicitly, as

$$\vec{f'}_L^d = (\vec{P}\cdot\nabla)\vec{e} + \frac{\partial\vec{P}}{\partial t}\times\vec{b}. \tag{A.9}$$

This expression gives the force density produced in the target medium considering that the medium is composed of dipoles in terms of the microscopic field.

Combining the previous results with the microscopic Maxwell equations leads to

$$f_i^d = P_j \nabla_i e_j + \frac{\partial}{\partial t} \left(\vec{P} \times \vec{b} \right)_i . \tag{A.10}$$

Considering an electrostatic problem, the time dependence vanishes, since the macroscopic polarization is $\vec{P} = \epsilon_0(\epsilon - 1)\vec{E}$, one has that

$$\vec{f^d} = \frac{1}{2}\epsilon_0 \left(\epsilon - 1\right) \nabla \vec{E}^2. \tag{A.11}$$

For monochromatic radiation, the electric field can be given as the real part of a complex macroscopic field. Then, the forces acting on dipoles are described by

$$f_i^d = \frac{1}{4}\epsilon_0 \left(\epsilon - 1\right) \nabla_i \mid E \mid^2 . \tag{A.12}$$

Appendix B

Diode laser and optical fibers specifications

B.1 Diode laser

Lumics - LU0980M500	
Wavelength	$980\,nm$
Power (maximum)	$500\,mW$
Current (maximum)	$750\,mA$
Thermistor resistance	$10\,kOhm$

Table B.1: Typical laser features for optimal operation.

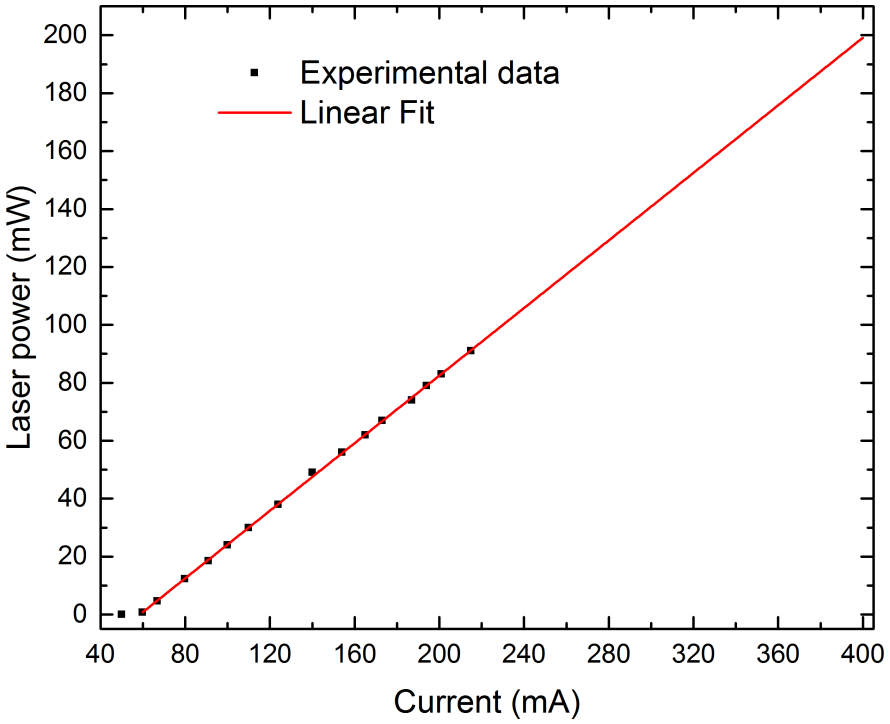

Figure B.1: Laser Lumics - LU0980M500 characterization: power versus current.

B.2 Optical fibers

Optical fiber	**Thorlabs SM** $980-5.8-125$	**Corning HI** 980	**Thorlabs AFS** 50/125**Y**
NA range	$0.13-0.15$ $@980\,nm, 1064\,nm, 1550\,nm$	0.21	0.22 ± 0.02
Silica index (cladding) @ 25^oC	$1.451@980\,nm$ $1.450@1064\,nm$ $1.444@1550\,nm$	-	-
Refractive index (core)	$1.457-1.458@980\,nm$ $1.456-1.457@1064\,nm$ $1.450-1.452@1550\,nm$	$1.471@651\,nm$	$1.45702@635\,nm$ $1.44692@1310\,nm$
Mode field diameter	$5.3-6.4\,\mu m@980\,nm$	$4.2\pm0.3@980nm$	-
Core diameter	-	$3.5\,\mu m$	$50\,\mu m\pm2\,\%$
Cladding diameter	$125\pm1\,\mu m$	$125.0\pm0.5\,\mu m$	$125.0\pm1.0\,\mu m$

Table B.2: Optical fiber data, provided by the suppliers.

Appendix C

Optical trapping video files

Examples of trapping videos acquired in the course of this thesis can be found in the following link Optical trapping with optical fibers.